GRID AND PIPE FLOW TURBULENCE IN POLYMER SOLUTIONS

John J Allan

Thesis submitted for the Degree of
Doctor of Philosophy

University of Edinburgh

May 1978

CONTENTS

DECLARATION

I declare

a) that this thesis has been composed by myself

and

b) that the work described is my own.

John J Allan
Department of Physics
University of Edinburgh
May 1978

ACKNOWLEDGEMENTS

I wish to thank the two supervisors of this research, Dr C A Greated and Dr W D McComb, for their encouragement and assistance. I gratefully acknowledge the financial support provided by the Science Research Council.

I am pleased to record my appreciation of the excellent and friendly technical support from Mr D Molyneux and to thank Mrs R Gosden for her patience and competence in the typing of the thesis.

I am grateful to my wife for her support and for her assistance with many of the tedious tasks in the preparation of the thesis. I am particularly indebted to my parents for their help and encouragement at all stages of my education.

ABSTRACT

The structure of Grid-generated and Pipe flow turbulence was measured in water and solutions of high molecular weight water soluble polymers. The effect of polyethyleneoxide (Polyox grade WSR 301) on Grid-generated turbulence was investigated using laser anemometry and flow visualisation technique. It was found that the polymer additive reduced both the turbulent intensity and the rate of decay behind the grid. At typical drag-reducing concentrations, turbulent energy spectra were qualitatively the same as those in water, in agreement with the results of other investigations. However, at higher additive concentrations, the dissipation range spectra showed noticeable attenuation. This seemed to be a threshold effect with onset at a polymer concentration between 100 and 250 ppm. This result was supported by photographs of dye-injection tracer but in this case the onset concentration for small-eddy suppression was between 50 and 100 ppm.

Polyox WSR 301 and a polyacrylamide (Separan AP 273) were studied in Pipe flow turbulence using laser anemometry. Mean velocity profiles did not follow "Virk's ultimate profile" but were well described by the model of Van Driest at conditions of less than maximum drag reduction. Turbulent intensity profiles were qualitatively in agreement with the results of others with higher values in the intermediate region than for Newtonian flow. Profiles of local dissipation rate were inferred from measurements of the energy spectrum. These indicated that dissipation is higher than for Newtonian flow in the intermediate region and lower in the turbulent core. The energy spectra showed a threshold concentration for non-Newtonian behaviour at lower concentrations than for Grid flow. The spectra were modified significantly at all flow positions with small eddy suppression in all cases, the amount of suppression reducing with distance from the pipe wall.

CHAPTER I

INTRODUCTION

1.1 GENERAL

The phenomenon now known as drag reduction was discovered by B A Toms in 1949. Toms found that the addition of a small amount of polymethylacrylate to a solution of monochlorobenzine greatly reduced the frictional losses in the turbulent flow of the solution through a pipe. Since then, a large number of solute-solvent combinations have been found to give a similar effect and, in particular, a number of high molecular weight polymers dissolved in water have been found to give strikingly high reductions in drag at remarkably low concentrations. (A 40% drag reduction has been achieved, White (1966) with a polymer concentration of 0.5 ppm and drag reductions in excess of 95% have been obtained (Lee, Vaseleski and Metzner (1974)) in polymer solutions containing suspended fibres.)

Since the discovery of drag reduction, a great deal of research effort has been applied to exploit industrial applications of the phenomenon, to accumulate and correlate vast amounts of experimental data with varying pipe diameters, pipe roughnesses, polymer type and concentration and to investigate possible rheological models and proposed mechanisms which explain at least some of the properties associated with drag reduction. Several hundred papers have been published with at least seven major reviews Lumley (1967), Lumley (1969), Landahl (1972), Hoyt (1972), Lumley (1973), Virk (1975) and Dimant and Poreh (1976).

Hoyt's review is especially notable for its discussion of the industrial applications of the Toms effect in, for example, ship propulsion, fire fighting and land irrigation, as well as for the

discussion of flows around rotating discs and cylinders and over flat plates. A wide range of solute-solvent combinations are tabulated and over two hundred publications are cited. A historical account of some of the theories of drag reduction is also included.

Dimant and Poreh consider the even more difficult problem of heat transfer in drag reducing fluids in their review whereas Landahl's review concentrates on giving a short history of proposed mechanisms followed by the development of a new model. Lumley's most recent review also discusses proposed mechanisms of drag reduction. Virk's review is most notable for an extensive and detailed tabulation and review of most of the available experimental evidence on drag reduction in pipe flow which is interpreted using a phenomenological model describing many of the observed features of drag reduction.

Despite the great interest in drag reduction, the phenomenon is as yet poorly understood. Most of the work has been concerned with the dependence of friction factor on polymer and flow parameters and the main features of this dependence are now clear. However, the experimental evidence concerning changes in velocity profile and turbulent intensity profile with changing polymer and flow parameters is far from comprehensive since many of the early measurements were made with pitot tubes and hot film probes which have subsequently been shown to be inaccurate in polymer flows. Even less well understood is the underlying mechanism explaining drag reduction although a great many suggestions have been made, nearly all of which assume that the most significant modification to the flow occurs near the wall where the turbulence is generated.

There is currently a large gap between theory and experimental evidence and there is a need for more extensive measurement of the structure of turbulence in drag reducing flows. At the same time

the theoretical work needs to be developed to a point where comparison with experiments can be made. A significant problem in this respect is the lack of commercially available polymers with narrow molecular weight distributions.

Given the comprehensive nature of the review material, this introduction will simply describe the essential established features of gross flow in polymer solutions without copious reference to the original sources on which the evidence is based. Since the main part of the work described in this thesis is concerned with detailed measurement of velocity profiles, turbulent intensities and spectra, a more detailed introduction will be given to the semi-empirical models of velocity profile during drag reduction together with a detailed review of the velocity measurements made in homogeneous solutions in drag reducing pipe flow. Finally, a number of models of drag reduction are outlined to illustrate some of the current theories on drag reduction.

1.2 GROSS FEATURES OF DRAG REDUCTION IN PIPES

The bulk of the published literature on drag reduction is concerned with the measurement of pressure gradient or wall shear stress in smooth straight axisymmetric flow as a function of Reynolds number, pipe diameter and with variation in polymer type, concentration, molecular weight distribution, and the amount of degradation. In this section of the introduction, the generally accepted features of gross flow will be outlined with the aim of forming a general introduction to polymer flow in pipes rather than an attempt to critically review the extensive range of work which has been published.

It is customary (see Chapter 2) to examine friction factor, f,

variation in polymer flows in terms of Prandtl-Karman plots of $f^{-\frac{1}{2}}$ versus Re* $\sqrt{f}$ where for Newtonian flow the data has a unique form for both laminar (Poiseuille's law) and fully turbulent flow (the Prandtl-Karman law). The behaviour of drag reducing flow can be described by reference to Figure 1.1 which shows the behaviour of three hypothetical drag reducing flows with increasing Reynolds number or flow rate.

For a moderate drag reducer (D.R.1) the Newtonian (solvent) fluid curve is followed in the laminar flow region. The Newtonian laminar to turbulent transition is present and is characterised by unstable pressure drop measurements giving a scatter to the friction factor measurements. This region is followed by a fully turbulent region where the Prandtl-Karman law is obeyed. Above a certain value of $Re\sqrt{f}$, the curve deviates from the solvent curve to form a straight line of increased slope. For a more efficient drag reducing fluid, the behaviour is similar but the onset of drag reduction, ie. the point where the data departs from the Newtonian form, occurs at a lower value of $Re\sqrt{f}$ and the difference in slope between the straight line and the Newtonian line is greater. In the best possible drag reducing situation, D.R.3, the curve departs from the Newtonian curve directly after laminar to turbulent transition and follows a maximum drag reduction asymptote, the form of which has been shown by Virk et al (1970) to be as follows

$$f^{-\frac{1}{2}} = 19 \pm 0.4 \ (\log_{10} Re\sqrt{f}) - 32.4 \pm 1.2$$

The existence of a maximum asymptote was first suggested by Virk et al (1966) and there is ample evidence to show that this asymptote is

---

* The Reynolds number, Re, is normally based on solvent kinematic viscosity ν, ie. $Re = U\,d/\nu$ where U is the bulk flow velocity and d is the diameter of the pipe.

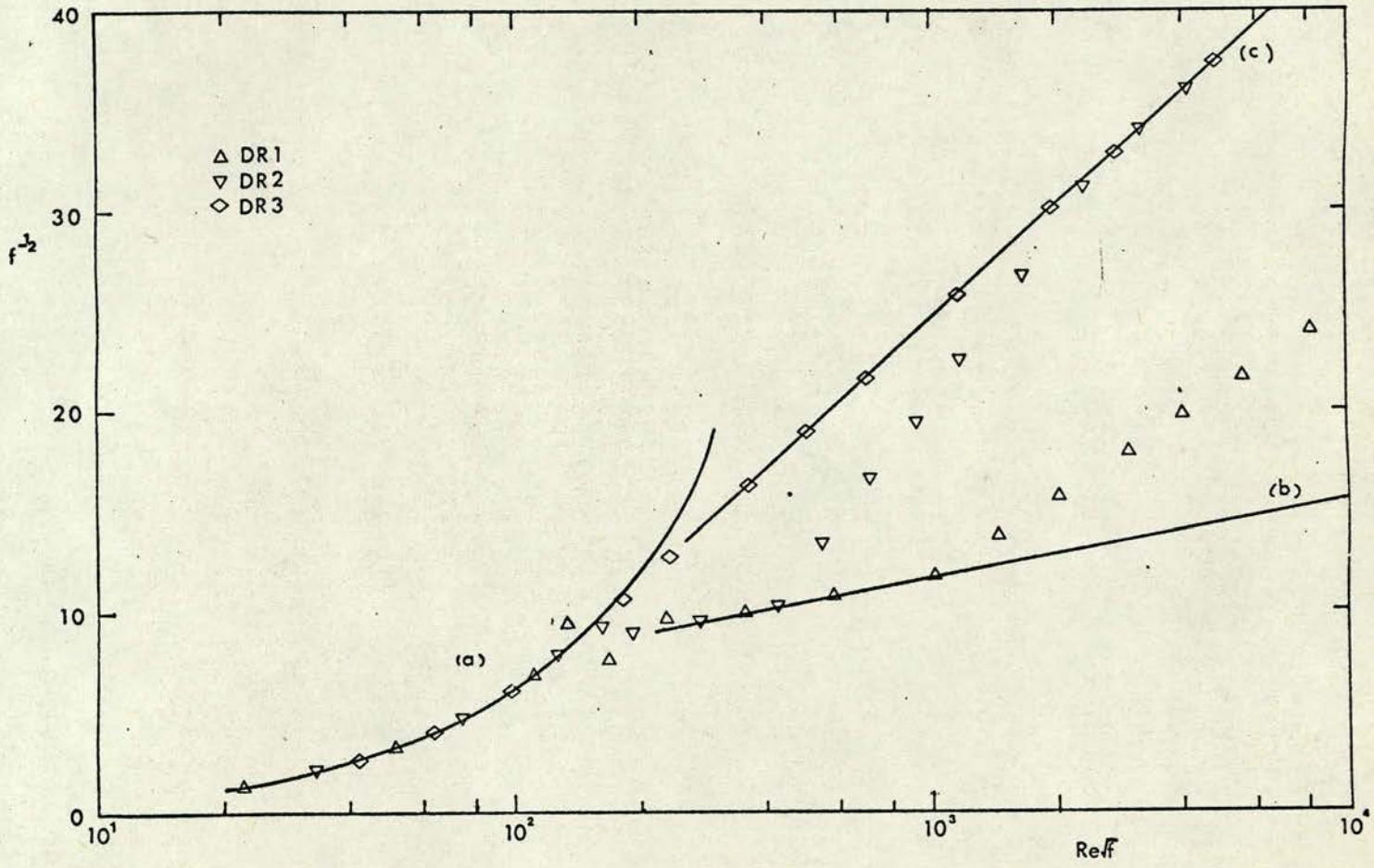

Figure 1.1

Gross flow behaviour of three typical drag reducing solutions. Solid lines are:
a) Poiseuilles Curve b) Prandtl-Karman Curve c) Virk's Maximum Drag Reduction Asymptote

independent of all polymer and pipe flow parameters. In Virk's review (1975) no less than forty different flow situations from six different sources and with seventeen polymer/solvent combinations show points clustered along Virk's asymptote. Note that although this line is a maximum, it may not be attainable for a given solution simply by increasing the Reynolds number as can be seen by studying the behaviour of D.R.1 in Figure 1.1.

At conditions of less than maximum drag reduction the amount of drag reduction is a complicated and as yet not fully understood function of both polymer and flow parameters but each fluid/flow situation can be characterised by two parameters viz. the onset point and the difference between the slope in the drag reducing region and the slope of the Prandtl-Karman curve.

For flows with the same polymer solution, the Reynolds number at onset varies with pipe diameter and $Re\sqrt{f}$ at onset is proportional to the pipe diameter. This "diameter effect" can be re-stated by saying that onset occurs when a fixed value of wall shear stress is exceeded independently of pipe diameter. Virk (1971) has also found that onset occurs at the same wall shear stress in rough pipes as for smooth. There is also much evidence to suggest that onset is independent of concentration for dilute solutions of very effective drag reducers although some concentration effects on onset shear stress have been observed with less efficient drag reducing fluids. For a given polymer species, eg. polyethylene oxide, there is often a range of types or designations with slightly different chemical structures and/or different molecular weight distributions. For the same polymer species, the onset shear stress decreases and the slope increment increases with increasing average molecular weight. For

dilute solutions, the slope increment, δ, has been found to be proportional to the square root of the polymer concentration for a number of polymer types. For any given solution, the slope increment is independent of pipe diameter.

A central problem in drag reduction research has been to relate both the onset shear stress τ_w and the slope increment δ to polymer and flow properties. Two correlations predicting onset shear stress in terms of flow parameters have been postulated, the first based on length scale comparisons and the second on time scales. The length scale hypothesis, Virk et al (1966), relates the radius of gyration R_g of a polymer molecule to the wavenumber characteristic of the dissipation range in the spectrum of the turbulence. The following relationship is then obtained

$$R_g (\tau_w)^{\frac{1}{2}} = \text{constant}$$

The time hypothesis suggested by Fabula et al (1966) relates the characteristic relaxation time of the polymer molecule to a characteristic frequency of the fluid leading to the relationship

$$R_g^3(\tau_w) = \text{constant}$$

Although Virk's theory has been found to give a better fit to some of the experimental data than the time scale theory, the scatter is largely due to the difficulty of estimating R_g for a polymer sample containing a broad band of molecular weights. Fabula's theory predicts fluid and flow time scales of similar magnitude whereas the characteristic length scale of the turbulence at onset is much greater than the polymer length scale.

To resolve the question of whether length scales or time scales are important, Berman and George (1974) studied the effect of solution viscosity variation without polymer concentration change on the value

of wall shear stress at onset. The time scale hypothesis predicts a decrease in onset shear stress as the solution viscosity is increased whereas the length scale theory suggests that onset shear stress should increase. The results of Berman and George for a solution of polyethylene oxide in a solution of water and glycerine show that the time scale hypothesis is correct.

Major problems of reproducibility frustrate the experimentalist in the study of drag reduction. These are primarily due to the frequently observed degradation of the polymer solutions by molecular scission under shear. Further complications arise in that the age of the prepared solution and the different molecular weight distributions of different batches of commercially available polymers can also affect measurements made in apparently identical flow situations with the same polymer concentrations. In general, the most effective drag reducing polymers are those which have high molecular weights and an extended molecular structure with few side branches to the main molecular chain. Such polymers are also the most susceptible to degradation. A systematic study of polymer degradation by Patterson and Abernathy (1970) led to the observation that it was the concentration of the highest molecular weight band in the molecular weight distribution that was important in determining a polymer's drag reducing potential. It was further suggested that the turbulent shear field attacked preferentially the longest chain molecules in the distribution. Added support for the first of these two observations was recently provided by Hunston and Reischman (1976). Using two samples of polystyrene with different average molecular weights and narrowband weight distributions, Hunston and Reischman showed that onset occured at the same point in a solution containing both polymer samples as in a solution containing only the high molecular

weight sample.

As well as molecular weight distribution polymer conformation, which can be influenced by the type of solvent used, affects the drag reducing ability of a polymer type. By varying the pH of the solution of polyelectrolyte polymers several studies (eg. Parker and Hedley (1972), White and Gordon (1975)) have shown that the greater the average molecular extension in solution, the better is the drag reduction.

Although the behaviour so far described is typical of drag reducing polymer flow, it is possible for polymers which are normally good drag reducers to actually increase drag under certain conditions. This phenomenon has been called "early turbulence" and occurs in pipe flow when the onset shear stress occurs at a Reynolds number below the value for Newtonian laminar to turbulence transition. This happens in small diameter (capillary) tubes (eg. Little and Wiegard (1970)) or in solutions of high solvent kinematic viscosity (Forame et al (1972)).

1.3 VELOCITY PROFILE MODELS OF DRAG REDUCTION

To understand the semi-empirical models of mean velocity profile during drag reduction it is necessary to consider first of all the accepted form of the velocity profile in Newtonian flow. In Chapter 2, this form is discussed in more detail in terms of the variation of dimensionless velocity u^+ with dimensionless distance y^+ from the pipe wall. u^+ and y^+ are defined as follows

$$u^+ = \frac{u}{u_\tau} \quad \text{with} \quad u_\tau = \sqrt{\frac{\tau_w}{\rho}} \quad \text{and} \quad y^+ = \frac{u_\tau y}{\nu}$$

where ρ is the fluid density and u_τ is called the friction velocity.

In terms of these dimensionless variables, the Newtonian

velocity profile consists of the following four zones (from the wall edge to the centre line)

(1) The laminar sub-layer $u^+ = y^+$

(2) The buffer (transition) region

(3) The turbulent core region $u^+ = A \log y^+ + B$

(4) The outer wake region $u^+ = c(\xi, f) = A \log y^+ + B$

For simplicity the profile is often approximated by regions (1) and (3) only, and, in the integration of velocity profile to derive the Prandtl-Karman relationship, the profile is approximated by region (3) alone. The term $c(\xi, f)$ in region (4) is a correction term to describe the departure of the outer wake region from the straight line behaviour of region (3) on a semi-logarithmic plot. The form of $c(\xi, f)$ has been experimentally determined and is independent of friction factor f and relative distance from the pipe wall $\xi = y/R$ where R is the pipe radius.

Probably the earliest model of velocity profile for drag reduction was that suggested by Elata et al (1966) who envisaged that the ability of polymer solutions to store energy elastically would have the effect of increasing the stability of the flow within the buffer region and the nett effect would be to increase the extent of the laminar sub-layer. The flow in the core region would then be upshifted by an amount ΔB on the plot of u^+ versus y^+ without a change in the slope, A. The resultant profile is shown qualitatively in Figure 1.2 (a). This model was further developed by Rollin and Seyer (1972) by applying a wake correction term, $c(\xi, f)$ of the form proposed by Bogue and Metzner (1963) for a wide range of Newtonian fluids. Since $c(\xi, f)$ has a negligibly small value outside the outer wake region the so-called "corrected" plot of $u^+ - c(\xi, f)$ versus y^+

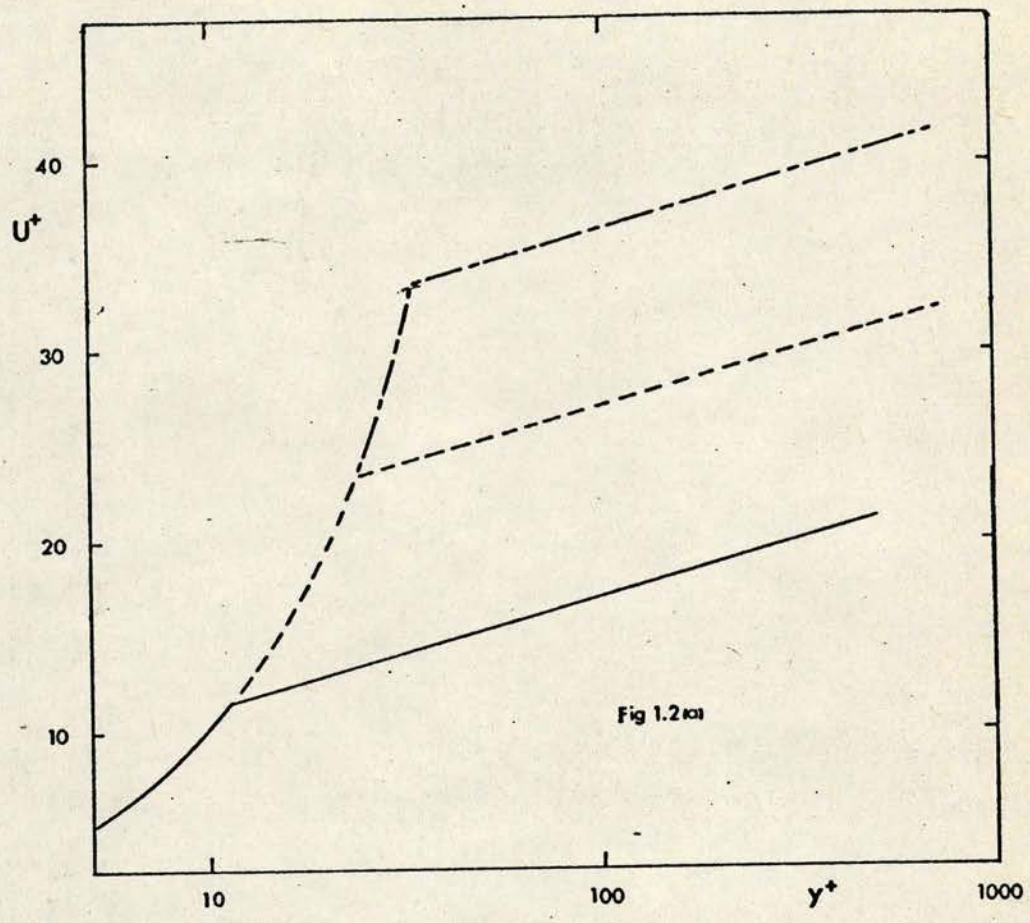

Figures 1.2 (a) - (e)

Models of Velocity Profile during Drag Reduction due to

(a) Elata et al (1966)

(b) Virk et al (1967), Squire et al (1967)

(c) Van Driest (1970)

(d) Virk et al (1970)

(e) Dimant and Poreh (1976)

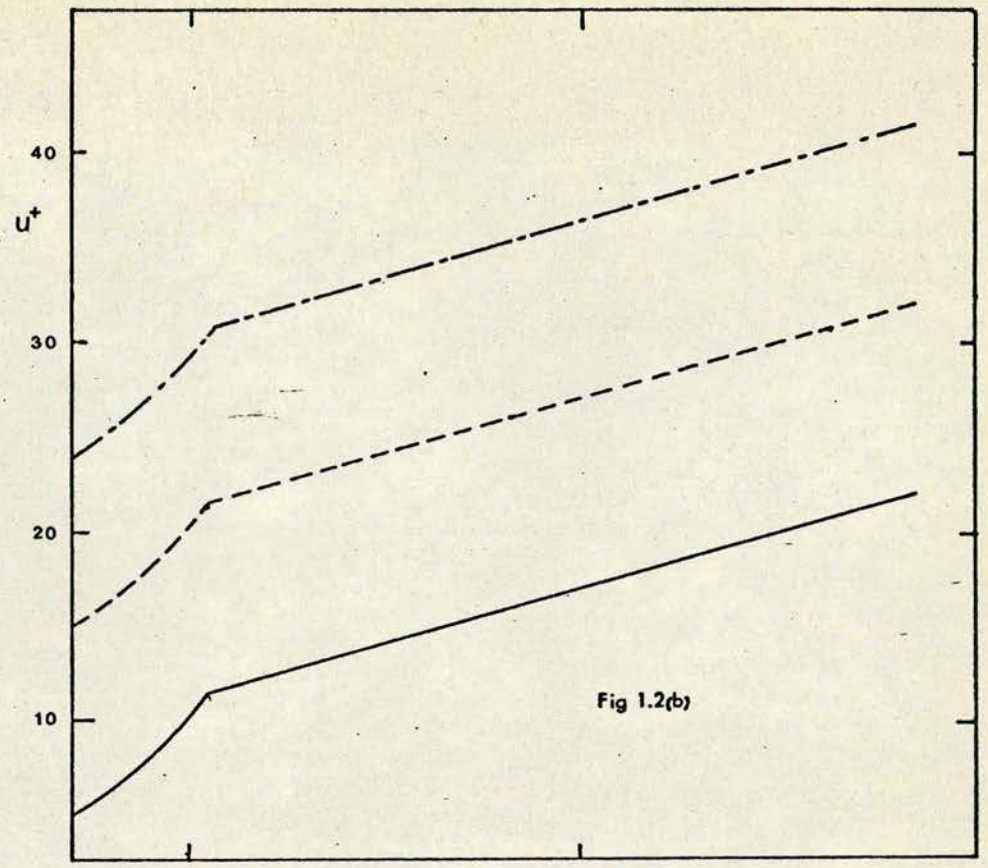

Fig 1.2(b)

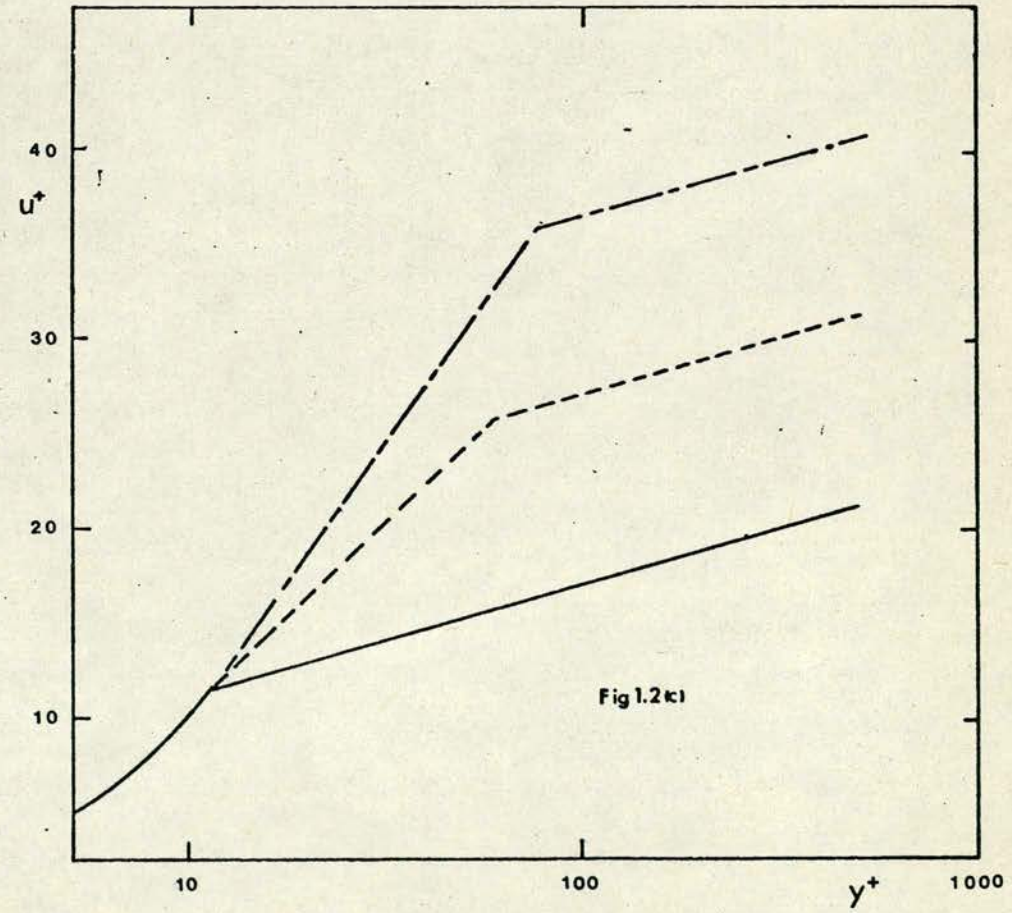

Fig 1.2(c)

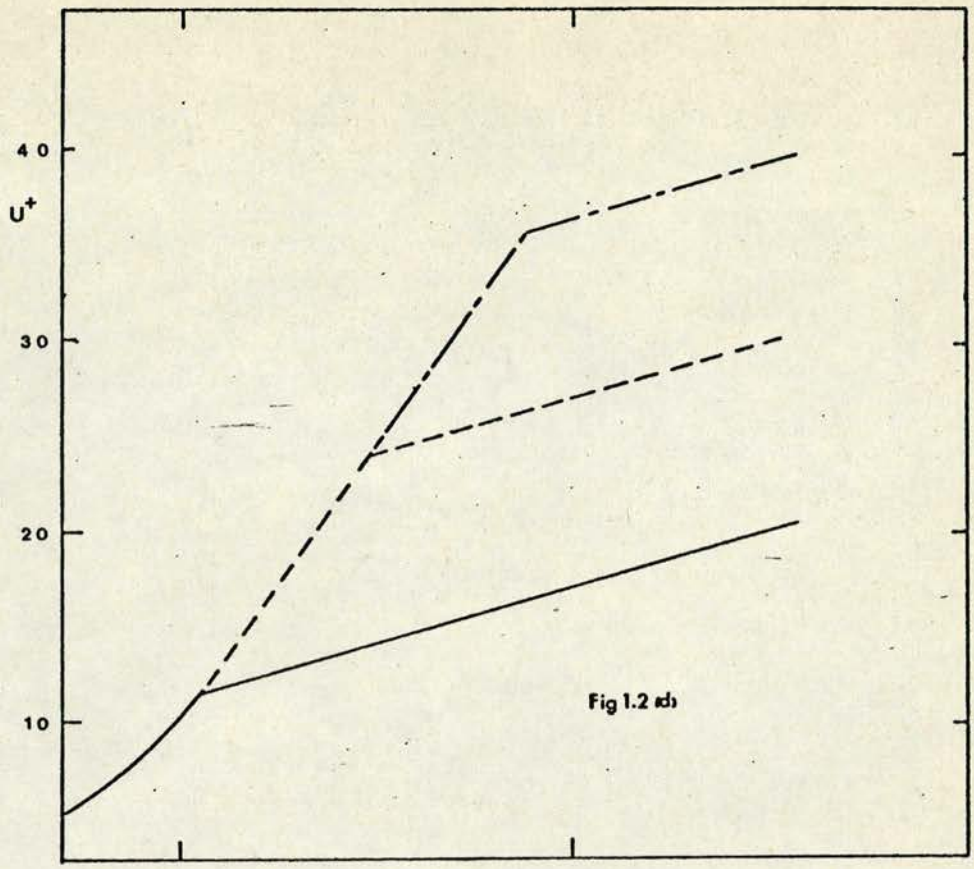

Fig 1.2 (d)

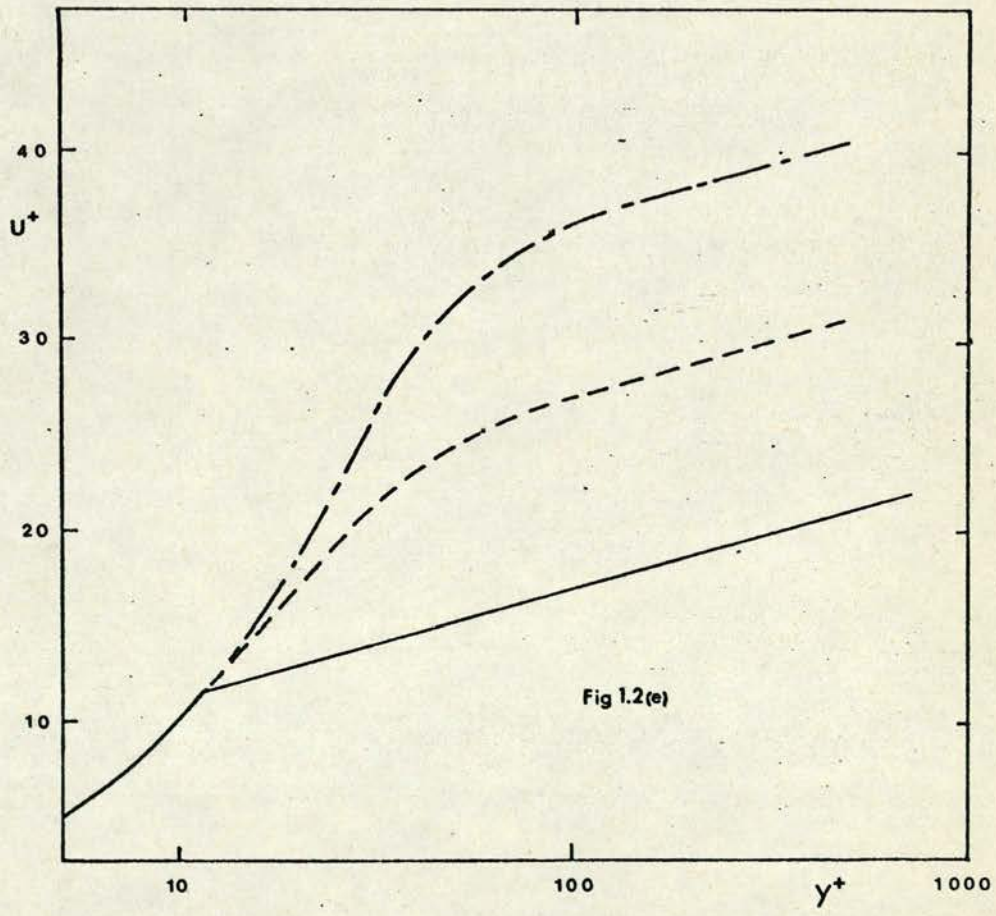

Fig 1.2(e)

has an extended straight line form on a semi-log. plot leading to a greater degree of accuracy in determining the values of A and B.

Another early model, independently suggested by Virk et al (1967) and by Squire et al (1967) is the effective slip model which predicts profiles of the shape shown in Figure 1.2 (b). Expressed simply, the velocity in polymer flow at a relative pipe distance ξ from the wall is related to the solvent velocity at the same pipe position by

$$U_{polymer}(\xi) = U_{solvent}(\xi) + U_{slip}$$

where

$$U_{slip} = V_{polymer} - V_{solvent}$$

and V is the bulk flow or space averaged velocity. This model differs from the previous model in having a sharp reduction or discontinuity in velocity at the pipe edge and in having the intersection of the laminar sub-layer with the turbulent core at the same value of y^+ for both polymer and solvent flow. Beyond the sub-layer, both models predict the same upshifted profile shape. Kozuki and Tiu (1968) combined the ideas of both of these models and considered a model with an effective slip and an increased sub-layer thickness.

In contrast to these models, Van Driest (1970) argued that although the turbulent core was as suggested by the other models, the viscous sub-layer was unchanged in polymer flow. He postulated the existence of an intermediate layer between these two regions where the Prandtl mixing length (K = 1/A) was reduced compared to the Newtonian value for the turbulent core. With this model the profile is composed of (Figure 1.2 (c))

(1) Newtonian viscous sub-layer $\quad u^+ = y^+$

(2) Intermediate "elastic" layer $\quad u^+ = C \log y^+ + D$

(3) Turbulent core $$u^+ = A \log y^+ + B + \Delta B$$

$$(A < C)$$

This model has two parameters, C and ΔB which can vary with increasing drag reduction.

Virk et al (1967 and 1970) inferred a profile model from their observation of a maximum drag reduction asymptote. It was argued that at maximum drag reduction, the velocity profile consists of a Newtonian laminar sub-layer followed by a turbulent core of increased slope (lower mixing length) compared with the Newtonian case. For Newtonian flow, the constants M and N in the friction factor - Reynolds number relationship

$$f^{-\frac{1}{2}} = M \log(Re\, f^{\frac{1}{2}}) + N$$

are uniquely related to the constants A and B describing the velocity profile in the turbulent core

$$u^+ = A \log y^+ + B$$

(The exact form of the relationship is derived in Chapter 2.) Using the same relationship for polymer flow, the ultimate velocity profile can be inferred if M and N can be found for conditions of maximum drag reduction. Using data from nine different sources with three polymer species, the form of the ultimate velocity profile was postulated to be

1) Laminar sub-layer $$u^+ = y^+$$

2) Elsewhere $$u^+ = 11.7 \ln y^+ - 17.0$$

At conditions of less than maximum drag reduction, it was further postulated that a three layer model similar to Van Driest's model would be valid but that C and D would have the values of the ultimate profile constants viz. 11.7 and - 17.0 respectively. The only

variable with change in drag reduction is then the extent of the intermediate region and Virk (1975) developed a model to relate the extent of the layer to polymeric parameters including concentration and molecular structure.

Huang's (1974) four layer model is similar to Virk's model but with an outer wake region in addition to the three layers suggested by Virk. With this model the ultimate profile constants C and D were found to be 13.2 and - 10.2 respectively. Although Huang's correlation was based on velocity data rather than data obtained by inference from gross flow measurements, the amount of data used was rather less than Virk's.

A slightly more complicated but similar model is due to Tomita (1970) who included a Newtonian buffer layer between the elastic sub-layer and the Newtonian turbulent core. His model is then

1)	Laminar sub-layer	$u^+ = y^+$
2)	Elastic sub-layer	$u^+ = A_1 \ln y^+ - B_1$
3)	Newtonian buffer layer	$u^+ = A_2 \ln y^+ + B_2$
4)	Turbulent core	$u^+ = A_3 \ln y^+ + B_3$

As with the two previous models, A_1 and B_1 (c.f. C and D) do not change with drag reduction.

Finally, a recent model, suggested by Dimant and Poreh (1976), is expressed in differential form which can be integrated to give a smooth velocity distribution. This model is based on the modification of a model due to Van Driest (1956) for Newtonian flow. The form of the Prandtl mixing length is assumed to be

$$\ell = k y \left[1 - \exp \left(\frac{y^+}{A^+} \right) \right] \quad , \quad A^+ \text{ is a semi-empirical parameter}$$

and the following relationship between shear stress and velocity

gradient is obtained

$$\frac{du_1^+}{dy} = \frac{2\tau^+}{1 + \sqrt{1 + 4k^2 y^{+2} \left[1 - \exp(-y^+/A^+)\right]^2}}$$

By assuming a linear variation in shear stress across the pipe, ie.

$$\tau^+ = 1 - \frac{y^+}{R^+}$$

the above equation can be integrated to yield a velocity profile. To this profile is applied a wake correction term postulated to be of the following form

$$u_2^+ = \frac{K}{k} \left[1 - \cos(\pi y^+/R^+)\right] \left[1 - \exp(-2R^+/A^+)\right]$$

where K = 0.67 and is a universal constant for pipe flow. The final profile is then

$$u^+ = u_1^+ + u_2^+$$

Accepting that the Prandtl mixing length constant is unchanged for large values of y^+ compared with Newtonian flow, k can be set to 0.4 and profiles for a given pipe radius can be plotted as a function of A^+ which is presumed to vary with drag reduction. As A^+ increases, the upshift in the turbulent core increases as does the velocity gradient at the start of the elastic sub-layer. The predictions of this model with increasing drag reduction are shown in Figure 1.2 (e).

In summary, it is clear that all of the models agree in predicting an upshifted Newtonian turbulent core, neglecting wake correction effects. Effective slip or thickened laminar sub-layer models can be applicable only for modestly drag reducing flows and fail to predict the observed form at maximum drag reduction. (With these models, laminar flow throughout the pipe is the predicted flow at maximum drag reduction.) Experimental data is needed to see

whether, at less than maximum drag reduction, velocity profiles follow Virk's ultimate profile line in the elastic sub-layer or whether the mixing length in this region depends on polymeric parameters as suggested by Van Driest's model. It is also to be seen whether, at maximum drag reduction, the Newtonian turbulent core is still present, though reduced in extent, as predicted by Dimant and Poreh, or whether the elastic sub-layer extends throughout the flow beyond the laminar sub-layer as suggested by Virk.

1.4 VELOCITY MEASUREMENTS IN DRAG REDUCING SOLUTIONS

Some of the earliest measurements of velocity profiles in drag reducing solutions were those of Shaver and Merrill published in 1959. Using a number of commercial polymers, including sodium carboxymethyl-cellulose (C.M.C.), Shaver and Merrill found that, at a given Reynolds number, a pseudoplastic polymer solution has a "less blunt" velocity profile than a Newtonian fluid.

Elata et al (1966) used Guar Gum, a popular drag reducer in the early days, for their measurements of velocity profiles. Using a 3 mm diameter pitot tube probe in a 5.08 cm diameter pipe flow, profiles were obtained in polymer concentrations from 50 ppm to 10,000 ppm at a constant flow rate. The results were interpreted as indicating an increased laminar sub-layer, the core region having the same slope as the Newtonian profile but displaced upwards by an amount ΔB. ΔB was found to increase with increasing concentration up to a maximum of 3000 ppm, higher concentrations having less than the maximum value of ΔB.

With Guar Gum in smaller tubes (1.65 cm and 3.63 cm dia.) Wells (1965) measured velocity profiles at concentrations of 500, 1000, 2000 and 5000 ppm at several Reynolds numbers ranging from 3.22×10^4

to 1.36×10^5. Wells interpreted his data as indicating an increased slope in the semi-log profiles, the slope increasing with increased concentration. His results also indicated a possible increase in the extent of the viscous sub-layer although, as with Elata et al, no measurements were obtained within the sub-layer.

Ernst (1966) was able to make measurements of velocity within the viscous sub-layer in C.M.C. solutions by using a very small pitot probe (0.013 cm dia.) in pipe flows of 2.3 cm and 5 cm diameter. Ernst found an upward shift in the semi-logarithmic profile without change in slope. B was found to increase with increasing Reynolds number at constant polymer concentration (0.05%). The results obtained in the smaller tube indicated no change in the extent of the viscous sub-layer. Ernst extended his work with C.M.C. (1967), making measurements at a range of Reynolds numbers up to 10^5 in five pipe diameters from 0.33 cm diameter to 3.81 cm. Using a very small pitot probe as before, Ernst found that the ΔB shift could be correlated by the following equation

$$\Delta B = \alpha \log \left(\frac{u_\tau}{u_{cr}}\right)$$

where α and u_{cr} are properties of the polymer type and concentration. This correlation gave good agreement at the concentration used (0.05%) between the measured friction factor and the friction factor deduced from the profile model. (A scatter of 8% in ΔB estimates was found in a ten-fold range of pipe diameter.)

Wells et al (1968) completed an extensive set of measurements in a 0.05% solution of C.M.C. including measurement of turbulence intensities and energy spectra. A novel type of velocimeter was used based on pressure measurement using piezoelectric transducers. It was found that the centreline turbulence level, when made

dimensionless using friction velocity u_τ, was constant for a wide range of Re (more than a factor of twenty) ie.

$$\frac{\overline{(u'^2)}^{\frac{1}{2}}}{u_\tau} = 0.8 \qquad \text{(all Re)}$$

Although the data showed some scatter, the Newtonian intensity profiles were in rough agreement with classic results in air flow. The polymer intensity profiles, made dimensionless with respect to u_τ showed less variation with Re than did the water results and indicated an increase in intensity towards the wall ($\xi < 0.25$) comparedwithwater, the intensity elsewhere being approximately the same as water. Energy spectra were presented, normalised with friction velocity, as a function of frequency and were also plotted in a dimensionless form by dividing by $\overline{u'^2}$ and multiplying by the wavenumber of the pipe diameter. The frequency spectra showed a reduction in energy at low frequencies although the wavenumber dependent spectra showed the same shape and contained most of the energy in the same range of dimensionless wavenumbers.

Using pitot tubes, Goren and Norbury (1967) measured velocity profiles in Polyox WSR 301 at concentrations of 5.5 to 50 ppm at several Reynolds numbers (up to 1.5×10^5) in a 5.08 cm diameter pipe. It was found that for a given value of y^+, values of u^+ were greater in polymer solutions than in water, that the slope of u^+ versus log y^+ varied with concentration reaching a maximum at 10 ppm and decreasing thereafter, and that at any particular concentration the slope increases with increasing Reynolds number. From velocity defect plots, it was observed that the defect ($u^+_{\text{centreline}} - u^+(\xi)$) in polyox at all concentrations was the same as water for $\xi > 0.25$ but that the defect was much greater in polyox near the pipe edge, the difference increasing with increased concentration up to 20 ppm.

Polyox N 3000 was the polymer studied by Virk et al (1967) using pitot tubes to measure mean velocity profiles and a constant temperature cylindrical hot film probe for measurements of intensity and turbulent spectra. Profiles were obtained for a 1000 ppm solution in a 3.21 cm dia. pipe at two values of Re (36,000 and 180,000) and compared with water flow at the same flow rate. Intensity profiles were obtained at the higher Re as were energy spectra at the pipe centreline and near the edge (ξ = 0.033). From these results, Virk et al suggested the effective slip model of velocity profile described earlier. The intensity profiles showed that $\overline{(u'^2)}^{\frac{1}{2}}/u_\tau$ near the wall but still in the outer region beyond the viscous sub-layer is unchanged in polymer flow although nearer the centre and nearer the edge higher values were obtained. Energy spectra were found to be unchanged in polymer flow near the pipe edge but centreline spectra were markedly different, there being no region of - 5/3 slope in the polymer spectrum.

The reliability of measurements made in polymer solutions using pitot tubes and hot film probes has been questioned by a number of investigators and several workers found anomalous response to velocity changes from such devices. These results, described in more detail in Chapter 3, suggest that, particularly with pitot tubes of small diameter and with cylindrical hot film probes, the measurements obtained in polymers must be treated with caution and may be subject to considerable error. (It is significant that when Virk reviews the available experimental evidence seven years later he excludes from consideration his measurements of energy spectra mentioned above.)

Given the limitations of the standard instrumentation, flow visualisation or particle tracer techniques are attractive methods

of flow analysis although normally only a limited amount of data can be collected as the methods of data analysis are time consuming and tedious. Seyer and Metzner (1969) used a bubble tracer technique to measure axial mean velocity and axial and radial intensities in a 2.54 cm dia. pipe with two solutions (0.1% and 0.01%) of ET 597, a high molecular weight polyacrylamide. While the mean velocity profiles were found to be less blunt in polymer flow, there were two few measuring positions to give a confident model prediction. Conditions were such that it was possible to obtain turbulent flow both with and without drag reduction. In the absence of drag reduction, both radial and axial intensity profiles were the same as Newtonian values, when normalised using bulk flow velocity, within the limits of experimental accuracy. (Error bars at a 90% confidence level were estimated at ± 20%.) In the drag reducing regime, radial intensities were found to be the same as in water flow but axial intensities at all points in the profile were found to be about 20% lower implying a shift towards isotropy and a lowering of Reynolds stress.

Using an improved bubble tracer technique, Rollin and Seyer (1972) investigated mean velocity profiles in (in drag reducing terms) relatively high concentrations of Separan AP 30 (100 ppm and 1000 ppm) in two tubes (2.54 cm dia. and 6.98 cm dia.) at Reynolds numbers ranging from 5,200 to 80,400. Examining the data on the semi-logarithmic plot, the data could be interpreted in one of two ways. If it were assumed that the profiles were unchanged in slope compared with water flow, poor fits to the data were obtained. Better fits would be found if the slope were allowed to increase. Rollin and Seyer also studied the data after the "correction" suggested by Bogue and Metzner (1963) had been applied to the data. With the modified data, a better fit was found by assuming that the profiles

all had the same slope in the turbulent core and it was concluded that a model predicting intercept increase without change in slope would give a good fit to the data. It was also suggested that with a 1000 ppm solution a Reynolds number of 10^5 may be necessary to obtain fully turbulent flow.

Arunachalam et al (1972) used photo-chromic dye injection to examine drag reducing flow in Polyox Coagulant 701 dissolved in water-alcohol solvents in a 1.36 cm diameter tube. (A mixed solvent of 70% alcohol by weight and 30% water was necessary since the polymer was insoluble in alcohol and the dye in water.) Dye trace photographs clearly indicated an increase in the extent of the viscous sub-layer for both fresh and degraded 5.5 ppm solutions. Mean velocity profiles were correlated with an intercept shift model of the form

$$B = 5.75 \left[\frac{u_\tau (\text{water})}{u_\tau (\text{polymer})} \right]^3$$

Axial intensities were plotted relative to local mean velocity and also to friction velocity. Based on friction velocity, intensities were found to be slightly higher in polymer solutions for $\xi < 0.1$ and much higher for smaller values of ξ, reaching a maximum of nearly twice the Newtonian value at $\xi = 0.075$.

With Polyox WSR 301 in a 5.08 cm tube, Taylor and Middleman (1974) calculated radial turbulent intensities at the centreline by measuring the turbulent dispersion of a dye plume injected along the pipe axis. When divided by centreline velocity, the radial intensity was found at all concentrations measured (up to 50 ppm) to be lower than for water flow.

It is important to remember that flow visualisation techniques give a Lagrangian description of the flow field whereas measurements

from probes fixed in the flow yield Eulerian flow information. Even for Newtonian fluids the form of the transformation relating Eulerian and Lagrangian statistics is not yet known so that the results from flow visualisation techniques cannot be compared quantitatively with fixed probe measurements.

Laser velocimeters have a fundamental advantage over pitot and hot-film probes since their response is the same in polymer flows as in water. Using a laser velocimeter, Goldstein et al (1969) investigated the ratios of centreline velocity and turbulent intensity to bulk flow velocity in water and in 50 ppm WSR 301 in a 1.4 cm dia. pipe over a wide range of Reynolds numbers including the laminar to turbulence transition region. No significant difference between water and the polymer solution was found for either ratio.

In a 1.19 cm diameter pipe, Chung and Graebel (1972) measured mean velocity profiles, axial intensities and energy spectra in Polyox WSR 301 and Separan AP 30 using a laser velocimeter. Although there was some scatter in the data and no clear trends with increasing concentration, the measurements of axial intensity, when made dimensionless with centreline mean velocity, indicated that for both polymers, intensities are higher near the wall $\xi < 0.3$ and generally lower elsewhere. Energy spectra were measured in Polyox at concentrations of 20 ppm and 50 ppm for Reynolds numbers of 51,500 - 58,800 at four positions in the flow. Presented as a function of wave number, the spectra for Polyox and water were similar along the pipe centreline. At $\xi = 0.365$, the Polyox spectra were higher throughout the range of wavenumber measured and at $\xi = 0.015$ the spectra were higher in the low wavenumber range compared with water. At $\xi = 0.042$, the polymer spectrum (50 ppm Polyox) was higher than water only for $32.8 < k < 75.4$ (cm^{-1}).

Since signal quality and optical alignment difficulties are present when using laser velocimeters in round tubes, Rudd (1972) and Logan (1972) used square sectioned 1.27 cm closed channels for their investigations of drag reduction. Rudd found that a solution of 100 ppm AP 30 produced a blunter velocity profile than the profile for water at the same flow rate. Axial turbulent intensities, normalised with friction velocity, were found to be very much higher in polymer flow near the wall ($\xi < 0.4$) reaching a peak value which was almost twice as great as the equivalent water value and the position of the peak was found to be displaced slightly away from the wall, indicating an increased viscous sub-layer. An increased sub-layer was also indicated by the mean velocity profiles.

Logan measured profiles of Reynolds stress as well as radial and axial intensities in water and a 50 ppm Polyox solution in a square pipe with sides of 1.27 cm. Logan found (as did Rudd) that the turbulence levels measured for water in the square sectioned pipes were much higher than typical levels in similar round pipes due to the existence of secondary flows. He found the peak in the axial intensity profile was shifted in the same way as Rudd's results although the magnitude at the peak was not greatly increased. He found radial intensities in the polymer solution showed lower values and less variation across the pipe than for water and a marked reduction in the Reynolds stress was observed for $0 < \xi < 0.125$ in the polymer flow.

The usefulness of applying results obtained in a square sectioned tube with secondary flow to describe drag reduction and velocity profiles in axisymmetric pipe flow has been questioned by a number of authors including Reischmann and Tiederman (1975) who made measurements with a laser velocimeter in a channel of rectangular cross-section. Using a high aspect ratio (10:1) a good approximation

to two dimensional flow between parallel plates was obtained in regions away from the narrow walls. Magnifloc, Separan AP 273 and Polyox WSR 301 were used at Reynolds numbers ranging from 20196 to 52449 and mean velocity profiles were presented on the usual semi-logarithmic plots. The profiles were interpreted using Van Driest's three layer model and ΔB was found to increase with increasing concentration. In the intermediate region, the profiles did not follow the ultimate profile of Virk. Intensities in the Newtonian flow compared well with the results of Hussain and Reynolds (1970) and Ecklemann and Reichardt (1971) for Newtonian pipe flow, being much lower than the values found by Rudd and Logan for square sectioned tubes. No sharp peak was found in the turbulent intensity and the intensity profiles when normalised with friction velocity were found to be similar to the Newtonian flow throughout most of the profile and were only slightly higher in a limited region $10 < y^+ < 80$ than for Newtonian flow.

1.5 PROPOSED MECHANISMS TO EXPLAIN DRAG REDUCTION

Since much of the literature has been concerned with possible mechanisms which explain drag reduction, it is important that this be discussed as part of the introduction. However, it is true to say that none of the theories presented to datehas received general acceptance and that many of the theories put forward cannot be tested against the experimental evidence currently available. As the work in this thesis is aimed at adding to the experimental evidence and since no new mechanism is proposed, it is intended that this section outlines the main assumptions on which theoretical work has been based rather than to debate the detailed predictions of different models. It will become clear that even the main assumptions on which any theory must be based have not been generally established.

Concurrently with his announcement of the drag reduction effect, Toms (1949) suggested that a shear thinning layer was formed very close to the wall in a drag reducing fluid. The viscosity near the wall he suggested was much less than the viscosity elsewhere thus reducing the friction factor compared with the solvent flow. This explanation is no longer considered to be correct since, at least for the dilute high molecular weight polymer fluids, drag reducers have been shown to exhibit Newtonian viscosity values at steady rates of shear. Also, Walsh (1967(a)) discovered a good drag reducer which is in fact a shear thickening substance.

Lumley (1967) suggested that entanglement of the polymer molecules was the cause of drag reduction and that the polymer significantly alters the flow only close to the wall. As the wall shear rate is increased, Lumley predicted that the probability of molecular entanglement increases until, above the critical shear rate for onset, the entanglements are sufficiently extended to inhibit the formation of streamwise vortices. The net effect is to increase the stability of the sub-layer and reduce the friction factor compared with the solvent flow. Later, Lumley (1973) revised his model in the light of experimental evidence of the behaviour of drag reducers as the concentration is increased. A theory based on molecular entanglement would not predict the observed drag reduction at very low concentrations found by White (1966) and also it would be expected that a doubling of polymer concentration would result in more than twice the drag reduction. Lumley (1973) suggested that molecular extension is the likely mechanism. At sufficiently high shear rates, the polymer molecules are thought to be extended to a much greater length than their usual random coil dimension leading to an increased effective viscosity in the buffer region of the flow. (Nearer the wall in the sub-layer the

molecules are not significantly stretched.) Increased effective viscosity leads to the suppression of small eddies, increased stability and a reduced friction factor.

An intriguing explanation postulated by El'perin et al (1967) is that adsorption of the polymer molecules on the wall of the pipe causes drag reduction by modifying the near wall region of the flow. This idea was based on the observation that drag reduction occurs in solvent flow through tubes which have previously contained polymer solutions. The work of El'perin et al was developed by others including Arunachalam and Fulford (1971), Bryson et al (1971), Hand and Williams (1973) and Little (1969). In this laboratory, McComb (1974(a)) observed adsorption of polyethylene oxide on the walls of flexible PVC tubing.

Arunachalam and Fulford found different polymer concentrations in a drag reducing flow at the pipe centreline and within 0.1 mm of the wall, suggesting that polymer adhesion to the wall is present during drag reduction. Bryson et al developed a model based on adsorption in which it was assumed that the polymer molecules adhere to the wall and reduce the effective diameter of the pipe. It is assumed that within a layer of thickness h from the wall, the fluid is effectively at rest with the usual viscous sub-layer beyond. The model was developed and h estimated from dispersion measurements to be at least 0.05 mm for the flows studied. If this is the case, it is clear that either molecular entanglement or the build-up of successive layers of molecules is involved rather than the adhesion of a mono-layer of polymer molecules. Hand and Williams studied the build-up of adsorbed layers of a polymer (PMMA) on the walls of a flow cell using an infra-red light adsorption technique to detect the polymer layers. By observing the process of build-up and subsequent wash-off it was

concluded that "an adsorbed-entangled layer at the boundaries of flows of dilute polymer solutions is responsible for much - if not most - of the drag reduction behaviour".

Some of the early evidence in favour of an adsorption theory was subsequently questioned by Little (1969) amongst others. Little showed that the percolation of polymer solutions into the pressure tappings could give rise to an apparent drag reduction when polymer solution was replaced by the solvent alone. Little and co-workers at the Naval Research Laboratory in Washington made a number of further investigations into the role of polymer adsorption in explaining drag reduction. A number of papers were published and the work is summarised in an overview (Little et al (1975)). By studying the results of rotating disc experiments with a wide range of disc surfaces and several polymer types, it was concluded that although adsorption did occur, the adsorbed layer did not play a major part in the drag reduction effect.

Walsh (1967(b)) argued that neither adsorption nor entanglement is the mechanism explaining drag reduction in dilute solutions at moderate shear rates. He suggested that it is the reduced generation of turbulence which gives drag reduction and that turbulence, once generated, is unaffected by the polymer molecules. By storing energy elastically, the polymer molecules slightly alter the turbulent energy balance near the wall. Since all large scale disturbances away from the wall were once small disturbances at the wall it is suppression of the small scale disturbances that ultimately gives reduced friction factors. The effect of the alteration to the energy balance is that many small scale disturbances are destroyed by viscous dissipation.

Black (1969) considered the effect of polymer addition on his own model (Black (1968)) for Newtonian wall turbulence. Black argued that Newtonian wall turbulence is composed of an organised non-random primary motion on which a secondary random motion is superimposed. He suggested that polymer additives increase the stability of the sub-layer either by modifying the process of vortex stretching or by reducing the intensity of the secondary motion. He warned that intensity measurements in polymers could be misleading since velocity fluctuations could increase in polymer flows because of the increased viscous activity in the sub-layer although turbulent fluctuations could in fact be reduced.

Implicit in Walsh's theory is that elasticity is related to drag reduction and a large amount of theoretical work has been centred around the assumption that visco-elasticity is involved in explaining drag reduction. In visco-elastic fluids, the stress is dependent on both the amount of strain (elastic response) and the rate of strain (viscous response). In general, the approach has been either to assume a certain form for the constitutive equation (ie. the relation between stress and strain) for the fluid as a whole or, alternatively, to consider the response of individual molecules in a Newtonian solvent. Im many cases these different approaches lead to similar or equivalent conclusions.

Notable examples of the continuum approach include McComb (1974(b)) who studied the behaviour of a Maxwell fluid in grid-generated turbulence and Hansen (1972) who considered the same model in a transient laminar shear flow. The use of the Maxwell model to describe drag reducing fluids has been criticised by Ting (1972) and Little et al (1975) who point out that the more general Oldroyd model is necessary. Gordon (1970) compared the predictions of the Maxwell model with the

Dumbell model of macromolecular response for three simple flow situations viz. simple shear flow, pure deformation and small amplitude oscillatory shearing. Gordon shows that the predictions of both models are equivalent except for the simple shear flow where the Maxwell model shows a viscosity which is dependent on the rate of shear.

Three properties of visco-elastic fluids have been suggested as being responsible for drag reduction. Metzner and Park (1964) suggested that the ratio of elastic to viscous stresses is an important measure of the effectiveness of the drag reducer whereas Seyer and Metzner (1967) argued that it is the polymer's high resistance to stretching which causes drag reduction. Vleggaar et al (1968), like Walsh, suggested that it is the ability of the polymer to store energy elastically that is responsible for drag reduction. Ting (1972) studied the behaviour of the dumbell model in both oscillatory and elongational flows. He concluded that the polymer's high resistance to elongation was the primary mechanism explaining drag reduction. Little et al considered an oscillatory flow superimposed on a steady shear flow to simulate wall turbulence. He suggested that the action of the polymer is to increase the rate of decay of such a disturbance and thus decrease the amount of turbulence generated.

Comparison of the above models with the available evidence on turbulence structure in drag reducing flows immediately shows the gap between theory and experiment in this field. Many of the detailed predictions of the models concerning the average shape of the polymer molecules at various flow positions would be extremely difficult to test experimentally. Equally, it is difficult to develop the ideas above into quantitative predictions of intensity and spectral profiles. However, most of the proposed mechanisms assume that the action of the drag reducing additive in altering the turbulent structure is effectively

confined to a region near the wall. It is clear from Section 1.4 that the available evidence on turbulent structure in drag reducing pipe flow is insufficient to confirm or deny this assumption although flow visualisation measurements by Gadd (1965) in turbulent jets and Barnard and Sellin (1969) in grid-generated turbulence indicate that drag reducers can alter free stream turbulence by suppressing small scale eddies. More detailed measurements of turbulent structure in drag reducing pipe flows would resolve this point.

CHAPTER 2

SOME ASPECTS OF NEWTONIAN TURBULENCE

2.1 HOMOGENEOUS ISOTROPIC TURBULENCE

The aim of this chapter is not to provide a completely general introduction to Newtonian turbulence but simply to bring together some aspects of Newtonian turbulence against which turbulent polymer flow can be compared. The contents are selected mainly because the terms, definitions and results outlined are used elsewhere in this thesis.

Hinze (1975) defines turbulence as a "motion of irregular condition of flow in which various quantities show a random variation with time and space co-ordinates so that statistically distinct average values can be discerned". The study of turbulence is therefore a statistical problem although the motion is described by Navier-Stokes equations. This apparent contradiction is resolved by showing that only slightly different initial conditions can lead to resulting flows which diverge greatly as time goes on. Leslie (1973) suggests that proper specification of the initial conditions is unattainable and that the randomness of the final turbulent motion is due to amplification of the initial molecular randomness.

An important statistical quantity in the study of turbulence is the average value of velocity at a point. In the experimental study, the time average value $\overline{U}$ is normally measured. It is defined as follows

$$\overline{U} = \lim_{T\to\infty} \frac{1}{T} \int_0^T u(t)dt \qquad (2.1)$$

Clearly, averaging for an infinite time is impossible in practice but, by making T large enough, $\overline{U}$ can be determined to within a specified

accuracy. The theory of turbulence requires a different averaging process. It is imagined that an identical set of experiments are subject to the same initial conditions and started at the same time. If the experiments are labelled 1, 2, ... N with velocity records $u_1(t)$, $u_2(t)$, ... $u_N(t)$ then the ensemble average

$$\langle u(t) \rangle = \lim_{N \to \infty} \frac{1}{N} \sum_{i=1}^{N} u_i(t) \tag{2.2}$$

If $\langle u(t) \rangle$ is independent of t then the flow is said to be stationary. Stationarity is a necessary condition for the ergodic theorem to hold. If the ergodic theorem is valid then

$$\langle u \rangle = \bar{U} \tag{2.3}$$

This is one of the main assumptions in turbulence research.

The instantaneous velocity can be written as the sum of the mean velocity and a fluctuating component thus

$$u(t) = \bar{U} + u'(t) \tag{2.4}$$

The intensity of turbulence is defined as

$$\overline{u'^2} = \lim_{T \to \infty} \frac{1}{T} \int_0^T u'(t)^2 \, dt \tag{2.5}$$

Clearly, these are vector quantities which can be written in terms of Cartesian components, u_1, u_2, u_3 or u, v, w, or in the case of axi-symmetric flow for example, in terms of cylindrical components u_r, u_θ, u_z.

Another quantity of interest is the energy spectrum of turbulence, first introduced by Taylor (1938) which gives the distribution of the kinetic energy of turbulent fluctuation as a function of frequency of fluctuation. The one-dimensional energy spectrum function is defined as (in u, v, w notation)

$$\phi(f) = 2 \lim_{T\to\infty} \frac{1}{T} \left| \int_0^T u'(t) \exp\left[2\pi i f t\right] dt \right|^2 \qquad (2.6)$$

where

$$\int_0^\infty \phi(f)\, df = \overline{u'^2}$$

$\phi(f)$ is related to the time auto-correlation function $R(t)$ which is defined as follows

$$R(t) = \frac{1}{\overline{u'^2}} \lim_{T\to\infty} \frac{1}{T} \int_0^T u'(t-\tau)\, u'(t)\, d\tau \qquad (2.7)$$

since $\phi(f)$ and $R(t)$ are Fourier transform pairs (Hinze (1975)). ie.

$$\phi(f) = 4\,\overline{u'^2} \int_0^\infty R(t) \exp\left[-2\pi i f t\right] dt \qquad (2.8)$$

$$R(t) = \frac{1}{\overline{u'^2}} \int_0^\infty \phi(f) \exp\left[2\pi i f t\right] df \qquad (2.9)$$

If a velocity record is obtained from one fixed probe $\phi(f)$ can be computed directly from the velocity record or indirectly by first computing $R(t)$. Although $R(t)$ is experimentally convenient to measure, the space and auto-correlation function $f(r)$ is a more useful quantity for theoretical study. $f(r)$ is defined as

$$f(r) = \frac{1}{\overline{u'^2}} \overline{u'(x)\, u'(x+r)}$$

and the associated spectrum function is the wavenumber function $\phi(k)$. Taylor's hypothesis (Taylor (1938)) can be used under certain circumstances to relate $f(r)$ and $R(t)$. For flows with only one mean velocity component in the x direction, Taylor's hypothesis is that

$$\frac{d}{dt} = -\overline{U} \frac{\partial}{\partial x} \qquad (2.10)$$

Equation (2.10) is approximately true provided that $\overline{u'^2}$, $\overline{v'^2}$, and $\overline{w'^2}$ are all much less than $\overline{U}$. When Taylor's hypothesis is valid, $\phi(f)$ and

$\phi(k)$ are simply related as follows

$$\phi(k) = \frac{\bar{U}}{2\pi} \phi(f) \qquad \text{with} \qquad k = \frac{2\pi}{\bar{U}} f \tag{2.11}$$

Although we have considered only correlations between one velocity component and with a scalar displacement r along the x axis, other correlations are possible and the general form of the correlation function is (changing to u_1, u_2, u_3 notation)

$$R_{ij}(\underline{x}, \underline{r}) = \frac{\overline{u_i'(\underline{x})\, u_j'(\underline{x} + \underline{r})}}{\overline{u_\ell'(\underline{x})\, u_\ell'(\underline{x})}} \tag{2.12}$$

where underscores are used to denote vector quantities.

A simple type of turbulence is a turbulent flow which is both homogeneous and isotropic. In a homogeneous flow all statistical quantities are independent of the origin of the co-ordinate system. The flow is isotropic if all statistical properties are invariant under arbitrary rotations or reflections of the axes of reference. Homogeneous isotropic turbulence has received extensive theoretical study because of its relative simplicity. As an example of the simplifications possible with assumptions of homgeneity and isotropy, $R_{ij}(\underline{x}, \underline{r})$ simplifies to

$$R_{ij}(\underline{x}, \underline{r}) = \left[\frac{f - g}{r} r_i r_j - g(\delta_{ij}) \right] \tag{2.13}$$

where

$$\overline{u_1'^2(x)}\, f(r) = \overline{u_1'(x)\, u_1'(x + r)} \qquad \overline{u_2'^2(x)}\, g(r) = \overline{u_2'(x)\, u_2'(x + r)}$$

For homogeneous isotropic turbulence the three dimensional energy spectrum function E(k) is related to $\phi(k)$ by

$$\phi(k) = \int_k^\infty \frac{E(k')}{k'} \left(1 + \frac{k^2}{k'^2}\right) dk' \tag{2.14}$$

$$\text{or} \quad E(k) = k^2 \frac{\partial^2 \phi}{\partial k^2} - k \frac{\partial \phi}{\partial k} \tag{2.15}$$

The exact form of E(k) has been studied theoretically. The production of turbulent energy occurs mainly in the large eddy (low wavenumber) region while the destruction of kinetic energy by viscous dissipation to heat occurs mainly in the high wavenumber region. The transfer of energy from the production region to the dissipation range is primarily by localised inertial transfer. The production eddies transfer energy inertially to eddies of a slightly smaller size which in turn transfer energy to even smaller eddies in a cascading process until the viscous effect becomes important. From this picture of turbulent energy decay come two hypotheses due to Kolmogoroff (1941 (a), (b)). Firstly, provided the Reynolds number is large enough, the production and dissipation regions are separated by an intermediate region which is characterised by the wave number k and the amount of energy ε being transferred through the range. Secondly, assuming that the inertial transfer is predominantly between eddies of only slightly different sizes, at wavenumbers much higher than the end of the production range of wavenumbers, the turbulent energy spectrum must be independent of the way in which the turbulence is produced. At high wavenumbers, the spectrum is characterised by ε, k, and the kinematic viscosity, ν. Dimensional analysis leads to the following form for E(k), viz.

$$E(k) = \varepsilon^{2/3} k^{-5/3} F(k/k_K)$$

where

$$k_K = \left(\frac{\varepsilon}{\nu^3}\right)^{1/4}$$

and F is of universal form provided k is sufficiently large. In the inertial transfer region F is a universal dimensionless constant K. Much of the turbulence theory is aimed at finding the correct form of

$F(k/k_K)$ outside this region.

The description of turbulent energy decay has been presented in terms of the three dimensional energy function E(k). It is easy to show from Equation (2.14) that $\phi(k)$ has the same power law dependence as E(k) in the inertial subrange and that the constant α in the following equation

$$\phi(k) = \alpha \varepsilon^{2/3} k^{-5/3} \qquad (2.17)$$

is related to K by

$$\alpha = \frac{18}{55} K$$

The experimental test of the existence of an inertial subrange is to measure $\phi(k)$ rather than E(k). A large inertial subrange is difficult to achieve in laboratory experiments as large Reynolds numbers are needed. (Conditions necessary for the existence of such a subrange in practical flows are discussed in Chapter 5.) Measurements have been made in geophysical flows where production occurs at very low wavenumbers, ie. large eddies and large Reynolds numbers are common.

Pond et al (1966) measured spectra in the atmospheric boundary layer over the sea and Boston and Burling (1972) measured spectra in air over a tidal mud flat. The most comprehensive measurements to date are those by Grant Stewart and Molliet (1963) obtained from a specially mounted hot film probe towed behind a ship travelling along a tidal channel. With a Reynolds number of the order of 3×10^8, spectral values within the inertial subrange were found for three decades of wavenumber variation and a value of 0.47 ± 0.02 was found for α.

The rate of dissipation of turbulent energy ε has been discussed without proper definition. For homogeneous flow ε is defined as follows (Hinze (1975))

$$\varepsilon = \nu \sum_{i,j} \overline{\frac{\partial u'_i}{\partial x_j} \frac{\partial u'_i}{\partial x_j}} \tag{2.18}$$

It can be shown that for homogeneous isotropic turbulence ε defined in this way is related to the function $k^2E(k)$ such that

$$\varepsilon = \nu \int_0^\infty k^2 E(k)\, dk \tag{2.19}$$

and $k^2 E(k)$ is called the dissipation spectrum. In terms of $\phi(k)$, the following relation holds (Hinze (1975))

$$\varepsilon = 15\, \nu \int_0^\infty k^2 \phi(k)\, dk \tag{2.20}$$

It follows from Kolmogoroff's concept of local isotropy at high wavenumbers that equations (2.19) and (2.20) can be approximately true for all types of turbulence provided the Reynolds number of the flow is large. Experimental support for this has been provided by Lawn (1971) in the case of pipe flow turbulence and his work is described in detail in Chapter 6 and Appendix 2. Experimental evidence indicates that at a Reynolds number of 90,000, equation (2.20) is a good approximation for 90% of the pipe radius or to within 10% of the pipe wall.

A result which is of use in our discussion of grid-generated turbulence in Chapter 5 is obtained by considering the situation where a turbulent field is generated in some way and subsequently allowed to decay with time without energy input. In this case, the rate of decay of turbulence intensity is approximately equal to the total viscous dissipation, hence

$$\frac{d}{dt} \left(\overline{u'^2 + v'^2 + w'^2}\right) = \varepsilon(t) = 15\, \nu \int_0^\infty k^2 \phi(k, t)\, dk \tag{2.21}$$

In grid-generated turbulence, the turbulence is generated at the grid and swept along with mean velocity $\overline{U}$ as it decays with time.

Assuming Taylor's hypothesis, we can write $dx = \bar{U}\, dt$ and obtain from (2.21) the following relation

$$\epsilon(x) = \bar{U} \frac{d}{dx} \left[\overline{u'^2 + v'^2 + w'^2} \right] = 15 \nu \int_0^\infty k^2 \phi(k, x)\, dk$$

where x is the distance of the measurement point from the grid.

2.2 TURBULENT PIPE FLOW

Laminar flow of an incompressible Newtonian fluid is described by a set of three Navier-Stokes equations together with the continuity equation. For each component of velocity u_i, the Navier-Stokes equation is

$$\frac{du_i}{dt} = \rho g_i - \frac{\partial p}{\partial x_i} + \mu \frac{\partial^2 u_i}{\partial x_j \partial x_j} \qquad (2.22)$$

Since this equation must also apply to the instantaneous velocity components in stationary turbulent flow, equations can be derived from equation (2.22) to describe turbulent flow in terms of time averaged quantities. The Reynolds equations are then derived and are as follows

$$\frac{d\bar{U}_i}{dt} = \rho g_i - \frac{\partial \bar{P}}{\partial x_i} + \mu \frac{\partial^2 \bar{U}_i}{\partial x_j \partial x_j} - \frac{\partial}{\partial x_j} \left(\overline{u'_i u'_j} \right) \qquad (2.23)$$

where $\bar{P}$ is the time averaged pressure.

Comparing equations (2.22) and (2.23) it is clear that the equations describing turbulent flow contain additional terms called Reynolds stress or eddy stress terms. With ten unknowns, $\bar{P}$, $\bar{U}_1$, $\bar{U}_2$, $\bar{U}_3$, $\overline{u'_1 u'_2}$, $\overline{u'_1 u'_3}$, $\overline{u'_2 u'_3}$, $\overline{u'^2_1}$, $\overline{u'^2_2}$, $\overline{u'^2_3}$ and only four equations including the continuity equation, additional assumptions or hypotheses are necessary to obtain aprroximate solutions of these equations, even for the simplest flows of practical interest. Such hypotheses include the Prandtl mixing length theory, Von Karman's similarity theory, Bouissinesq's eddy viscosity theory, and Van Driest's modified mixing length theory.

Prandtl's theory, applied to flow between two parallel planes not too far apart, assumes that the Reynolds stress term $\overline{u_1' u_2'}$ can be described in terms of a "mixing length" ℓ defined in the laminar sub-layer by

$$\ell = \kappa y$$

where κ is a universal constant to be found from experiment.

It is also assumed that

$$-\rho \overline{u_1' u_2'} = \rho \ell^2 \left| \frac{d\bar{U}}{dy} \right| \frac{d\bar{U}}{dy} \tag{2.24}$$

throughout the flow. For the flow between two parallel plates $\bar{U}_1 = \bar{U}_1(y)$, $\bar{U}_2 = 0$, $\bar{U}_3 = 0$, substituting equations (2.24) into the Reynolds equation yields the following equation (Pao (1967))

$$\mu \frac{d\bar{U}}{dy} + \rho \kappa^2 y^2 \left(\frac{\partial \bar{U}}{\partial y}\right)^2 = y \frac{\partial}{\partial x} (p + \rho g h) + \tau_w \tag{2.25}$$

where τ_w is the shear stress at the wall which is a constant for steady flow and μ is the fluid viscosity. Though it is difficult to find a general solution to equation (2.25), the equation can be simplified to describe the flow in the near wall region and also in the turbulent core.

Very close to the wall, as $y \to 0$, equation (2.25) simplifies to

$$\mu \frac{\partial \bar{U}}{\partial y} = \tau_w \tag{2.26}$$

Integrating equation (2.26) with $\bar{U} = 0$ at $y = 0$ the velocity distribution is seen to be

$$\bar{U} = \frac{\tau_w}{\mu} y$$

or in dimensionless form,

$$u^+ = y^+ \qquad \text{where} \quad u^+ = \frac{\bar{U}}{u_\tau} \qquad u_\tau = \sqrt{\frac{\tau_w}{\rho}}$$

and $$y^+ = \frac{u_\tau y}{\nu}$$

At some distance from the wall, viscous stresses are much less than the eddy stresses, ie.

$$\rho\kappa^2 y^2 \left(\frac{d\bar{U}}{dy}\right)^2 >> \mu \frac{d\bar{U}}{dy} \tag{2.27}$$

and if the plane walls are not too far apart, a region exists where the following inequality also holds.

$$\rho\kappa^2 y^2 \left(\frac{d\bar{U}}{dy}\right)^2 >> y \frac{\partial}{\partial x}\left[p + gh_z\right] \tag{2.28}$$

In the region where both (2.27) and (2.28) are valid, equation (2.25) simplifies to

$$\rho\kappa^2 y^2 \left(\frac{d\bar{U}}{dy}\right)^2 = \tau_w \tag{2.29}$$

Taking square roots of both sides of this equation, separating the variables and integrating gives the following solution

$$\frac{\bar{U}}{u_\tau} = \frac{1}{\kappa} \ln y + B \tag{2.30}$$

Between these two regions lies the buffer zone where both viscous and eddy stress terms are important and the flow is transitional in nature.

Fully developed turbulent flow in smooth pipes is closely similar to the flow between parallel plates just described and, as a matter of experimental observation, three similar flow regions have been identified and are described approximately by the following three equations (from the pipe edge outwards).

The laminar sub-layer

$$u^+ = y^+ \tag{2.31}$$

the buffer zone

$$u^+ = C \ln y^+ + D \tag{2.32}$$

and the turbulent core

$$u^+ = A \ln y^+ + B \qquad (2.33)$$

Using pitot tube probes, Nikuradse (1933) measured velocity profiles in turbulent flow in both smooth and rough pipes. For smooth pipes in the turbulent core he found

$$u^+ = 5.75 \log y^+ + 5.5 \qquad (2.34)$$

to be the best fit to his experimental data. Such values for A and B are now accepted as typical though slightly different values have been found for different tube diameters and Reynolds numbers.

If equation (2.29) holds also at the pipe centreline then the velocity at a distance y from the wall within the turbulent core can be found in terms of the centreline velocity $\bar{U}_c$ since

$$\frac{\bar{U}_c}{u_\tau} = A \ln \frac{R}{u_\tau} \qquad \text{and} \qquad \frac{\bar{U}}{u_\tau} = A \ln \frac{y}{u_\tau} + B$$

it follows by subtraction that

$$\frac{\bar{U}_c - \bar{U}}{u_\tau} = A \ln \left(\frac{R}{y}\right) \qquad (2.35)$$

The left-hand side of equation (2.35), $(u_c^+ - u^+)$ is called the Velocity Defect and velocity profiles are often plotted in terms of the velocity defect both for Newtonian and non-Newtonian flows even when equation (2.35) is not satisfied.

Beyond the laminar sub-layer and buffer zone, measured velocity profiles have been found to deviate from the form of equation (2.33) particularly near the pipe centreline where the measured values of u^+ normally lie above the predicted straight line on the semi-logarithmic plot. (Equation (2.33) cannot hold at the centreline in any case as the velocity gradient must be zero because of the symmetry of the flow.) Because of this, many authors, eg. Hinze (1959), Millikan (1939), Reichardt (1951), Bogue and Metzner (1963) have proposed an additional

correction term to describe the flow throughout the fully turbulent region. Bogue suggested a correction term of the following form as a result of experimental observation

$$u^+ - c(\xi, f) = 5.57 \log y^+ - 5.57 \tag{2.36}$$

where

$$c(\xi, f) = 0.05 \sqrt{2/f} \exp \frac{(\xi - 0.8)^2}{0.15} \tag{2.37}$$

Although the term "corrected" data is used, this term is not well chosen since it implies that the original data is in error. It is important to realise that the reason for plotting "corrected" data is to obtain more accurate values for A and B from the straight line fitting process on a semi-logarithmic plot and that uncorrected data is in fact perfectly correct.

The friction factor f is an important quantity in pipe flow measurement. Experimentally, to measure frictional losses in pipe flow the pressure drop between pressure tappings set into the pipe wall a distance apart is measured using a U-tube manometer or a pressure transducer. The pressure drop dp over a distance dx is related to the wall shear stress τ_w by

$$\tau_w = \frac{R}{2} \frac{dp}{dx} \tag{2.38}$$

A dimensionless pressure gradient can be defined by writing $p^* = p/\rho V^2$ and $x^* = x/R$ where V is the volume flow rate. The Fanning friction factor is defined as

$$f = \frac{dp^*}{dx^*}$$

and is clearly related to the wall shear stress by

$$f = \left(\frac{2}{\rho V^2}\right) \tau_w \tag{2.39}$$

Equation (2.36) can be rewritten in the following form

$$u^+ = A^+ \ln y^+ + B + c(\xi, f) \qquad (2.40)$$

By multiplying equation (2.40) by $2\pi r$ and integrating across the pipe radius the volume flow rate can be found and a relationship between friction factor and Reynolds number can be obtained. Algebraic manipulation, outlined in Massey (1975), leads to the result that

$$f^{-\frac{1}{2}} = \left(\frac{A}{\sqrt{2}}\right) \ln \left(Re \sqrt{f} + \left[B - A \ln \sqrt{8} - \frac{3}{2} A\right]\right)$$

provided that

$$\int_0^1 (1 - \xi)\, c(\xi, f)\, d\xi$$

is small. Since $c(\xi, f)$ has been assumed to be appreciable only near the centreline where $(1 - \xi)$ is small this condition is normally satisfied and the general friction factor - Reynolds number relationship

$$f^{-\frac{1}{2}} = M \log (Re \sqrt{f}) + N$$

is widely supported by experimental evidence and is known as the Prandtl-Karman law.

CHAPTER 3

THE MEASUREMENT OF VELOCITY IN DRAG REDUCING SOLUTIONS

3.1 RESPONSE OF PITOT AND HOT FILM PROBES

Of the early measurements made in polymer solutions, the most reliable were those obtained using particle tracers or dye injection techniques (eg. Seyer and Metzner (1969), Arunachalam et al (1972)). However, only a limited amount of data can be obtained using these techniques and many researchers used pitot tubes and hot film probes in polymer flows. Doubts were raised as to the reliability of these devices when large discrepancies were found between volume flow rates calculated from mean velocity profiles and the volume flow rates measured using other techniques such as "bucket and stop watch" methods. There were also difficulties in obtaining consistent and repeatable results and these problems led to experimental investigations and theoretical considerations of the response of both pitot tubes and hot film probes in polymer solutions.

Astarita and Nicodemo (1966) considered the effect of normal stresses on the apparent velocity measurement by pitot tube and concluded that for visco-elastic fluids, the apparent velocity in turbulent flow should always be less than the true value and could in fact be negative near a wall. Volume flow rates were compared with averaged apparent velocity profiles for a number of concentrations of ET 597 and a range of Reynolds numbers. With a Reynolds number of 5870 and a polymer concentration of 1000 ppm, the discrepancy was found to be 30%.

Smith et al (1967) measured apparent velocity profiles in water and polyethylene oxide solutions using several pitot tubes (0.025 cm, 0.055 cm and 0.168 cm diameter) and a cylindrical hot film probe.

Using the same volume flow rate for the solvent and drag reducing flows, measurements of mean velocity profile for the solvent and polymer were compared for each probe. It was found that the measured profiles in the water flow were the same for each pitot tube. In polymer flow however, different profiles were measured and the volume flow rate calculated by integration of the velocity profile varied with pitot tube diameter. The smallest tube under-estimated the volume flow rate whereas with the 0.168 cm diameter tube the measured flow rate was excessively large. From static calibrations of the hot film in solvent and polymer solutions, the relative heat transfer coefficients were obtained as a function of velocity. The heat transfer coefficient was lower in polymer solutions and varied with polymer degradation and also with velocity. The heat transfer coefficient also varied with position in the pipe, polymer molecular weight and concentration.

Astarita and Nicodemo (1969) further investigated probe response this time by towing probes through a static test tank to eliminate normal stress effects and to allow accurate measurements of velocity to be independently made. Reliable data was obtained which indicated that the heat transfer coefficient was lower in polymer solutions and a function of polymer concentration. With pitot tubes, it was observed that the apparent velocity differed from the true value by as much as 40% the discrepancy increasing with reducing tube diameter although significant errors were observed with a pitot tube of 1.0 cm diameter.

Distinguishing between the dependence of the measurements on the many variables mentioned above and on actual change in flow velocity is very difficult and the reliability of some of the early profile measurements must be in doubt. It is clear that, at best, these instruments are capable of reliable measurements of mean velocity only

if extensive calibration tests are made for each solution and re-checked in the presence of degradation. Even then, the effect of normal stress variations cannot easily be compensated for.

When making spectral measurements, it was discovered (Friehe and Schwarz (1969)) that the shape of the hot film probe affects the apparent measurement. It was found that using a cylindrical probe the shape of the velocity spectrum in a grid generated turbulent polymer flow gave a power law dependence at high wave numbers whereas a conically shaped probe indicated an exponential-like dependence although both probes yielded identical spectral shapes in pure water flows. One of these results is reproduced in Figure 3.1 for a 50 ppm J100 polymer solution.

Since the first development of the laser velocimeter by Yeh and Cummins (1964) a great deal of research and development has resulted in the widespread use of the laser velocimeter both as an alternative to the conventional devices and in flow situations (such as velocity measurement in flames) where velocity measurement using physical probes would be difficult if not impossible.

Laser velocimeters have some fundamental advantages over both hot wire and pitot tube instruments in the measurement of velocities in polymers. The response to velocity is linear and is unchanged in water or polymers. The response is unaffected by polymer degradation or variation in concentration. Also no physical probe is placed in the flow so the flow is not disturbed. However the measurement of energy spectra using laser velocimeters has some limitations which will now be outlined although it should be noted that these apply equally to Newtonian and non-Newtonian flows.

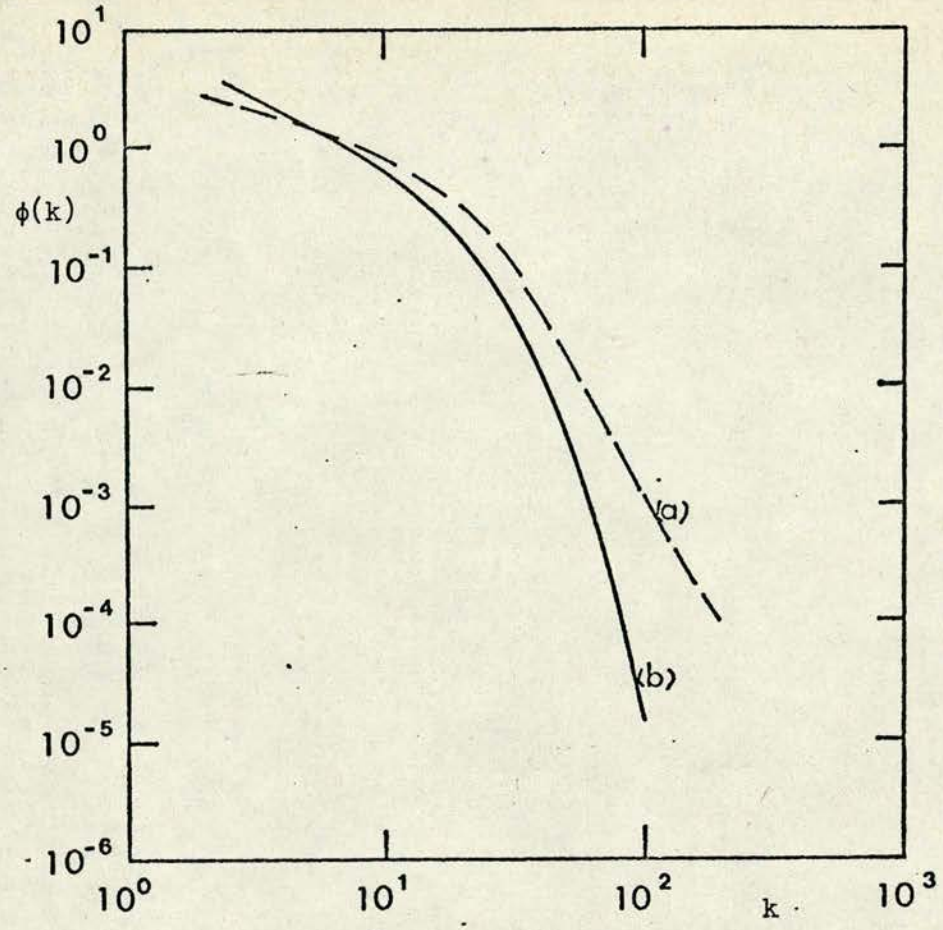

Figure 3.1

One Dimensional Energy Spectra
in J100 Polymer Solution Measured by
Friehe and Schwarz using
(a) cylindrical hot film probe, (b) conical hot film probe

3.2 THEORY OF THE LASER VELOCIMETER

Most of the early work on laser velocimetry was concerned with the development of different optical arrangements and a great number of systems have been successfully operated using a wide range of optical components. Nearly all systems employ a laser as the light source because of its high monochromaticity, as well as some device for splitting the beam into two components which are subsequently recombined either at the flow measurement position or on the surface of the photodetector. A discussion of the merits of a number of the early arrangements can be found in a paper by Durst and Whitelaw (1971).

Nearly all the arrangements are variations of either the heterodyne (reference beam) system or the real fringe system. In the real fringe mode, the laser beam is split into two beams of equal intensity which intersect at a point (or strictly a small volume) in the fluid forming a pattern of equally spaced fringes. As a particle in the fluid passes through the measuring point the intensity of light scattered by the particle varies as the particle crosses the fringes, the frequency of variation being proportional to particle velocity. In the heterodyne mode, the two beams are of unequal intensity and it is not essential that both beams pass through the fluid. The stronger beam passes through the fluid and the beam intensities are adjusted so that the intensity of light scattered by particles crossing the measuring point received by the photo-detector is approximately equal to the intensity of the weaker reference beam which is aligned directly onto the photo-detector. The scattered light is of a slightly different frequency from the incident light (and hence the reference beam frequency) due to the doppler effect. The scattered light and the reference beam interfere on the surface of the photo-detector giving a beat frequency signal, the frequency of which is proportional to the particle velocity.

It is important to remember that the L.D.V. measures the velocity of the light-scattering particles in the flow rather than the flow itself. Large particles cannot follow small scale motions of dimension less than the particle size. Also large particles scatter a large amount of light and contribute disproportionately to the total detected intensity.

It is sometimes possible to filter the flow to remove large particles of dust, etc, normally present in the liquid and to add scatterers which are neutrally buoyant and of a regular small size. However to avoid degradation, most of the experiments in polymers were carried out in once-through flow systems and, because of this, the cost of using commercially available particles was prohibitive.

Figures 3.2 (a) and 3.2 (b) show simple arrangements of the real fringe and heterodyne systems respectively. For the real fringe system the detected frequency is independent of the angle of light collection and the schematic in Figure 3.2 (c) can be used to discuss either system. This figure is also used to define the relevant co-ordinate systems which will be used in the following discussion.

Durrani and Greated (1977) show that the total electric field incident on a point (x', y') on the surface of the photo-detector is given by

$$E_D(x', y') = E_r(x', y') + E_s(x', y') + E_{rs}(x', y')$$

where E_r is the direct field due to the reference beam, E_s is the field due to light scattered from the scattering beam and E_{rs} is the field due to light scattered from the reference beam.

The method of detection is normally by using either photo-multiplier tube or a solid state photo-detector. In both cases, the output current of the device is given by

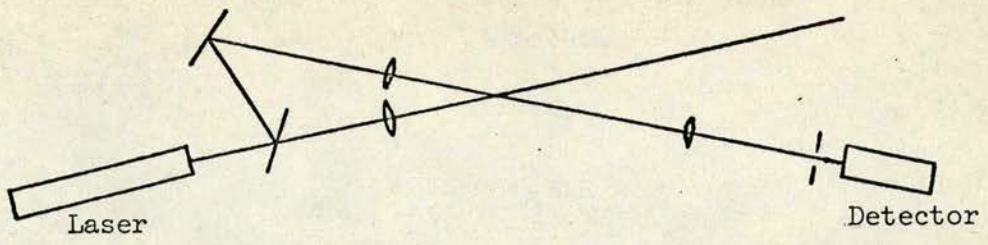

(a)

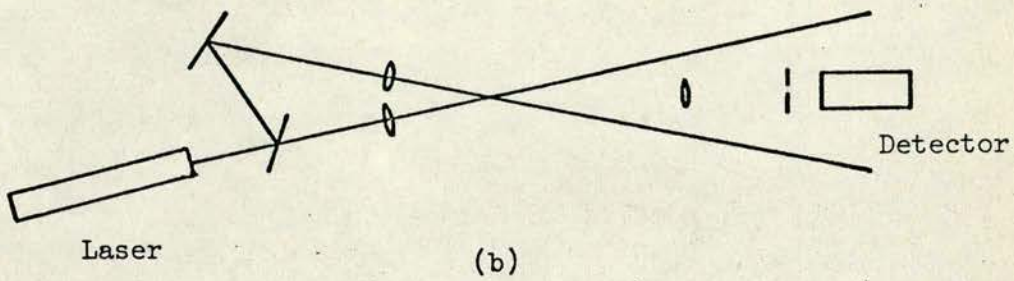

(b)

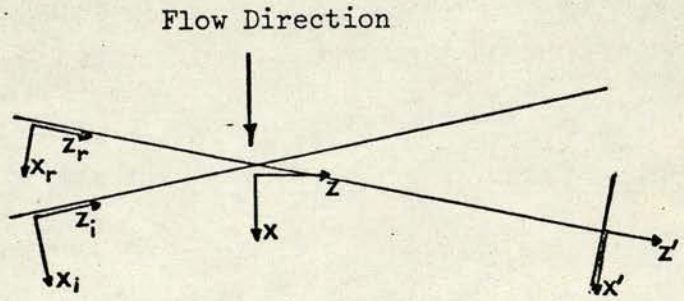

(c)

Figure 3.2

Simple Optical Arrangements of the (a) Heterodyne and (b) Real Fringe types. Figure 3.2 (c) shows the co-ordinate systems used in the discussion of the theory of the Laser Velocimeter

$$i_T = \eta \int |E_D|^2 \, dA$$

where η is a property of the detector and the integration is performed over the surface area A of the detector. Simple substitution gives the following expression

$$i_T = i_o + i_{RH} + i_F + i_{DH}$$

where

$$i_o = \eta \int |E_r|^2 + |E_{is}|^2 + |E_{rs}|^2 \, dA$$

$$i_{RH} = \eta \int (E_r E^*_{rs} + E^*_r E_{rs}) \, dA$$

$$i_F = \eta \int (E_{rs} E^*_s + E^*_{rs} E_{is}) \, dA$$

and $$i_{DH} = \eta \int (E_r E^*_s + E^*_r E_{is}) \, dA$$

Since the detectors normally used do not respond to optical frequencies, i_o is essentially a d.c. term. For the fringe system, both direct beams are masked from the detection optics and only the Fringe current term i_F contributes to the doppler signal. In the heterodyne system where $|E_{rs}|^2 << |E_r|^2$, the Doppler Heterodyne term i_{DH} dominates the detected beat signal. It is clear that by altering the relative beam intensities and moving the detector a system can be operated in either of the two modes.

Since the real fringe mode was used in all the work presented in this thesis, it will now be considered in more detail. For most of the results presented here concerning the fringe system, equivalent if not identical expressions can be found for the reference beam system. George and Lumley (1973) give an excellent account of the theory of the reference beam system. The system to be considered here is that shown in Figure 3.3 where the two beams of equal intensity are focussed using the same lens to an intersection point in the fluid and where the direct beams are masked from the collection optics.

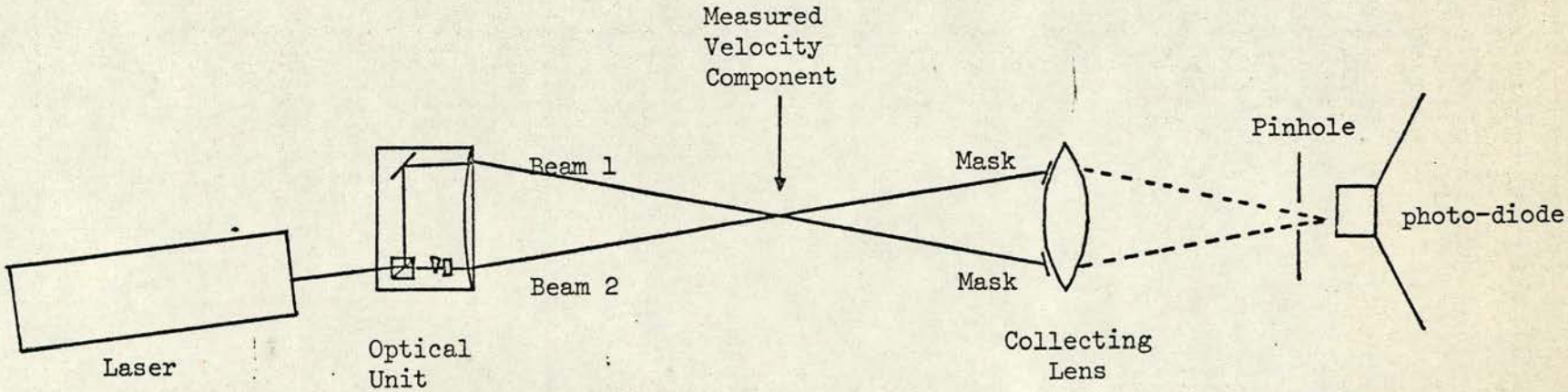

Figure 3.3

The Optical Arrangement of our Laser Velocimeter

The intensity of an unapertured laser beam can be approximated by a Gaussian distribution. It has been shown (Kogelnik (1965)) that a focussed laser beam also has a Gaussian intensity distribution at the focal point and the diffraction limited spot size is related to the initial diameter d (at the e^{-2} points of the intensity distribution) of the laser beam by

$$2\sigma = \frac{2F\lambda}{\pi d} \tag{3.0}$$

where F is the focal length of the lens and λ is the wavelength of the laser light source and 2σ is the spot size at the e^{-2} points.

We shall now consider the signal detected by placing a stationary spherical particle in the measuring volume at a point (x, y, z). The electric field incident on the particle due to beam 1 is given by

$$E_1(x_1 y_1 z_1) = E_o \exp\left[- \frac{x_1^2 + y_1^2}{2\sigma^2} + j\, k\, z_1 \right] \quad \text{where } j = \sqrt{-1} \tag{3.1}$$

and that due to beam 2 is

$$E_2(x_2 y_2 z_2) = E_o \exp\left[- \frac{x_2^2 + y_2^2}{2\sigma^2} + j\, k\, z_2 \right] \tag{3.2}$$

Employing Mie scattering theory for spherical radiators, Durrani and Greated derive the following expression for the photo-detector current.

$$i_F = \eta(\tfrac{1}{2} M C_{sc})^2 \left[|E_1|^2 + |E_2|^2 + 2\, \mathrm{Re}\, (E_1 E_2^*) \right] \tag{3.3}$$

where

C_{sc} is the scattering cross section of the particle

M is the magnification factor of the receiving optics.

Substitution of equations (3.1) and (3.2) into (3.3) and transforming to the particle co-ordinate system gives

$$i_F = \eta(\tfrac{1}{2} M C_{sc})^2 E_o^2 \exp\left[-\frac{x^2\cos^2\theta + y^2 + z^2 \sin^2\theta}{\sigma^2}\right] \times$$

$$\left[\cosh\left(\frac{xz}{\sigma^2} \sin 2\theta\right) + \cos\left(\frac{4\pi}{\lambda} x \sin\theta\right)\right] \qquad (3.4)$$

It can be seen from equation (3.4) that the photo-current is a maximum at the centre of the measuring volume. The extent of the volume can be defined by assuming that i_F is appreciable only when it is a certain fraction of the maximum. The so-called $1/e^2$ points are normally used although some authors, including Durrani and Greated, prefer the 1/e points. The surface where the field intensity is $1/e^2$ of maximum is given by

$$x^2 \cos^2\theta + y^2 + z^2 \sin^2\theta = 2\sigma^2$$

which is an ellipsoid, the axes of which define the characteristic dimensions of the measuring volume

$$2\sigma_x = \frac{2\sigma}{\cos\theta} \quad , \quad 2\sigma_y = \frac{2\sigma}{\sin\theta} \quad , \quad 2\sigma_z = 2\sigma \qquad (3.5)$$

The photo-current due to one particle crossing the measuring volume with uniform velocity $\bar{U}$ in the x direction can be found by writing $x = \bar{U}t$ in equation (3.4). For the pth particle Durrani and Greated show that equation (3.4) with the substitution can be re-written in the following form

$$i_p(t) = \kappa K_p W(t)\left[1 + \cos\frac{4\pi}{\lambda}\bar{U} t\right]$$

Both κ and K_p are time independent terms. κ is a constant for a given optical geometry and K_p is dependent on the properties and concentration of the particles. The weighting function of the doppler signal is given by

$$W(t) = \exp\left(-\frac{\bar{U}^2 t^2 \cos^2\theta}{\sigma^2}\right)$$

In most practical systems the photo-detector signal is high-pass

filtered before analysis thus removing the low frequency term W(t). The high frequency cosine term contains the velocity information, the frequency of the detected signal, f, being related to the flow velocity by

$$f = \frac{2\bar{U}}{\lambda} \sin\theta = K\,\bar{U} \qquad (3.6)$$

For flows where the concentration of scattering particles is low, as for example in un-seeded air flow, the flow velocity can be measured simply by measuring f for each particle crossing the fringe volume. In this case the photo-current is a series of non-overlapping signal bursts.

Often, as in our case for naturally occurring scattering particles in tap water flow, a large number of particles are present in the measuring volume at any instant and the photo-detector current is a superposition of a large number of signal bursts with varying phases. The total photo-current is then

$$i(t) = \sum_{p=-\infty}^{\infty} i_p\,(t - t_p)$$

where t_p is a random sequence of particle arrival times at the measuring volume.

The effect of random particle arrival on the doppler signal has been considered by Durrani and Greated (1973) and George and Lumley (1973) using results derived by Rice (1944) and Middleton (1960) for shot noise. The continuous doppler signal for this case can be written as

$$i(t) = H(t) \cos\left[\, 2\pi\, f_o(t)t - \phi(t) \right] \qquad (3.7)$$

hence the instantaneous detected doppler frequency is given by

$$f_i(t) = f_o(t) - \frac{1}{2\pi}\,\phi'(t) \qquad \text{(Hz)} \qquad (3.8)$$

The measured signal frequency contains an additional term commonly called the "ambiguity term". Since the velocity statistics are obtained from f_o rather than f_i is is necessary to know the statistics of ϕ' so that velocity statistics can be deduced from the measurement of the statistics of $f_i(t)$.

An early method of analysing the doppler signal, used for example by Goldstein et al (1969), was to pass the high-pass filtered doppler signal through a spectrum analyser. The mean frequency of the resulting Gaussian doppler spectrum gives a direct measurement of the mean velocity. The width of the spectrum can be used to determine the turbulence level once correction has been made to account for the ambiguity. For a uniform flow with a low level of turbulence and well aligned optics, the measured spectral width is related to the turbulence level by (Durrani and Greated (1973))

$$\Delta f^2 = K^2 \overline{(u'^2)} + \left(\frac{\bar{U}}{2\sqrt{2\pi}\sigma_x}\right)^2 \qquad (3.9)$$

It can be seen from equation (3.9) that even for laminar flow with no velocity gradient a non-zero r.m.s. value for the doppler spectrum is obtained.

Other broadening effects have been considered theoretically. Edwards et al (1971) considered broadening due to molecular diffusion of the scattering particles and demonstrated that this effect is negligible provided that the following inequality holds.

$$u \gg \frac{8\pi D}{\lambda} \sin\theta \qquad (3.10)$$

where D is the molecular diffusivity. For our system the right-hand side of equation (3.10) is of the order of 4×10^{-3} cm/sec and hence equation (3.10) is satisfied for our measurements of velocity which ranged from 30-100 cm/sec.

Edwards et al also considered the effect of a mean velocity gradient across the measuring volume on the detected doppler frequency. It was shown that if the velocity gradient were constant throughout the measuring volume then the measured mean velocity was the same as the centre point mean velocity. However, the width of the measured spectrum was shown to be increased as a result of "velocity gradient" broadening.

George and Lumley (1973) considered theoretically the effect of turbulence on the measured doppler frequency spectrum. Two competing effects were found. The measured r.m.s. values are increased because of spatial variations in the turbulent velocity within the measuring volume but the measured spectrum of velocity fluctuation is attenuated at high frequencies if the measuring volume dimensions are of the order of or larger than the corresponding turbulence microscales. The first of these effects gives an additional term which we will call "turbulence broadening".

If the signal due to each of the broadening effects has a Gaussian spectrum and the effects are uncorrelated then the total variance in the angular frequency of the detected frequency is

$$\Delta\omega^2 = \Delta\omega^2_{u'^2} + \Delta\omega_1^2 + \Delta\omega_2^2 + \ldots. \qquad (3.11)$$

where $\Delta\omega^2_{u'^2}$ is the variance due to centre point velocity fluctuations and $\Delta\omega_1^2$, $\Delta\omega_2^2$, ... are the variances due to the other effects.

Berman and Dunning (1973) have tested the validity of equation (3.11) in turbulent pipe flow by measuring spectral widths using several sizes of measuring volume. By combining expressions due to George and Lumley (1973) for random particle broadening and turbulence broadening with a first order approximation of the general expression

derived by Edwards et al (1971) for velocity gradient broadening, the following result was obtained

$$\Delta f^2_{measured} = K^2 \overline{(u'^2)} + \Delta f^2 \qquad \text{(Hz)}$$

where

$$\Delta f^2 = \left(\frac{\bar{U}}{2\sqrt{2}\,\pi\sigma_x}\right)^2 + \left(-K\frac{d\bar{U}}{dy}\,\sigma_y\right)^2 + \frac{4}{15}K^2\left(\frac{\varepsilon}{\nu}\right)(\sigma_y^2 + \sigma_z^2) \qquad (3.12)$$

$$= \begin{pmatrix}\text{Random}\\ \text{Particle}\\ \text{Broadening}\end{pmatrix} + \begin{pmatrix}\text{Velocity}\\ \text{Gradient}\\ \text{Broadening}\end{pmatrix} + \begin{pmatrix}\text{Turbulence}\\ \text{Broadening}\end{pmatrix}$$

Velocity gradients and turbulence dissipation rates were estimated from the measurements of Ecklemann (1970) and Laufer (1954) in Newtonian flow. The measured spectral widths were found to be in good agreement with those calculated using equation (3.12).

Although direct measurement of the doppler spectrum is a convenient method of signal analysis it is inadequate for the measurement of velocity correlations or spectra since real time information is lost in the analysis. F.M. demodulators have therefore been used, for example by Chung and Graebel (1972), and a number of instruments have been specifically designed for the processing of the laser doppler signal. These frequency tracking instruments provide an output voltage which is proportional to the instantaneous frequency of the input and normally incorporate a feedback loop to improve the detection of signals with a low signal/noise ratio. The central part of these instruments is a narrowband I.F. filter with a variable centre frequency. The feedback loop is used to match this centre frequency to the incoming doppler frequency and the resulting signal is demodulated using a frequency discriminator and a low-pass filter. The output voltage can be analysed using analogue instruments to measure mean velocity (digital voltmeter), turbulence level (true r.m.s. meter) or velocity

spectrum (wave analyser). In our case the velocity records were digitised and analysed by computer.

Of particular interest in our work was the measurement of the spectrum of velocity fluctuation. To measure this accurately the effect of the various ambiguity terms must be accounted for. Durrani and Greated have considered the effect of "random particle" broadening on the measurement of the energy spectrum of velocity fluctuation. The problem is one of determining the spectrum of ϕ' defined by equation (3.8) throughout the frequency range of interest. Durrani and Greated have shown that the spectrum function $\mathcal{J}$ of the ambiguity term ϕ' is

$$\mathcal{J}_{\phi'}(f) = \frac{f}{2\sqrt{\pi}} \sum_{m=1}^{\infty} \frac{1}{m^{3/2}} \exp\left[-\frac{1}{4m}\left(\frac{f}{\Delta f}\right)^2\right]$$

where Δf is the doppler spectrum bandwidth for laminar flow. Since the doppler spectrum bandwidth, Δf, is normally much greater than the highest frequency of velocity fluctuation, $\mathcal{J}$ is essentially flat over the frequency range of interest and can be approximated by its value at $f = 0$. Thus

$$\mathcal{J}_{\phi'}(f) \simeq 0.7369 \ \Delta f \qquad (\text{Hz})^2/\text{Hz} \qquad (3.13)$$

Here we have established the relationship between the width of the ambiguity doppler spectrum term and the spectrum of ϕ' for random particle broadening. The measured spectrum of doppler frequency fluctuation can then be related to the actual spectrum of velocity fluctuation using equation (3.6) to convert from units of doppler frequency (Hz) to units of velocity. Hence

$$\mathcal{J}_{u'}(f) = \frac{\mathcal{J}_{f_i}(f)}{K^2} - \frac{0.7369\ \Delta f}{K^2} \qquad (\text{cm/sec})^2/\text{Hz} \qquad (3.14)$$

Although similar relations have not been derived to account for the other forms of broadening, Berman and Dunning (1973) found good agreement

between theory and experiment by assuming that equation (3.13) is valid for all types of broadening.

3.3 OPTICAL ALIGNMENT AND SIGNAL PROCESSING

The actual optical arrangement used for all measurements is shown in Figure 3.3. The light source was a Helium Neon gas laser with an operating wavelength of 632.8 nm and a rated output power of 5 mW. The laser beam was plane polarised with a beam diameter of 0.65 mm at the $1/e^2$ points. An integrated optical unit (Disa type 55L01) was used to form the fringe pattern. This unit employs a biprism as the beam splitter and has an adjustable beam separation and a range of converging lenses, giving scope to vary the measuring volume dimensions. All optical components were mounted on a 1.5 m optical bench and the optics were aligned so that the measuring volume was in line with the centre-line of the optical bench. The collection optics could then be aligned centrally on the optical bench.

For the grid turbulence measurements the alignment procedure was as follows. The beam separation was adjusted to the maximum possible which is 5 cm. The optical unit was mounted on the optical bench and the laser adjusted so that the first beam (beam 1 in Figure 3.5) was parallel to the optical bench and in a horizontal plane. Beam 2 was then similarly adjusted, this time by adjusting the two glass wedges in the optical unit. The shortest focal length lens, focal length 13 cm, was attached to the optical unit and the unit adjusted until the measuring volume was positioned along the optical axis. The collection lens was then adjusted so that the beams were re-combined on the optic axis. The photo-diode and pinhole were adjusted so that the direct beams were focussed to intersect on the surface of the photo-detector. The optical bench was then moved so that the measuring

volume intersected at a point in the flow. The collection optics were adjusted, by moving the components along the optical bench, to compensate for the change in refractive index and the optical bench was rotated so that the direct beams were again focussed on the photo-detector surface thus ensuring that the optic axis was perpendicular to the channel walls. Finally the direct beams were masked off from the collection optics. In pipe flow experiments the alignment procedure is similar although in this case the height of the optic axis is critical since the beams must be aligned across the diameter of the pipe.

Using equations (3.0) and (3.5) the measuring volume dimensions were calculated to be

$$2\sigma_x = 0.0082 \text{ cm} \quad , \quad 2\sigma_y = 0.0080 \text{ cm} \quad , \quad 2\sigma_z = 0.0426 \text{ cm}.$$

Block diagrams of the signal processing systems are shown in Figures 3.4(a) and (b). Contained in the housing for the photo-diode (Mullard BPY 13A) was an a.c. coupled pre-amplifier circuit and the pre-amplified signal was high-pass filtered using a Kemo type VBF/1 filter (cut-off frequency 50 kHz, roll-off 24 dB/octave) before being fed into the frequency tracker. The frequency tracker used was a Disa Model 55L20 Doppler Signal Processor which was operated in the frequency range 0.225-1.5 MHz and with an I.F. filter bandwidth of 60 kHz. This particular model has a "drop-out" detection circuit. When the incoming signal falls below a pre-set voltage no correction is made to the centre frequency of the filter. Thus if no particles were present in the measuring volume at any instant the instrument would not follow the variation in the instantaneous frequency of the background noise but would remain at the same frequency until an acceptable signal was present. A meter indicates the proportion of

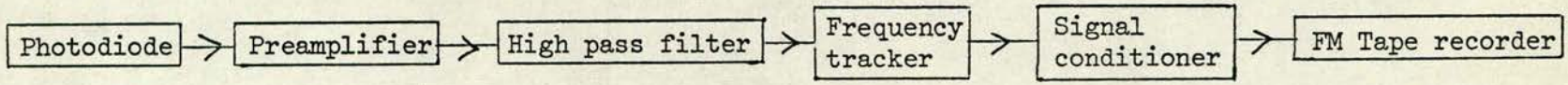

(a)

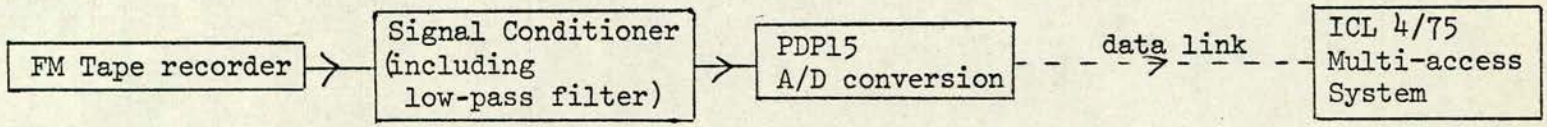

(b)

Figure 3.4

Signal Processing System for

(a) Recording the velocity record

(b) Digitising the velocity record

the time that the drop-out circuit is in operation and thus gives an indication of the quality of the incoming signal. In nearly all cases the drop-out detected was less than 5% although, near the pipe wall, it was sometimes as high as 10%.

Most of our measurements were made in "oncethrough" systems where the time available for measuring was limited. Conventional wave analysers using one narrow band pass filter which is swept through the frequency range of interest could not give reliable estimates within the short time of each experiment. Three other methods of analysis were possible.

a) Recording analogue signals using a magnetic tape recorder and then replaying over an extended period through a conventional wave analyser.

b) Recording analogue signals and replaying into an Analogue to Digital (A/D) convertor for subsequent digital analysis.

c) Real time A/D conversion using either a PDP 8 or PDP 11 computer. Digital analysis on a small machine or data transfer by link to a larger machine.

Method (a) was immediately available but is tedious when many spectra have to be measured over a large range of frequencies. Methods (b) and (c) involved a considerable amount of computer programming.

Method (c) was considered unsuitable for several reasons. The PDP 11 is used primarily to control and collect data from several experiments over long periods of time. Our requirement was for almost exclusive use of the machine, in particular the available core store, for a very short period of time. Using the PDP 8 was rejected because the available core store was insufficient to hold the number of data points needed for the PSD computation. Using either computer, the PSD

calculations could not have been carried out immediately. Transferring the data to the large computer system is as inconvenient as using method (b) in relation to the time lag between measurement and obtaining the results. Method (b) was therefore used throughout.

To calculate the mean velocity from the tracker output it is necessary to retain the D.C. contribution of this output and a frequency modulated (F.M.) tape recorder must be used. The recorder used was a Thermionic Model T300 reel to reel F.M. tape recorder. Operated with a tape speed of 15 inches per second the frequency response was D.C. - 5 kHz with a linearity of ± 1.5% and an overall signal to noise ratio of 39 dB (record and re-play). To ensure maximum sensitivity the tracker was biased or D.C. offset and amplified using a Disa "Signal Conditioner" type 55D26. Calibration of the tape recordings was achieved by recording two extra records of D.C. signals corresponding to two known Doppler frequencies at the end of each experimental run.

Analogue to digital conversions were carried out at the Edinburgh Regional Computing Centre using a PDP 15 computer. Since this was a standard facility provided by the centre, the necessary programming had already been written and the digitising process was straight forward. The digitised data was stored on magnetic tape and the data was subsequently transferred by link to the large multi-access computer system for analysis.

An inherent problem in analogue to digital conversion is that of aliasing where periodic continuous signals of different frequencies appear identical at the sampling points. This is illustrated in Figure 3.5(a). In calculating power spectra digitally the highest frequency estimate f_c is one half of the digitiser sample rate. Any estimate of

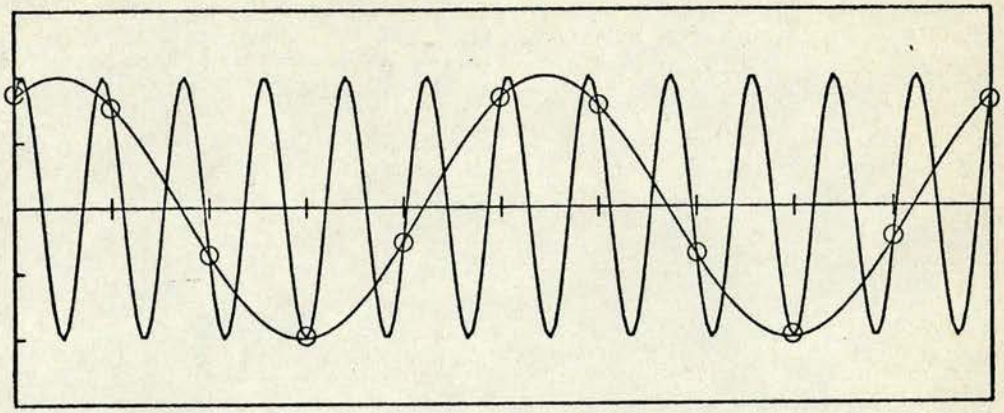

(a)

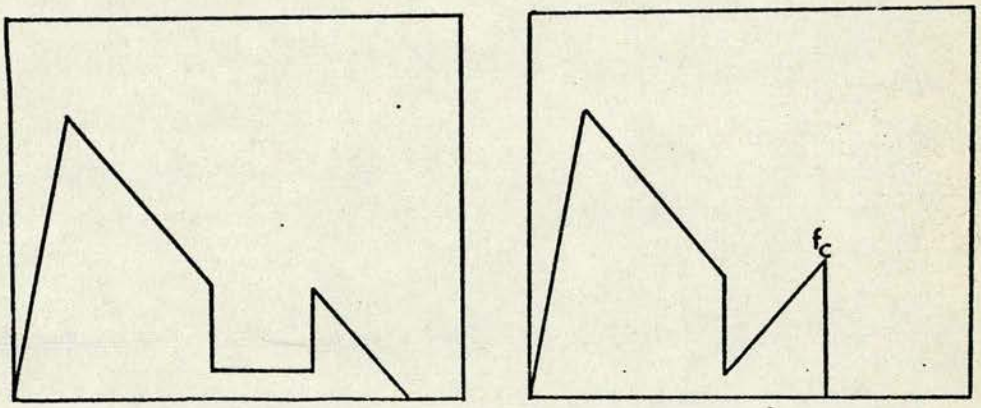

True Spectrum (b) Aliased Spectrum

Figure 3.5

The Effect of "Aliasing" on (a) the Time Series, (b) the Spectrum

the power frequency f will contain contributions from a range of higher frequencies

$$(2f_c \pm f), \quad (4f_c \pm f), \quad \ldots\ldots \quad (2nf_c \pm f)$$

This result follows from the periodicity of both $\sin^2$ and $\cos^2$ functions. The effect of aliasing on the spectrum illustrated for a hypothetical function in Figure 3.5 (b).

Low pass filtering of the analogue output can be used to attenuate the unwanted higher frequency components and reduce the aliasing effect. Filtering can be done before or after tape recording or both. For all the spectra presented in this thesis, filtering was carried out after recording, ie. on replay so that the tape recordings could be re-digitised at a different sample rate should this be thought desirable.

The perfect low pass filter passes all frequencies below the cut-off frequency f_c and rejects completely all frequencies above f_c. A measure of the efficiency of a filter is its slope measured in decibels per octave. It is important that the filter cut-off be as sharp as possible (ie. large slope) for two reasons. The filter cut-off frequency is the so-called 'half power point' where the power of an incoming sine wave of frequency f_c would be attenuated by 50% on passing through the filter. A range of frequencies below f_c are attenuated in some manner, the extent of that range being related to the filter slope. It is also clear that the more efficient filter attenuates frequencies above f_c to a greater extent than the less efficient filter and hence reduces the extent of the aliasing problem. The choice of sample rate and filter cut-off frequency is discussed in detail in Chapter 4.

Only a fixed set of values can be taken by any sampled voltage

which is digitised. This results in a quantization error in the digitised record. It can be shown that the standard deviation of such an error is 0.29 scale units. The digitisation was carried out to 12 bit precision (ie. 1 part in 4096) within the range ± 5 volts. The standard deviation of the error was 0.71 mV which is negligible comparedwithother errors.

3.4 ESTIMATION OF THE AMBIGUITY EFFECT IN PRACTICE

In Section 3.2 some theoretical results were outlined which relate the statistics of the instantaneous doppler frequency to the flow velocity statistics. In this section we look at the practical limitations of calculating the ambiguity effect and, in particular, of correcting the measured spectrum of apparent velocity fluctuation to yield the true velocity spectrum. To do this we use the same approach as that of Berman and Dunning (1973), which is to calculate Δf using equation (3.12) and to assume that equation (3.13) is valid for all types of broadening. Since all three types of broadening in equation (3.12) are significant in turbulent pipe flow we will consider the effect of the ambiguity on flow measurements in Newtonian pipe flow at a Reynolds number of 24,600. These measurements are described in detail in Chapter 6 where they are compared with polymer flow.

Equation (3.12) can be re-written as (with obvious abbreviations)

$$\Delta f^2 = \Delta f_{RP}^2 + \Delta f_{VG}^2 + \Delta f_T^2 \qquad (3.15)$$

Random particle broadening can be calculated using the values of mean velocity estimated from the digitised velocity records. To calculate velocity gradient broadening the velocity gradients at the measuring points are estimated graphically from the hand fitted velocity profiles. Turbulence broadening is calculated using estimates

Table 3.1

The Theoretical Ambiguity Effect
for Newtonian Pipe Flow Measurements
(Re = 24,600)

ξ	$K\,\Delta f_{RP}$	$K\,\Delta f_{VG}$	$K\Delta f_{T}$	Ambiguity level
0.05	0.26	1.71	4.31	57.2×10^{-5}
0.11	0.30	1.20	2.62	35.8×10^{-6}
0.16	0.31	0.74	2.33	30.4×10^{-6}
0.21	0.32	0.50	2.34	29.7×10^{-5}
0.32	0.34	0.41	1.72	22.2×10^{-5}
0.43	0.35	0.40	1.53	20.0×10^{-5}
0.54	0.37	0.40	1.37	18.2×10^{-5}
0.64	0.38	0.33	1.05	14.4×10^{-5}
0.81	0.40	0.19	0.95	12.8×10^{-5}
0.97	0.40	0.00	0.75	10.6×10^{-5}

Table 3.2

Comparison of Measured and Calculated Ambiguity Levels
for Newtonian Pipe Flow (Re = 24,600)

ξ	Calculated Ambiguity Level	Measured Ambiguity Level
0.05	52.2×10^{-5}	185×10^{-5}
0.11	35.8×10^{-5}	120×10^{-5}
0.16	30.4×10^{-5}	95×10^{-5}
0.21	29.7×10^{-5}	78×10^{-5}
0.32	22.2×10^{-5}	59×10^{-5}
0.43	20.0×10^{-5}	43×10^{-5}
0.54	18.2×10^{-5}	34×10^{-5}
0.64	14.4×10^{-5}	28.5×10^{-5}
0.81	12.8×10^{-5}	16.5×10^{-5}
0.97	10.6×10^{-5}	15.5×10^{-5}

of ε obtained by identifying the inertial sub-range in the measured spectrum using a procedure outlined in detail in later chapters.

Substituting equation (3.15) into (3.14) gives the following equation

$$\phi_{u'}(f) = \frac{\phi_{f_i}(f)}{K^2} - 0.7369 \left[\frac{\Delta f_{RP}^2}{K^2} + \frac{\Delta f_{VG}^2}{K^2} + \frac{\Delta f_T^2}{K^2} \right]^{\frac{1}{2}} \qquad (3.16)$$

We shall call the second term on the right-hand side of equation (3.16) the "ambiguity level". The relative importance of the three types of broadening in determining the ambiguity level at different pipe positions can be seen by studying Table 3.1. (It can be seen for example that the velocity gradient broadening is dominant near the pipe edge but is zero at the pipe centreline.)

The calculated ambiguity levels can be compared with values estimated from the measured spectra. The measured wavenumber spectrum is related to $\phi(k)$, the true wavenumber spectrum, by

$$\phi(k) = \phi_{(k)_{measured}} - C$$

where C is a constant. Hence from equation (2.19) it can be seen that

$$\varepsilon = 15\nu \int k^2 \left(\phi_{(k)_{measured}} - C\right) \, dk$$

Using this relationship the constant C can be calculated accurately since, typically, a 10% variation in the value of C gives a 100% variation in the value of the integral. C is simply related to the value of the ambiguity level in the measured frequency spectrum by the frequency to wavenumber spectrum conversion factor.

Table 3.2 shows a comparison between measured ambiguity levels and those calculated from equation (3.16) for each measuring position. Although the predicted trend of increased ambiguity level as ξ is

Table 3.3

Comparison of Measured Ambiguity Levels
for Newtonian Pipe Flow (Re = 24,600)
with Values Calculated Assuming Enlarged Measuring Volume

ξ	Calculated Ambiguity Level (σ = 0.0315)	Measured Ambiguity Level
0.05	85.6×10^{-5}	185×10^{-5}
0.11	53.3×10^{-5}	120×10^{-5}
0.16	45.2×10^{-5}	95×10^{-5}
0.21	44.2×10^{-5}	78×10^{-5}
0.32	32.7×10^{-5}	59×10^{-5}
0.43	29.4×10^{-5}	43×10^{-5}
0.54	26.6×10^{-5}	34×10^{-5}
0.64	20.6×10^{-5}	28.5×10^{-5}
0.81	18.1×10^{-5}	16.5×10^{-5}
0.97	14.4×10^{-5}	15.5×10^{-5}

reduced is borne out by the measured values the agreement between measured and calculated values is not good and the difference in levels cannot be accounted for by simple subtraction of a presumably constant level of electronic noise.

The actual dimensions of the measuring volume depend on the quality of the optical components and the accuracy of optical alignment which can change when the system alignment is re-checked between experiments. To test whether the poor agreement between theoretical and experimental values could be accounted for by the measuring volume dimensions being larger than the ideal lens calculation predicts, theoretical values of ambiguity level were calculated for measuring volumes of similar shape but larger dimensions. Better agreement was obtained by assuming a measuring volume which is approximately 50% larger than the theoretical value although the predicted levels are consistently lower than the measured values near the pipe edge. Changing the shape of the measuring volume (by increasing σ_z in the calculation of ambiguity level) gave no further improvement to the fit. The poor agreement may well be a reflection on the accuracy of the spectra obtained in positions near the wall where the level of background stray reflected light is relatively high giving a high level of optical noise in the detected signal and where there are high turbulence levels and considerable spatial velocity variations within the volume. It may also be that equation (3.13) is not valid for forms of broadening other than random particle broadening.

For most of the spectra computed, it will be seen from Chapter 4 that the error bounds for each spectral estimate at a 90% confidence level are of the order of ± 10% and the measured spectra show fluctuations about the constant level of around 10%. In the corrected spectra, these fluctuations are greatly amplified. Figure 3.6 shows the result

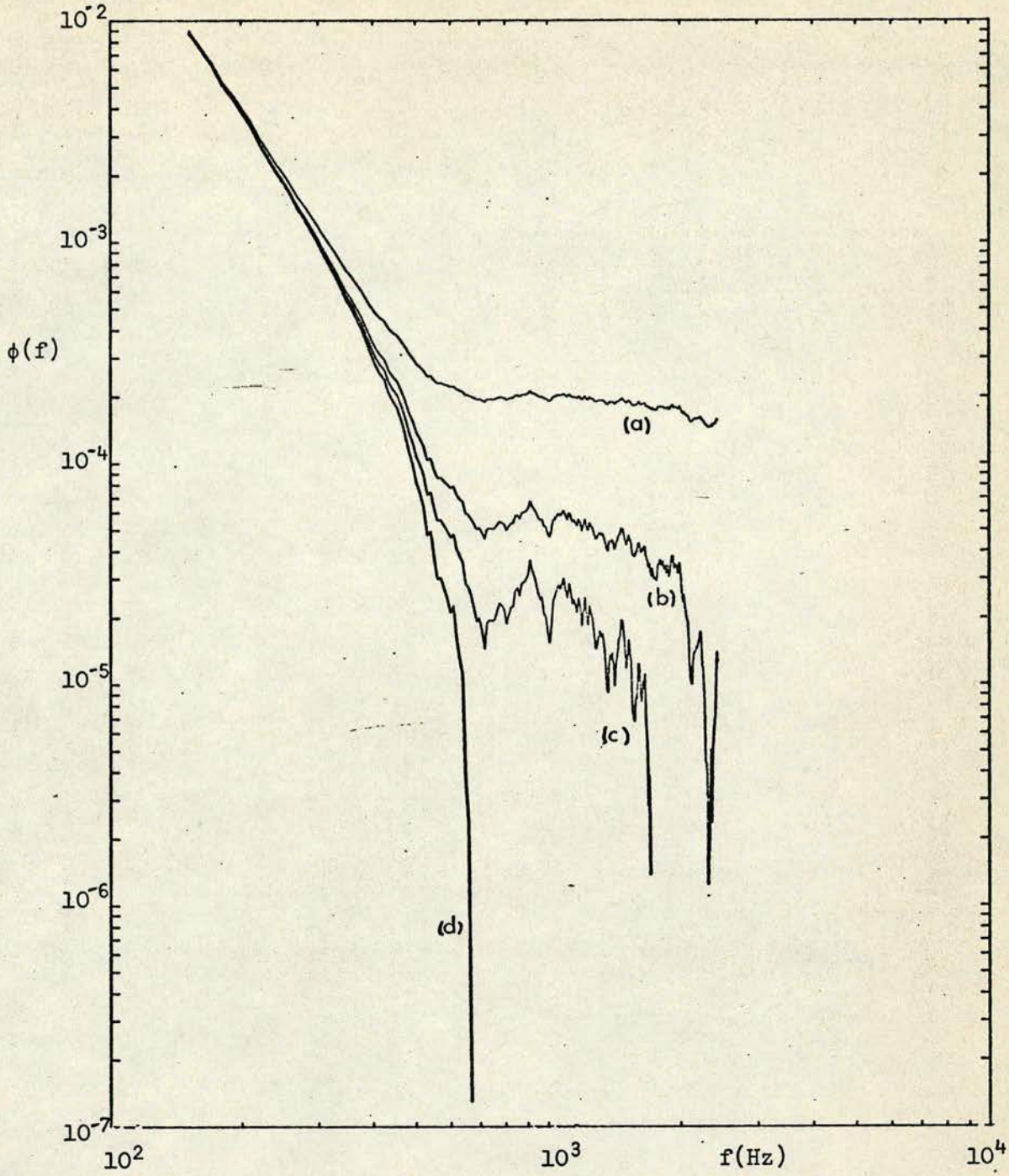

Figure 3.6

The Effect of Ambiguity Subtraction on the Energy Spectrum Measured in Newtonian Pipe Flow at $\xi = 0.97$. Subtracted levels of (a) = 0, (b) = 14.4×10^{-5}, (c) = 17.5×10^{-5} and (d) = 20×10^{-5}.

of subtraction of a range of levels and illustrates the two severe problems in attempting to significantly extend the spectral range by applying the correction, viz. the uncertainty in the original spectral estimates and the uncertainty in the value of the level to be subtracted. It is clear from Figure 3.6 that the correction process is capable of increasing the spectral range by at most a quarter of a decade. Because of the difficulty in accurately extending the spectral range by subtracting the ambiguity level, all spectra presented in this thesis have not been corrected to remove the ambiguity effect.

It is concluded that the presence of doppler ambiguity places a significant limitation on the accurate estimation of the very high frequency small scale velocity fluctuations. Nevertheless, in view of the anomalous response of hot film probes, the laser velocimeter appears at present to be the most suitable instrument to use for spectral measurements in polymer solutions.

CHAPTER 4

DIGITAL ANALYSIS OF THE VELOCITY RECORDS

4.1 DEFINITIONS

To analyse the digitised velocity records a program package was developed (Allan (1976)) to compute good estimates of the mean velocity, turbulence intensity and energy spectrum. The description is in terms of a general time series x(t) which could be the velocity record $u_1(t)$ and the corresponding power spectral density function $G_x(f)$ which in our case is the one dimensional frequency spectrum of turbulent fluctuation, $\phi(f)$.

For an ergodic random process, the mean value of x is given by

$$\mu = \lim_{T\to\infty} \frac{1}{T} \int_0^T x(t)\, dt \qquad (4.1)$$

the variance of x is

$$\sigma^2 = \lim_{T\to\infty} \frac{1}{T} \int_0^T (x(t) - \mu)^2\, dt \qquad (4.2)$$

and the one-sided power spectral density function $G_x(f)$ is (Bendat and Piersol (1971))

$$G_x(f) = 2 \lim_{T\to\infty} \frac{1}{T} E\left[|X(f, T)|^2 \right] \qquad (4.3a)$$

where

$$X(f, T) = \int_0^T x(t) \exp\left[2\pi i f t\right] dt \qquad (4.3b)$$

and E denotes the usual expectation operator.

A good estimator $\hat{Z}$ of the parameter Z is one which is consistent, unbiased and efficient.

An estimator is said to be unbiased if

$$E\left[\hat{Z}\right] = Z$$

The estimate is said to be a consistent estimator if for any $\varepsilon > 0$

$$\lim_{N\to\infty} \text{Prob}\left[|(\hat{Z} - Z)|^2 > \varepsilon\right] = 0$$

A sufficient, though not necessary, condition for an estimator to be consistent is (Bendat and Piersol (1971))

$$\lim_{N\to\infty} E\left[(\hat{Z} - Z)^2\right] = 0$$

An estimator $\hat{Z}$ is said to be more efficient than estimator $\hat{Z}_1$ if

$$E\left[(\hat{Z} - Z)^2\right] \pi \leq E\left[(\hat{Z}_1 - Z)^2\right]$$

For N independent estimates $x_1, x_2, \ldots\ldots x_n$, the estimator

$$\bar{x} = \frac{1}{N} \sum_{i=1}^{N} x_i \tag{4.4}$$

can be shown to be both a consistent and unbiased estimate of the mean value μ of x. It can also be shown that the estimator

$$s^2 = \frac{1}{N-1} \sum_{i=1}^{N} (x_i - \bar{x})^2 \tag{4.5}$$

is both a consistent and unbiased estimator of the variance σ^2 of x.

The estimator of the power spectral density function G(f) given by $\hat{G}_x(f, T)$ where

$$\hat{G}_x(f, T) = \frac{2}{T} |X(f, T)|^2 \tag{4.6}$$

is an inconsistent estimator of the power spectral density (PSD) function. This can be shown if x is a Gaussian process since

$$|X(f, T)|^2 = X_R^2(f, T) + X_I^2(f, T)$$

is the sum of squares of two independent Gaussian variables. Hence each frequency estimate will have a sampling distribution

$$\frac{\hat{G}_x(f, T)}{G(f)} = \frac{\chi^2}{2}$$

where χ^2 is a chi-square variable with two degrees of freedom irrespective of the value of T. Hence increasing the total sample time does not change the random error of the estimate and the estimator is not consistent (Bendat and Piersol (1971)).

Furthermore, the normalised error ε_r is

$$\varepsilon_r = \left(\frac{2}{n}\right)^{\frac{1}{2}} = 1 \qquad \text{when} \quad n = 2$$

ie. the standard deviation of the estimate is as great as the value of the estimate itself.

A consistent estimator can be obtained if smoothing or averaging of neighbouring frequency estimates is performed or by averaging equivalent estimates from several realisations or time records. These procedures are named frequency averaging and segment averaging respectively. Except when G"(f) = 0 (for example, white noise) these operations can lead to a bias in the final estimates (Bendat and Piersol (1971)). A consistent unbiased estimator of the PSD of a Gaussian process with arbitrary PSD function is not known.

4.2 COMPUTING THE POWER SPECTRUM FROM A TIME SERIES RECORD

Traditionally, PSD functions were calculated from the Fourier Transform of the correlation function (Blackman and Tukey (1958)) but with the advent of Fast Fourier Transform (FFT) techniques using the algorithm of Cooley and Tukey (1965), calculation by direct Fourier transformation of the time series has become popular. This method was used in all our computations since an FFT sub-routine was available in the Edinburgh IMP Program Library.

The discrete form of equation (4.3b) is

$$\hat{X}(f, T) = \sum_{n=0}^{N} x_n \exp\left[2\pi i f n\Delta t\right] \Delta t$$

where Δt^{-1} is the digitising sample rate and

$$x_n = x(n\Delta t), \qquad n = 0, 1, \ldots\ldots N$$

and $T = N\,\Delta t$

Using FFT procedures, the function X is evaluated for equally spaced values of frequency f_k such that

$$f_k = k\,\Delta f \qquad \text{where} \qquad \Delta f = \frac{1}{T} \qquad k = 1, 2, \ldots\ldots \frac{N+1}{2}$$

Thus

$$\hat{X}_k(f_k, t) = \sum_{n=0}^{N} x_n \exp\left[2\pi i\, kn\, \Delta f \Delta t\right] \Delta t \tag{4.7}$$

$$= \sum_{n=0}^{N} x_n \exp\left[2\pi i \frac{kn}{N}\right] \Delta t$$

An inconsistent estimator of the PSD is then

$$\hat{G}_k(f_k, T) = \frac{2}{T} \left| \sum_{n=0}^{N} x_n \exp\left[2\pi i \frac{kn}{N}\right] \Delta t \right|^2 \tag{4.8}$$

The FFT routine requires that the number of data points be a power of 2. In some case it may be necessary to add zeros to the data to extend the length to the required size. For all our applications the analogue tape recordings were much larger than required and sufficient data was digitised to meet this requirement.

4.3 LEAKAGE REDUCTION

For this section only, we will consider x(t) defined for $\frac{-T}{2} < t < \frac{T}{2}$ rather than from 0 to T.

Then

$$X(f, T) = \int_{-\frac{T}{2}}^{\frac{T}{2}} x(t) \exp\left[2\pi i\, ft\right] dt \qquad \text{(cf Eqn. 4.3b)}$$

$$= \int_{-\infty}^{\infty} y(t)\, x(t) \exp\left[2\pi i\, ft\right] dt$$

where

$$y(t) = \begin{cases} 1 & -\frac{T}{2} < t < \frac{T}{2} \\ 0 & \text{Otherwise} \end{cases}$$

ie. the box car function.

Thus X(f, T) can be considered to be the complete range Fourier transform filtered by a filter function y(t). Writing the complete range Fourier transforms of x and y respectively as X and Y it can be shown that

$$X(f, T) = X * Y$$

where * denotes the convolution operator. Since the filter has significant values for $| f | > \frac{1}{T}$, power outwith the range $f \pm \Delta f$ contributes to the spectral estimate of f. This "leakage" can be reduced by using a different data window to give smaller "side lobes". This can be achieved by multiplying the time series by a data window function or by convolving the raw FFT estimates with the Fourier transformation of the data window function. These two procedures are named here respectively as data tapering and frequency smoothing.

Data tapering using a cosine window is a common method of leakage reduction. All data tapering leads both to a reduced variance in the time series used to calculate the Fourier transformation (which however can be compensated for) and to a reduction in the number of degrees of freedom per spectral estimate. Durrani and Nightingale (1973) have shown that frequency smoothing does not result in a loss

of degrees of freedom when the data is uncorrelated and has a Gaussian distribution. Frequency smoothing was used in all our computations.

Otnes and Enochson (1972) discuss the merits of various smoothing functions commonly used and suggest a method for constructing a data window. Durrani and Nightingale (1973) analyse both the leakage suppression and statistical stability of five commonly used smoothing functions and demonstrate the conflicting demands of these two requirements. Although both the Hanning (high leakage suppression) and the Goodman-Enochson-Otnes (high stability) window functions were available in the program package, the G.E.O. window was used in computing all of the spectra presented in this thesis.

The expression $\hat{X}_k(f_k, T)$ defined in equation (4.7) can be written as the sum of real and imaginary parts

$$\hat{X}_k(f_k, T) = \hat{a}_k + i\,\hat{b}_k$$

After frequency smoothing a new function $\hat{X}_{s_k}(f_k, T)$ is obtained such that

$$\hat{X}_{s_k} = \hat{a}_{s_k} + i\,\hat{b}_{s_k}$$

where

$$\hat{a}_{s_k} = C \sum_{q=-s}^{s} \alpha_q \hat{a}_{k+q} \qquad (4.9(a))$$

and

$$\hat{b}_{s_k} = C \sum_{q=-s}^{s} \alpha_q \hat{b}_{k+q} \qquad (4.9(b))$$

where $[\alpha_q]$ is a set of weighting coefficients characteristic of the particular window chosen and C is a normalising constant defined by

$$C^{-2} = \sum_{q=-s}^{s} \alpha_q^{\,2}$$

The weighting coefficients for the G.E.O. and Hanning windows are given in Table 4.1.

Table 4.1

	α_{-3}	α_{-2}	α_{-1}	α_0	α_1	α_2	α_3
G.E.O.	0.0625	-0.875	0.3125	1	0.3125	-0.875	0.0625
Hanning	-	-	-0.25	0.5	-0.25	-	-

Near the end points (ie. for $k < s$ and $k > \frac{N}{2} - s$) the summations in equations (4.9(a), (b)) were performed over a reduced number of points, the maximum available.

A new spectral estimator can now be defined as

$$\hat{G}s_k\,(f_k, T) = \frac{2}{T} \mid \hat{X}s_k \mid$$

4.4 METHODS OF INCREASING THE STABILITY OF SPECTRAL ESTIMATES

We have seen that the frequency resolution of a spectrum obtained using equation (4.8) is $f = T^{-1}$ where T is the total sample time. However, such spectral estimates have standard errors which are usually unacceptably large. By reducing the frequency resolution (ie. by increasing the effective bandwidth), the standard error can be reduced by averaging over ℓ neighbouring spectral estimates. A new (consistent) spectral estimator is formed thus

$$\hat{H}_k = \frac{1}{\ell} \sum_{j=-p}^{+p} G_{k+j} \qquad \text{with} \qquad \ell = 2p + 1$$

with $\hat{G}_k = \hat{G}_k(f_k, T)$ defined by equation (4.8).

If $\hat{H}_k$ is computed for each $k = 1, 2, 3, \ldots \frac{N}{2}$ a Moving Average is performed. If it is performed only for $k = p + 1, 3p + 2, 5p + 3 \ldots$ then a Fixed Average is performed. In either case, the effective bandwidth is

$$B_e = \frac{2p + 1}{T} = (2p + 1)\,\Delta f$$

By increasing the data length and computer time, the stability of the spectral estimates can be increased, without loss of frequency resolution, by a procedure known as segment averaging. The data can be analysed in several sets or segments and a set of spectral estimates $\hat{G}_k$ can be found for q sets of data. The Segment Average estimator $\hat{J}_k$ is then

$$\hat{J}_k = \frac{1}{q} \sum_{j=1}^{q} \hat{G}_{k_j}$$

4.5 THE ACCURACY OF FINAL ESTIMATES

For uncorrelated Gaussian data PSD estimates which are frequency averaged over ℓ points and segment averaged using q segments, the normalised error is

$$\varepsilon_r = \left(\frac{1}{\ell q}\right)^{\frac{1}{2}}$$

and the number of degrees of freedom is $2\ell q$. Durrani has shown that when frequency smoothing precedes such averaging, the effective number of degrees of freedom is reduced by a factor β. For G.E.O. smoothing $\beta = 0.78$, hence for G.E.O. smoothing followed by both frequency and segment averaging, the effective number of degrees of freedom is $1.56\ell q$. This effective number can be used to place confidence limits on the spectral estimates for a given confidence level. Sentman (1974) quotes the following formula which is an approximation of more exact calculations of Edmonds (1966)

$$F_c = \exp\left[\frac{2.3b}{10\sqrt{k-1}}\right] \qquad (4.9)$$

where F_c is the confidence factor for a given confidence level

k is the effective number of degrees of freedom

b is given as follows

b	Confidence
8	50%
16	80%
20	90%
25	96%
29	98%

Error bars can be applied to the final spectral estimates for a given confidence level. For final estimates L_k the upper and lower bounds are

$$L_k \sqrt{F_c} \quad \text{and} \quad \frac{L_k}{\sqrt{F_c}} \tag{4.10}$$

Much of the analysis presented here relies on the data being Gaussian and white (ie. uncorrelated, with a flat spectrum). Since there seems little point in computing PSD's for data known a priori to be white, this is a severe limitation on the strict applicability of the results quoted. Correlated data reduces the number of degrees of freedom compared to uncorrelated data so the confidence limits calculated from equations (4.9) and (4.10) can be used only as a guide to the accuracy of the estimates. However, the general technique of using frequency and segment averaging to increase the stability of PSD estimates is widely applied.

4.6 THE PROGRAM PACKAGE

The program package was developed around a standard FFT routine to compute estimates of the mean velocity, turbulence intensity and energy spectrum from the digitised velocity records. The package incorporated leakage suppression routines for both G.E.O. and Hanning frequency smoothing as well as routines for segment averaging and both fixed and moving frequency averaging. Written in the Edinburgh IMP language, the package consists of two principal routines and a small

master program. Flow diagrams are contained in Figures 4.1 (a)-(c). By editing the master program the amount and types of smoothing can be varied as well as the amount of input data. Since the master program is small, little computer time is used in altering the program for different types of spectra. Additional programs were written to compute scaling factors from calibration records and to plot the computed spectra on a Calcomp plotter.

It will be seen in Chapters 5 and 6 that nearly all measurements were made in "once through" flow systems where measurement time was limited. Hence the time-span of the velocity record was naturally defined. To set the sampling rate, an upper limit to the frequency range of interest must be deduced. In our case both the lower and upper frequency ranges were naturally defined. Good accuracy and resolution is not required for frequency estimates below the inertial sub-range where the turbulence spectrum is not universal. Similarly the levelling off of the turbulence spectrum due to ambiguity can be used to determine the upper frequency limit. Clearly it is necessary to measure some spectra to find the optimum values for sample rate and spectral resolution and accuracy. Although a number of approaches could have been used, the method of selecting the optimal values of the various parameters was as follows.

Since the widest possible dynamic range was needed the number of data points per segment was the maximum possible with the available core store which was 8192. The number of segments which could be analysed was determined by the time-span of the recorded signal, the sampling rate and the number of points in each segment. A fixed frequency average was performed over sets of eight spectral estimates to reduce the number of points to be plotted in the final spectrum as well as to increase the stability. Finally, a moving average was

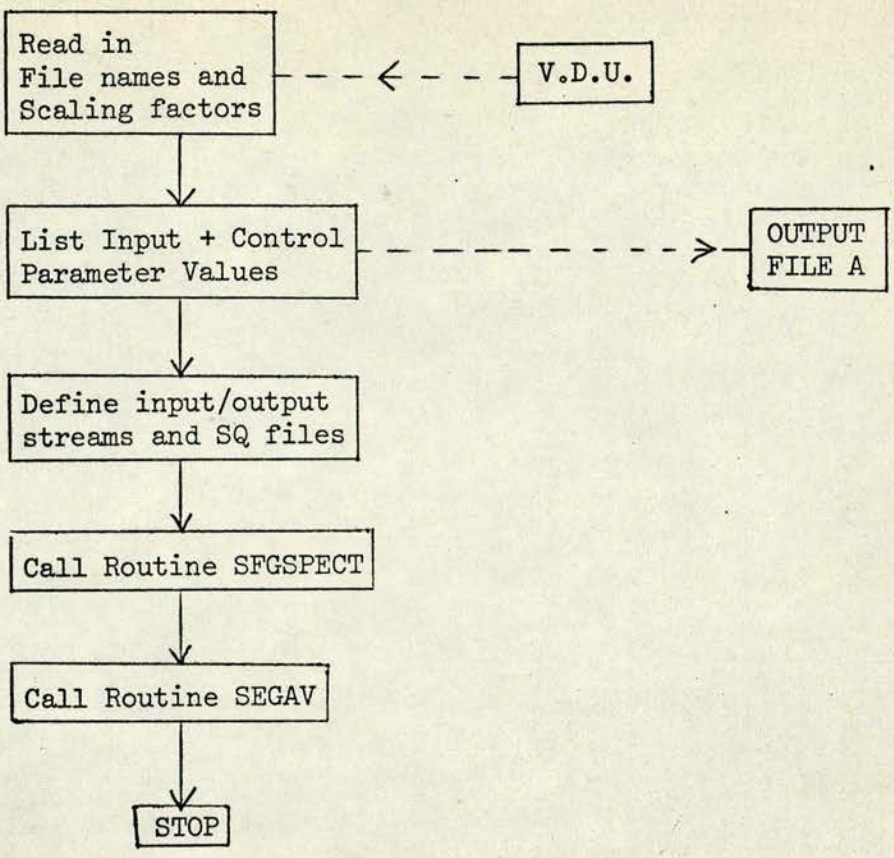

Figure 4.1 (a)

Flow Diagram for MASTER Program

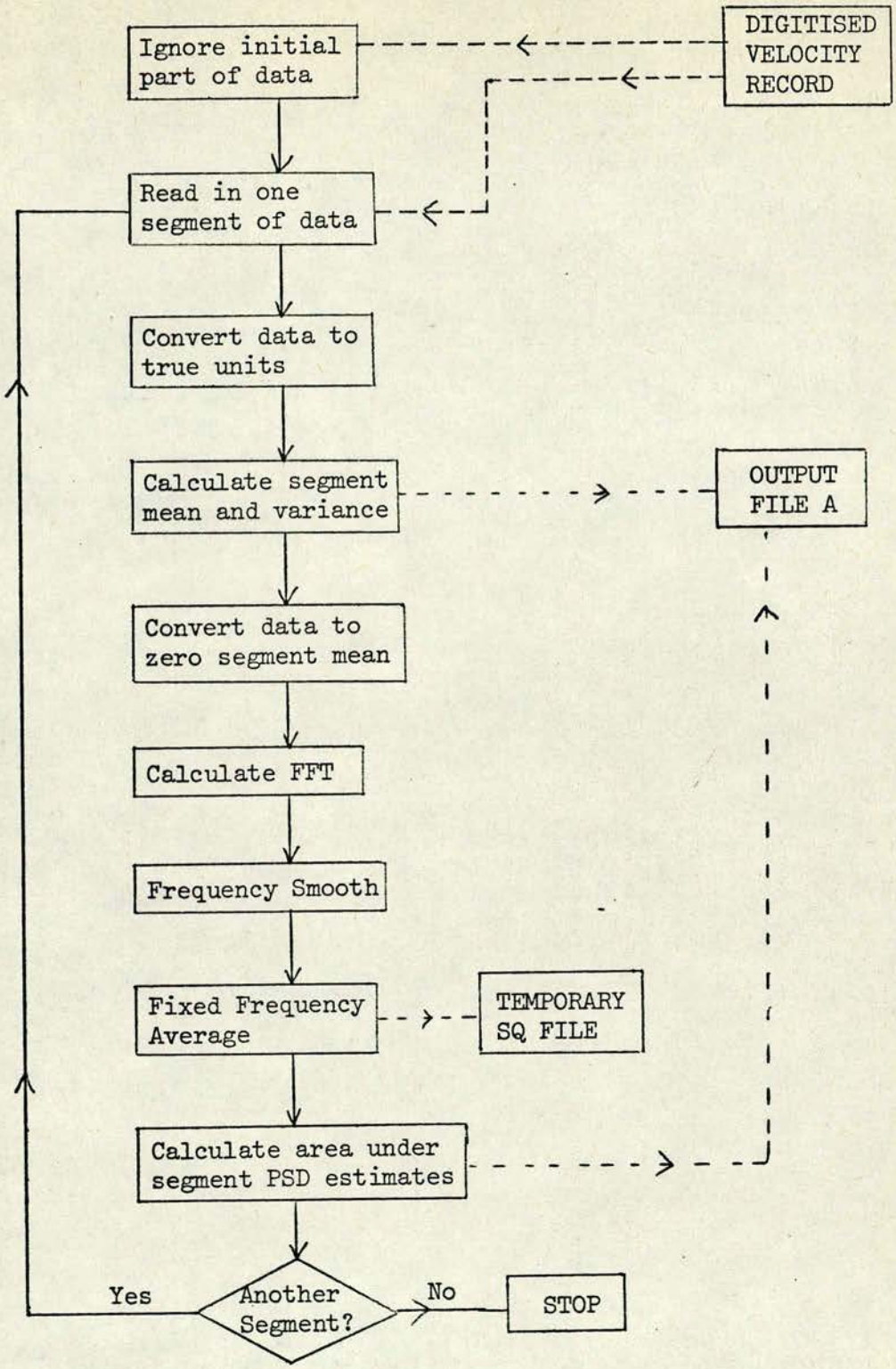

Figure 4.1 (b)

Flow Diagram for Routine SEGSPECT

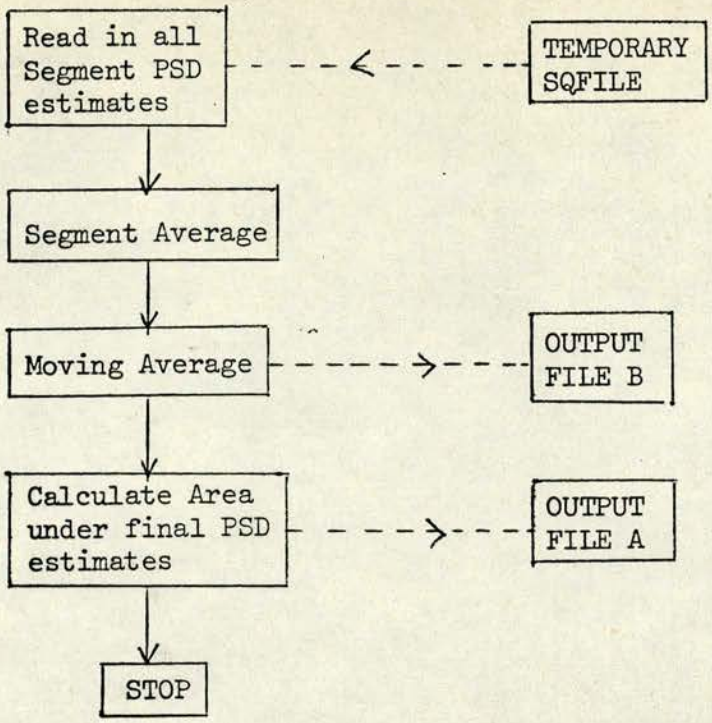

Figure 4.1 (c)

Flow Diagram for Routine SEGAV

performed to yield a smooth spectral shape within the frequency range of interest. Figures 4.2 (a) and (b) show how the final moving averaging process increases the stability of the spectral estimates. Since the resolution can affect the shape of the turbulence spectrum at low frequencies, all spectra which are compared in diagrams presented in later chapters were computed with the same resolution.

For all measurements in grid-generated turbulence described in Chapter 5, 5 segments of data sampled at a rate of 2 kHz were used to compute the spectra with a fixed averaging over 8 points per estimate followed by a moving average over 11 points, the "accuracy factor", $\sqrt{F_c}$, being 1.13 at a 90% confidence level. For the pipe flow measurements the velocity records from three of the experimenatal runs were sampled at a rate of 5 kHz. For both Newtonian experiments (Runs 1 and 2 in Table 6.1) as well as the Run with 50 ppm Polyox at a high flow rate (Run 4 in Table 6.1) eight segments of data were analysed with fixed and moving averaging of 8 and 11 points respectively. With a 5 kHz sample rate the resulting resolution was 54 Hz with an accuracy factor of 1.10. All other pipe flow velocity records were sampled at 3 kHz with the same amount of smoothing to give a resolution of 32 Hz and a value of $\sqrt{F_c}$ of 1.10. For comparison with the polymer spectra, the Newtonian spectra were re-computed, this time with a moving average of only 7 points to give nearly the same resolution as the polymer spectra (34 Hz) but with slightly less accuracy, $\sqrt{F_c}$ being 1.13.

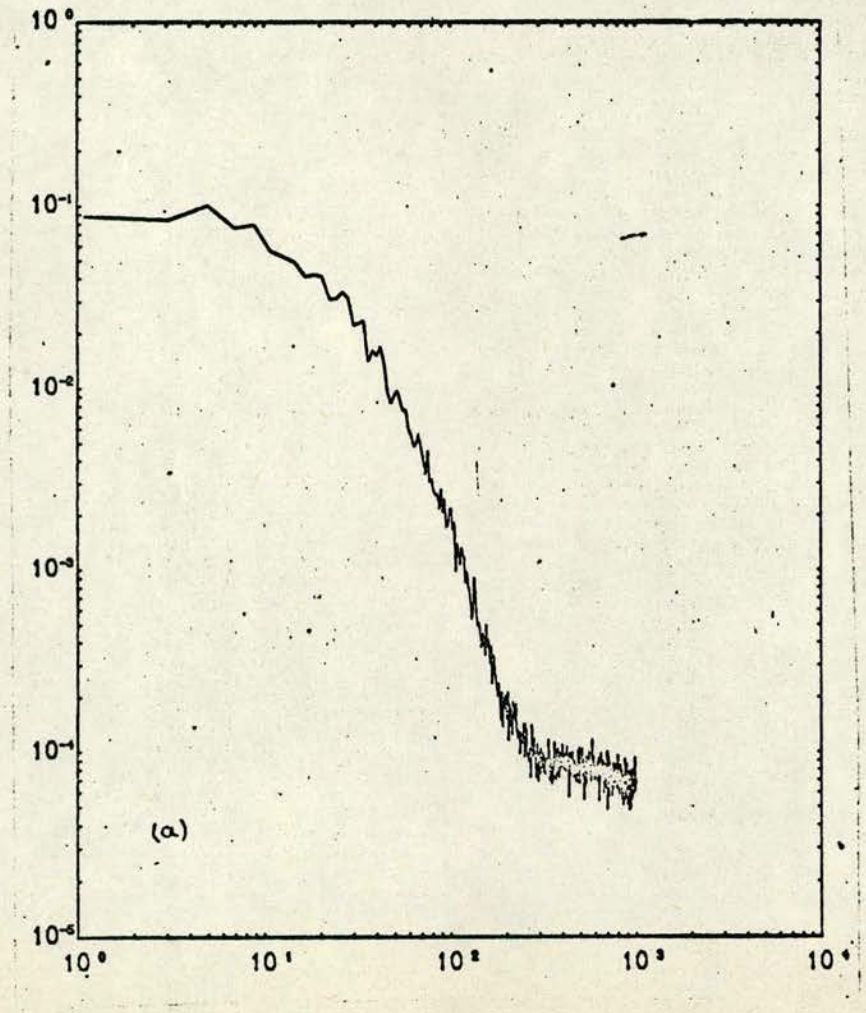

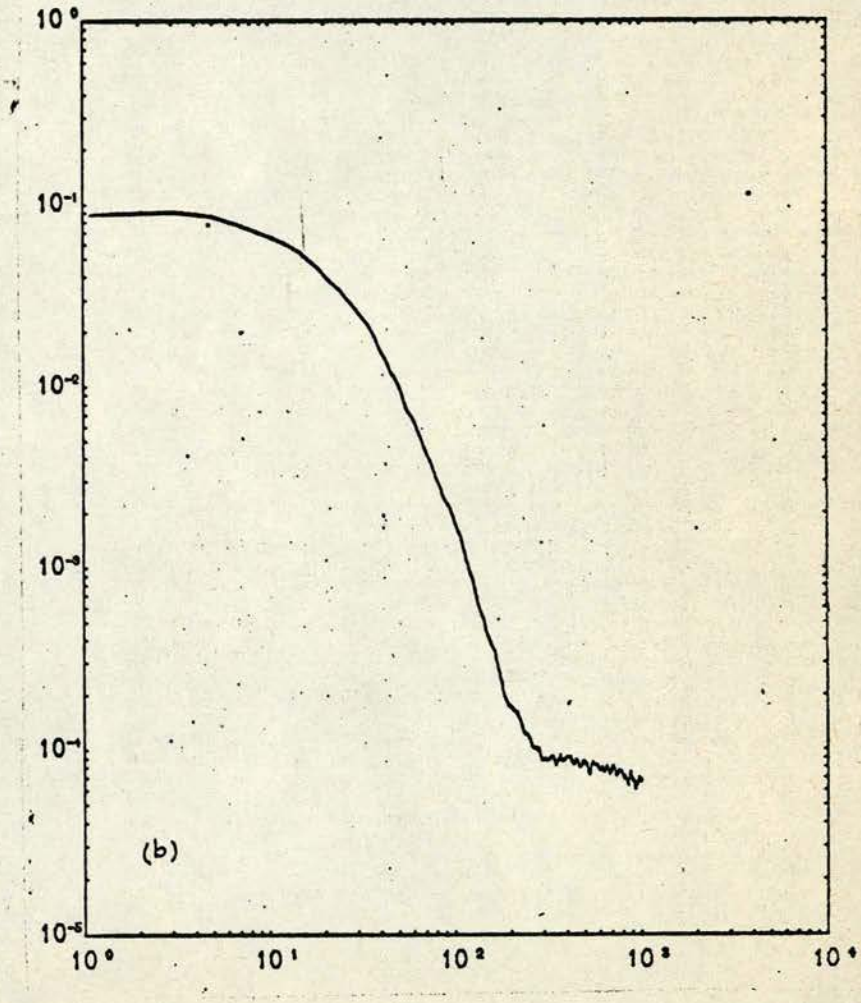

Figure 4.2

Typical Plot of Spectral Estimates

(a) before the final moving averaging process and (b) after final moving averaging

CHAPTER 5

MEASUREMENTS IN GRID-GENERATED TURBULENCE

5.1 GRID TURBULENCE IN NEWTONIAN FLUIDS

The use of a regular grid in a uniform stream to generate turbulence in Newtonian fluids was reported as early as 1934 by Simmons and Salter and has been given considerable attention theoretically and experimentally since Taylor's analysis and measurements were published in 1935. It is one of the easiest methods of generating turbulence in the laboratory and is one of the closest approximations to homogeneous isotropic turbulence which can be experimentally achieved since, in spite of the inhomogeneity and strong directional character of the grid producing the turbulence, the turbulent field at a distance from the grid (typically greater than twenty to thirty grid mesh lengths) is very nearly statistically homogeneous (Corrsin (1963)) in planes parallel to the grid and is approximately isotropic when the mean flow is subtracted. In the absence of significant mean shear beyond the grid, the turbulence decays with distance downstream of the grid, the rate of decay of turbulent energy being close to the rate of viscous dissipation.

Experimentalists have measured the effect of grid Reynolds number ($Re_M = \frac{\overline{U}M}{\nu}$, M = grid mesh size), grid geometry and grid solidity (solidity σ = ratio of projected solid area of grid bars to flow cross-sectional area at the grid) on the isotropy and energy decay rates. Although Taylor suggests a simple equation to relate streamwise intensity to distance from the grid of the form

$$\frac{\overline{U}^2}{\overline{u'^2}} = A + B\left(\frac{x}{M}\right) \qquad (5.1)$$

(with A and B as adjustable parameters), a more general power law

equation was found to be a better fit to the data of Batchelor and Townsend (1947, 1948), namely

$$\frac{\bar{U}^2}{\overline{u'^2}} = A\left(\frac{x}{M} - \frac{x_o}{M}\right)^n \qquad (5.2)$$

This equation has three unknowns (A, x_o and n) which can be found experimentally by measuring $\overline{u'^2}$ at various distances from the grid. In general, the "effective origin" term x_o/M is small, typically less than 4 for the results tabulated by Comte-Bellot and Corrsin (1965), and the equation

$$\frac{\bar{U}^2}{\overline{u'^2}} = A\left(\frac{x}{M}\right)^n \qquad (5.3)$$

is most commonly used to represent the decay.
(In our case, the precision of the decay data did not allow an estimate of x_o/M to be made with any reasonable degree of accuracy.)

It has been found experimentally that the assumption of isotropy is poor since, in general, $u'^2 > v'^2$ and $u'^2 > w'^2$ and an equation of similar form to equation (5.3) but with different values of A and n is necessary to describe the decay of v'^2 and w'^2, namely

$$\frac{\bar{U}^2}{\overline{v'^2}} = A_1\left(\frac{x}{M}\right)^{n_1} \qquad (5.4)$$

Measurements of the decay parameters reported in nine separate papers dating from 1942 to 1974 are tabulated in a paper by Gad-el-Hak and Corrsin (1974) for a wide range of Grid Reynolds numbers ($Re_M = 5.5 - 2420 \times 10^3$) and a wide range of grid types and solidities ($\sigma = 0.13 - 0.44$). These measurements indicate that n reduces with increasing solidity and that as Re_M reduces, n is increased and A is reduced. It is also clear that grid geometry cannot be ignored when comparing results with comparable Reynolds numbers and solidities. The most relevant of these results, ie. those most easily compared

with our results and those of Friehe and Schwarz (1969) are incorporated in Table 5.1.

Table 5.1

Streamwise Decay Rate Parameters for Newtonian Grid Turbulence

Source	Grid Solidity	Re_M ($\times 10^3$)	A	n
Corrsin (1963)	$\sigma = 0.44$	8.5	20.0	1.30
Batchelor & Townsend (1947, 1948)	$\sigma = 0.34$	5.5 11.0	70.0 48.0	1.13 1.25
Harris (1965)	$\sigma = 0.25$ $\sigma = 0.31$	8.2 6.1	- -	1.43 1.23
Friehe & Schwarz (1970)	$\sigma = 0.06$	9.55 10.4 15.8 19.7 23.7	- - - - -	1.47 1.47 1.37 1.37 1.47
Our Results				
(x/M = 20 - 60)	$\sigma = 0.38$	7.6	1.2	1.9
(x/M = 30 - 60)	$\sigma = 0.38$	7.6	4.1	1.6

Anistropy affects flow properties other than the turbulent intensity levels. Frenkiel and Klebanoff (1967) have investigated the effect of anistropy on the second order correlation functions in grid turbulence in air using constant current hot wire probes. (Digital techniques were used to compensate for the non-linearity of probe response.) With a grid Reynolds number of 25,600 and measuring at a position 48.5 mesh lengths from the grid, substantial differences were found between the correlation functions $R_{uv}(h)^{\dagger}$ and $R_{vu}(h)$.

$^{\dagger}\ R_{uv}(h) = \dfrac{\overline{u'(x)\ v'(x+h)}}{(\overline{u'^2(x)})}$

Comte-Bellot and Corrsin (1966) improved the isotropy in their wind tunnel by installing a secondary contraction with a 21% area reduction positioned downstream of the grid. Without the contraction it was found that u'^2/v'^2 was as high as 1.24 whereas, with the contraction in place at 9 or 18 mesh lengths from the grid position, u'^2/v'^2 was in every case within 5% of unity.

Stewart and Townsend (1951) measured energy spectra, decay rates and double and triple autocorrelation functions in grid-generated turbulence with several grid geometries and Reynolds number ranging from 2000 to 100,000. Constant current hot wire anemometers were used and one dimensional spectra were obtained both by direct measurement using frequency analysers and by Fourier transformation of the auto-correlation functions. Except very close to the grid, isotropy was found in the sense that $\overline{u'^2} = \overline{v'^2} = \overline{w'^2}$. Local similarity was found at large wave numbers but no appreciable inertial subrange (ie. a region of $k^{-5/3}$ dependence in the spectrum) was observed even at the largest Reynolds numbers. It was suggested that to ensure the existence of an inertial subrange, a Reynolds number of $Re_\lambda > 1730$ would be necessary where Re is the Reynolds number based on the microscale defined (Bradshaw (1967a)) in terms of dissipation by the following equation

$$\varepsilon = 15\nu \frac{\overline{u'^2}}{\lambda^2}$$

The corresponding value of grid Reynolds number is of the order of 10^7.

Gibson and Schwarz (1963) measured spectra of velocity and scalar fields in grid turbulence in salt water. Using constant temperature hot film anemometry, velocity spectra were measured at three different positions at three grid Reynolds number namely $Re_M = 20 \times 10^3$ with $x/M = 80$, $Re_M = 30 \times 10^3$ with $x/M = 40$ and $Re_M = 40 \times 10^3$ with $x/M = 20$. Decay law measurements were not made but it was assumed that the decay

was the same as that measured by Batchelor and Townsend (1948) for a geometrically similar grid (ie. the same ratio of mesh size to rod diameter).

Comparing the measured spectra with the spectra of Grant, Stewart and Molliet (1962) and Stewart and Townsend (1951), the hypothesis of universal similarity and local isotropy in the high wave number region (dissipation range) was supported by the experimental evidence. Criteria for the existence of an inertial sub-range were put forward and the condition that

$$Re_\lambda >> 567$$

was concluded as being necessary. On the basis of the measurements made and the assumption concerning intensity decay (necessary to calculate ε), a value for the one dimensional Kolmogoroff constant of 0.44 ± 0.02 was determined for grid turbulence within the range of Reynolds numbers where measurements were made.

Kistler and Vrebalovich (1966) measured spectra in grid-generated turbulence at very high grid Reynolds numbers (1.2×10^5 - 2.4×10^6), in a high speed wind tunnel. By varying the density of the air the Reynolds number was varied without changing the flow rate. Initial period decay curves were found for both $\overline{u'^2}$ and $\overline{v'^2}$ and spectra were obtained at $x/M = 45$. In general, the results obtained indicated that the essential features of the flow were similar to grid flow at much lower Reynolds numbers although the value for α (defined by equation (2.17)) of 0.68 is now thought to be rather high. The extent of the sub-range was observed to decrease with a decreasing Reynolds number based on the integral scale and it was deduced that for a slope of - 5/3 to persist for at least a factor of two in wave-number variation the condition

$$Re_L \geq 300$$

is necessary. Re_L is a Reynolds number calculated using the integral scale as the length scale and is defined as

$$Re_L = \frac{\bar{U} L}{\nu} \quad \text{where} \quad \overline{u'^2} L = \int_0^\infty \overline{u(x)\, u(x+r)}\, dr$$

In terms of Re_λ an equivalent condition would be

$$Re_\lambda > 30$$

5.2 PREVIOUS MEASUREMENTS OF GRID TURBULENCE IN POLYMER SOLUTIONS

The earliest measurements in grid-generated turbulent flow in polymer solutions are those of Fabula (1966). To minimise the effect of degradation of the polymer molecules, Fabula towed the grid and probe through the stationary polymer solution at a constant speed of 36.2 cm/sec. With a grid mesh size of 11.8 cm (solidity = 0.32) a grid Reynolds number of nearly 40,000 was achieved. Two methods of solution preparation were used, namely, by direct mixing into the flow tank or by dilution from a prepared concentrated master solution. Velocity measurement was by hot film anemometry and both conical and cylindrical sensors were employed. With cylindrical probes, Fabula found that sensor response in polymer solutions changed with time. The cause of this was said to be the build up of gelatinous polymer blobs along the probe stagnation line. The use of conical probes avoided this build up and probe response was more consistent.

Measurements were made in Polyox WSR 301, Polyox Coagulant, Guar Gum and two types of polyacrylamide (Separan AP 30 and J 100). A signal raggedness (ie. large high frequency fluctuations in the apparent velocity signal) was present in most of the polymer solutions and

was thought to be anomalous. The signal "blips" were said to be due to agglomerates of polymer molecules striking the probe and were absent only for Polyox solutions which had been aged though not degraded. The effect of solution inhomogeneity on the probe meant that reliable spectral measurements could be made only for these aged Polyox solutions. None of the other polymer types showed a reduction in signal raggedness with ageing.

With the freshly prepared solutions, the spectral levels near the grid showed a greater experimental scatter compared to the results for Newtonian flow and there was some spectral distortion due to signal raggedness. With the aged solutions, the difference between the measured polymer spectra and those for water could be explained by the predicted increase in solution viscosity. Qualitatively, the polymer spectra were of the same shape as the solvent spectra where signal raggedness was not present.

Barnard and Sellin (1969) used a flow visualisation method in their measurements of grid-generated turbulence in a 10 cm square sectioned flow channel. With a grid mesh size of 1 cm (solidity = 0.41) a nominal Grid Reynolds number of 10,000 was achieved. A master solution of 1000 ppm Polyox WSR 301 was injected 2 m upstream of the grid and the polymer concentration was calculated from the injection flow rate by assuming that the polymer concentration was uniform at the grid. Milk was injected 3 cm downstream of the grid and the dye trace was photographed against a black background with lighting above and below. Photographs were taken with both short (1 msec) and long (1 sec) exposure times. From the short time exposed photographs, a reduction in the "fuzziness" of the edges of the dye trace was observed indicating a reduction in turbulent energy in the high frequency range. From the photographs with long exposure times a maximum value for $v/\bar{U}$

was found experimentally by measuring the transverse displacement of the edge of the dye trace with distance from the grid. For solutions greater than 5 ppm, around 50% reduction was found for $v_{max}/\bar{U}$ compared to the values for water flow. These results indicate that a reduced level of turbulent intensity is present at least in the transverse velocity component in polymer grid flow.

Greated (1969) used a laser velocimeter to measure turbulent intensity and energy spectra in grid-generated turbulence in water and 80 ppm Separan AP 30. With a 5 mm grid spacing in a rectangular cross-sectioned (5 cm x 6 cm) channel, a rather low grid Reynolds number of 1000 was obtained. Reduced streamwise turbulence intensities were found for polymer flow compared to water at all measurement positions from x/M = 14 — x/M = 50. The energy spectrum, plotted as a function of k and normalised to unit area, was measured 7 cm and 17 cm from the grid. At x/M = 14, the energy spectrum showed reduced energy at high wavenumbers compared to the Newtonian result whereas the spectrum at x/M = 34 was unchanged with polymer addition although at this position it was acknowledged that wall generated turbulence was contributing to the level of turbulence and that the measurements were not fully representative of grid-generated turbulence alone.

Although Fabula could not collect useful spectra data from J100 solutions, Friehe and Schwarz (1970) did not meet any difficulties with signal raggedness in their study of J100 solutions in a re-circulating flow facility. Grid turbulence was studied in a square sectioned tunnel (15 cm x 15 xm) and with a grid mesh size of 12 mm, grid Reynolds numbers of up to 23,700 were attained. Streamwise turbulent intensity decay rates were measured for Newtonian flow at several Reynolds numbers and energy spectra were obtained at x/M = 31.75 and x/M = 51.75 using conical and cylindrical hot film probes. In an

earlier paper Friehe and Schwarz (1969) found that the response of cylindrical probes in polymer solutions differed from the response of conical probes although both gave identical results in water. Since conical probes gave an exponential roll-off in the high frequency spectrum in polymer flow (as was the case for both probes in water) the conical probe was chosen for the study of grid turbulence.

Although there was some scatter, and no clear trends with increasing concentration, the turbulence levels were found to be increased compared to water at the same dimensionless position and the rate of decay of turbulent intensity was greater in the polymer solutions. Spectra measured in polymer concentrations of 30, 100 and 300 ppm at two flow positions were qualitatively of the same shape as the spectra measured in water. Although the Newtonian spectra were made dimensionless using Kolmogoroff transformations, the polymer spectra were made dimensionless using a transformation based on Lumley's concept of effective viscosity (Lumley (1964)) and on a dissipation rate calculated by assuming that the inertial sub-range was the same in water and polymer flow. The effective viscosity was determined from measurements of the dissipation spectrum using the following definition of effective viscosity, ν_e,

$$\varepsilon = 15\, \nu_e \int k^2 \phi(k)\, dk$$

The resulting spectral transformation is

$$\tilde{\phi}_{FS}(\tilde{k}) = \frac{\phi(k)}{\nu_e^2 k_D} \quad , \quad \tilde{k} = \frac{k}{k_D} \quad \text{where} \quad k_D = \left(\frac{\varepsilon}{\nu_e^3}\right)^{\frac{1}{4}}$$

Using this transformation, the polymer spectra were found to collapse onto the universal curve found from the Newtonian flow results.

If differences due to polymer type and concentration are not significant, the results of these investigations contain a number of

inconsistencies. In view of the different response of differently shaped probes in polymers and the extensive experimental evidence described in Chapter 3 concerning the anomalous response of these probes in polymers, the results of Friehe and Schwarz cannot be considered conclusive. On the other hand, the experiments of Greated were of a preliminary nature and his flow system was inadequate. The aim of the work detailed in the rest of this chapter was to construct a flow rig which was capable of producing a representative grid-generated Newtonian turbulent flow and to make extensive measurements of streamwise turbulence decay and energy spectral measurements in water and a range of concentrations of Polyox WSR 301. The quantitative measurements using a laser velocimeter are complemented by dye injection photographs similar to some of those of Barnard and Sellin. Most of the results presented in the remainder of this chapter were published in a paper (McComb et al (1977)) which is included here as Appendix 1.

5.3 EXPERIMENTAL DETAILS

Figure 5.1 shows a schematic of the experimental set-up. The fluid flows under the action of gravity from the top tank through the water tunnel to the bottom tank on the floor below, the total head being approximately 6.3 m. The flow control valve, V1, is used to set a nominal flow rate of 12,000 litres per hour which is monitored using a conventional Rotameter (G.E.C. Elliot Process Instruments). Valve V2 was closed during the down flow to prevent the fluid siphoning directly into the lower tank.

The water tunnel consisted of an expansion section, settling chamber, contraction and working section. The tunnel was mounted on a steel framework and a platform was built spanning the full usable length of the working section to support the laser system. The

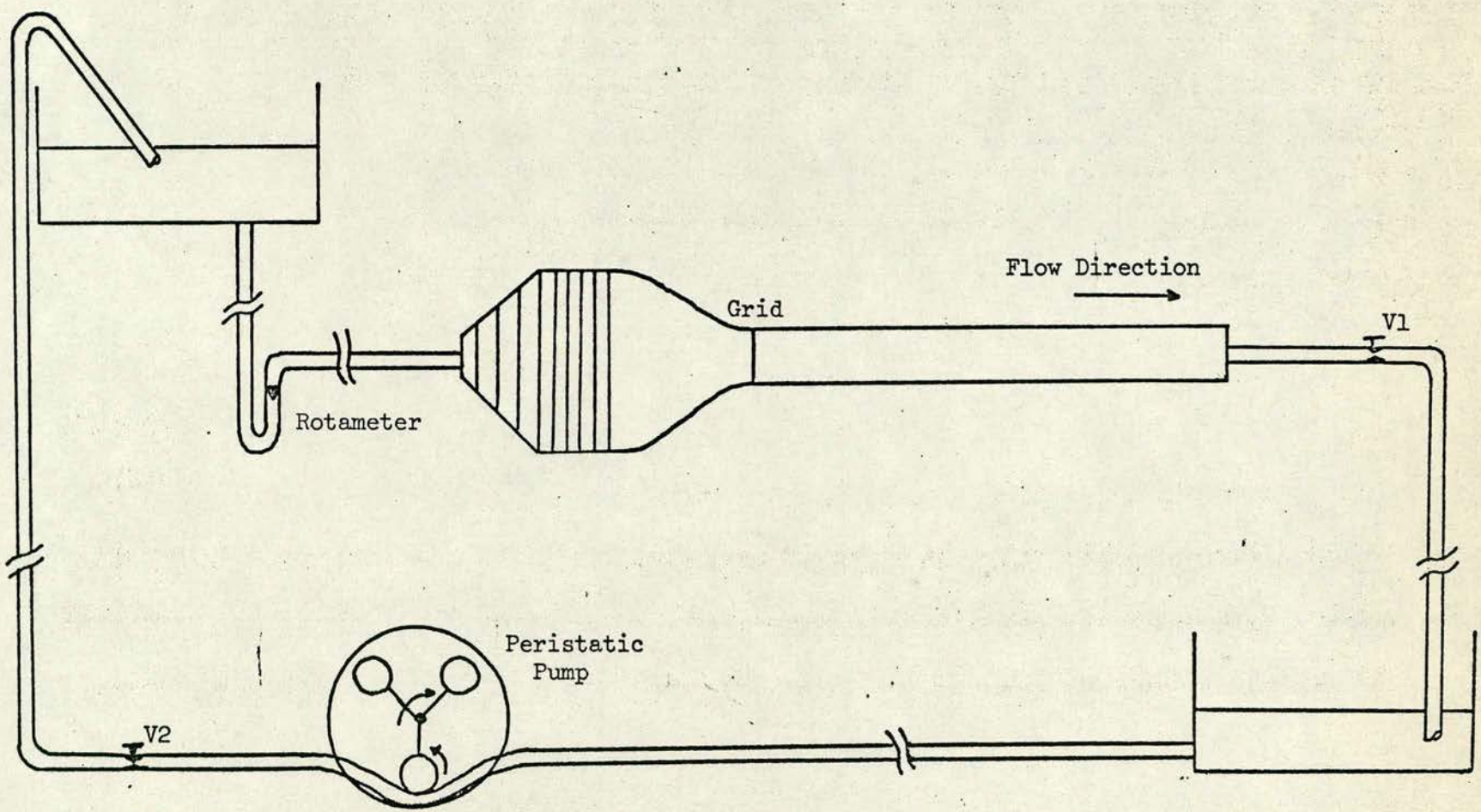

Figure 5.1

A Schematic Diagram of the Grid Turbulence Flow Facility

settling chamber contained a set of four nylon screens with a mesh size of 1.0 mm. The contraction was made from thin perspex sheeting which was shaped and reinforced in a fibre glass casing. The area contraction ratio over a distance of 37.5 cm was 16:1. A bleed screw in the top of the settling chamber was used to remove air trapped in the tunnel when the system was emptied and refilled. The tunnel could be dismantled for cleaning purposes by separating the settling chamber from the contraction.

The working section had a square cross-section, width 7.6 cm, throughout its 1.2 m length terminating abruptly in a square to round cross-sectional change. To accommodate the grid, slots were carefully machined in the perspex sides, base and top of the tunnel downstream of the contraction so that the frame containing the grid could be fitted flush with the channel walls. The grid was inserted by removing a small panel in the roof of the channel.

The grid was made of 2.37 mm diameter round brass rods soldered together in a square sectioned brass frame. The grid solidity was 0.38 and the mesh size was 12 mm, giving a nominal grid Reynolds number of 7.6×10^3. For the dye injection experiments, one of the central solid grid rods was replaced by a longer tube of the same diameter which was closed at one end. The dye was allowed to flow through a 0.73 mm diameter hole drilled in the side of the tube facing downstream. The tube projected through the roof panel and was connected to the dye reservoir using plastic tubing.

The peristaltic pump was a Watson Marlow H.R. flow inducer type L.H.R.S. This type of pump was used by Rudd (1972) and is reported to minimise degradation since the moving parts of the pump do not come into contact with the fluid. The principle of operation of these pumps is described as follows. An elastic tube is clipped to a multi-

curved track and locked into the machine, where the central curve is concentric with a rotor carrying three rollers. As they rotate, the rollers pass over the tube flattening it against the track at the point of contact only. This "flat" moves around the central curve of the track, driving anything in the tube before it. At the same time, the restitution of the tube behind each roller creates a powerful suction, drawing in more fluid to be pushed by the following roller. Clearly, this type of flow inducement leads to a pulsatile flow and absorbers, constant head devices, etc, are necessary if a smooth continuous flow is desired. In use, the pump set up considerable vibration which affected the L.D.V. signal noticeably. Furthermore, the maximum possible flow rate of 8500 litres/hour with the largest tubing size of $1\frac{3}{4}$" was insufficient to attain the required grid Reynolds number. For these reasons, as well as the need to minimise degradation, the pump was only used to re-prime the system and was not operated when flow measurements were made.

Most of the pipe work was 6.4 cm diameter steel pipe work with threaded joints sealed with P.T.F.E. tape although part of the return section was of clear plastic tubing of the same diameter. Flexible rubber tubing was used to connect the water tunnel to the fixed pipe-work to reduce vibrational disturbances. The system was filled using hose reels to both tanks and emptied by siphoning from the top tank only.

The dye traces were photographed with Ilford H P 4 film using a Zenith E 35 mm SLR camera which was mounted on a tripod. To ensure sufficient depth of field and increased constrast, apertures of f8 and f11 were used and the film was overdeveloped by 50%. The lighting was projected directly towards the camera from the far side of the channel through a white plastic diffusing screen. The main light

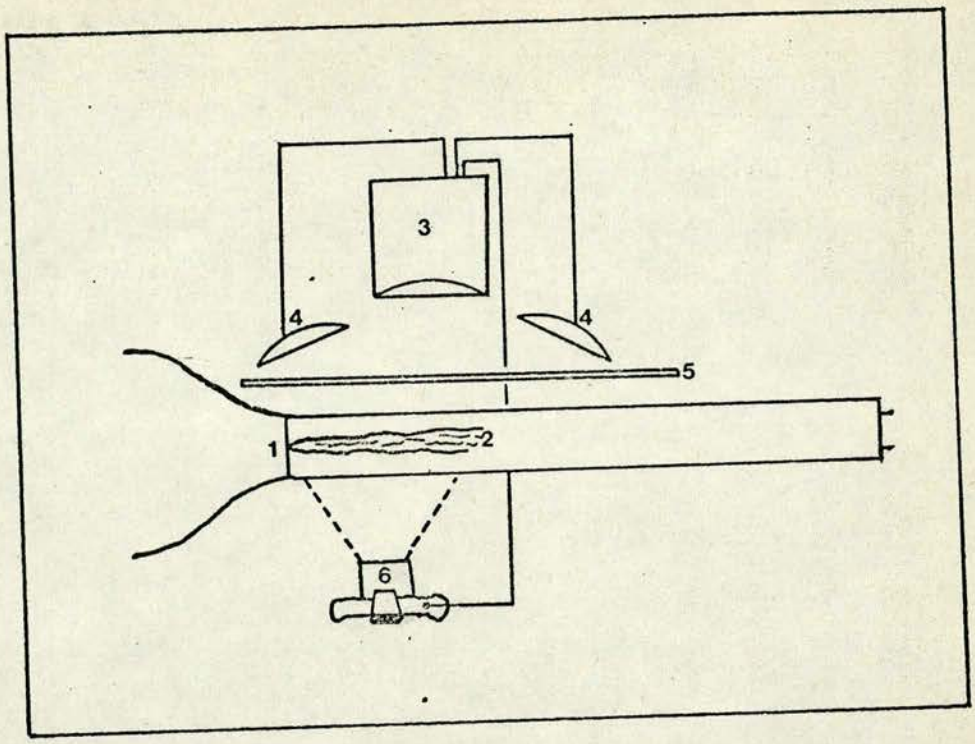

Figure 5.2

The Photographic Arrangement in the Dye Trace Experiments (1) Grid, (2) Dye Trace, (3) Stroboscope, (4) Flash Guns, (5) Diffusing Screen, (6) Camera

source was a Strobe Automation stroboscope, type 6K which was complemented by two electronic flash guns to produce a more even illumination along the channel length. The photographic arrangement is shown in Figure 5.2. The single light flash was triggered using the camera shutter and was of 10 μ sec duration. In all cases the dye used was potassium permanganate dissolved in tap water which was introduced through a hole in one of the central grid bars.

While the average total head during measurement was 6.3 m, the head varied during each run as the top tank was emptied and the lower tank refilled. Total run-down time was approximately 3 minutes and the velocity measurement time was at least 30 seconds to allow enough data to be collected. Both tanks had a rectangular cross-section measuring 96 cm x 76 cm so that, at a volume flow rate of 12,000 litres/hour, the total head change during measurement was 27.4 cm or 4.35% of the average total head. If the energy losses remain the same, this corresponds to a mean velocity change of 2.1%. When analysing the collected data, the mean velocity of each segment of data (approximately 5 seconds of data length) was computed and examined for a systematic mean velocity change of this order. This was not found. For the water results, for example, at all measurement positions there was an average increase in the mean velocity estimate between the first and last data segment, (average increase 0.77%, maximum 1.4%). It was concluded that the small change in total head during measurement had an insignificant effect on the flow system.

Polyox WSR 301 is a non-ionic homopolymer with an average molecular weight of approximately 4×10^6. It is soluble in water and certain organic solvents at room temperature and is known to be a very effective drag reducer at low concentrations in turbulent shear flows. It is also known to be very susceptible to degradation when

subjected to high rates of shear. It undergoes biological decomposition only very slowly so master solutions can be prepared and stored for some time. Although the average molecular weight is nominally 4×10^6, this can vary significantly from batch to batch and, moreover, there is a wide distribution of molecular weights about the average value. This may give rise to apparent inconsistencies when comparisons are made between similar experiments by different authors. Morgan and Pike (1972) were able to obtain narrow band molecular weight samples of Polyox by fractionation of the commercially available samples using gel permeation chromatography. However, only small amounts of polymer can be obtained in this way and the polymer is usually used, as in our case, as supplied by the manufacturers.

Although Polyox is completely soluble in tap water, care has to be taken to avoid causing agglomeration of particles as there is a tendency for the particles to gel into large lumps which are then difficult to dissolve. Since high-speed agitation must be avoided because of the resulting degradation a number of methods to dissolve the Polyox have been devised. A common technique (used for example by Goren and Norbury (1967)) is to make up highly concentrated solutions in an organic solvent such as methyl alcohol for subsequent dilution. Reischmann and Tiederman (1975) used isopropyl alcohol to prepare a master batch and allowed the dilute solution to age for eight to twelve hours before use. Barker (1973) prepared a master solution with water as the solvent which was allowed to age for twenty-four hours before dilution. The dilute solution was then mixed gently for two hours before use. Paterson and Abernathy (1970) prepared a Polyox suspension in a few millilitres of isopropyl alcohol and added distilled water to produce a 1000 ppm master solution which was diluted and used within twenty-four hours. For small amounts of polymer solution,

the manufacturers recommend forming a suspension in boiling water and allowing dissolution to take place as the temperature is reduced.

The preparation method used in this work was similar to the method of Ting and Little (1973) and involves direct dissolution to the desired concentration in both top and bottom tanks. (In calculating the amount of powder required, allowance was made for the volume of water in the working section and pipework.) Weighed amounts of Polyox were carefully dissolved by sprinkling the dry powder on the water surface for a few minutes and low speed agitation was used to disperse the particles throughout the tank. More Polyox was then sprinkled on the surface and the process was repeated until the required dilution was reached. When the powder appeared to be completely dissolved, the solution was left to age, with low speed agitation from time to time, for three days before use.

While the presence of visco-elasticity is often given as an explanation for some of the anomalous flow properties of polymer solutions, the rheological data presently available suggests that stress-strain relationships for most polymers are little different from a Newtonian type of behaviour at typical drag reducing concentrations.

Merril et al (1966) measured rheological properties of several grades of Polyox and PIB (Polyisobutylene) polymers using Ubbelodhe and Coutte flow viscometers and using light scattering methods to determine average molecular weight. Merril et al defined and calculated the critical concentration where the random coils will on average be touching each other and concluded that, for all grades of polymer investigated, for solutions of less than one third of the critical concentration, the solution viscosity is never more than 120% of the solvent viscosity and that viscoelastic properties are difficult to detect even with the most sensitive instrumentation.

Using a Well-Brookfield cone-plate microviscometer, Huang and Santelli (1971) collected rheological data on WSR 301 and other polymers. Although significant shear thinning behaviour was observed in other polymers, WSR 301 was found to behave like a Newtonian fluid for concentrations up to 500 ppm. The following relationship between solvent viscosity, μ_s, and solution viscosity, μ_p, was obtained at a temperature of 25°C and at a given rate of shear, γ, as

$$\mu_p(\gamma) = \mu_s(\gamma) \left\{ 1 + [\eta]\, c + 0.4\, [\eta]^2\, c^2 \right\}$$

where the intrinsic viscosity, η, is defined by

$$\eta = \lim_{\substack{\gamma \to 0 \\ c \to 0}} \frac{\mu_p [\gamma] / \mu_s [\gamma] - 1}{c}$$

and was found to be 17 dl/g and c is the polymer concentration.

Table 5.2

Comparison of measured kinematic viscosity of Polyox WSR 301 due to Ayyash with values calculated using Huang's formula

Polymer Concentration	Kinematic Viscosity (ν)	
	Measured	Calculated
50 ppm	1.05	1.08
100 ppm	1.10	1.28
250 ppm	1.33	1.49
500 ppm	1.73	2.14

Table 5.2 lists a comparison of viscosity measurements made in this Laboratory by Ayyash (unpublished) using an Ubbelohde viscometer and the corresponding values calculated using Huang's formula. The agreement is quite good although the measured values are consistently slightly lower than those of Huang, perhaps reflecting differences between the polymer batches used in the different experiments.

Since the polymer used by Ayyash was from the same batch as the Polyox used throughout the present work, his values of solution viscosity are used.

The experimental procedure was as follows. The laser velocimeter was set up as described in Chapter 3 and alignment and instrumentation were checked with several runs in water flow. The optical bench was positioned by hand so that the measuring volume was located at a dimensionless distance (x/M) of 20 from the grid. A continuous velocity record was obtained as the water passed through the system. (Valve V1 was closed before all the water had emptied from the top tank in order to stop air from entering the system.) The system was reprimed and measurements were made at x/M = 30, 40, 50 and 60 using the same procedure.

Velocity records were obtained at the same measuring positions in polymer solutions with concentrations of 50, 100, 250, 500 and 1000 ppm by weight. For each of the polymer concentrations, a fresh solution was prepared as described and two flow cycles (passes) were completed to thoroughly mix the solution before measurements were made. In making a complete set of measurements, each solution is passed through the system seven times in all before being discarded. (Two passes is approximately equivalent to all the solution having been pumped once.) When the measurements had been completed the flow rig was emptied completely, flushed thoroughly, refilled and emptied several times before another solution was prepared.

Solutions of the same concentrations were freshly prepared for the dye injection experiments. After completing two passes the solutions were passed a third time with the dye injector in operation and the photographs were taken. These solutions were then discarded and the rig cleaned before being used again.

Some investigations were made into the effect of degradation on intensity and spectral shape. A 500 ppm solution was prepared and velocity measurements were made at x/M = 30 as the solution was passed up to twenty times through the system. The results of these tests are described at the end of Section 5.4..

5.4 SUMMARY OF EXPERIMENTAL RESULTS

Turbulent intensities for water and polymer solutions are presented in Figure 5.3 where $\bar{U}^2/\overline{u'^2}$ is plotted against x/M on logarithmic scales. In all cases the data may be fitted by the power law

$$\frac{\bar{U}^2}{\overline{u'^2}} = A \left(\frac{x}{M}\right)^n$$

From Figure 5.3 it may be seen that the turbulent intensities tended to be smaller in the polymer solutions than in water. Fitting the power law to the data resulted in the values of the constants given in Table 5.3. The value n = 1.9 for water is large compared to the values in Table 5.1 from the data of others although a large value of n is expected for a low value of Re_M and a high solidity. Since measurements at x/M = 20 may be rather close to the grid for the turbulence to be independent of the initial conditions the power law was fitted to the data between x/M = 30 and 60 only, resulting in values of the constants given in Table 5.4. A value of n = 1.6 was obtained for water which is closer to the values found by others. Both tables indicate that the polymer additive tends to increase values of A and decrease values of n, thus indicating a reduced rate of decay.

The rate of decay of turbulent intensity may be calculated from the relation

$$\varepsilon = -\tfrac{1}{2} \frac{d}{dt} \left((\overline{u'^2}) + 2(\overline{v'^2}) \right)$$

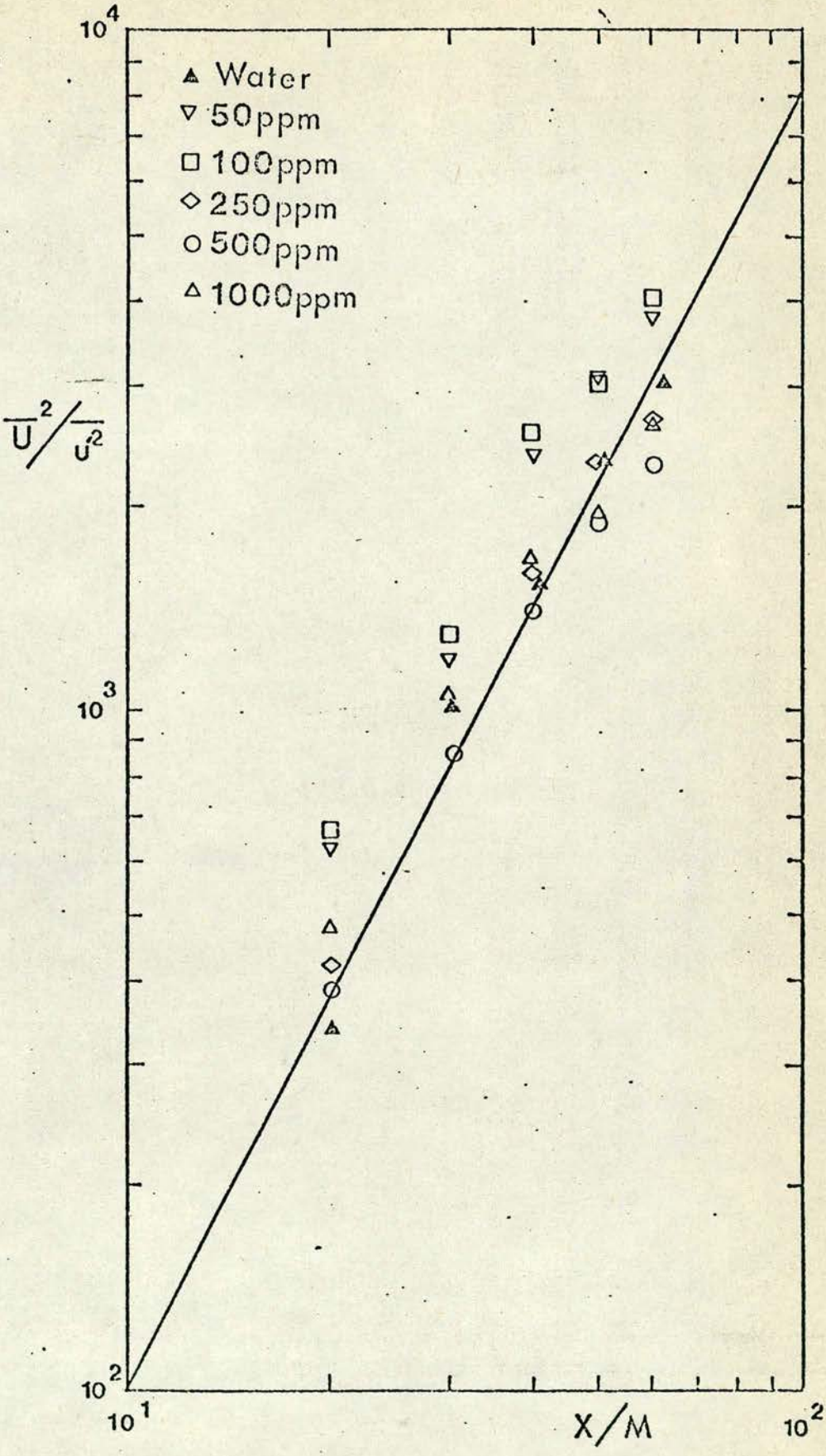

Figure 5.3

Variation of Turbulent Intensity with Downstream Distance from the Grid for Water and Polyox WSR 301

Table 5.3

Parameters describing turbulence decay between x/M = 20 and x/M = 60

Concentration	A	n
0	1.2	1.9
50	3.9	1.7
100	4.7	1.7
250	2.8	1.7
500	3.1	1.6
1000	5.7	1.5

Table 5.4

Parameters describing turbulence decay between x/M = 30 and x/M = 60

Concentration	A	n
0	4.1	1.6
50	3.9	1.7
100	5.4	1.6
250	7.7	1.4
500	5.4	1.5
1000	14.0	1.3

and making the transformation $dx = \overline{U}dt$ (ie. assuming the Taylor hypothesis) we obtain

$$\varepsilon = -\tfrac{1}{2}\frac{\overline{U}^3}{M}\frac{d}{d(x/M)}\left[\frac{\overline{u'^2}}{\overline{U}^2} + 2\frac{\overline{v'^2}}{\overline{U}^2}\right]$$

Neither of the transverse components was measured in our experiments but the relationship

$$\overline{v'^2} = 0.83\ \overline{u'^2}$$

was assumed, following the interpretation of Friehe and Schwarz (1969) of the results of Comte-Bellot and Corrsin (1966).

The one dimensional wavenumber spectrum $\phi(k)$ was made dimensionless using Kolmogoroff variables. That is

$$\tilde{\phi}(\tilde{k}) = \frac{\phi(k)}{\nu^2 k_K}$$

where $\tilde{k} = k/k_K$, $k_K = (\varepsilon/\nu^3)^{\frac{1}{4}}$ is the Kolmogoroff dissipation wavenumber. ε was calculated from the decay data for each concentration but, for simplicity, ν was taken to be the kinematic viscosity of water in all cases.

In Chapter 3 an expression was found for the ambiguity noise level in terms of mean velocity, velocity gradient and dissipation rate and the measuring volume dimensions. The practical effect of the ambiguity noise was checked by comparing the spectral measurements in water with the universal spectrum due to Pao (1965). Comparison of normalised spectra on a log-log plot against $\tilde{k}$ showed good agreement between measured spectra and the universal spectrum up to about $\tilde{k} = 0.5$. At wavenumbers greater than this, the measured spectra flattened off to a constant noise level. A typical comparison (x/M = 30) is shown in Figure 5.4.

As the dissipation spectrum involves the square of the wavenumber as a weighting factor it is therefore particularly sensitive at large wavenumbers to the wide-band spectrum of ambiguity noise. To assess this, the second moments of the measured spectra were plotted against $\tilde{k}$ on linear-linear co-ordinates and also compared to the universal curve of Pao (1965). Again good agreement (see Figure 5.5 for x/M = 30) was found between curves based on the measured spectra and the universal

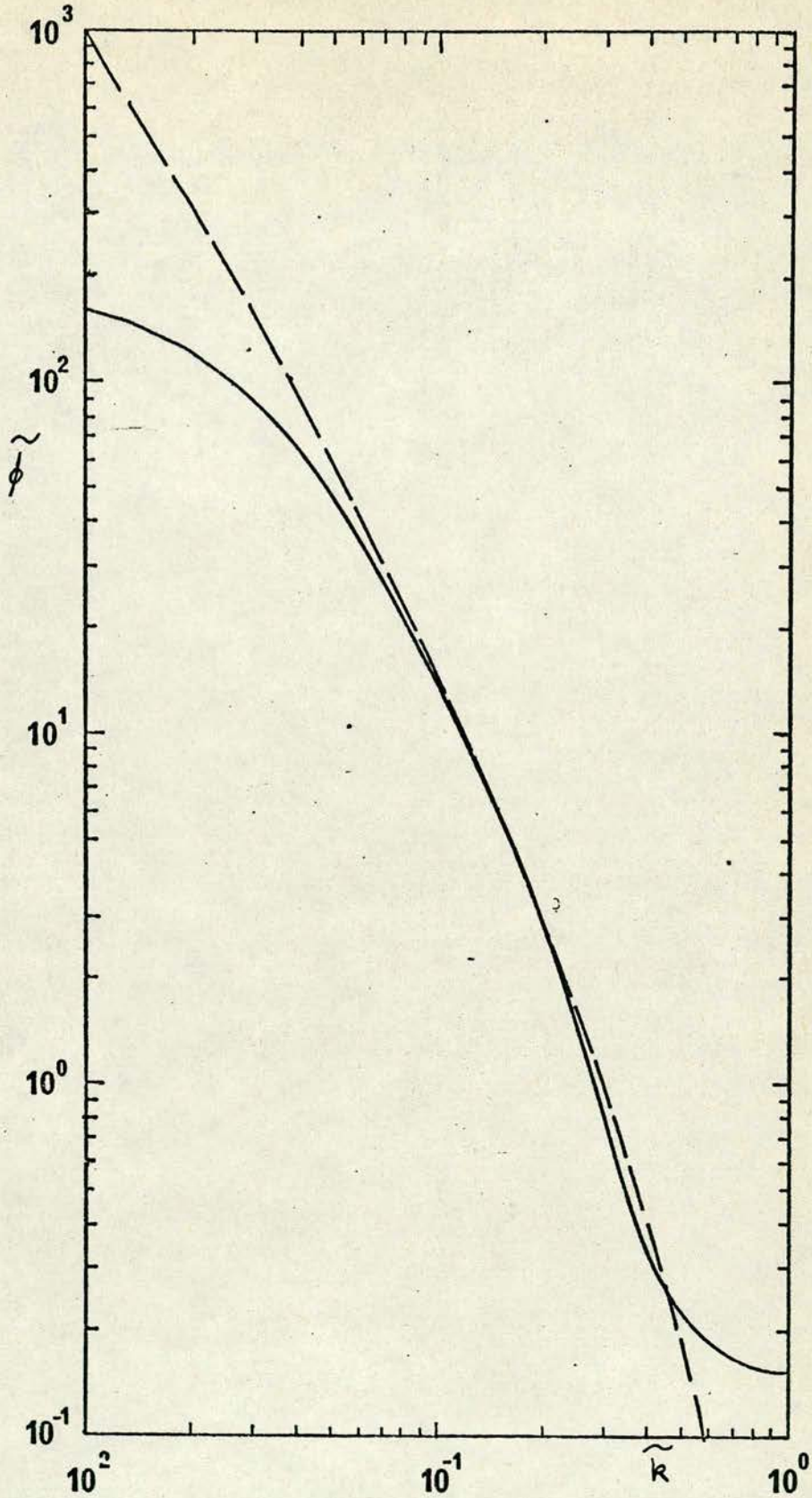

Figure 5.4

Comparison of Spectrum at x/M = 30 (solid line) for water with spectrum of Pao (dotted line) (1965)

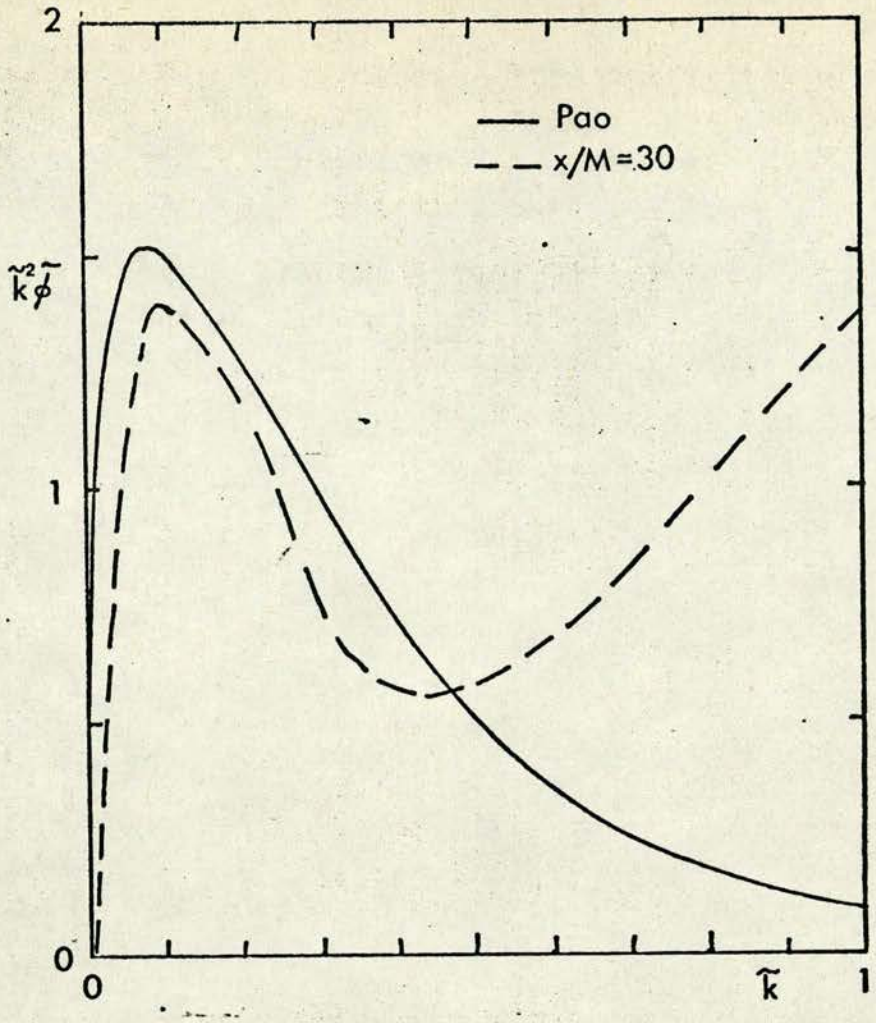

Figure 5.5

A Comparison between the Theoretical Dissipation Spectrum due to Pao and the Measured Spectrum at x/M = 30

spectrum up to $\tilde{k} \simeq 0.5$ where the noise level becomes important.

Evidently, measurements at values of k greater than about 0.5 should be disregarded in the present work if the spectra are not corrected for ambiguity effects. This leaves the approximate wavenumber band $0.1 < \tilde{k} < 0.5$ as representing the dissipation range. Although this is somewhat smaller than might be obtained by hot film methods, it was thought to be adequate to permit a comparison of results in water and polymer solutions. It was thought preferable to indicate clearly the limitations of the measurements rather than show spectra where an ambiguity level which was not accurately known had been subtracted. (Spectra for water and 500 ppm were examined after subtraction of several values of ambiguity level. These indicated that the behaviour for $\tilde{k} > 0.5$ was similar to $\tilde{k} < 0.5$ although the precision of the data was rather poor. The reasons for poor precision were explained in Chapter 3.)

To investigate the extent of the inertial sub-range, $k^{5/3}\,\phi(k)$ was computed as a function of k and the region of constant values (± 10%) was located. For all positions except x/M = 50 the largest wavenumber in the inertial sub-range was at least 2.5 times greater than the lowest wavenumber in the sub-range. Since the dissipation rates were known from the decay data, values of the Kolmogoroff constant α could be calculated and are tabulated in Table 5.5. The values of α obtained (with Re_λ ranging from 28 to 48) were found to be in agreement with the curve of Bradshaw (1967) of variation of α with Re_λ.

The spectra obtained for water and the five polymer concentrations at the five positions are plotted in Figures 5.6 - 5.10. The extent of the -5/3 slope was generally less for the polymer spectra than for the water results. However, at all positions, all the spectra exhibit

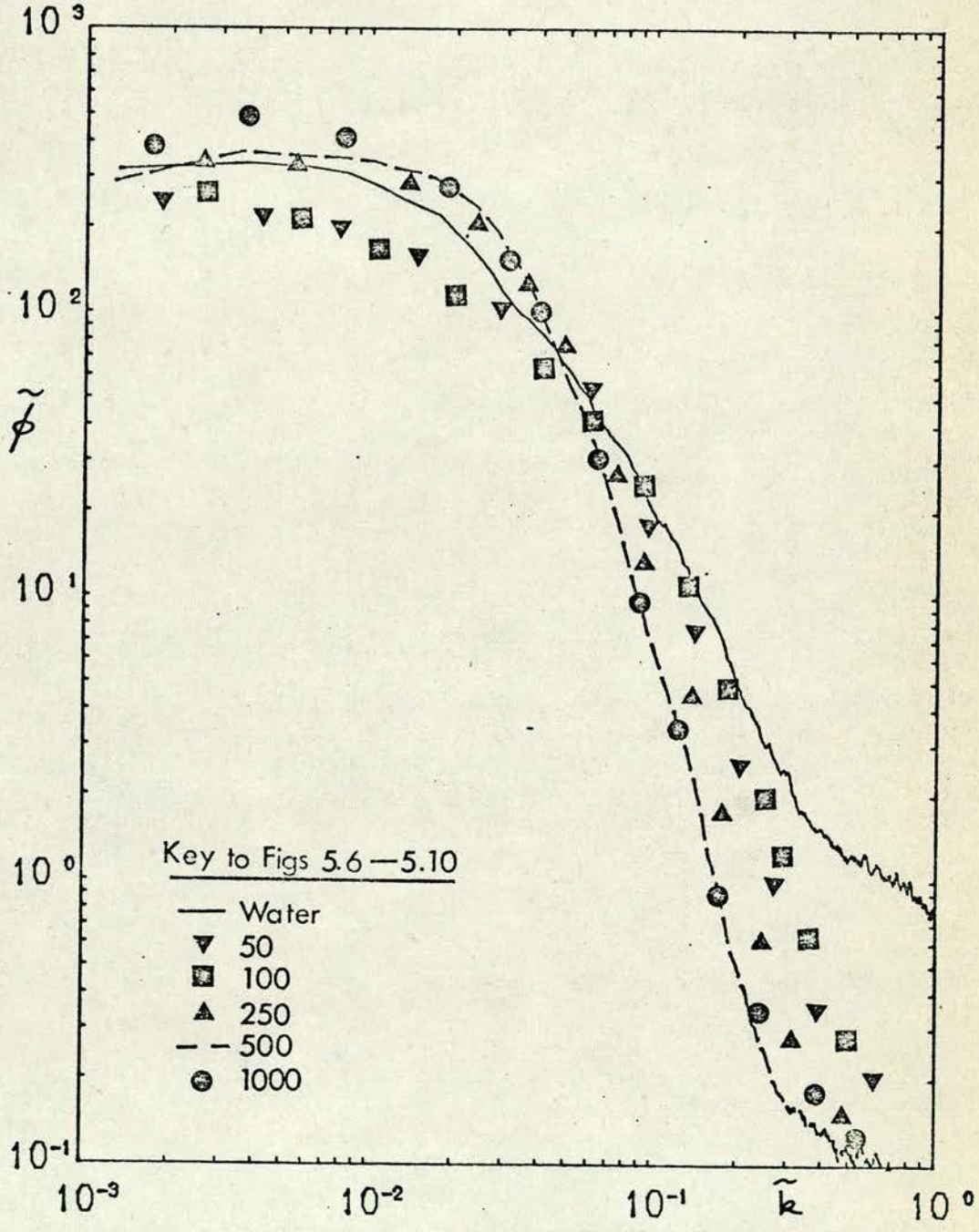

Figure 5.6

Dimensionless Spectra at x/M = 20

(Solvent Kinematic Viscosity used in scaling)

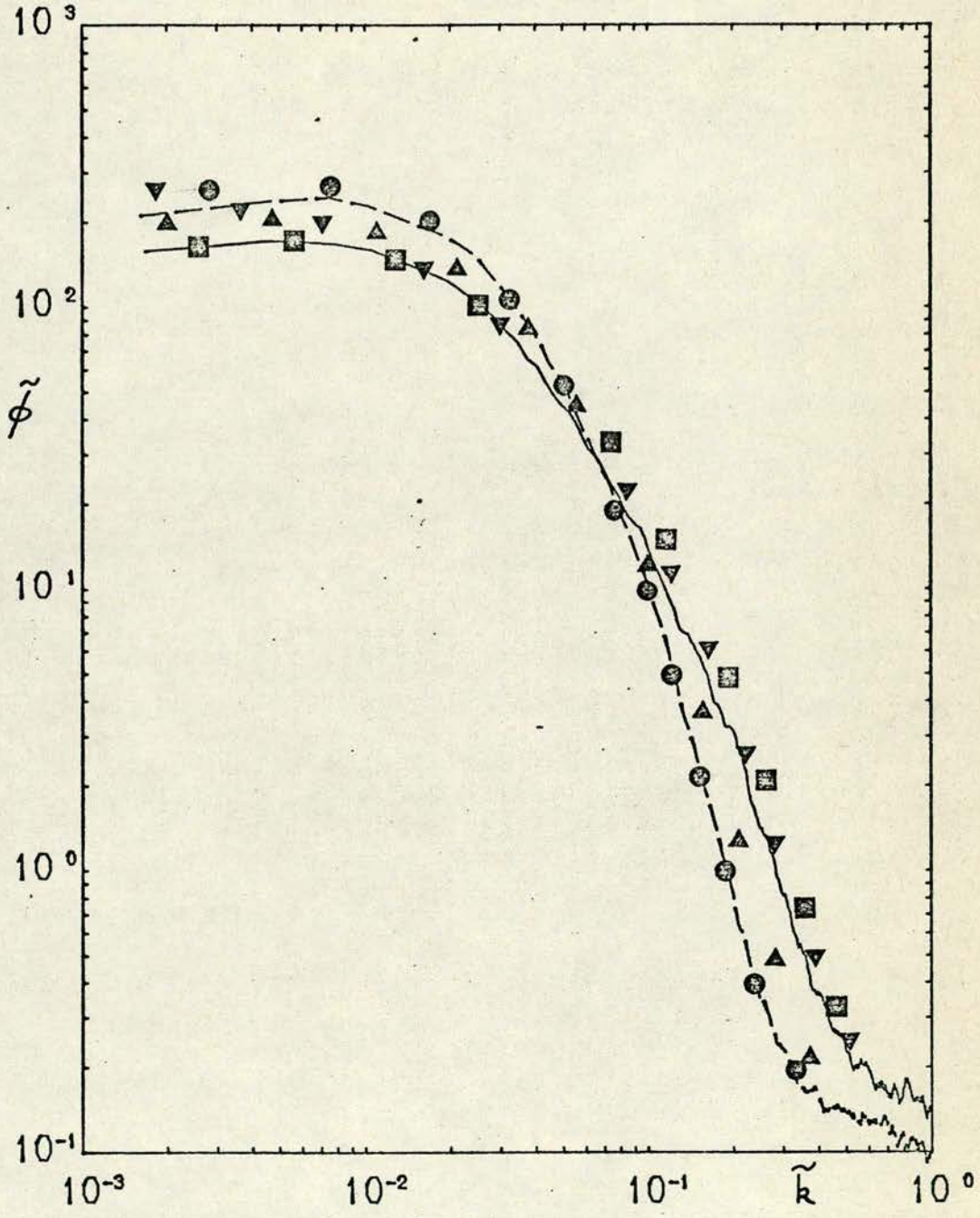

Figure 5.7

Dimensionless Spectra at x/M = 30

(Solvent Kinematic Viscosity used in scaling)

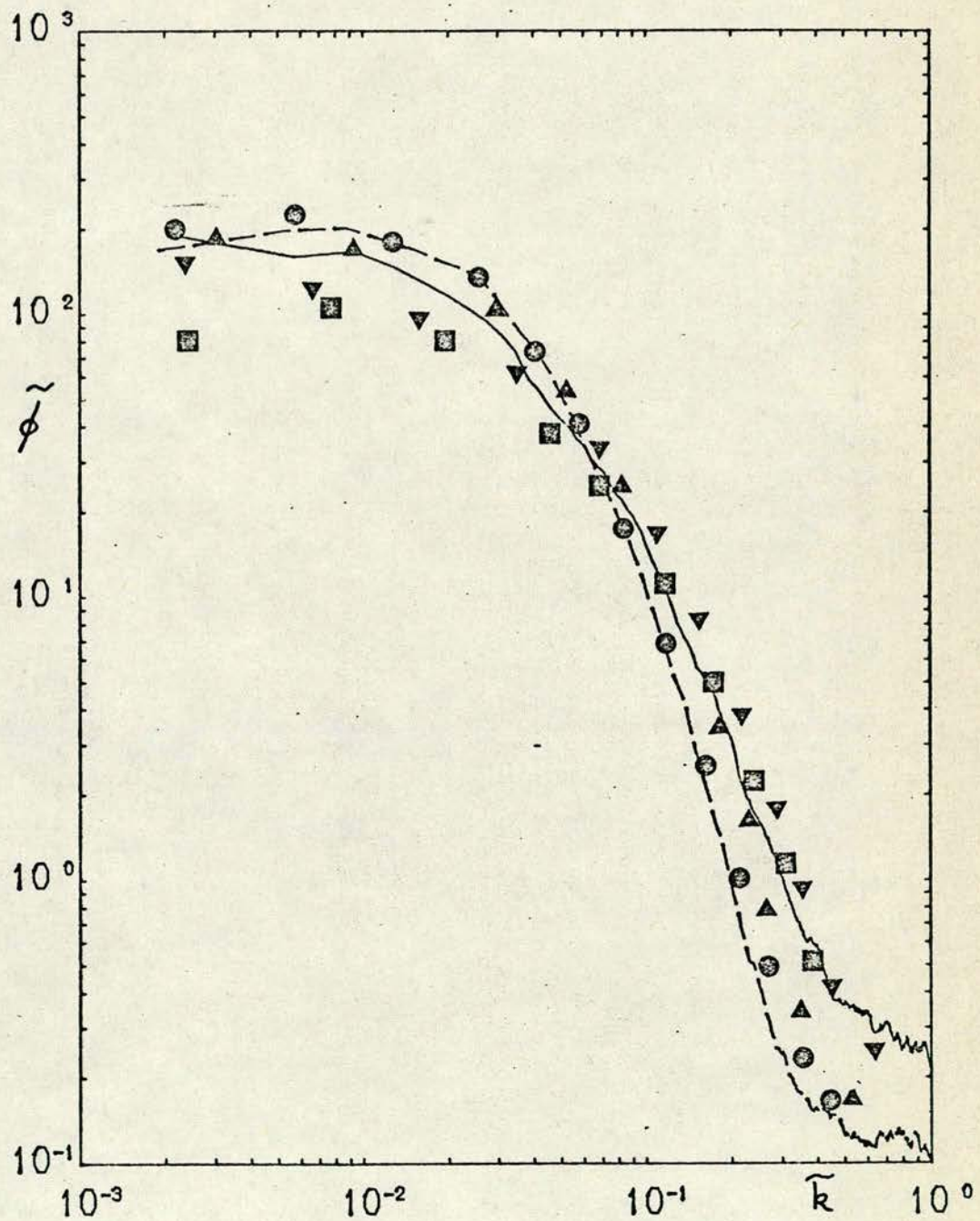

Figure 5.8

Dimensionless Spectra at x/M = 40

(Solvent Kinematic Viscosity used in scaling)

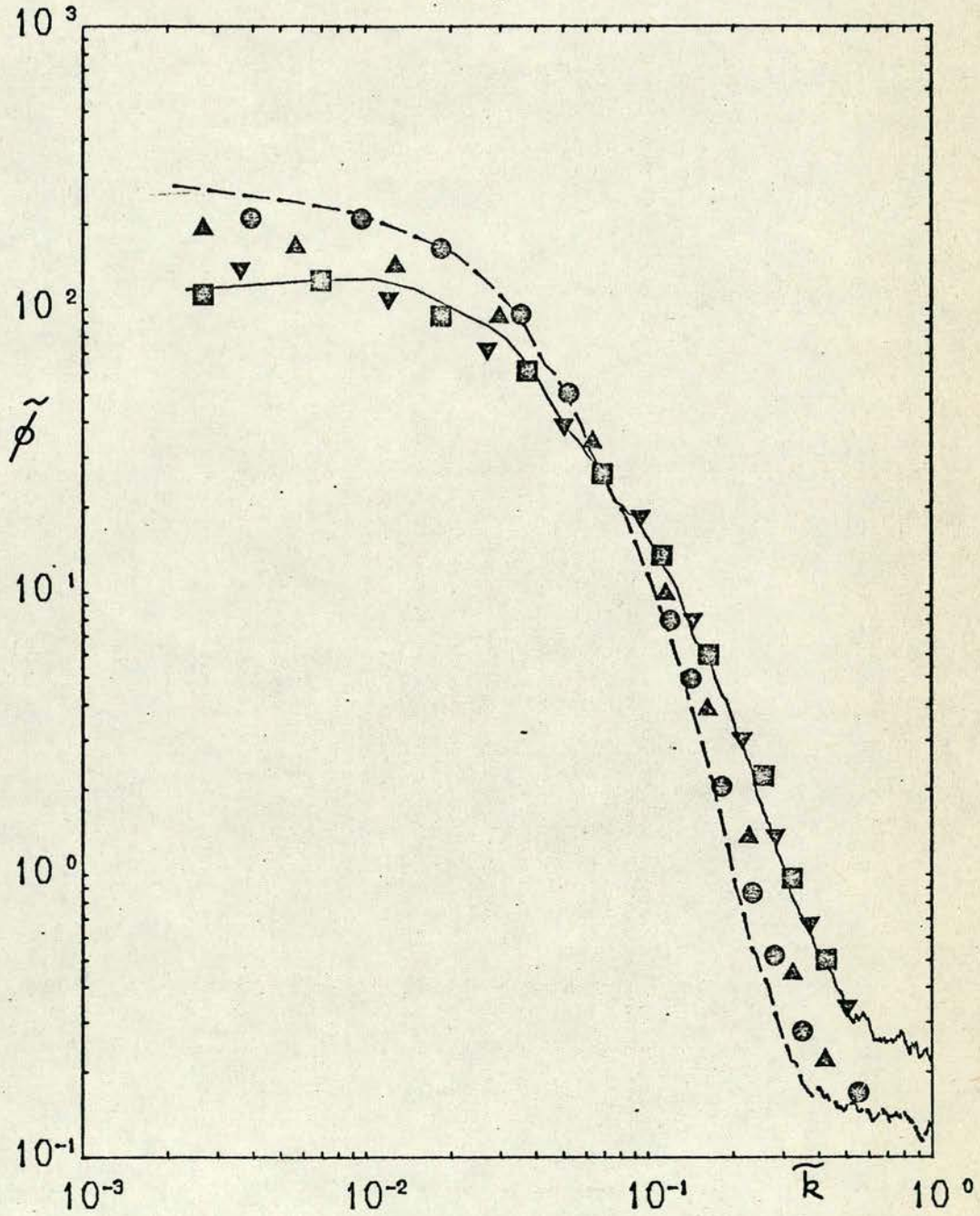

Figure 5.9

Dimensionless Spectra at x/M = 50

(Solvent Kinematic Viscosity used in scaling)

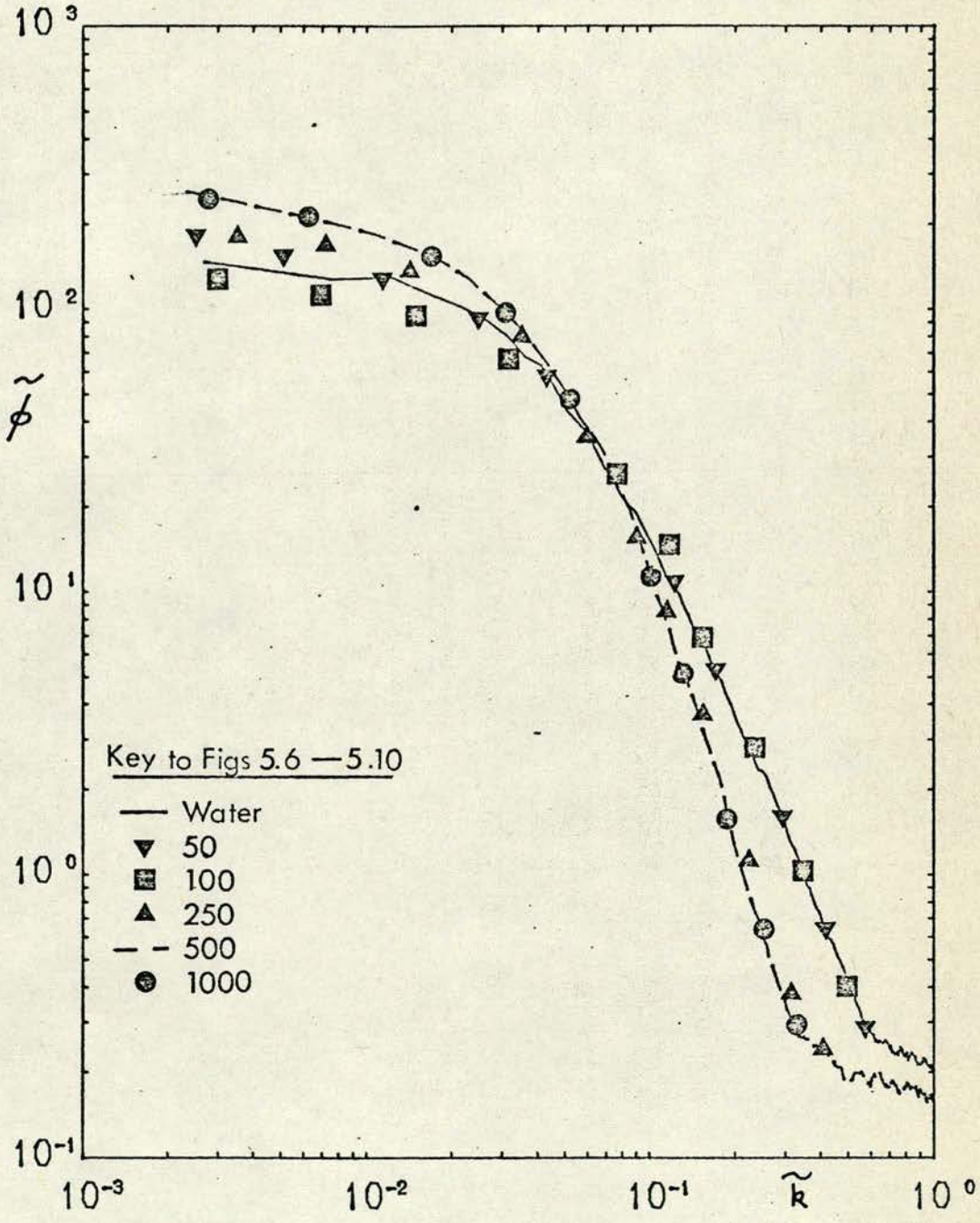

Figure 5.10

Dimensionless Spectra at x/M = 60

(Solvent Kinematic Viscosity used in scaling)

Table 5.5

Extent of Inertial Sub-range in Newtonian Grid Flow

Position (x/M)	Extent of Sub-range k_{max}/k_{min}	Re_λ	Average value of $k^{5/3}\phi(k)$ in Sub-range	α
20	2.7	48	7.4	0.45
30	2.7	30	2.4	0.30
40	2.5	30	1.4	0.32
50	1.7	27	0.98	0.33
60	3.3	28	0.65	0.32

(or are at least tangent to) a -5/3 slope over a limited range of wavenumbers. At the higher wavenumber (dissipation) range, two quite different forms of behaviour may be discerned, depending on polymer concentration. The results for the lower concentrations (50 and 100 ppm) fall quite close to the water curve, indicating little or no change in spectral shape, due to the additives. At the higher concentrations (250, 500 and 1000 ppm) the data points again cluster together but in this case the dissipation range curve falls off more steeply than the spectrum in water. Thus there is noticeable attenuation of the high frequency components.

So far as the lower polymer concentrations are concerned, our method of presenting normalised spectra based on the kinematic viscosity of water is probably not unreasonable. The effect of polyethyleneoxide on solution viscosity at concentrations up to (say) 100 ppm is (unlike certain other drag reducing polymers) quite small. On the other hand, at the higher concentrations these solutions are known to have larger viscosities. The problem is further complicated by the possible relevance of other effects such as solution elasticity or anomalous extensional viscosity. Thus, in the present state of knowledge, there is unlikely to be any definite answer to the problem of normalising spectra in these solutions.

Certainly it might seem simplest to follow Friehe and Schwarz and use an effective viscosity based on the r.m.s. rate of strain. To do this, one must obtain the dissipation rate and in practice this necessitates an assumption that the inertial range spectrum (including the constant of proportionality) is unchanged in the polymer solutions. It also means evaluating the integral of the second moment of the spectrum. In our case, we would have to subtract the effect of the

noise spectrum from the second moment in order to continue the integration to wavenumbers greater than 0.5 k_d. We did not feel that the accuracy of this process would be sufficient to justify the calculation of an effective viscosity.

However, the present use of the viscosity of water to scale the results for all solutions may be regarded as a lower bound on the spectral normalisation. Using the values of solution viscosity measured by Ayyash the results for 50 ppm and 500 ppm are re-plotted in normalised form and compared to the curves for water in Figures 5.11 - 5.15. It is clear from these graphs that the spectra in the 50 ppm solution were very little changed by this procedure. Also, the spectra in the 500 ppm solution still show some attenuation relative to the result for water in the dissipation range, although the magnitude of the effect is undoubtedly reduced by this scaling.

Presumably for shear-thinning solutions, the correct procedure may be thought to lie somewhere between these two extremes. Indeed Friehe and Schwarz found the effective viscosities for their 300 ppm polyacrylamide solution to be somewhat lower than their rheological values at the same rate of strain.

The results of the flow-visualisation experiments are presented in Figure 5.16 and show the effect of increasing polymer concentration on the dye jet. To some extent these photographs support the idea of a step change with increasing concentration as suggested by the measurements of spectra. The photographs show that there is much fine-scale structure in water and the 50 ppm solution but at 100 ppm this seems to have been suppressed. Thus the change in behaviour would appear to be between 50 and 100 ppm as opposed to a threshold of between 100 and 250 ppm for spectra.

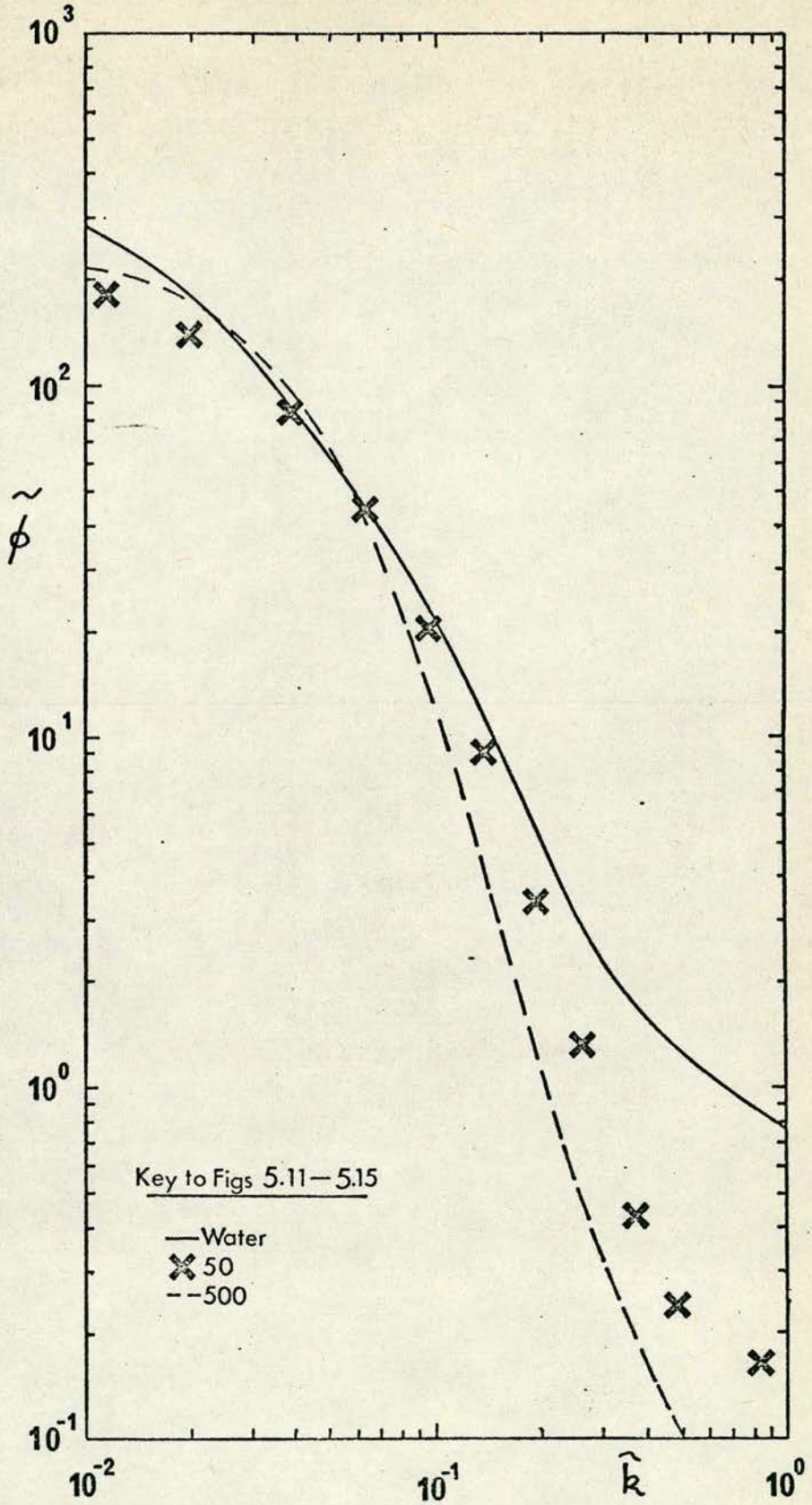

Figure 5.11

Dimensionless Spectra at x/M = 20

Solution kinematic viscosity used in scaling

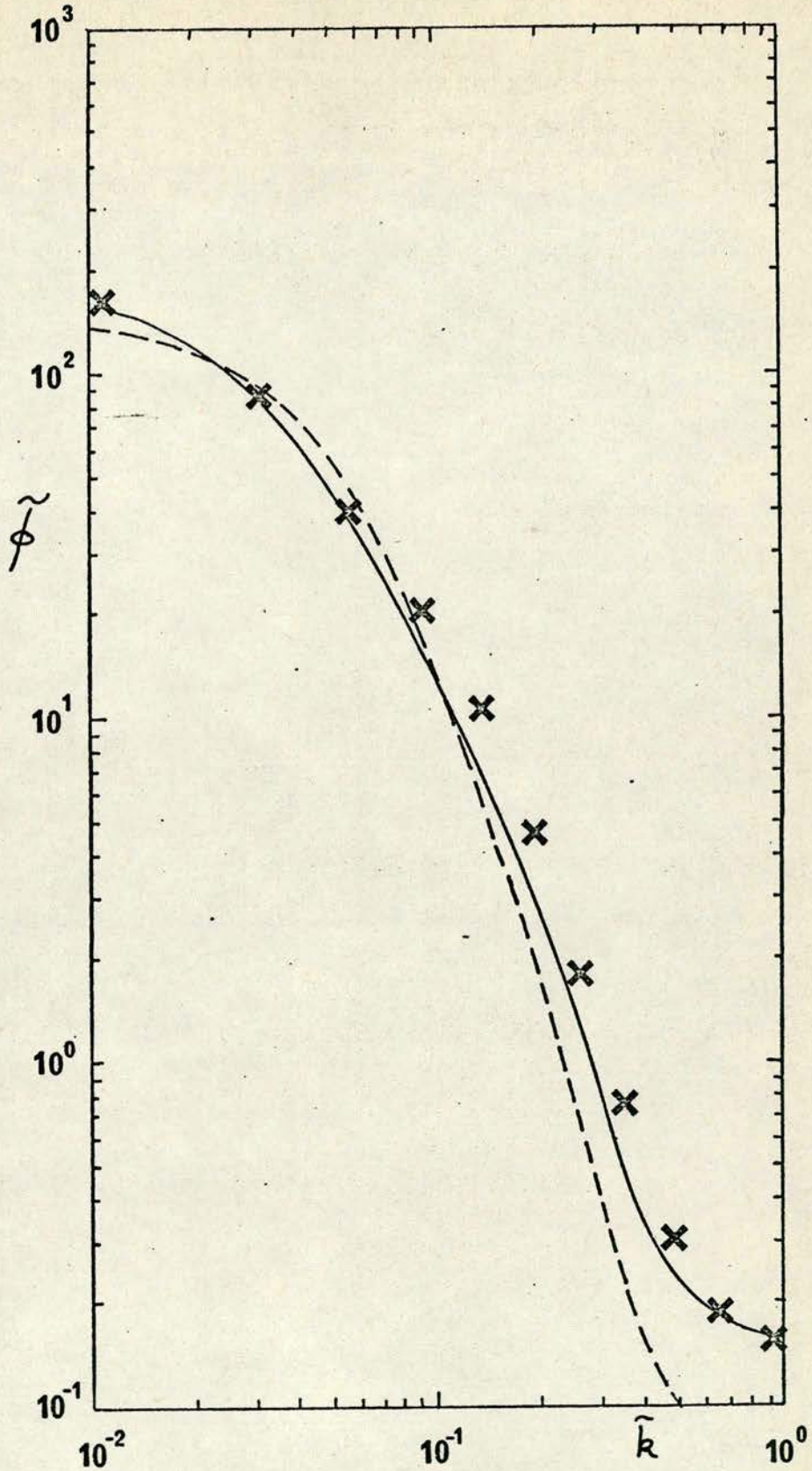

Figure 5.12

Dimensionless Spectra at x/M = 30

Solution Kinematic Viscosity used in scaling

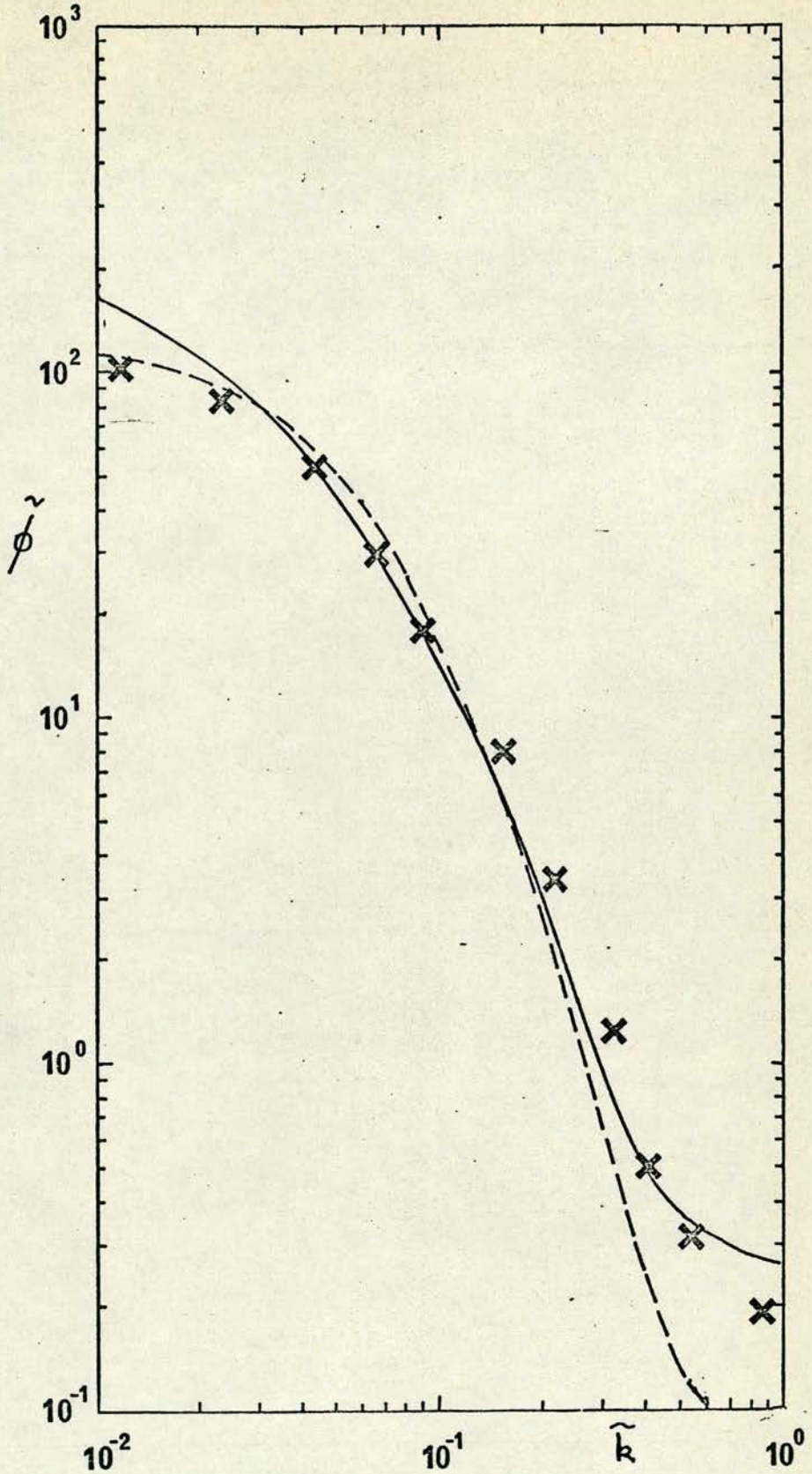

Figure 5.13

Dimensionless Spectra at x/M = 40

Solution Kinematic Viscosity used in scaling

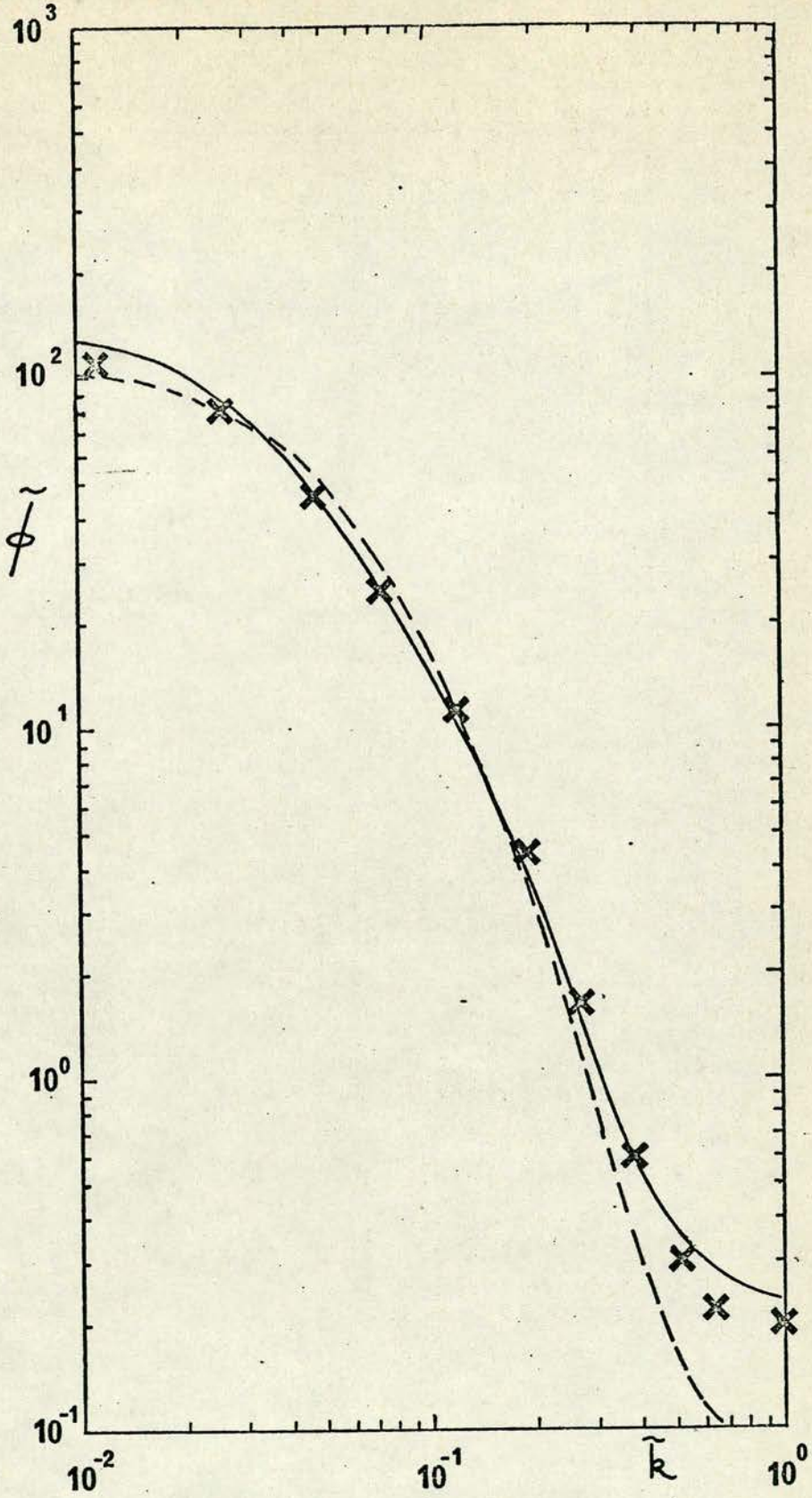

Figure 5.14

Dimensionless Spectra at x/M = 50

Solution Kinematic Viscosity used in scaling

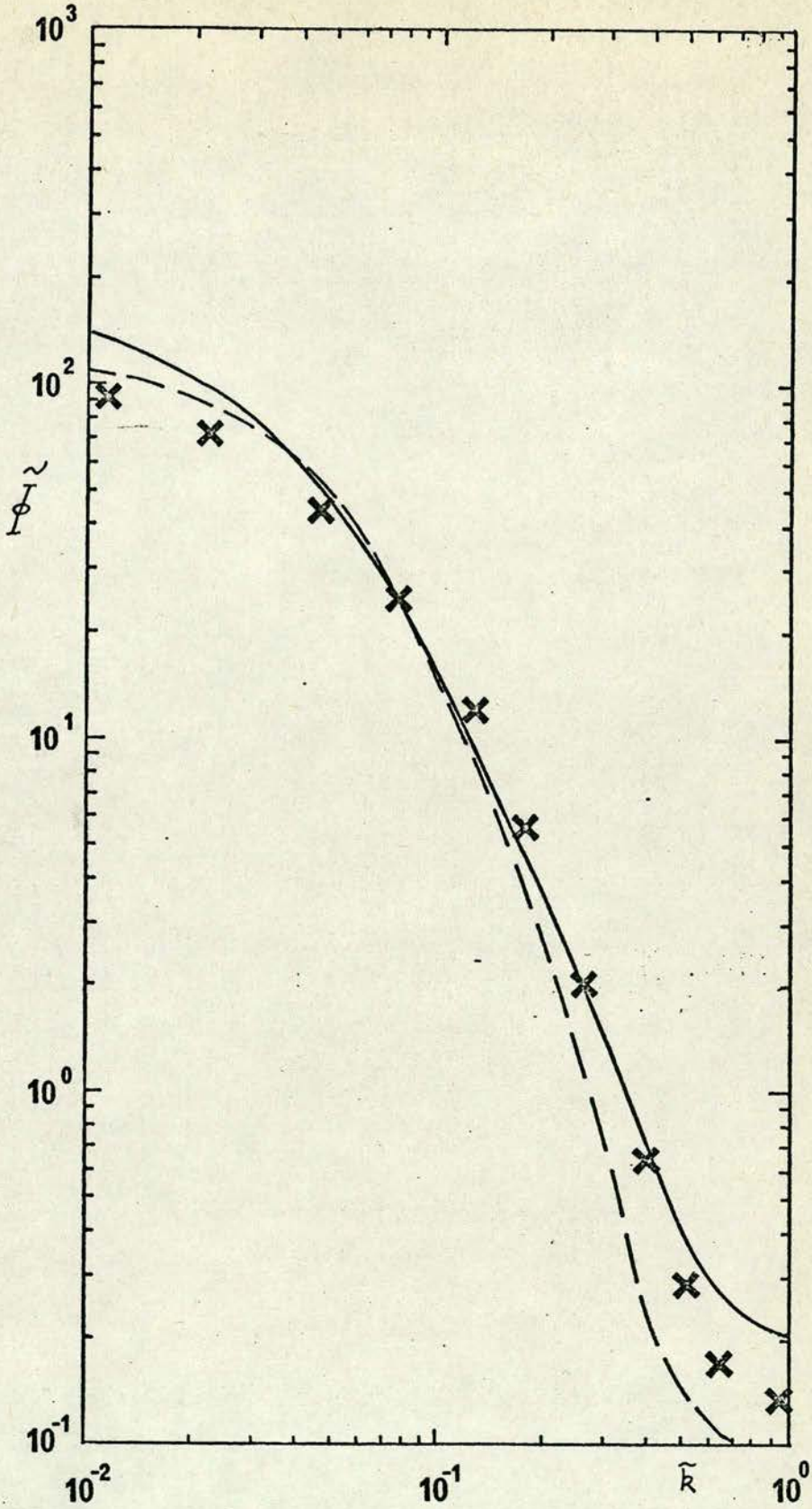

Figure 5.15

Dimensionless Spectra at x/M = 60

Solution Kinematic Viscosity used in scaling

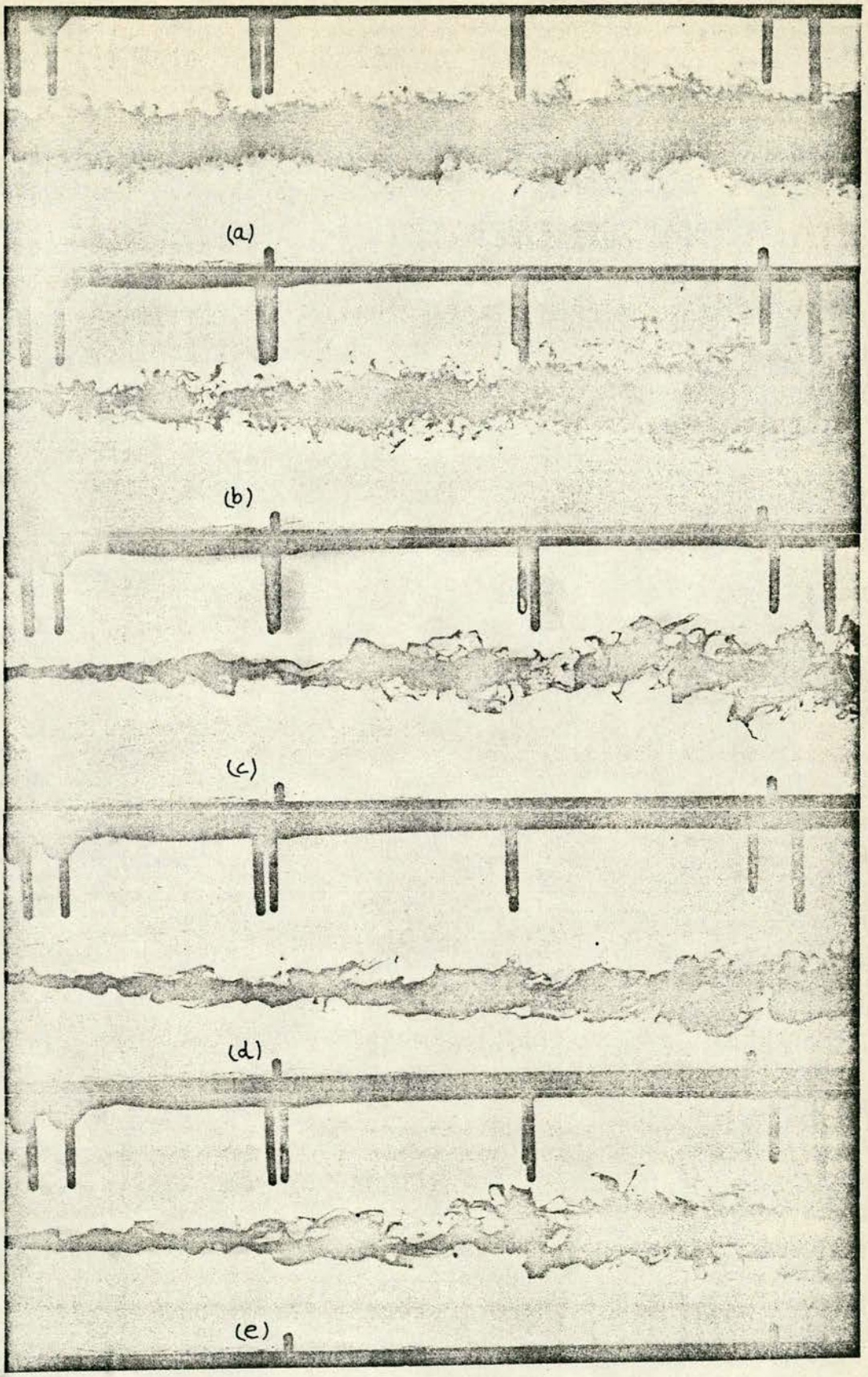

Figure 5.16

Photographs of the Injected Dye Trace for Concentrations of (a) 0, (b) 50, (c) 100, (d) 250, (e) 500 ppm Polyox WSR 301

The effect of degradation on the spectrum and intensity level in a 500 ppm solution at x/M = 30 is shown in Figures 5.17 - 5.18 as a function of number of passes through the system. At this position, the turbulent intensity is reduced slightly as the polymer is degraded. More importantly, there is a change in the shape of the spectrum with a reduction in the low wavenumber components and an increase in energy in the dissipation range as the polymer is degraded. After nine passes the spectrum was similar to the spectrum obtained in water at the same position. Thus the shape of the spectrum was found to be very sensitive to degradation and a normalised spectrum at x/M = 30, say, could not strictly be compared with one at x/M = 60 since the solutions had been degraded to different degrees. Since the same procedure was adopted for each solution, however, comparisons can be made between spectra at different concentrations at the same position as all the solutions had been degraded by the same amount.

5.5 DISCUSSION OF GRID TURBULENCE RESULTS

In summary, we have found that the presence of polymeric additives in grid-generated turbulence leads to reduced intensity levels and a change in the decay law. Like Friehe and Schwarz, we found that the exponent in the decay law was reduced in value by the additives but that there appeared to be no definite trend with increasing concentration. At typical drag reducing concentrations, turbulent energy spectra showed no qualitative change from those in water, but at higher concentrations some attenuation of small-scale (dissipation range) components was observed. This 'threshold' dependence on concentration was confirmed by the flow-visualisation experiments although, in this case, at a lower concentration.

Two points of disagreement between our results and those of

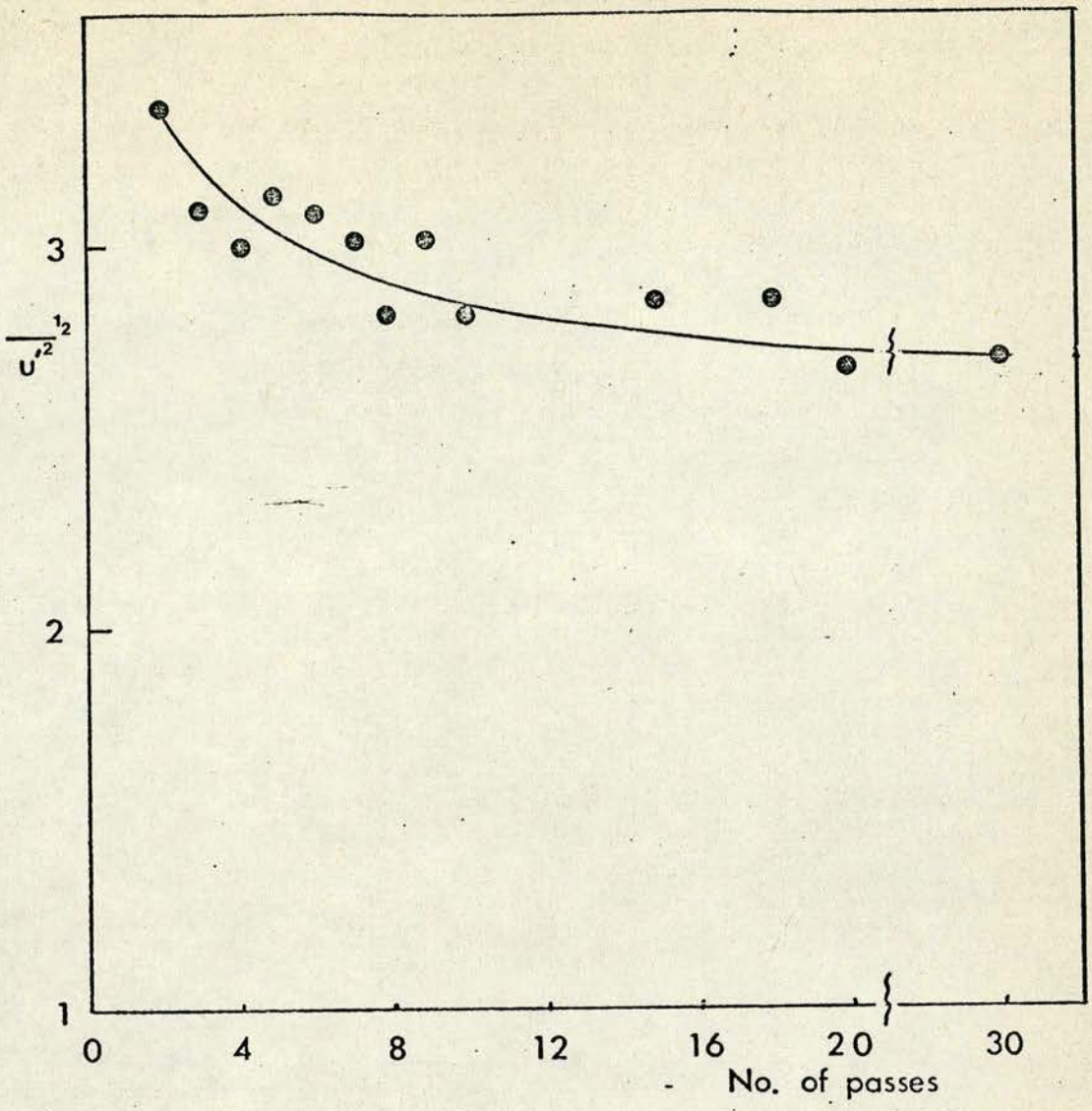

Figure 5.17

The Effect of Solution Degradation on the Turbulent Intensity at x/M = 30 for a 500 ppm Solution

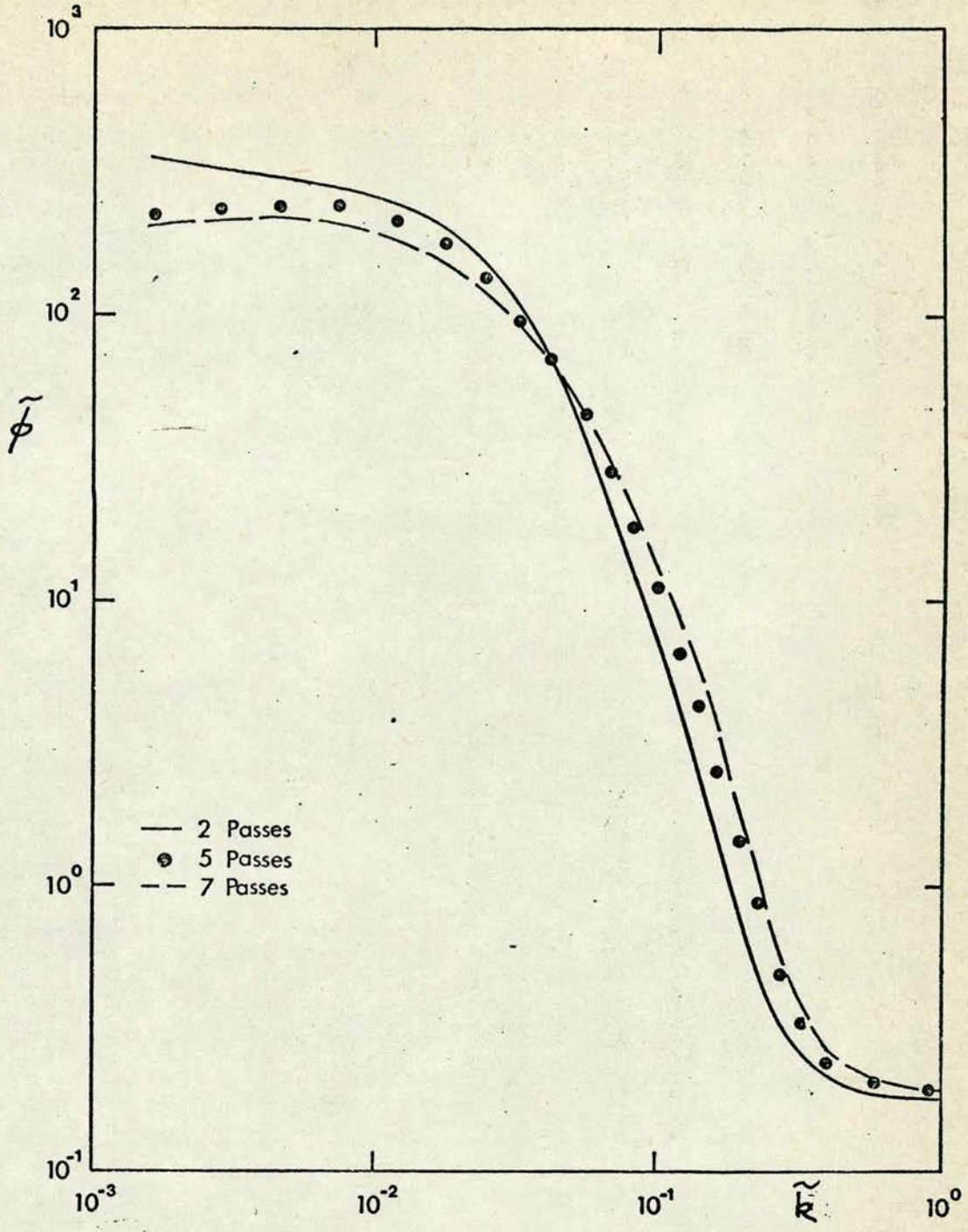

Figure 5.18

The Effect of Solution Degradation on the Energy Spectrum at x/M = 30 for a 500 ppm Solution

earlier experiments stand out. First, we found that Polyox WSR 301 decreased turbulent intensities whereas Friehe and Schwarz found the opposite effect with Dowell J-100. The explanation may lie in the different polymers used; and we note, in partial support of our own results, that Barnard and Sellin (1969) also used Polyox WSR 301 and deduced a reduction in intensity of a transverse component of velocity. Clearly a more comprehensive investigation, involving different types of polymer and the measurement of streamwise and transverse components of fluctuating velocity, would have much to recommend it.

Secondly, our photographs of the dye traces indicate that complete suppression of the turbulent fine structure must take place at a polymer concentration of between 50 and 100 ppm. This is in contrast to the results of Barnard and Sellin who found that a concentration of 20 ppm was sufficient for this purpose. Their experiments seem to be quite comparable with our own, the only major difference being that Barnard and Sellin injected a 1000 ppm solution, three metres upstream from the grid. Possibly this could have resulted in local concentrations higher than 20 ppm in the region of the dye injection. Certainly, Vleggaar and Tels (1973) report that the injection of concentrated polymer solutions (5000 ppm Separan) at the centreline of turbulent pipe flow resulted in a polymer 'thread' which remained intact for at least 200 tube diameters downstream (2 m in their experiments).

Finally, our results would seem to indicate that the discrepancy between flow-visualisation and spectral measurements is somewhat less than previously thought. Both types of measurement seem to suggest that there is a threshold additive concentration for suppression of high frequency components of the turbulence. The different values for this threshold may simply reflect the sensitivity of the relative diffusion

process to small changes in the fine structure of the turbulence. The existence of a threshold concentration is presumably to be related to some change in the structure of the fluid. Merrill et al (1966) discuss a critical concentration for polymer solutions, at which the random-coiling polymers just touch each other. For Polyox WSR 301 they estimate the critical concentration to be 406 ppm. This is apparently not a very precise criterion for non-Newtonian behaviour, but these authors comment that for concentrations less than one-third of critical concentration visco-elastic properties and gradient dependence of viscosity are difficult to detect, even with the most sensitive instruments. On this basis, our present results, which seem to indicate a concentration of between 100 and 250 ppm, for the onset of non-Newtonian behaviour in turbulent spectra, would seem to be quite reasonable.

CHAPTER 6

MEASUREMENTS IN PIPE FLOW TURBULENCE

6.1 EXPERIMENTAL DETAILS

Figure 6.1 shows a schematic of the "blow-down" flow rig which was used for all the experiments in pipe flow. The system, which is driven by compressed air, consists of a holding tank, pressure tank, working section of circular cross-section and a constant flow valve together with various control valves and connecting rigid and flexible pipework. The working section consists of three rigid perspex pipes (internal diameter 3.15 cm) connected together to give a total length of approximately 4 m. Six pressure taps (3 mm diameter) were set into the pipe spaced 45.8 cm apart and were connected to a manometer by way of a selector valve. With three metres of flexible tubing between the pressure tank and the working section, the measuring position was nearly 5.5 m (175 pipe diameters) from the tank and a well developed turbulent flow was obtained. The working section was fixed to a rigid table using wooden supports which were adjusted to ensure that the pipe was horizontal along its length. This was checked by observing the manometer readings with zero flow rate.

The flow cycle is described with reference to Figure 6.1 as follows. The system is filled from mains supply to the holding tank (tank 1 in Figure 6.1) and the water is allowed to drain into the pressure tank (tank 2) by opening valves V1 and A2 with valves V2 and A1 closed. Once sufficient fluid has been fed into the pressure tank the system is pressurised. The laboratory air supply is reduced from 125 psi to 30 psi using an adjustable pressure valve and compressed air is fed into tank 2 through valve A1 with valves V1, V2 and A1 closed. The pressure in the tank is monitored using a pressure gauge,

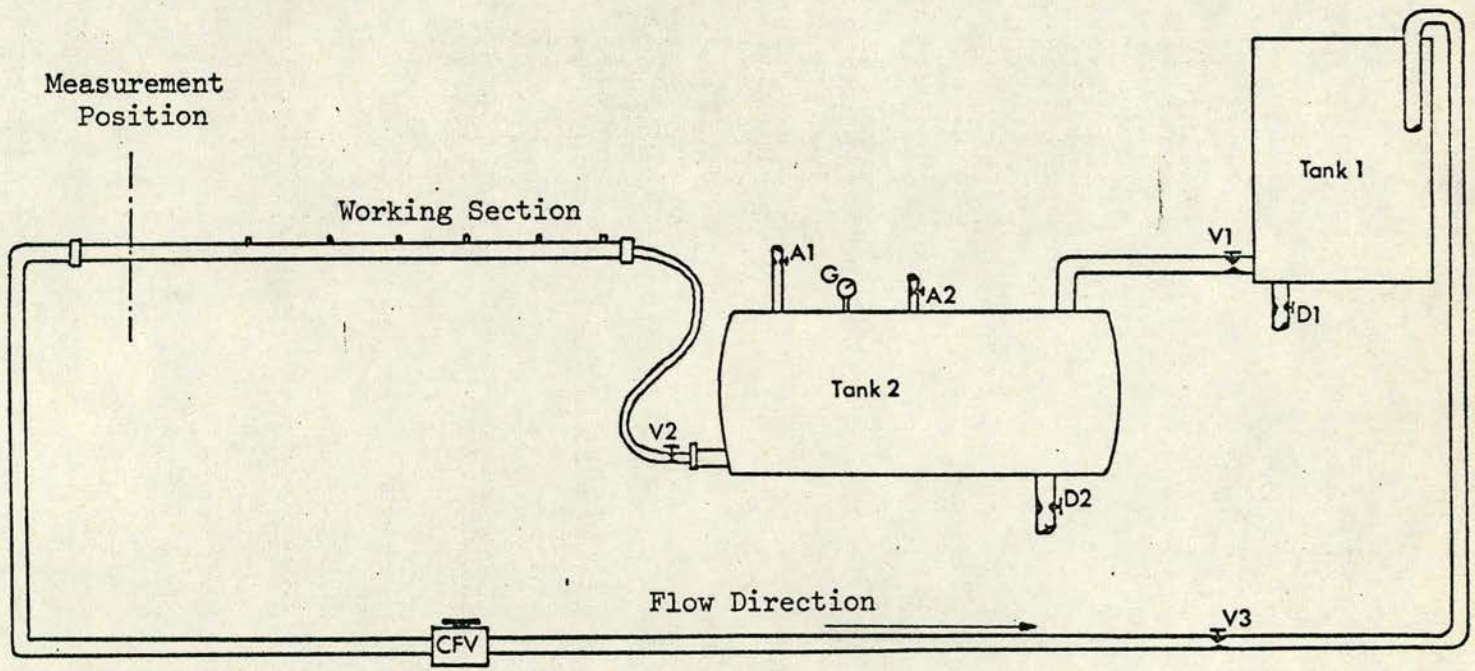

Figure 6.1

A Schematic Diagram of the Pipe Flow Facility

G, until the required pressure is reached whereupon the working section and flexible tubing are filled by releasing valve V2 with valve V3 fully open and the constant flowvalve (CFV) is adjusted to the required flow rate. Air which is trapped in the system is released by closing V3 and bleeding the air out through the pressure tap tubes. The manometer is then filled with "Airflow" manometer fluid (specific gravity of 1.585) and manometer bleeding is done to remove all remaining air from the system. Valve V3 is opened fully and the fluid is forced through the system into the holding tank. Throughout the "run down" period the pressure in Tank 2 is kept constant by the continuous addition of compressed air. When measurements are completed, valves V3 and A1 are closed and the air is released through the air escape valve A2. The system can then be drained through valves D1 and D2 until empty.

The method of solution preparation was similar to that used in the Grid flow experiments. Dry powder was mixed slowly in the holding tank as the tank was filled from the mains, low speed agitation being used to stir the polymer particles below the water surface taking care to avoid causing agglomeration. When the weighed amount of polymer had been added and the powder apparently completely dissolved, the solution was left to age, with low speed agitation from time to time, for three days before being used.

As part of the preliminary test programme, degradation measurements were made for solutions of 50 and 250 ppm Polyox WSR 301 by measuring the pressure drop as the solutions were passed through the system several times. It was found that the system had a severely degrading effect on both solutions which was subsequently found to be due to the constant flow valve. Because of this, all measurements presented here for polymer flows were obtained using solutions which

were passed through the system only once before being discarded.

Between each experimental run with polymer solutions, the system was flushed out thoroughly several times and pressure drop measurements were made to check that no polymer was left in the system. After completing all the measurements with Polyox solutions, special care was taken to clean out the system before the other polymer (Separan AP 273) was used. The working section was dismantled and thoroughly scrubbed and some velocity records were obtained in water flow and checked with the original Newtonian results.

To allow profiles of velocity to be measured, the laser velocimeter optical bench was mounted on a 1.25 cm thick steel plate measuring 2.1 m by 15 cm. The mounting plate was positioned on the table supporting the working section and was levelled using eight adjustable leg supports. Close fitting guides and a screw mechanism enabled the optical bench to be moved perpendicular to the pipe axis over a distance of 15 cm thus permitting the movement of the measuring volume across a pipe diameter. A micrometer screw barrel was used to measure the displacement of the bench and hence calculate the position of the measuring volume after allowing for the effect of the increased refractive index of water. To find the zero displacement point, or the point where the measuring volume was at the inside edge of the pipe wall nearer the laser, the following procedure was carried out. The laser and optical unit were aligned using the method described in Chapter 3 to form the beam intersection on the near side of the pipe in line with the pipe diameter. The optical bench was then traversed until the measuring volume was at the near side inside edge and the micrometer reading was noted. The optical bench was traversed further and the micrometer reading at the far side inside edge was noted. The centreline reading was calculated and the micrometer

barrel re-positioned to give a zero reading when the measuring volume was positioned at the near-side inside edge. The diameter of the pipe calculated from the optical bench displacement during a traverse was within 1% or 0.3 mm of the diameter measured using internal calipers.

Details of the experiments performed are listed in Table 6.1. Velocity records and pressure drop measurements were made in Newtonian flow (water) at two Reynolds numbers (Re = 24,633 and Re = 28,381) and compared with the classic results of Laufer (1954), Nikuradse (1933) and Patel (1965) and with the more recent results of Lawn (1971). The results from the lower Reynolds number flow were compared with results from four concentrations of Polyox WSR 301 (viz. 50, 100, 250 and 500 ppm) and four concentrations of Separan AP 273 (25, 50, 100 and 200 ppm) at the same bulk flow rate. In addition, results were obtained with a 50 ppm solution of WSR 301 with the flow rate adjusted to give the same wall shear stress as measured in the water flow at the lower Reynolds number. In all cases, a profile of velocity records was obtained across the pipe radius. Since the solutions were passed only once through the system and then discarded, the time available for all the measurements was limited. Velocity records of at least 40 seconds were obtained at between nine and eleven flow positions depending on the time available. (Between each measurement of velocity, the flow was shut off using valve V3 to maximise the amount of time available for data collection.) Measurements were made from the pipe centreline to as near to the near-side edge of the pipe as could be successfully measured by the frequency tracker without undue "drop-out". This position varied from $\xi = 0.053$ to $\xi = 0.16$ depending on local mean velocity, turbulence level and velocity gradient. The mean velocity, intensity level and energy spectrum were computed from the digitised velocity record at each measuring position although

Run	Solution	Relative Kinematic Viscosity	U_b (cm/sec)	Re	u_τ (cm/sec)	Drag Reduction
1	Water	1.0	90.1	28,381	4.38	0
2	Water	1.0	78.2	24,633	3.81	0
3	50 ppm WSR 301	1.05	75.3	23,710	3.28	23%
4	50 ppm WSR 301	1.05	103.0	32,391	3.81	32%
5	100 ppm WSR 301	1.10	77.2	22,099	2.76	47%
6	250 ppm WSR 301	1.33	74.8	17,671	2.76	45%
7	500 ppm WSR 301	1.73	71.1	12,971	2.65	47%
8	25 ppm AP 273	1.05	70.6	21,281	3.06	29%
9	50 ppm AP 273	1.15	74.5	20,319	2.62	50%
10	100 ppm AP 273	1.33	77.9	18,450	2.46	58%
11	200 ppm AP 273	1.81	72.9	12,689	2.26	62%

Table 6.1

Pipe Flow Measurements - Experimental Details

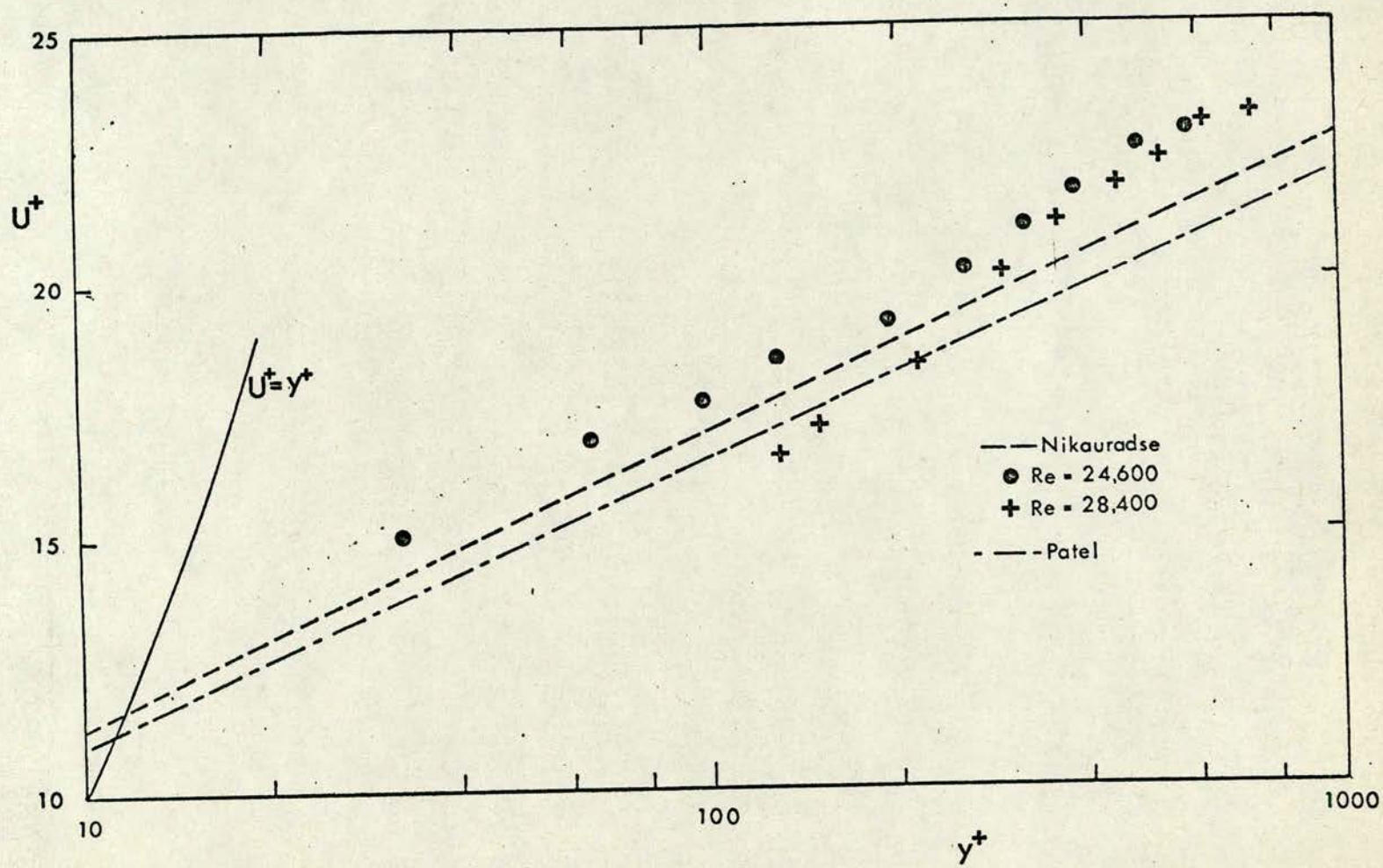

Figure 6.2

Newtonian Mean Velocity Profiles Compared with Curves of Nikuradse and Patel

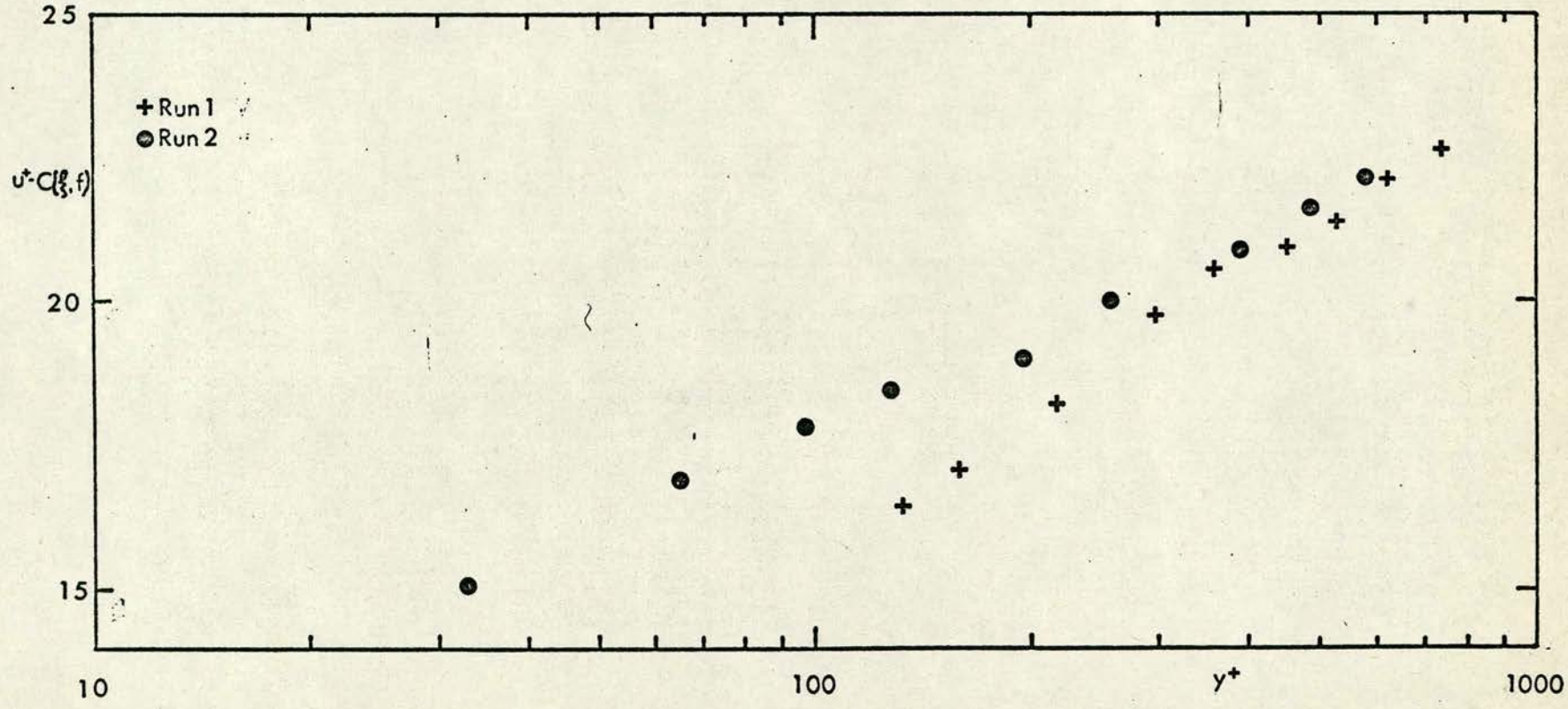

Figure 6.3

"Corrected" Newtonian Mean Velocity Profiles

estimates of these parameters (especially spectra) are subject to considerable uncertainty very close to the pipe wall. For this reason only spectra at relative positions greater than 0.2 from the wall are presented. Pressure drop measurements were made between the first and last pressure tapping to obtain values for the wall shear stress τ_w and the friction velocity u_τ.

6.2 SUMMARY OF EXPERIMENTAL RESULTS

Before considering the change in flow structure as a result of polymer addition, the results from Runs 1 and 2 for water flow were compared with the work of others. Mean velocity profiles are plotted (as u^+ versus $\log y^+$) for Runs 1 and 2 and compared with the semi-logarithmic profiles of Nikuradse (1933) and Patel (1965) in Figure 6.2. Agreement with Nikuradse's lines is fairly good although most of our data points lie slightly above the straight line. (Three of our measurements are thought to be incorrect due to an experimental error in determining tape calibration factors for the digitised velocity records. The points affected are those for the three lowest values of y^+ from Run 2.) Omitting the suspect points, a least squares fitting procedure was used to find the best values for A and B in the following equation

$$u^+ = A \log y^+ + B$$

Values of 6.26 and 5.35 were found for A and B respectively which are comparable with those of Nikuradse which were 5.75 and 5.5 for A and B respectively. The profiles are also plotted (Figure 6.3) after the Bogue "correction factor" had been applied, a procedure described in Chapter 2. Values of 5.48 and 6.76 were found for A and B from the corrected data which compare well with 5.57 and 5.57 estimated by Bogue. In addition, a least squares fitting was used to find the best

value for B with A fixed at Bogue's value of 5.57 and the best value for B was found to be 6.46. A check was made to test whether applying the Bogue correction significantly improved the linearity of the profiles on the semi-logarithmic plot. The average mean squared deviation of the data points from the best straight line was computed for both the corrected and uncorrected plots. It was found that the correction process reduced the average mean squared deviation by 43% showing that the correction process led to a better fit to the data.

Profiles of turbulent intensity, made dimensionless using friction velocity, are compared with the data of Laufer (1954) (Re = 50,000) and an average curve of Lawn (1971) (Re = 38,000 - 250,000) in Figure 6.4. The agreement between our results and the others is good despite the relatively low Reynolds numbers attained, our data points generally lying between those of Laufer and Lawn.

Local dissipation rate, ε, was calculated as a function of ξ by identifying the inertial sub-range of the energy spectrum at each radial position. The procedure adopted was similar to that used by Lawn and is discussed in detail in Appendix 2. Appendix 2 also contains estimates of the accuracy of the measurements of ε and estimates of the extent of the inertial sub-range for both water and polymer flow. Dissipation rate profiles, made dimensionless by defining $\varepsilon^* = \varepsilon R/u_\tau^3$, are plotted in Figure 6.5 and are compared with Lawn's results for a Reynolds number of 90,000. Given the large difference in Reynolds numbers, the agreement between our results and those of Lawn is very good, giving support to Lawn's assertion that ε^* is Reynolds number invariant for Newtonian turbulent pipe flow.

The spectra were transformed to Kolmogoroff co-ordinates and the accuracy of the normalising procedure was tested by comparing

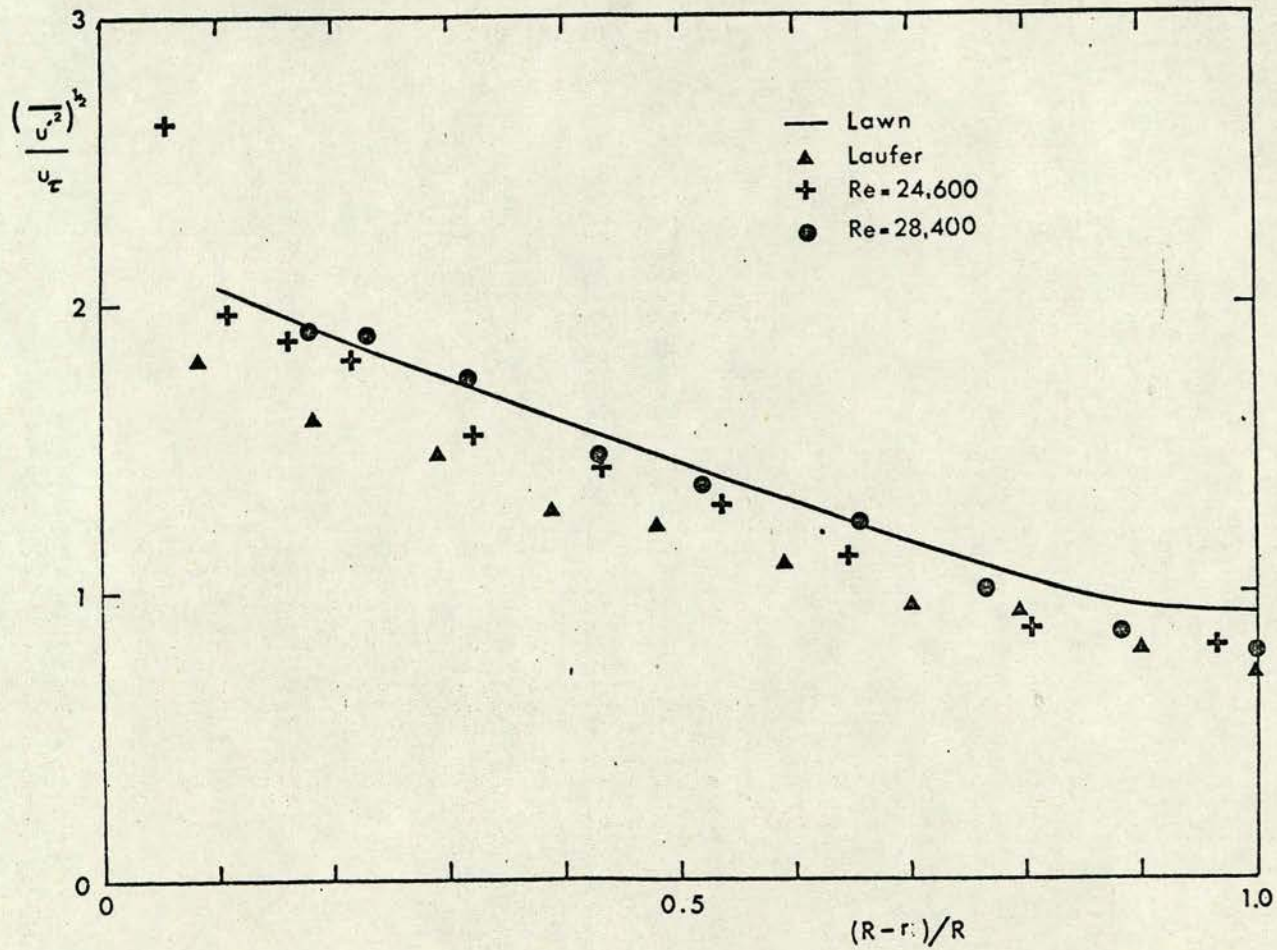

Figure 6.4

Newtonian Turbulent Intensity Profiles compared with Curves of Lawn and Laufer

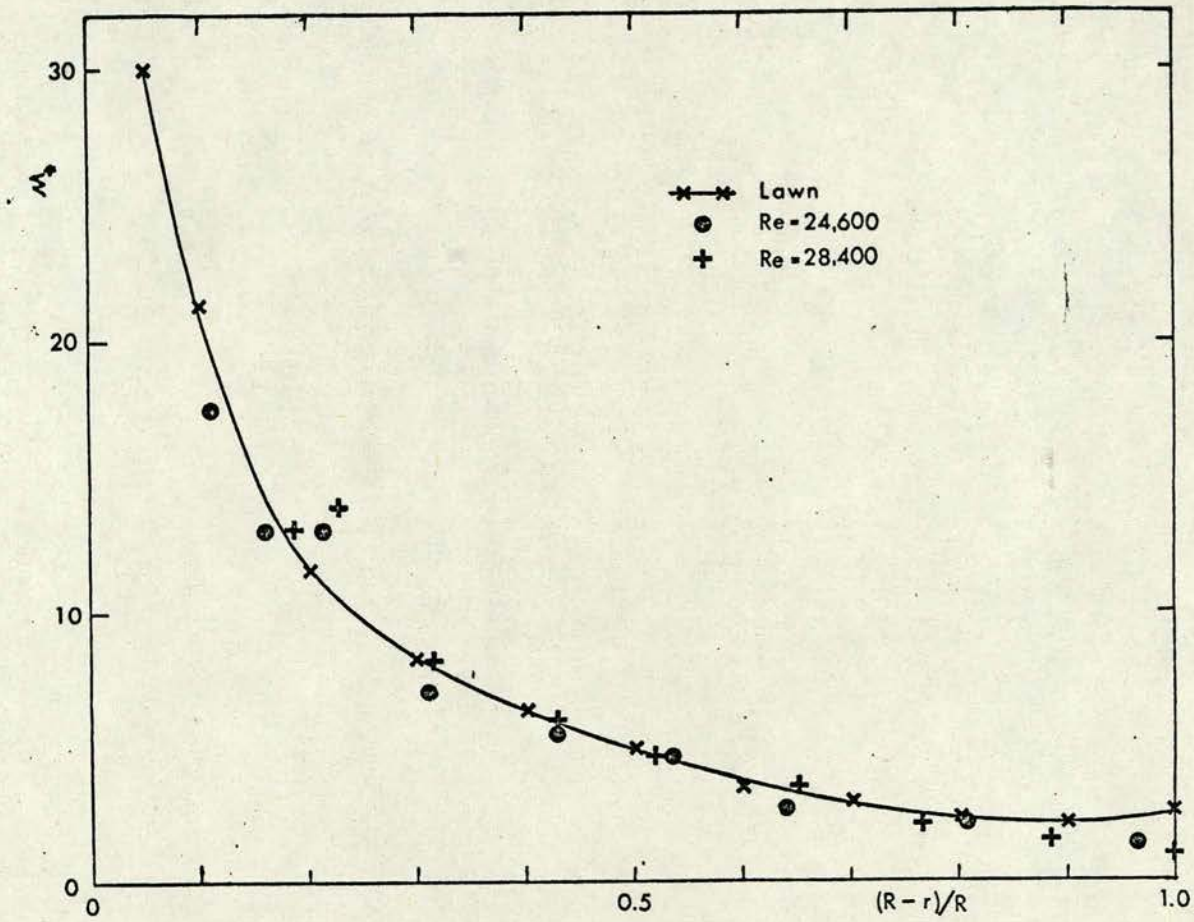

Figure 6.5

Dimensionless Dissipation Rates for Newtonian Flow compared with Curve of Lawn

spectra at the same pipe position but with different Reynolds numbers and also by comparing spectra at different positions in the pipe at the same Reynolds number. Figures 6.6 (a) - (c) show the spectra from Runs 1 and 2 at three pipe positions (ξ = 0.1, 0.43, 1 respectively). At all three pipe positions the agreement between the curves is very good at high wavenumbers although in the low wavenumber region before the start of the inertial sub-range there is slightly more energy in the spectra measured in the higher Reynolds number flow. Figure 6.7 shows a comparison of two spectra from Run 2 (Re = 24,600) near the centreline (ξ = 0.86) and towards the pipe edge (ξ = 0.21) with the theoretical spectrum of Pao (1965). The measured spectra are the same only for a limited range of wavenumbers ($0.06 < \tilde{k} < 0.15$) and within this range both curves lie above Pao's curve although the deviation is within the uncertainty in the spectral ordinates at a 90% confidence level. Outside this range of wavenumbers the two spectra are markedly different. As noted in Chapter 3, the ambiguity level varies with pipe position and is highest near the pipe edges (ie. where there is a large mean velocity gradient and a high level of turbulence) and lowest along the pipe centreline so that ambiguity affects the two spectra shown by different amounts. Although the difference is normally reduced when normalised spectra are compared it is clearly evident in Figure 6.7 and explains the departure of the spectra from Pao's curve at higher wavenumbers. As noted in Chapter 5, the ambiguity essentially reduces the range of wavenumbers in which the spectrum can be accurately measured. For the pipe flow measurements this range was generally less than for Grid flow measurements, the upper limit of dimensionless wavenumber being $\tilde{k} \approx 0.1 - 0.5$ depending on the measurement position.

On the basis of the evidence so far presented it was concluded

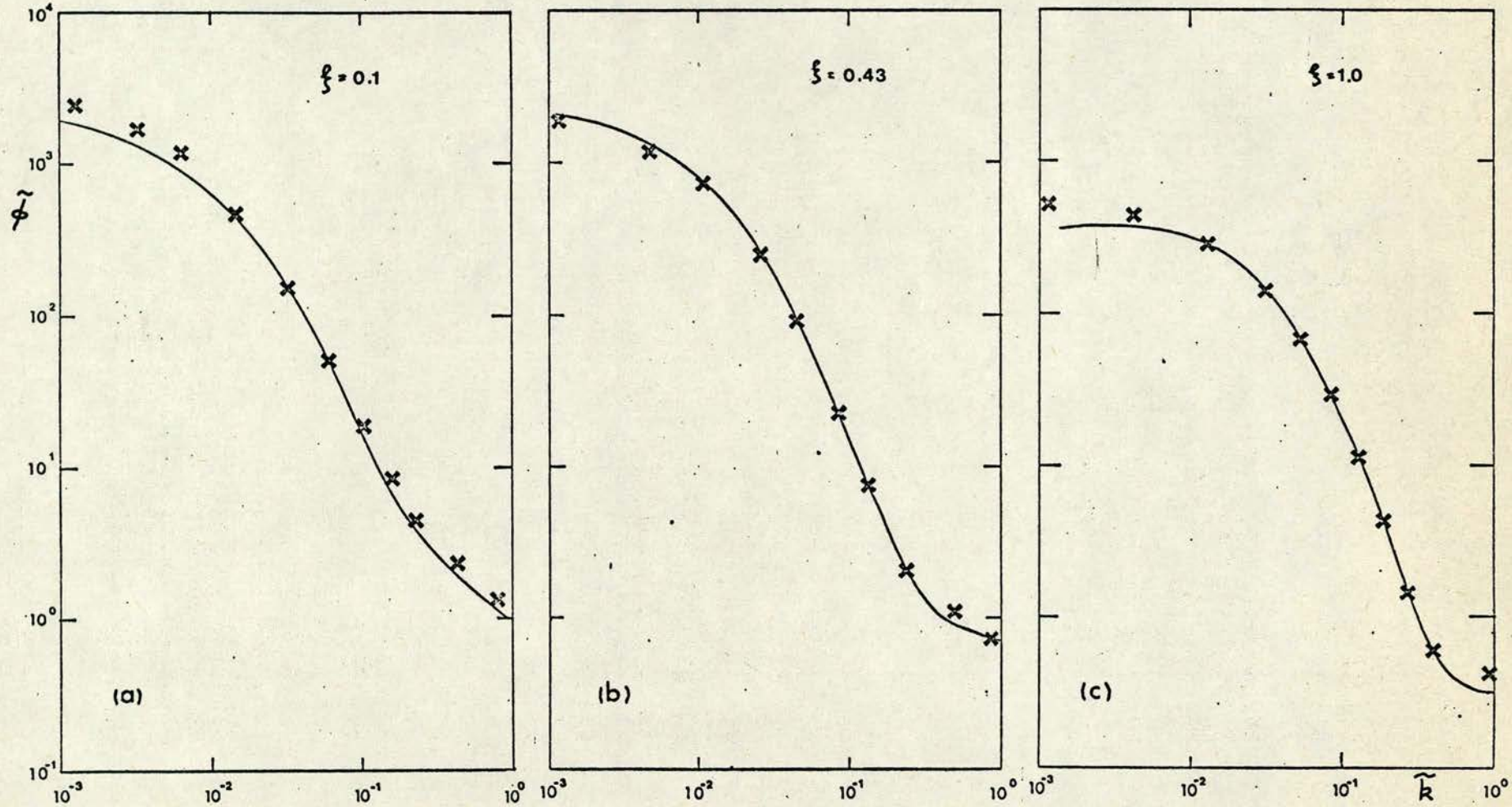

Figure 6.6

Dimensionless Energy Spectra for Newtonian Flow at Three Pipe Positions for Re = 24,600 (solid line) and Re = 28,600 (crosses)

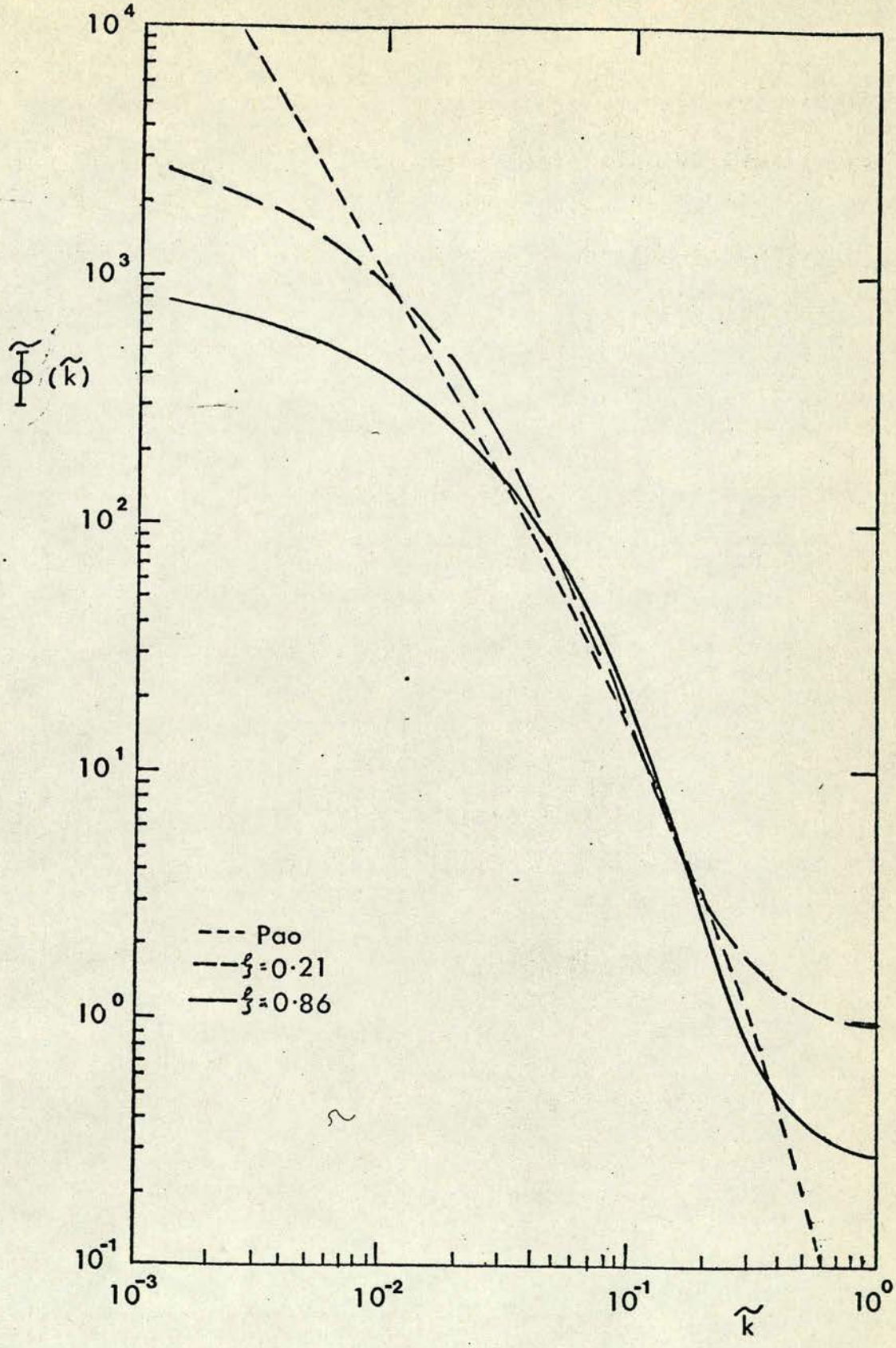

Figure 6.7

Newtonian Spectra for Re = 24,600 at Two Pipe Positions compared with Pao

that the results obtained in water flow were representative of fully developed Newtonian turbulent pipe flow.

From the experiments in Grid flow described in Chapter 5, it was concluded that a concentration of between 100 and 250 ppm of Polyox WSR 301 is necessary to show significant non-Newtonian effects in the energy spectrum and it was natural to study similar concentrations in pipe flow turbulence although this range of concentrations is perhaps an order of magnitude higher than would have been chosen for an investigation of the gross flow properties of the polymer in drag reduction. Preliminary study of the results from the Polyox experiments indicated significant effects at much lower concentrations than anticipated and it was decided to lower the range of concentrations studied in Separan to a range more typically found in studies of drag reduction. Although all of the measurements in Polyox were completed before the Separan solutions were studied, the main properties measured in both polymers will be described together to avoid unnecessary duplication in the comparisons with the same Newtonian data.

In discussions of turbulent drag reduction, two definitions of drag reduction are commonly used. For comparisons between Newtonian and drag reducing flows at the same volume flow rate the following definition is used

$$\text{Drag Reduction} = \left(\frac{\Delta P_{\text{solvent}} - \Delta P_{\text{polymer}}}{\Delta P_{\text{solvent}}}\right)_{\text{Constant Flow Rate, V}}$$

where ΔP is the pressure drop per unit distance along the pipe. Where comparisons are made at the same wall shear stress, τ_w, the second definition is used, viz.

$$\text{Drag Reduction} = \left(\frac{V_{\text{polymer}} - V_{\text{solvent}}}{V_{\text{solvent}}}\right)_{\substack{\text{Constant Wall Shear} \\ \text{Stress, } \tau_w}}$$

In all cases except Run 4, comparisons here were made at the same nominal volume flow rate although in practice there was some (± 5%) variation in the volume flow rate from run to run caused mainly by the inaccurate performance of the constant flow valve in polymer solutions. Drag reduction calculations were made using wall shear stress values which had been adjusted to the equivalent values for the flow rate of water in Run 2. The assumption used to do this was that

$$\tau_w^* = \tau_w\left(\frac{\bar{V}_{water}}{\bar{V}_{polymer}}\right)$$

where τ_w^* is the adjusted wall shear stress. This assumption was based on the behaviour of the 50 ppm solution of Polyox with increased flow rate. Values of 7.00 and 7.10 were found for V/τ_w for Runs 3 and 4 showing the above equation to be correct (at least for 50 ppm Polyox WSR 301) over a much broader range of flow variation than the range in which the correction was applied. The drag reduction for each experiment is shown in Table 6.1. Although the Separan polymer shows increased drag reduction with increasing concentration three of the Polyox concentrations (100, 250 and 500 ppm) show approximately the same level of drag reduction indicating that the concentration saturation point had been reached.

Reischmann and Tiederman (1975) suggested that drag reduction should be defined at constant Reynolds number rather than at constant volume flow rate. For typical drag reducing concentrations of highly effective drag reducers the difference in definitions is unimportant as the solution kinematic viscosity is close to that of the solvent alone. For many of the solutions studied here, however, the difference is significant. It is well known that Reynolds number similarity does not apply to the flow of drag reducing solutions (eg. the "diameter"

effect) and that the Reynolds number is of less importance than for Newtonian flow. Neither definition is completely satisfactory given that drag reduction varies with flow rate and the approach adopted here is to make comparisons at the same volume flow rates, it being thought that the practising engineer is more likely to be interested in the actual reduction in frictional losses when polymer is added to the flow than to know the change in the viscosity of the resultant solution. Similar arguments have led to the now common practice (eg. Hoyt (1972)) of displaying gross flow properties in Prandtl-Karman co-ordinates based on solvent viscosity even for relatively high solution viscosities.

Mean velocity profiles on linear-linear plots are shown in Figures 6.8 and 6.9 as a function of ξ for Polyox and Separan respectively and compared with results from water at the same nominal flow rate (Run 2). Compared to water, there is a general trend in Polyox for the mean velocity (made dimensionless by dividing by the bulk flow velocity) to be lower towards the pipe edge ($\xi \lesssim 0.25$) and to be higher towards the centreline ($\xi \gtrsim 0.35$). The same trend is even more apparent in the Separan profiles where the curves become sharper as the concentration is increased. The 200 ppm Separan solution has a much steeper profile than all others although the measured drag reduction is only slightly higher than for 100 ppm.

Velocity Defect profiles are shown in Figures 6.10 (Polyox) and 6.11 (Separan) and compared with the Newtonian results from Run 2. The defect is greater in Polyox for $\xi < 0.3$ than for water at all polymer concentrations although there is no clear trend with increasing concentration. The velocity defect curves for Separan show an increasing departure from the Newtonian values as ξ is reduced and as concentration or drag reduction is increased. The point where the curves first

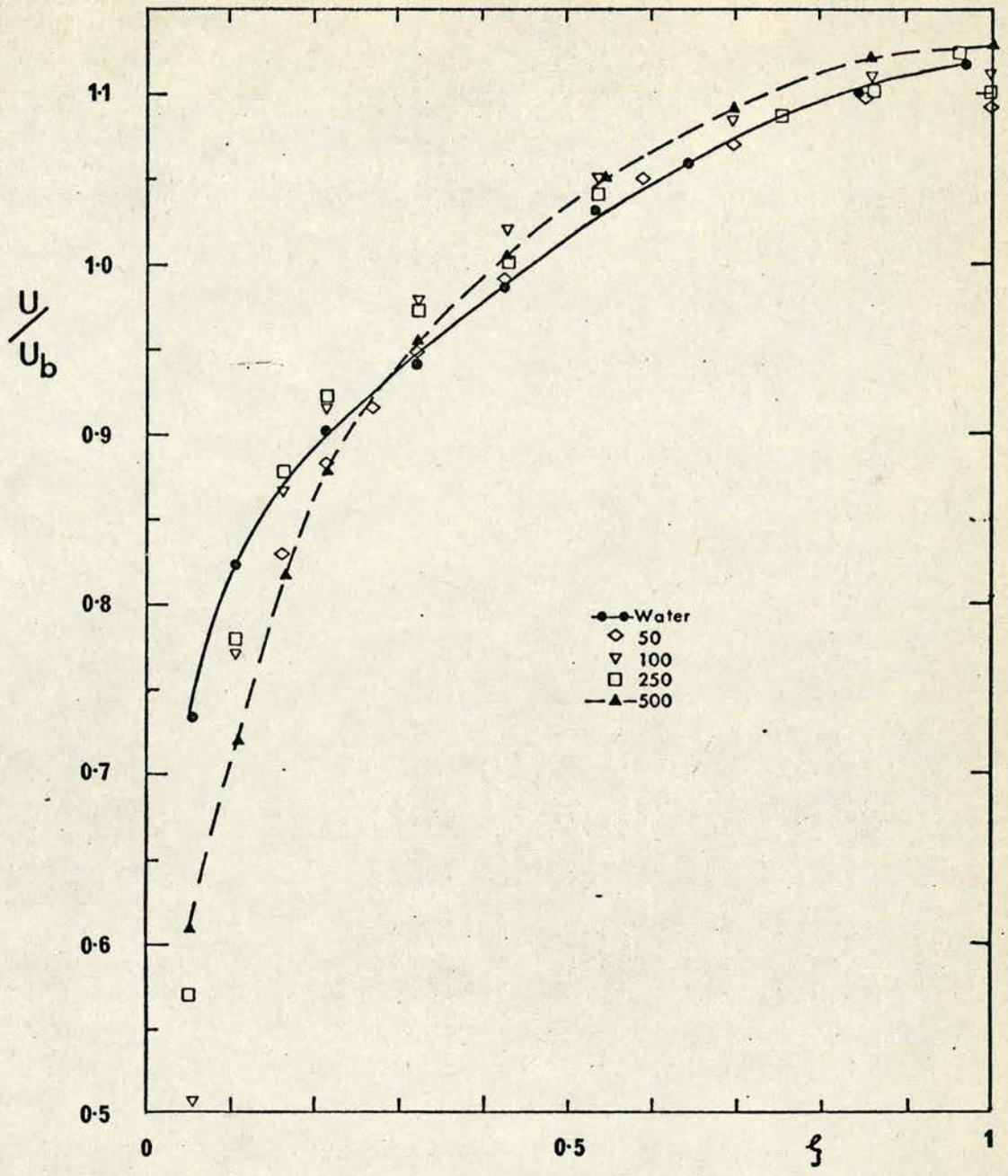

Figure 6.8

Dimensionless Mean Velocity Profiles
for Water and Polyox Solutions

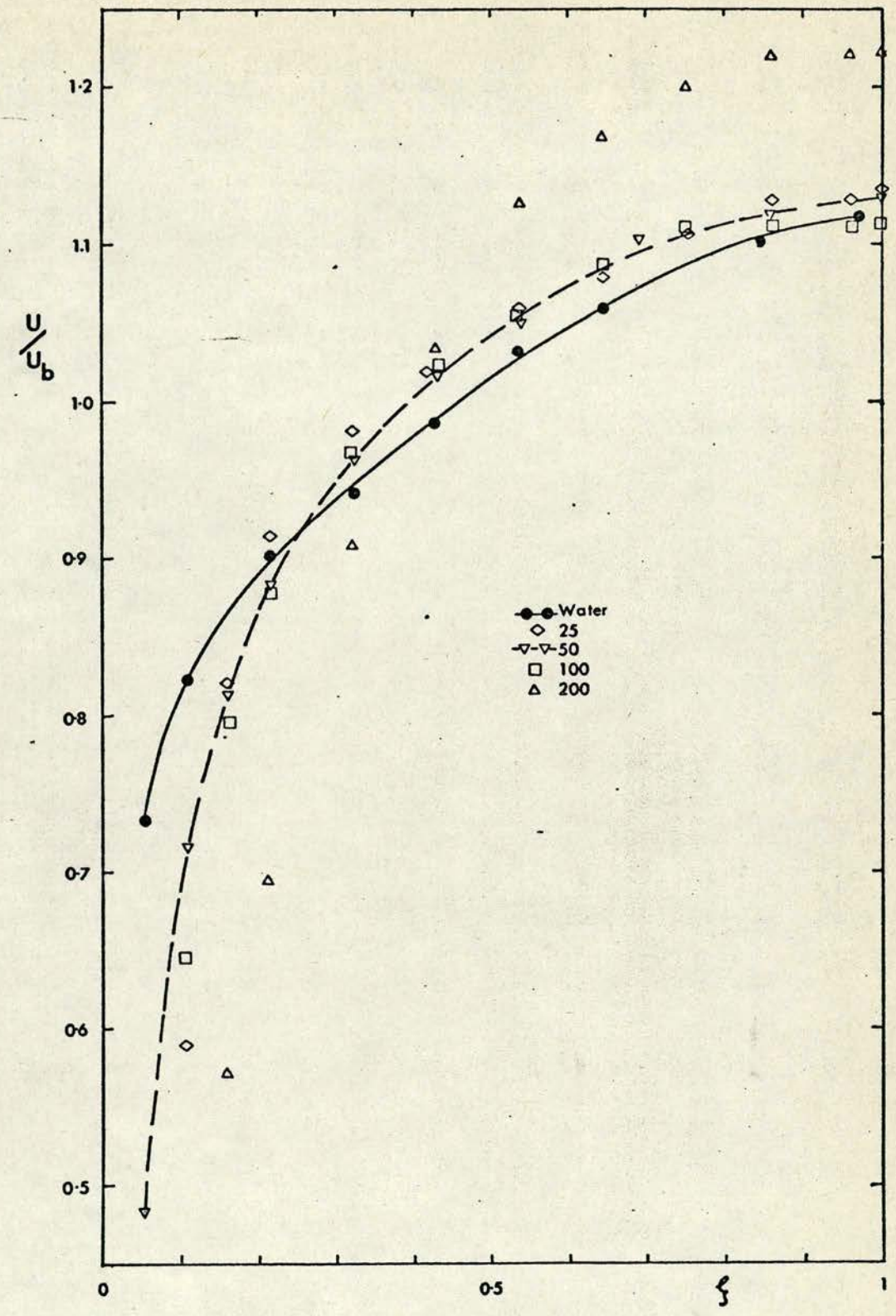

Figure 6.9

Dimensionless Mean Velocity Profiles
for Water and Separan Solutions

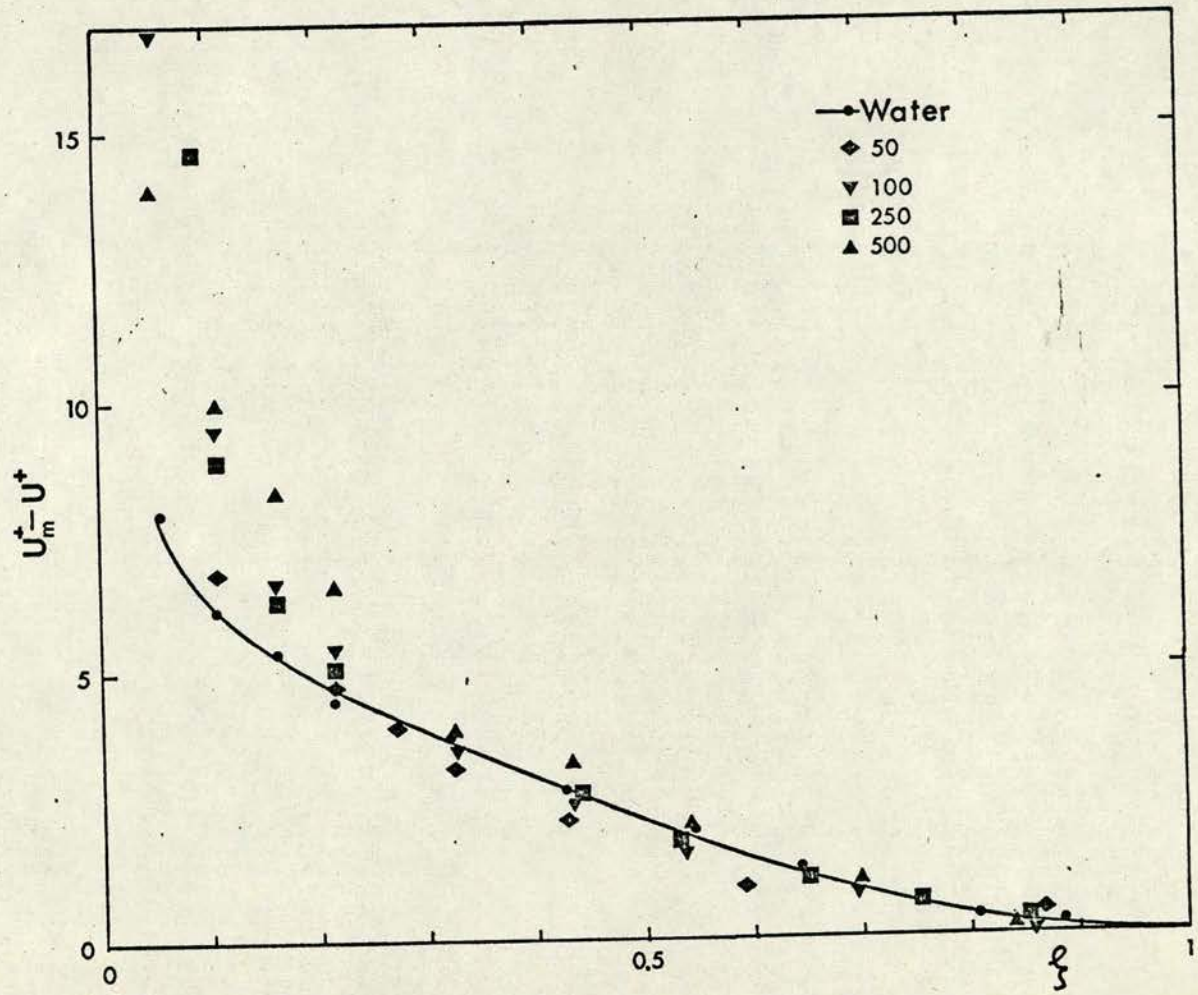

Figure 6.10

Velocity Defect Plots for Water and Polyox

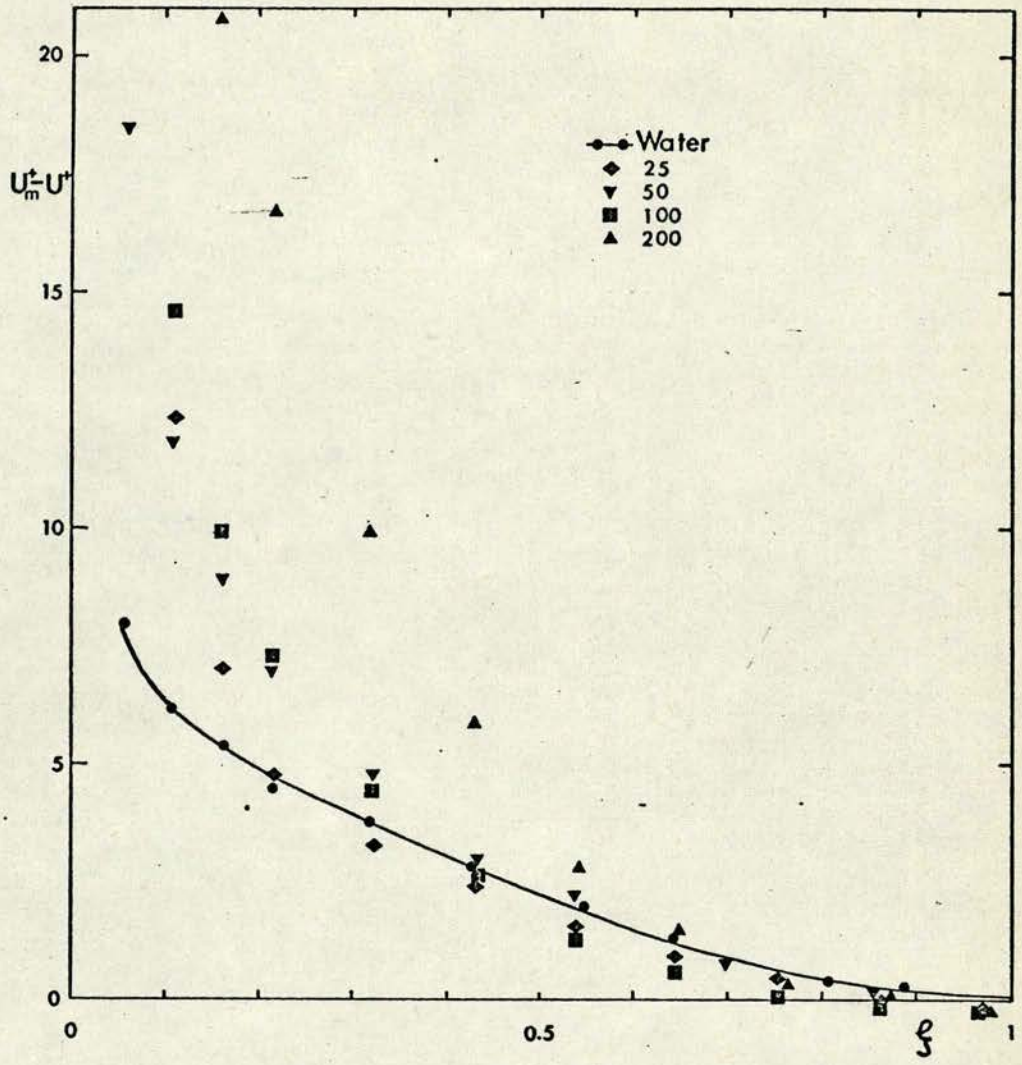

Figure 6.11

Velocity Defect Plots for Water and Separan

deviate from the Newtonian curve occurs further from the wall as the concentration increases.

Profiles of u^+ versus log y^+ are plotted in Figures 6.12 (Polyox) and 6.13 (Separan). Qualitatively, at the same nominal flow rates, the profiles for Polyox show higher values of u^+ for a given y^+ compared to water and the data points for three concentrations (viz. 100, 250 and 500 ppm) are clustered together. The 50 ppm data points lie generally between the results for water and the other polymer concentrations and the points from Run 4 (50 ppm Polyox at the same wall shear stress as water) are further from the water curve than the measured values from Run 3. The Separan profiles show an increased departure from the Newtonian values with increasing polymer concentration. Though both polymers show signs of a displaced Newtonian turbulent core region it is clear that Virk's ultimate profile is not followed in the intermediate region. The Bogue correction process for Newtonian flow was applied to the data (with the polymer value of friction factor) and the "corrected" profiles are plotted in Figures 6.14 and 6.15. The "corrected" profiles show the same qualitative trends as the uncorrected data.

The mean velocity data was analysed quantitatively using the three layer velocity profile model of Van Driest (1970). Defining the intermediate (elastic) layer and the turbulent core region respectively by the following two equations

$$u^+ = C \log y^+ + D \qquad \text{intermediate layer}$$

$$u^+ = A \log y^+ + B \qquad \text{turbulent core}$$

the extent of the elastic sub-layer was estimated graphically for each polymer concentration and least squared fitting was used to find values for A, B, C and D. The values found from the uncorrected data are

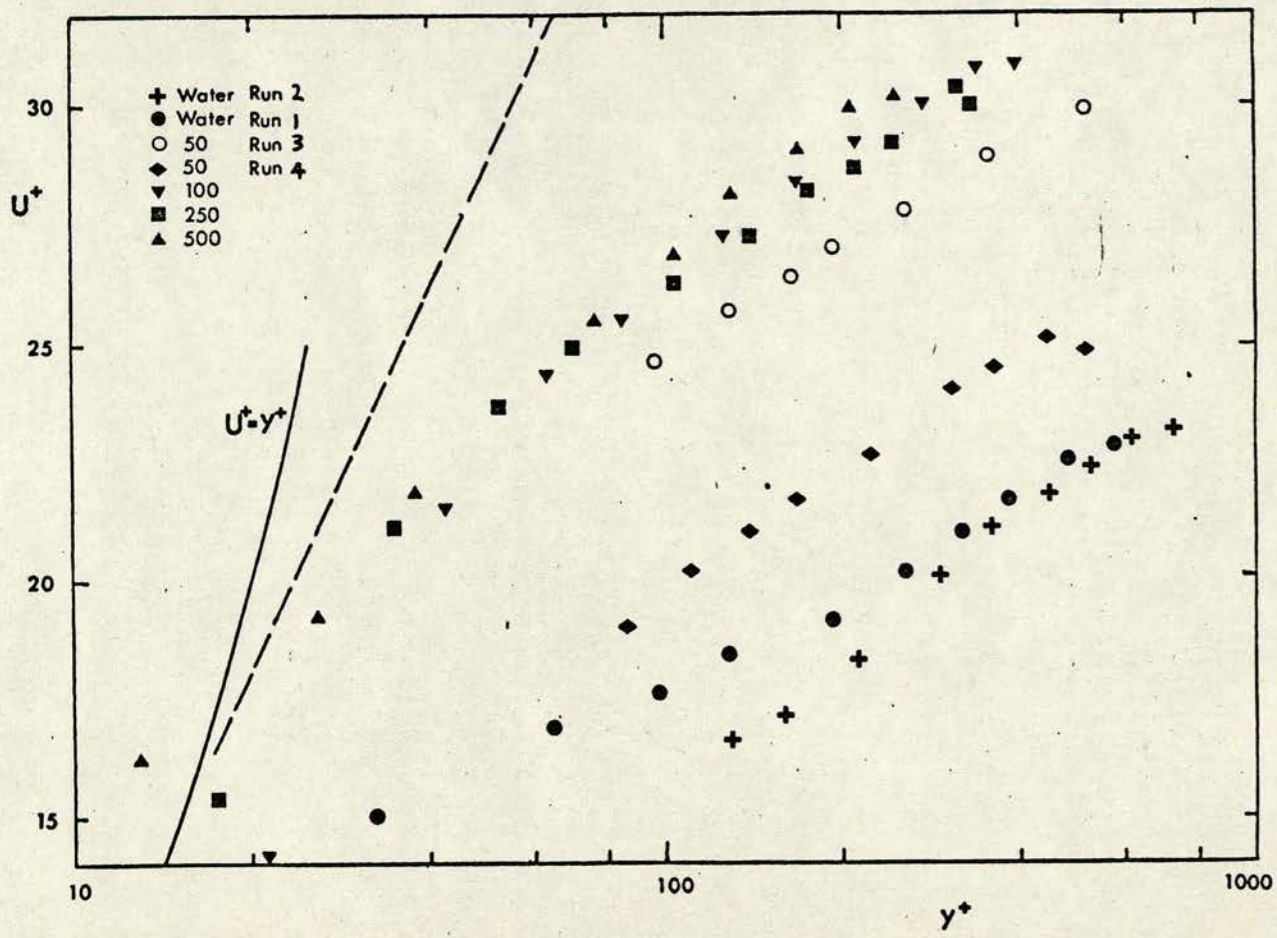

Figure 6.12

Profiles of u^+ versus log y^+ for Water and Polyox Solutions

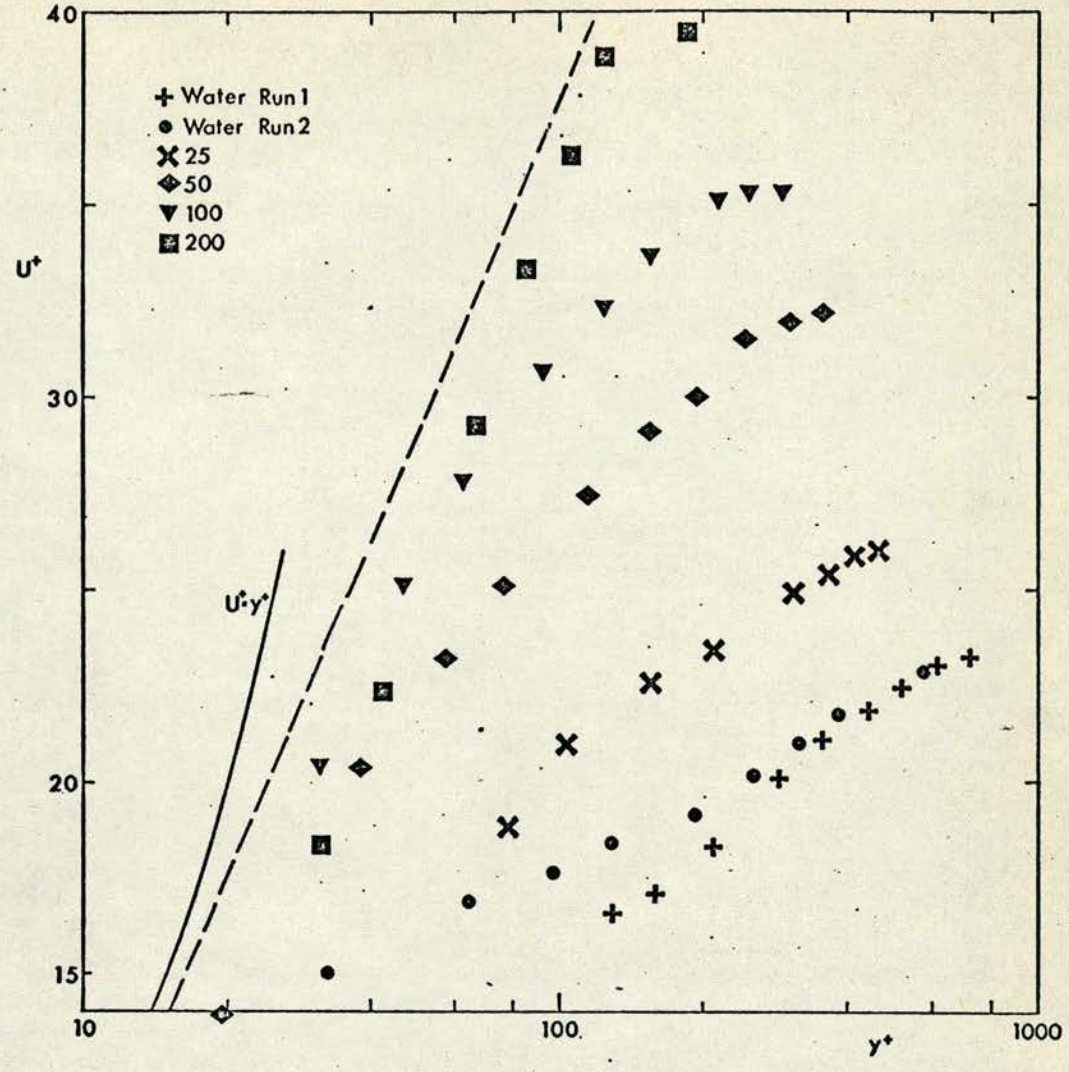

Figure 6.13

Profiles of u^+ versus log y^+ for Water and Separan Solutions

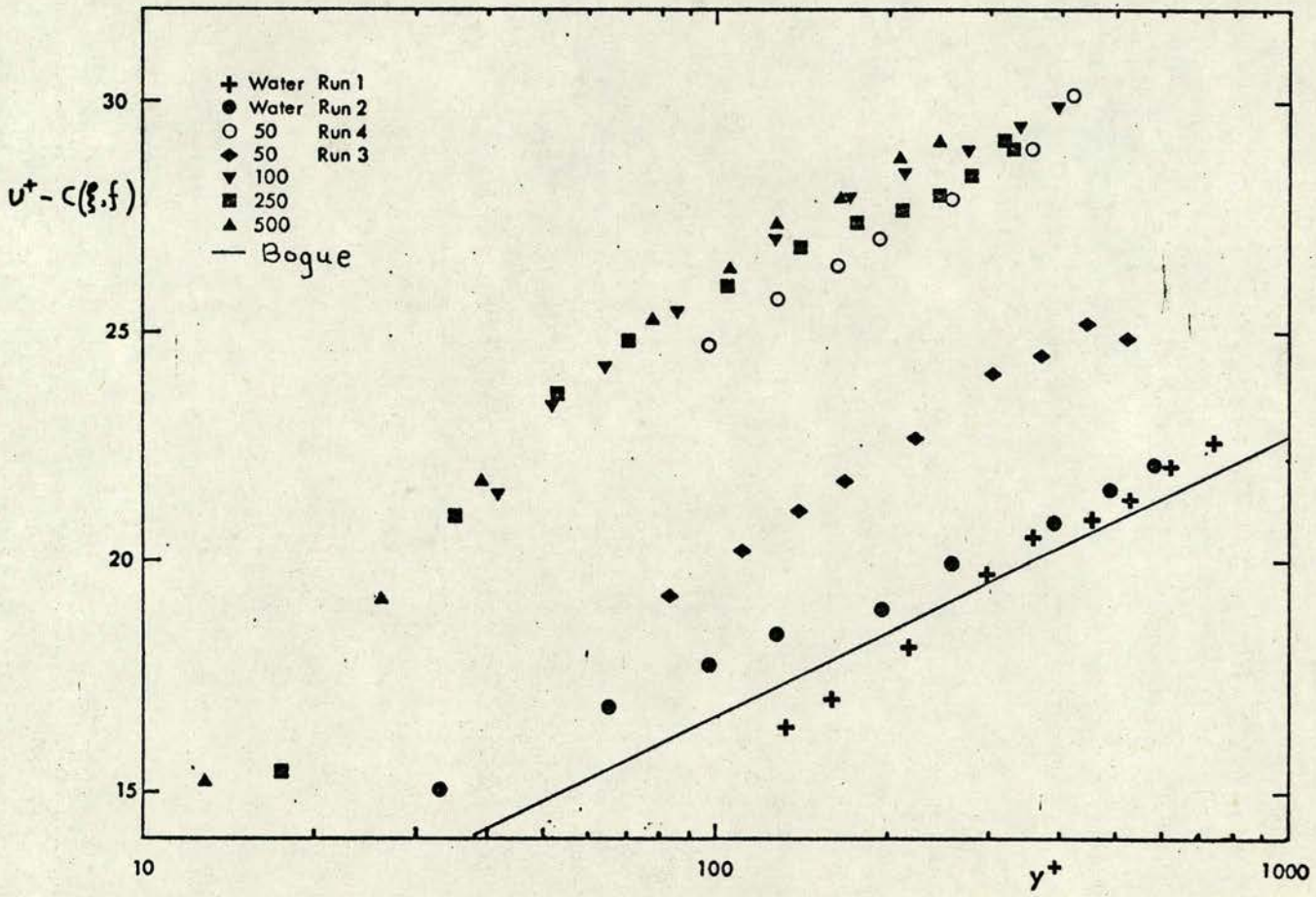

Figure 6.14

"Corrected" Profiles for Water and Polyox Solutions

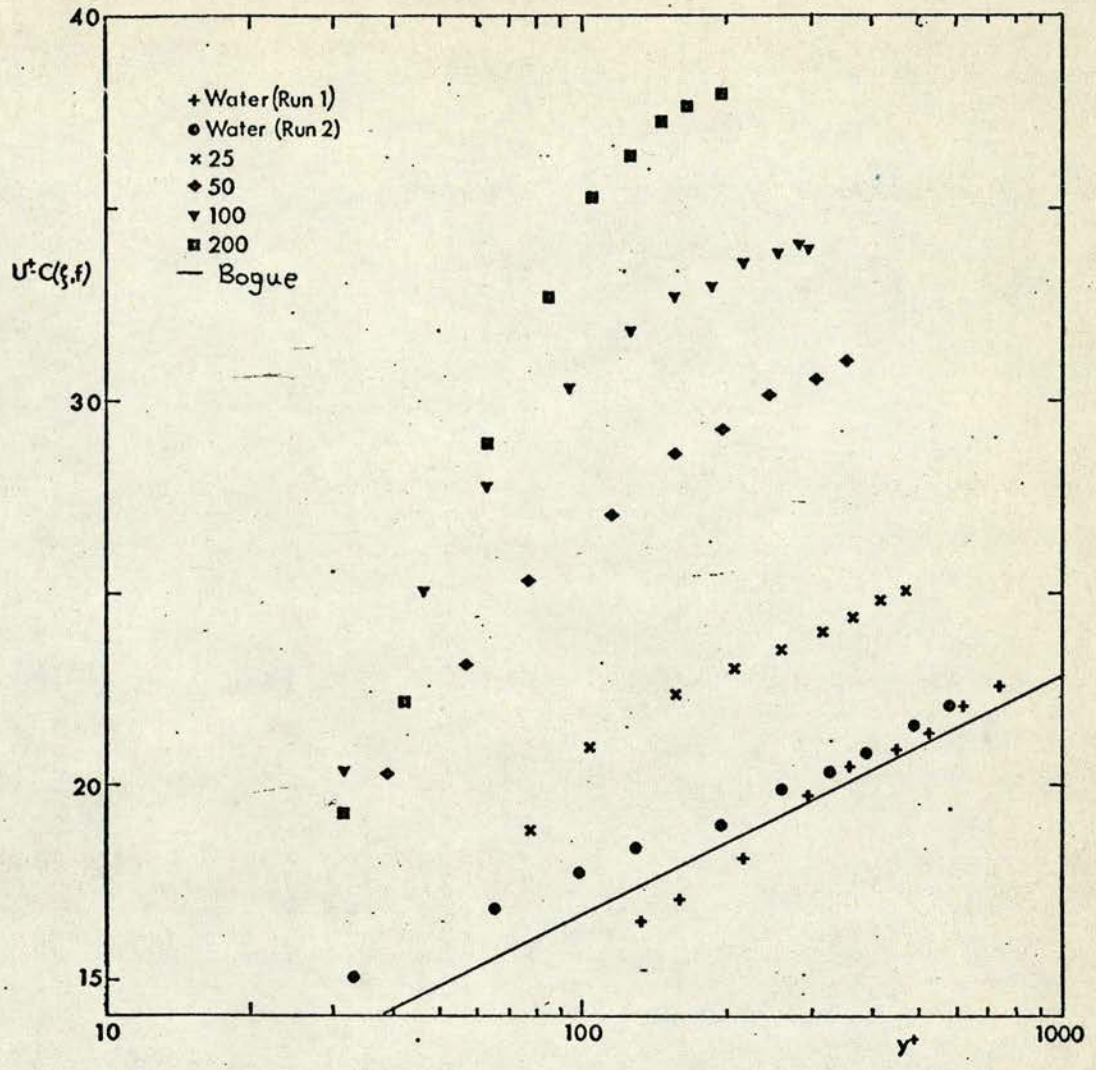

Figure 6.15

"Corrected" Profiles for Water and Separan Solutions

listed in Tables 6.2 (Polyox) and 6.3 (Separan). From the uncorrected data fits, little can be added to the remarks already made. Identifying the two regions is difficult, especially for the Polyox data, and including an extra point in the fitting process can lead to a significant change in the gradient of the best fitting line. It is clear that for Polyox, A is increased slightly at all concentrations compared to water and that B increases with increasing concentration up to 100 ppm. The values of B for higher Polyox concentrations are all approximately the same. C is also higher for the concentrations of 100-500 ppm than for 50 ppm. For Separan it can be seen that A is increased compared to water for only three of the four concentrations used and that B increases with increasing concentration.

With the "corrected" data it is easier to separate the two flow regions and the best fits are improved compared to the uncorrected data. The trends evident in Tables 6.4 and 6.5 for "corrected" data are similar to those for the uncorrected data. These can be summarised by saying that with increasing concentration B and C increase, with A showing some scatter about a constant value which is slightly higher than A for water.

Since A varied only slightly with concentration, another fit to the data was found with A fixed at the Newtonian value of 6.26. This procedure was repeated for "corrected" data with A set at 5.57 and the values for B found in both cases are tabulated in Tables 6.6 and 6.7 for Polyox and Separan respectively. The values of B found from the uncorrected data were compared with the correlation suggested by Arunachalam et al (1972) which was .

$$B = 5.75 \left[\frac{u_{\tau_{solvent}}}{u_{\tau_{polymer}}} \right]^{-3}$$ Constant flow rate

Concentration (ppm)	Intermediate Region				Core Region			
	Range of y^+		"Best Fit" Values		Range of y^+		"Best Fit" Values	
	y^+_{min}	y^+_{max}	C	D	y^+_{min}	y^+_{max}	A	B
50	83.1	190	8.9	2.0	222	517	6.3	8.1
100	42	85	13.7	- 5.3	170	395	7.1	12.8
250	17.5	70	16.1	- 4.3	105	326	7.9	10.4
500	13.0	78	12.3	2.4	130	242	7.7	12.0

Table 6.2

Velocity Profile Model - Best Fit Parameters for Polyox (Uncorrected Data)

Concentration (ppm)	Intermediate Region				Core Region			
	Range of y^+		"Best Fit" Values		Range of y^+		"Best Fit" Values	
	y^+_{min}	y^+_{max}	C	D	y^+_{min}	y^+_{max}	A	B
25	78	155	12.1	- 3.7	155	483	7.3	6.7
50	38	153	14.5	- 2.4	222	517	6.35	8.1
100	31	94	21.5	- 11.1	125	291	7.62	16.8
200	21	106	33.3	- 31.1	126	197	6.73	23.9

Table 6.3

Velocity Profile Model - Best Fit Parameters for Separan (Uncorrected Data)

Concentration (ppm)	Intermediate Region				Core Region			
	Range of y^+		"Best Fit" Values		Range of y^+		"Best Fit" Values	
	y^+_{min}	y^+_{max}	C	D	y^+_{min}	y^+_{max}	A	B
50	83	167	8.3	3.1	222	517	5.0	10.7
100	42	85	13.4	- 0.17	127	395	5.6	15.3
250	17.5	70	15.9	- 4.0	105	326	6.1	13.7
500	13.0	78	11.9	2.7	130	242	6.9	12.8

Table 6.4

Velocity Profile Model - Best Fit Parameters for Polyox (Corrected Data)

Concentration (ppm)	Intermediate Region				Core Region			
	Range of y^+		"Best Fit" Values		Range of y^+		"Best Fit Values"	
	y^+_{min}	y^+_{max}	C	D	y^+_{min}	y^+_{max}	A	B
25	77.7	155	11.5	- 2.65	155	483	5.7	9.85
50	19.2	153	16.3	- 6.3	153	357	6.9	13.5
100	31.3	93.8	20.9	- 10.3	125	291	5.85	19.7
200	21.1	106	32.1	- 29.3	148	197	6.58	22.3

Table 6.5

Velocity Profile Model - Best Fit Parameters for Separan (Corrected Data)

Concentration (ppm)	"Corrected" Data (A = 5.57)	Uncorrected Data (A = 6.26)
	B	B
50	8.9	8.3
100	15.4	14.9
250	14.9	14.5
500	15.7	15.3

Table 6.6

Velocity Profile Model for Turbulent Core Region in Polyox with A fixed

Concentration (ppm)	"Corrected" Data (A = 5.57)	Uncorrected Data (A = 6.26)
	B	B
25	10.1	9.4
50	16.6	16.0
100	20.3	20.1
200	25.3	25.0

Table 6.7

Velocity Profile Model for Turbulent Core Region in Separan with A fixed

The agreement between measured and predicted values of B can be seen from Table 6.8 to be very good for both polymer types.

Profiles of turbulent intensity, made dimensionless using bulk flow velocity, are plotted in Figures 6.16 (Polyox) and 6.17 (Separan) as functions of ξ. With some scatter, the data for Polyox shows that the relative intensities are higher in Polyox for $\xi \leqslant 0.3$ compared to water. Elsewhere the intensities are similar to those for water. The same general trend is shown for Separan with the exception of the 200 ppm solution where the intensity levels were much less than for water at all measuring positions.

Curves of turbulent intensity, made dimensionless using friction velocity are shown in Figures 6.18 and 6.19 and are compared with Lawn's average curve for Newtonian flow. The dimensionless intensities have higher values in all solutions of Polyox and Separan compared to water with the exception of the 200 ppm solution of Separan. The polymer points deviate more from the Newtonian curve towards the wall although in the case of Polyox, there is no clear trend with increasing concentration. For the Separan solutions the 50 ppm and 100 ppm values lie above the values for 25 ppm. The 200 ppm solution of Separan has lower values than water at all positions measured.

Estimates of the local dissipation rates were obtained in the same way as for water flow. In general, the extent of the inertial sub-range in polymer flow spectra was reduced compared to water and the accuracy in determining ε was less than for water flow. It was not possible to find an inertial sub-range for the spectra measured in the 200 ppm solution of Separan and estimates of ε for this concentration could not be obtained. Details of the accuracy of the estimates of and the extent of the sub-range are contained in Appendix 2. Figures

Polyox

Concentration (ppm)	Measured Value of B	Predicted Value of B
50	8.3	8.5
100	14.9	14.8
250	14.5	14.2
500	15.3	14.8

Separan

Concentration (ppm)	Measured Value of B	Predicted Value of B
25	9.4	9.5
50	16.0	16.5
100	20.1	21.4
200	25.0	24.8

Table 6.8

Comparison of Measured Values for B with Values Predicted by Arunachalam et al (1972)

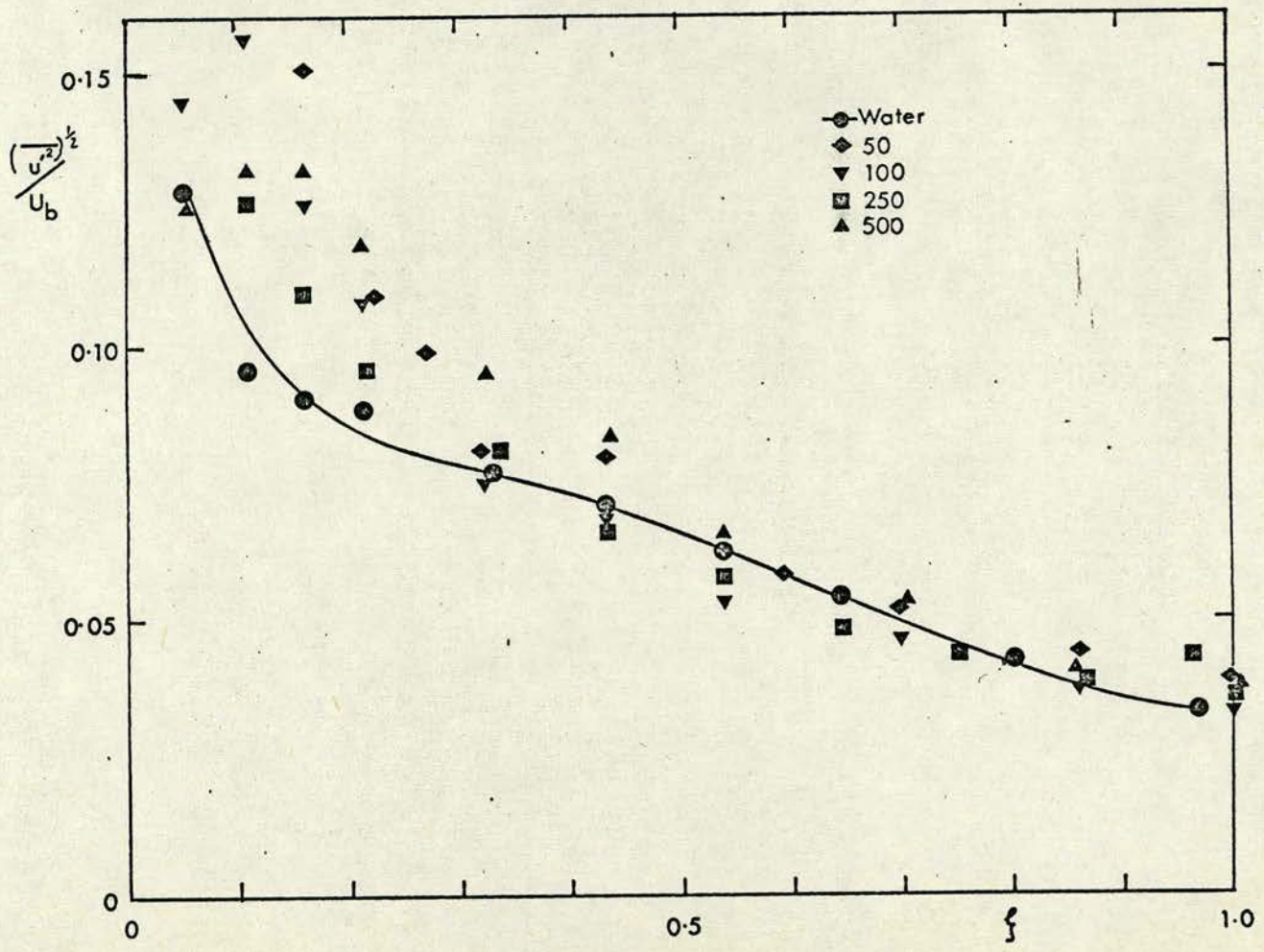

Figure 6.16

Profiles of $(\overline{u'^2})^{\frac{1}{2}}/U_b$ for Water and Polyox Solutions

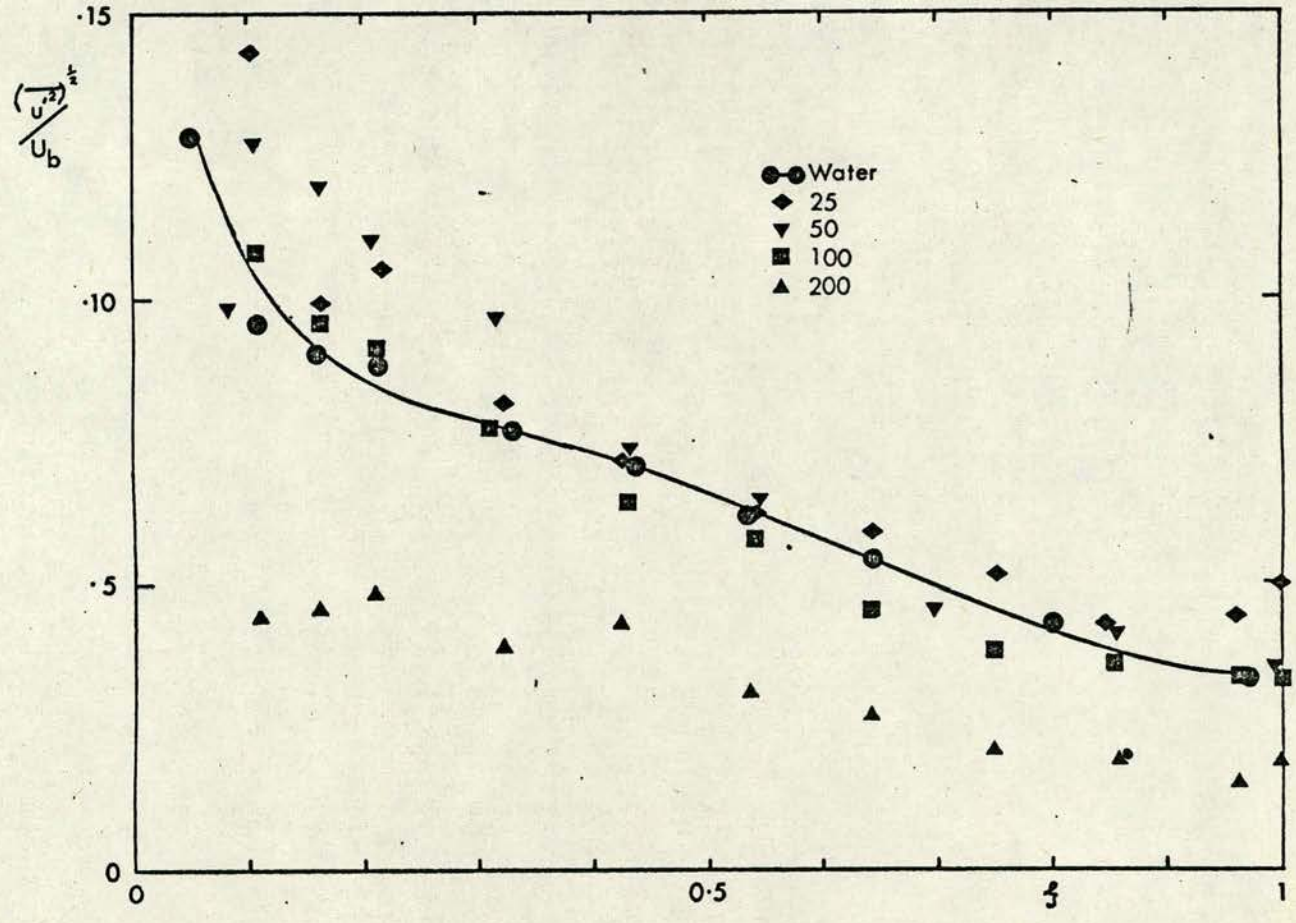

Figure 6.17

Profiles of $(\overline{u'^2})^{\frac{1}{2}}/U_b$ for Water and Separan Solutions

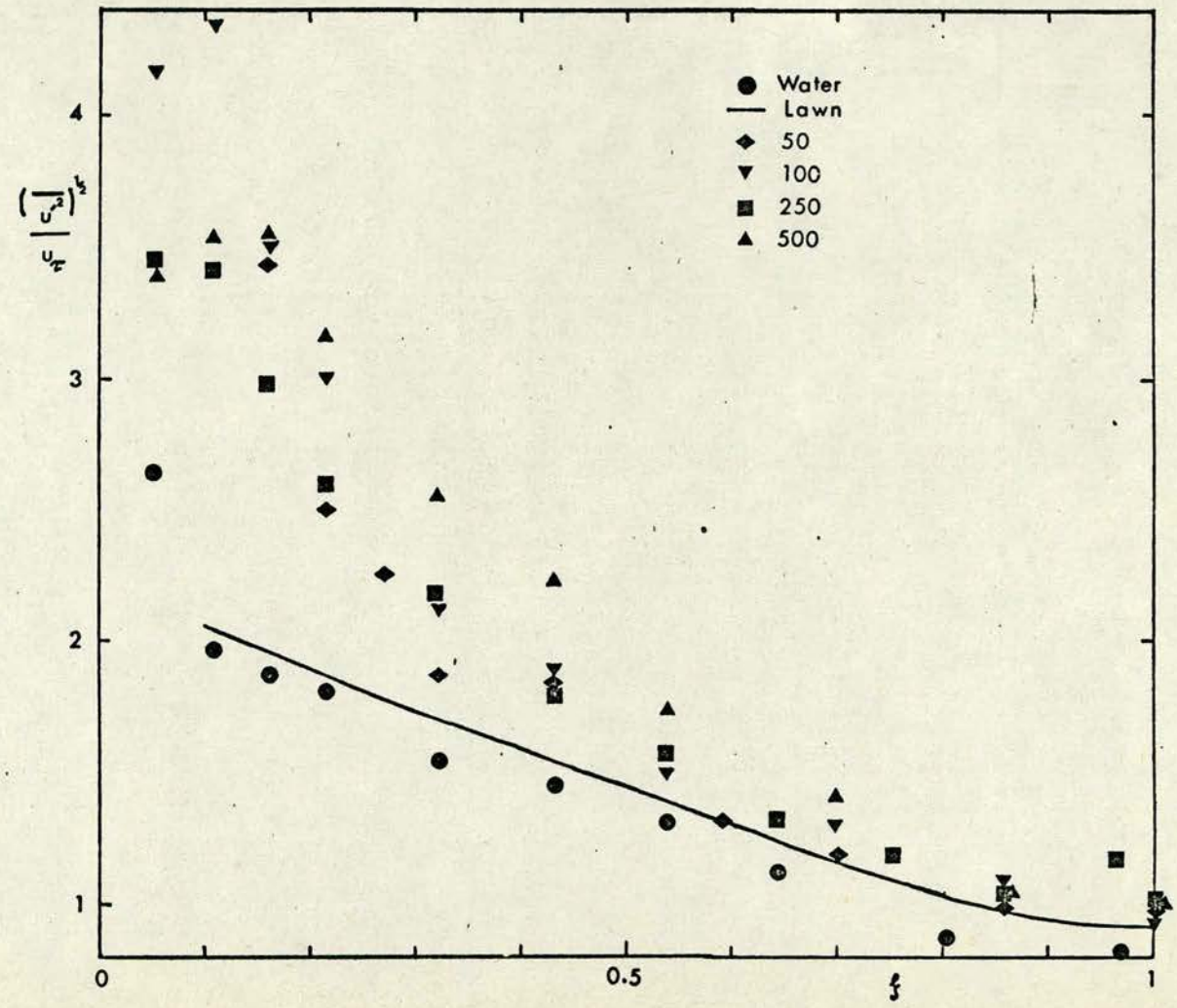

Figure 6.18

Profiles of $\overline{(u'^2)}^{\frac{1}{2}}/u_\tau$ for Water and Polyox Solutions compared with the Curve of Lawn

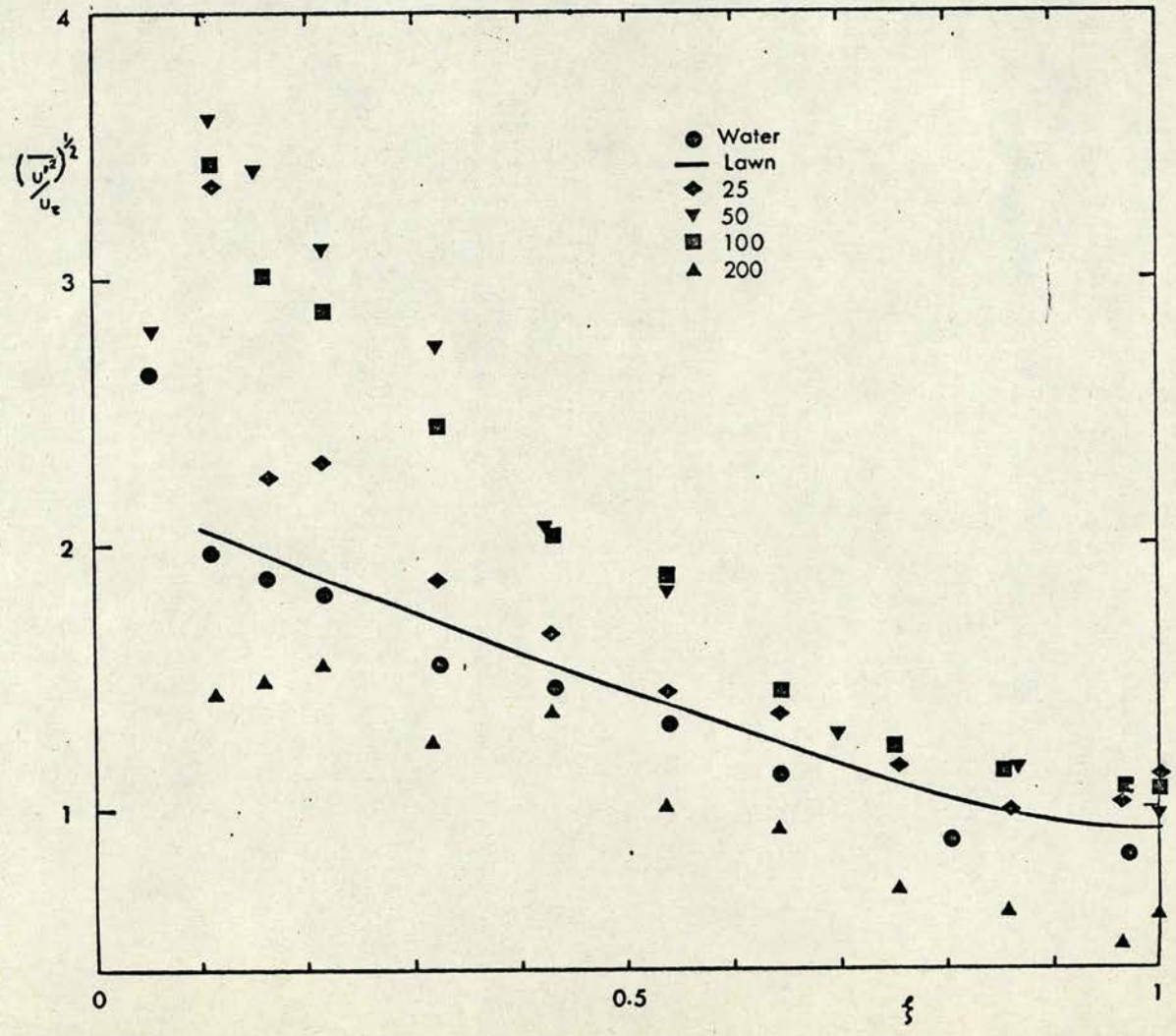

Figure 6.19

Profiles of $(u'^2)^{\frac{1}{2}}/u_\tau$ for Water and Separan Solutions compared with the curve of Lawn

6.20 and 6.21 show dissipation rate as a function of ξ for Polyox and Separan respectively. With only a few exceptions the dissipation rates were reduced in both polymers compared to water at the positions measured although there is a marked steepening of the polymer curves towards the edge for many of the concentrations and it may be that dissipation rates are in fact higher than for water at positions closer to the wall than could accurately be measured. ε^* is plotted in Figures 6.22 and 6.23 for Polyox and Separan and compared with Lawn's curve all concentrations of Polyox ε^* lies above Lawn's curve for $\xi \leq 0.5$ with ε^* being approximately the same for water and polymer nearer the pipe centreline. For Separan, profiles of ε^* lie below the water values for $\xi \geq 0.4$ and above the water curve nearer the wall.

Energy spectra were made dimensionless in two alternative ways using Kolmogoroff variables based on either the solvent or solution kinematic viscosity. Although the energy spectrum was computed at each measurement position, only four radial positions are presented for each polymer. Figures 6.24 (a), (b) to 6.27 (a), (b) show spectra for Polyox and water for ξ = 1, 0.86, 0.43 and 0.21 and Figures 6.28 (a), (b) to 6.31 (a), (b), show spectra for water and Separan at the same radial positions.

Since there is doubt as to the correct normalising procedure quantitative comparisons between the spectra are difficult to make. The spectra are therefore discussed qualitatively and, since the effect of using solution rather than solvent viscosity values is to reduce the differences between water and polymer spectra, the discussion will relate to the spectra which have been normalised using solution viscosity values.

Considering firstly the Polyox spectra, the 50 ppm solution has a spectrum which shows no significant deviation from the spectrum in

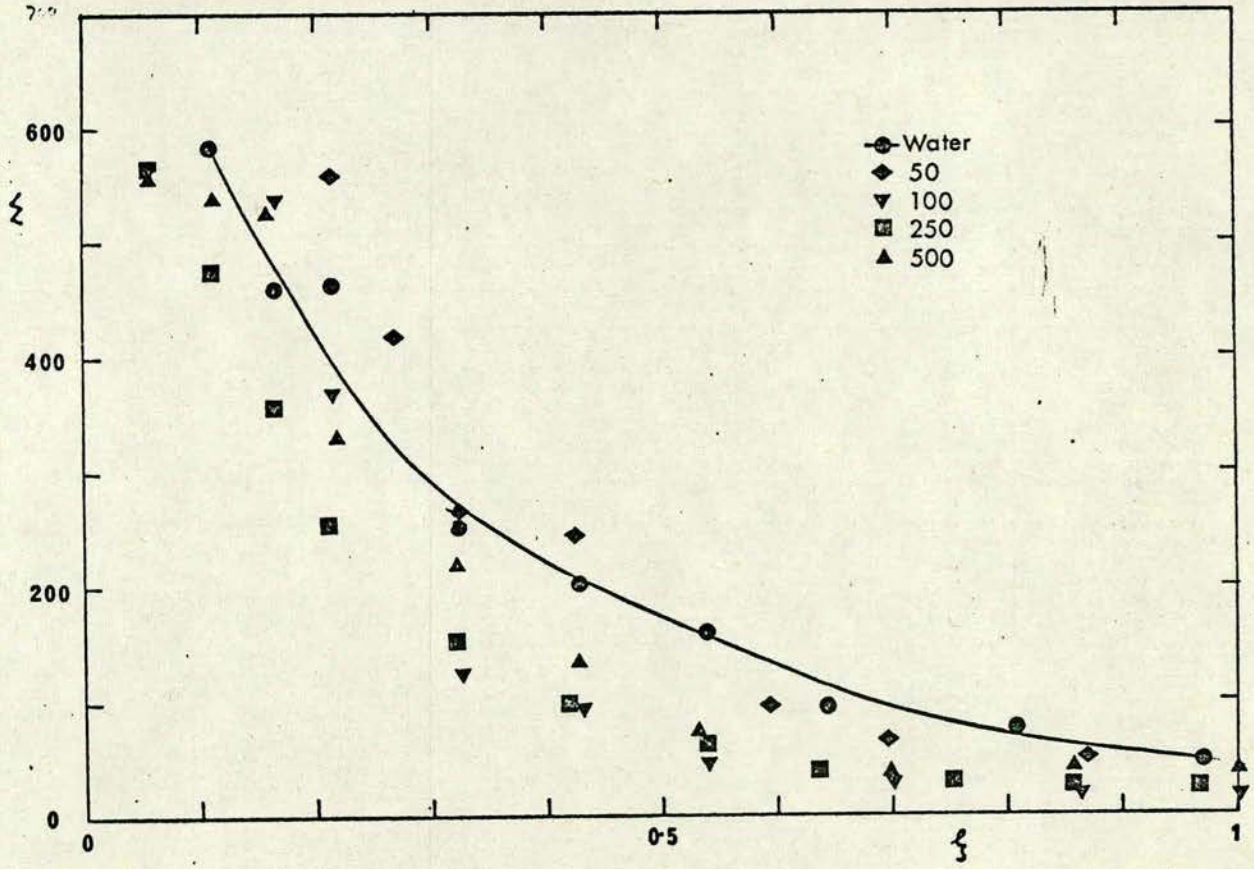

Figure 6.20

Profiles of Dissipation Rate for Water and Polyox Solutions

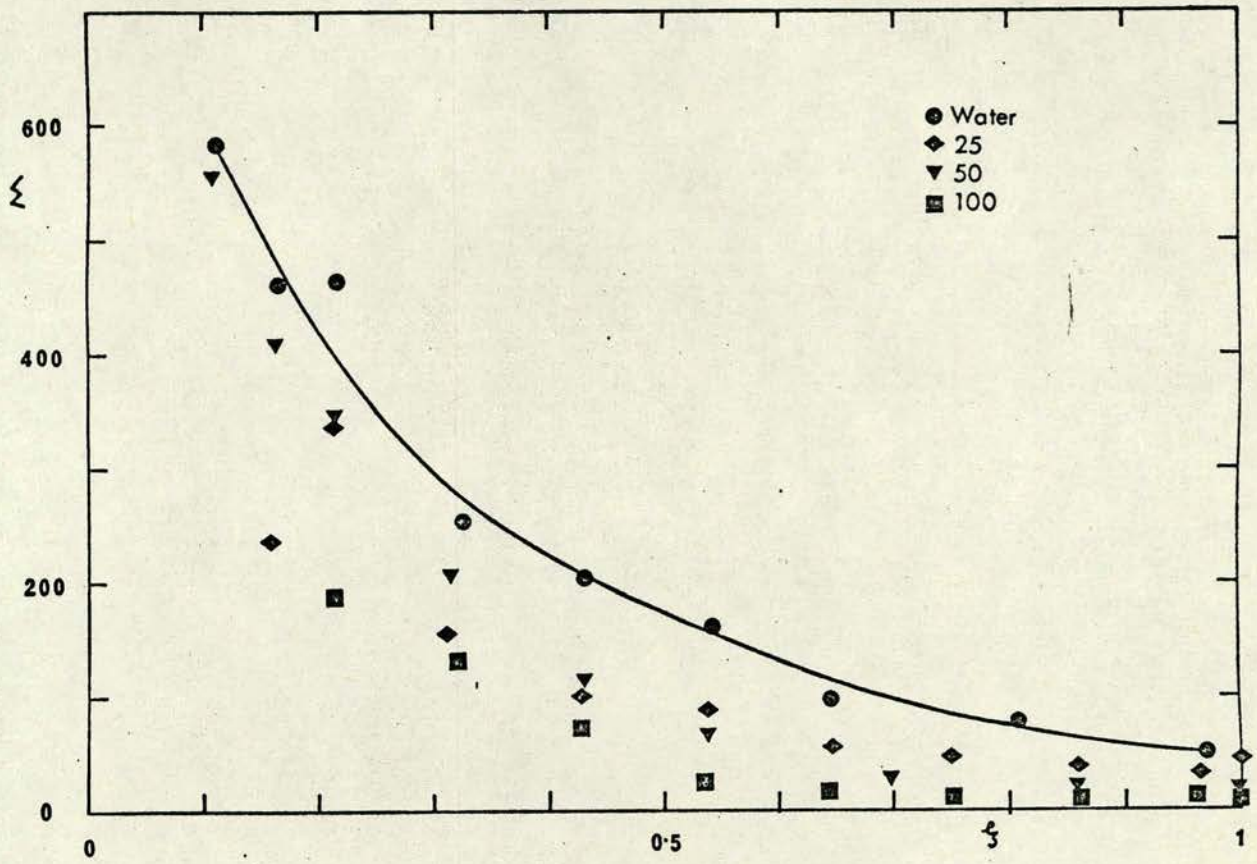

Figure 6.21

Profiles of Dissipation Rate for Water and Separan Solutions

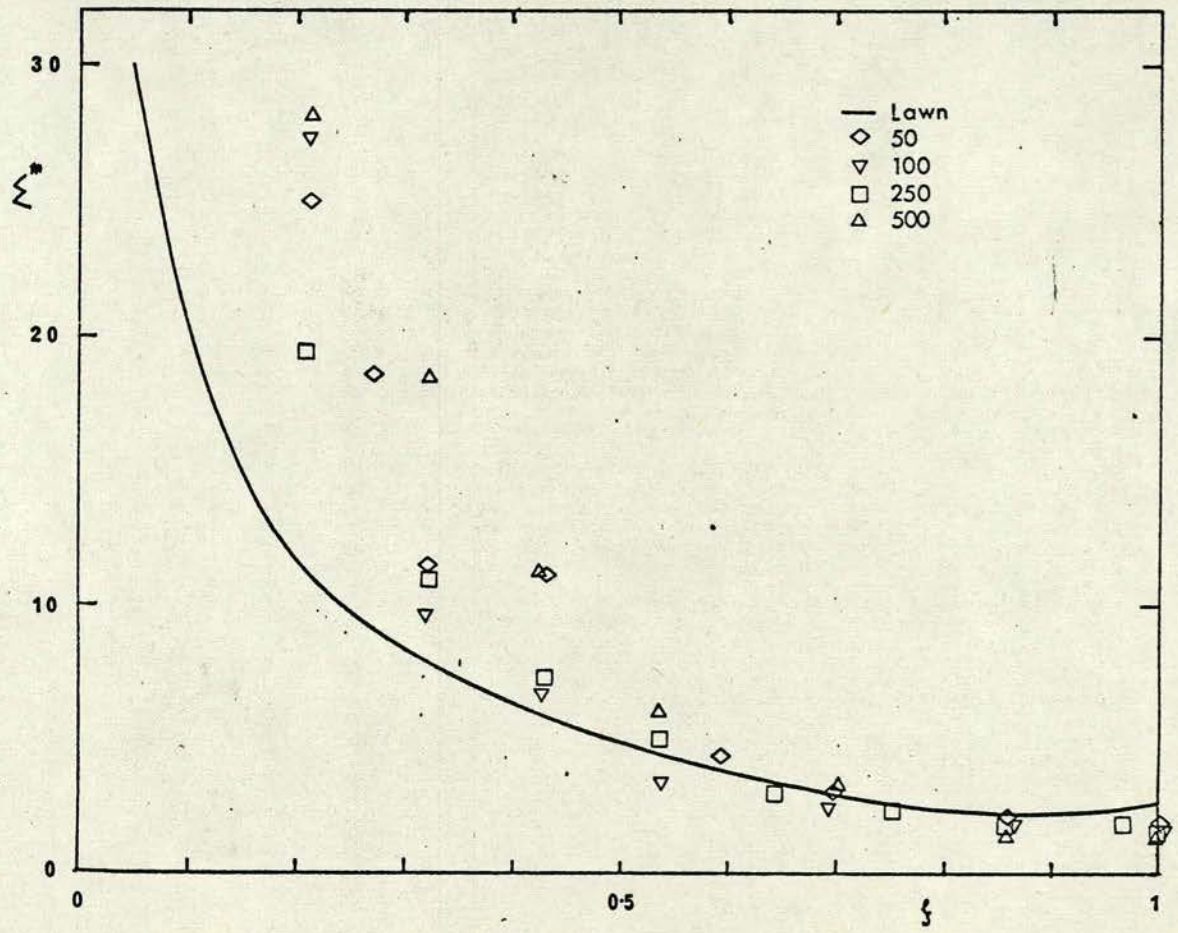

Figure 6.22

Profiles of Dimensionless Dissipation Rate for Polyox Solutions compared with the curve of Lawn

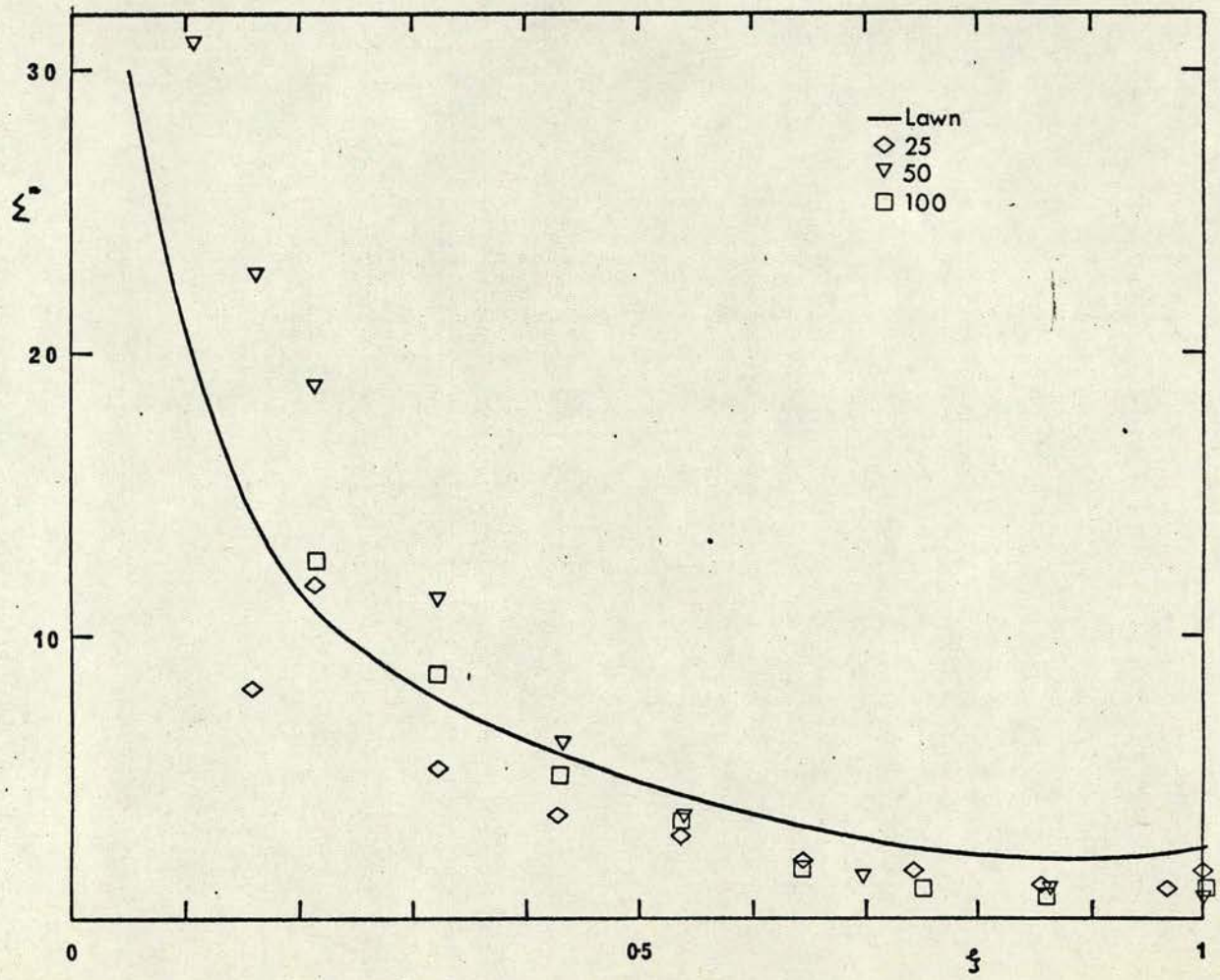

Figure 6.23

Profiles of Dimensionless Dissipation Rate for Separan Solutions compared with the curve of Lawn

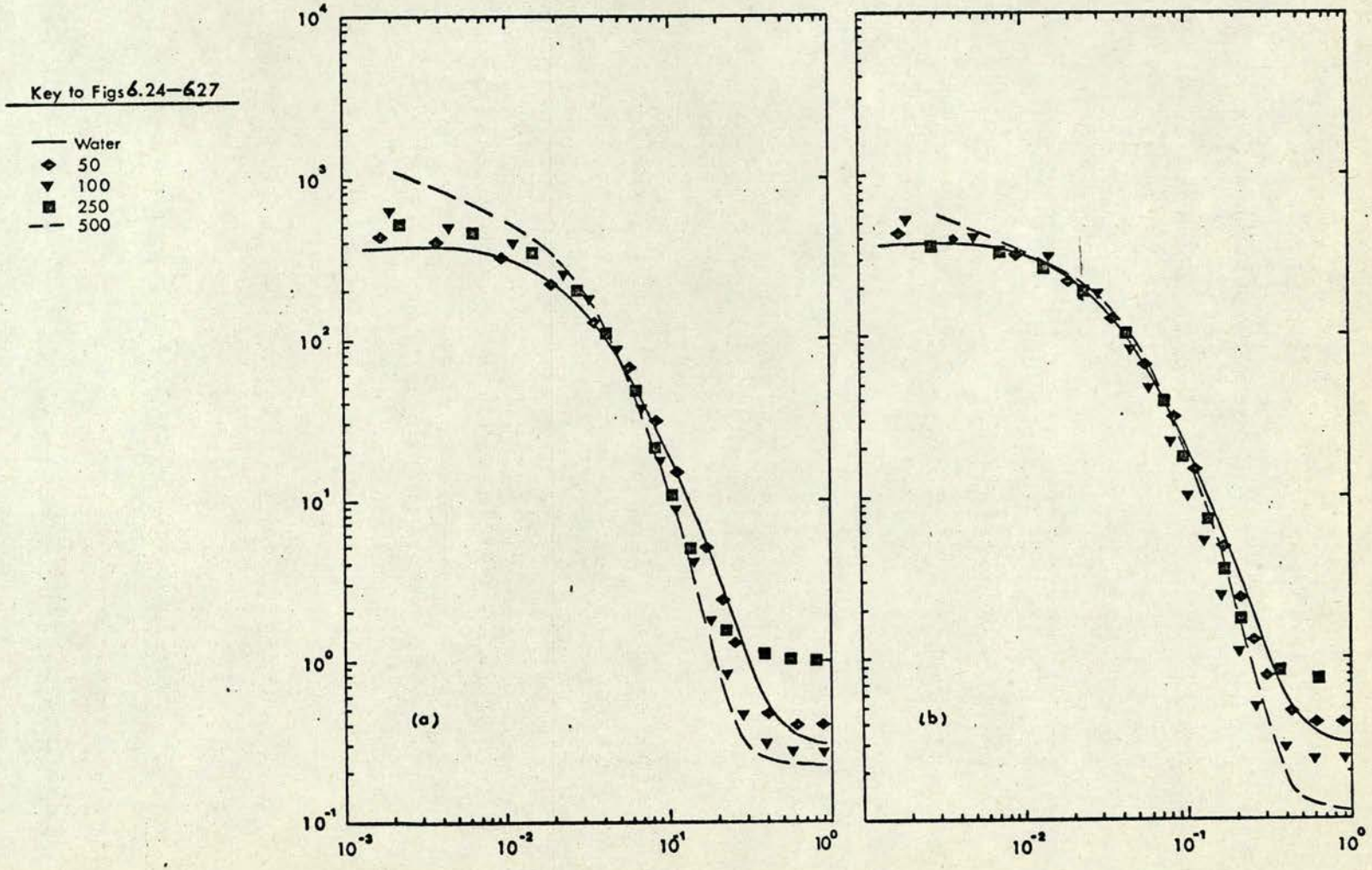

Figure 6.24

Energy Spectra for Water and Polyox Solutions at $\xi = 1$ made dimensionless, with (a) solvent kinematic viscosity and (b) solution kinematic viscosity

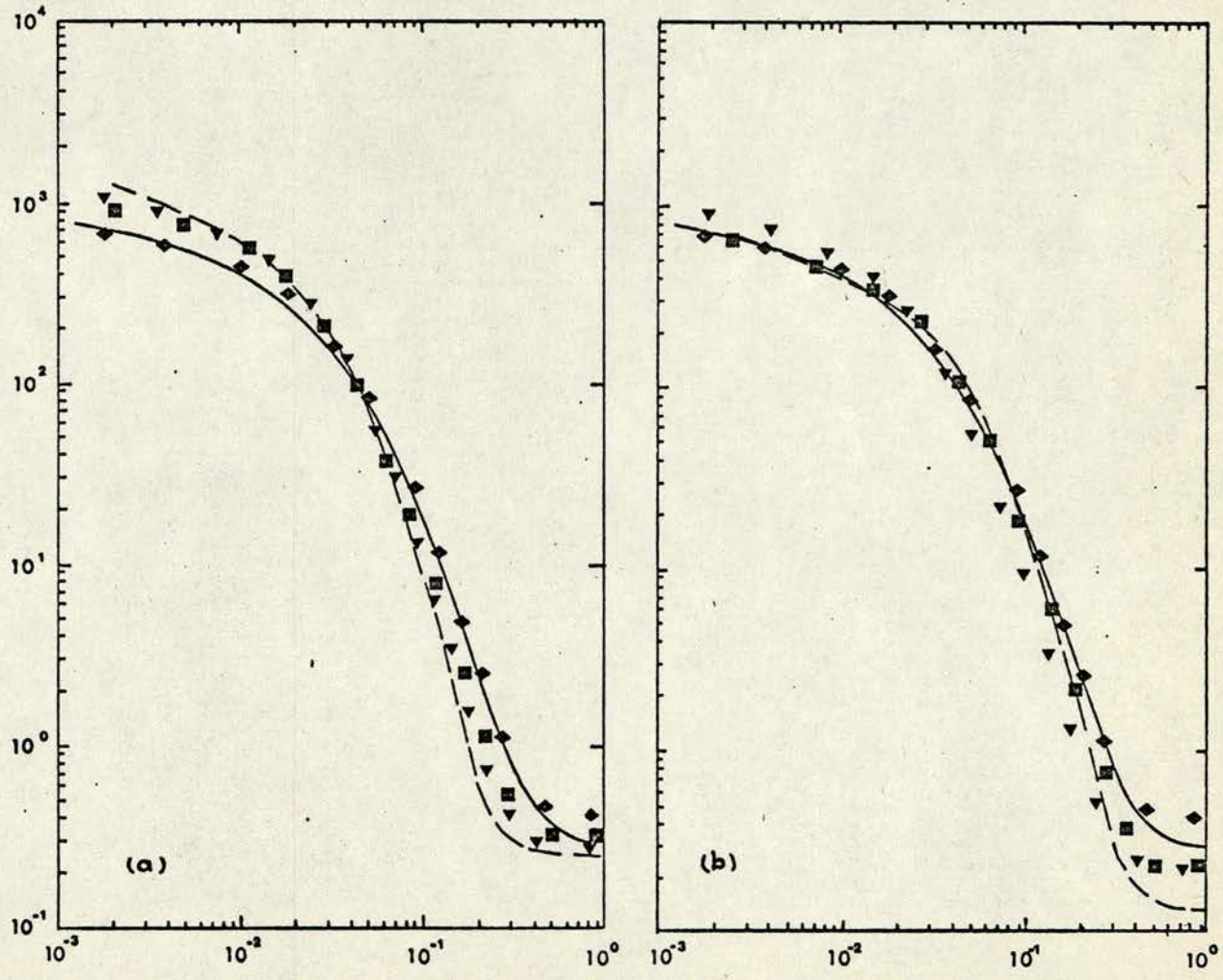

Figure 6.25

Energy Spectra for Water and Polyox Solutions at $\xi = 0.86$ made dimensionless with (a) solvent kinematic viscosity and (b) solution kinematic viscosity

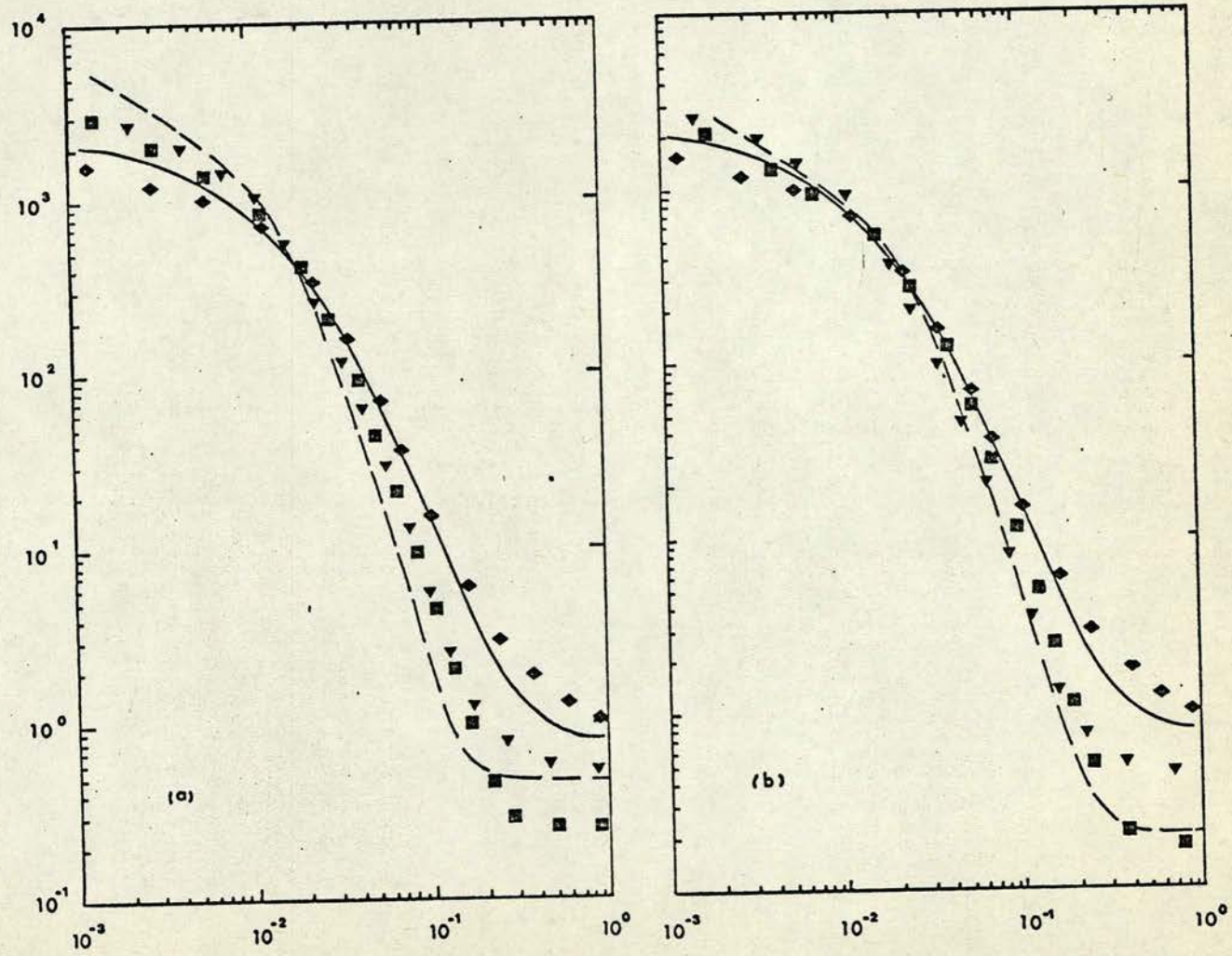

Figure 6.26

Energy Spectra for Water and Polyox Solutions at $\xi = 0.43$ made dimensionless with (a) solvent kinematic viscosity and (b) solution kinematic viscosity

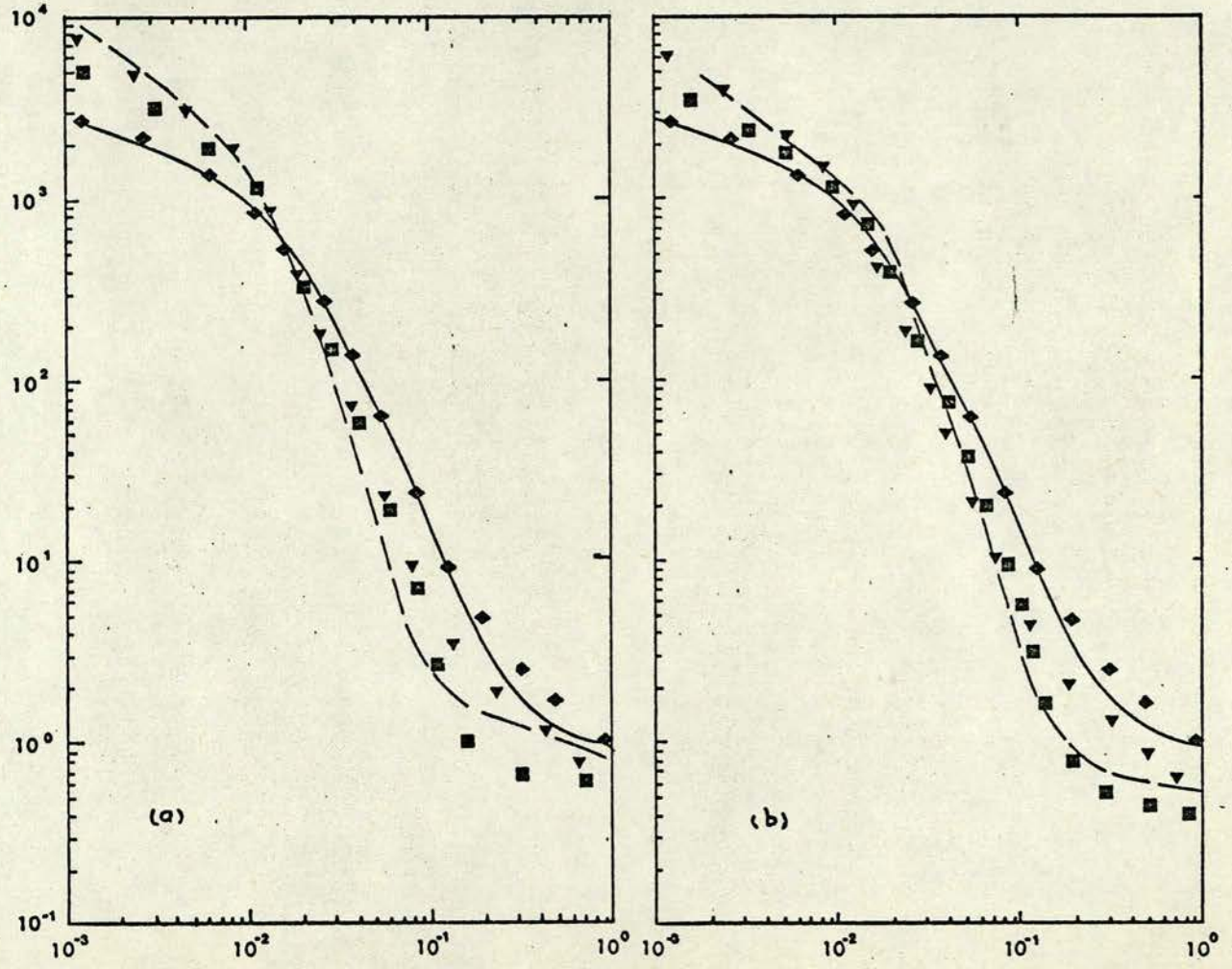

Figure 6.27

Energy Spectra for Water and Polyox Solutions at $\xi = 0.21$ made dimensionless with (a) solvent kinematic viscosity and (b) solution kinematic viscosity

water at all flow positions. All other Polyox concentrations (100 - 500 ppm) show reduced energy in the high wavenumber region compared to the spectrum in water. Both the dimensionless wavenumber at which the spectra deviate from or cross the Newtonian spectrum and the amount by which the energy is reduced compared to water at a given dimensionless wavenumber are increased towards the pipe edge as ξ is reduced. It is also clear that the spectra from the 100 ppm solution shows significant non-Newtonian effects which were not evident in our measurements of Grid flow. Where the curves are not affected by ambiguity noise there is a tendency for the spectral estimates at the higher concentrations (100 - 500 ppm) to cluster together at all flow positions.

From Figures 6.28 to 6.31 it can be seen that the 25 ppm solution of Separan has spectra which follow the Newtonian curves at all positions except at the centreline ($\xi = 1$). With $\xi = 1$ the spectrum shows an anomalously high level of ambiguity noise, the reason for which is not known. It was not typical of the other spectra from the 25 ppm solution and although the computer processing was re-checked and the analogue tape recording re-digitised, the noise effect was still evident at this tape position only. It is thought that this spectrum is incorrect perhaps due to a faulty section of magnetic tape. Both the 50 ppm and the 100 ppm solutions show the same effect as the higher concentrations of Polyox. The spectra from these solutions show higher energy in the low wavenumber region compared to water with much less energy in the higher wavenumbers. Both the 50 ppm and 100 ppm solutions have very similar spectra when normalised although the levels of drag reduction were significantly different, being 50% for the 50 ppm solution and 58% for the 100 ppm solution.

Key to Figs 6.28–6.31

— Water
◆ 25
▼ 50
– – 100

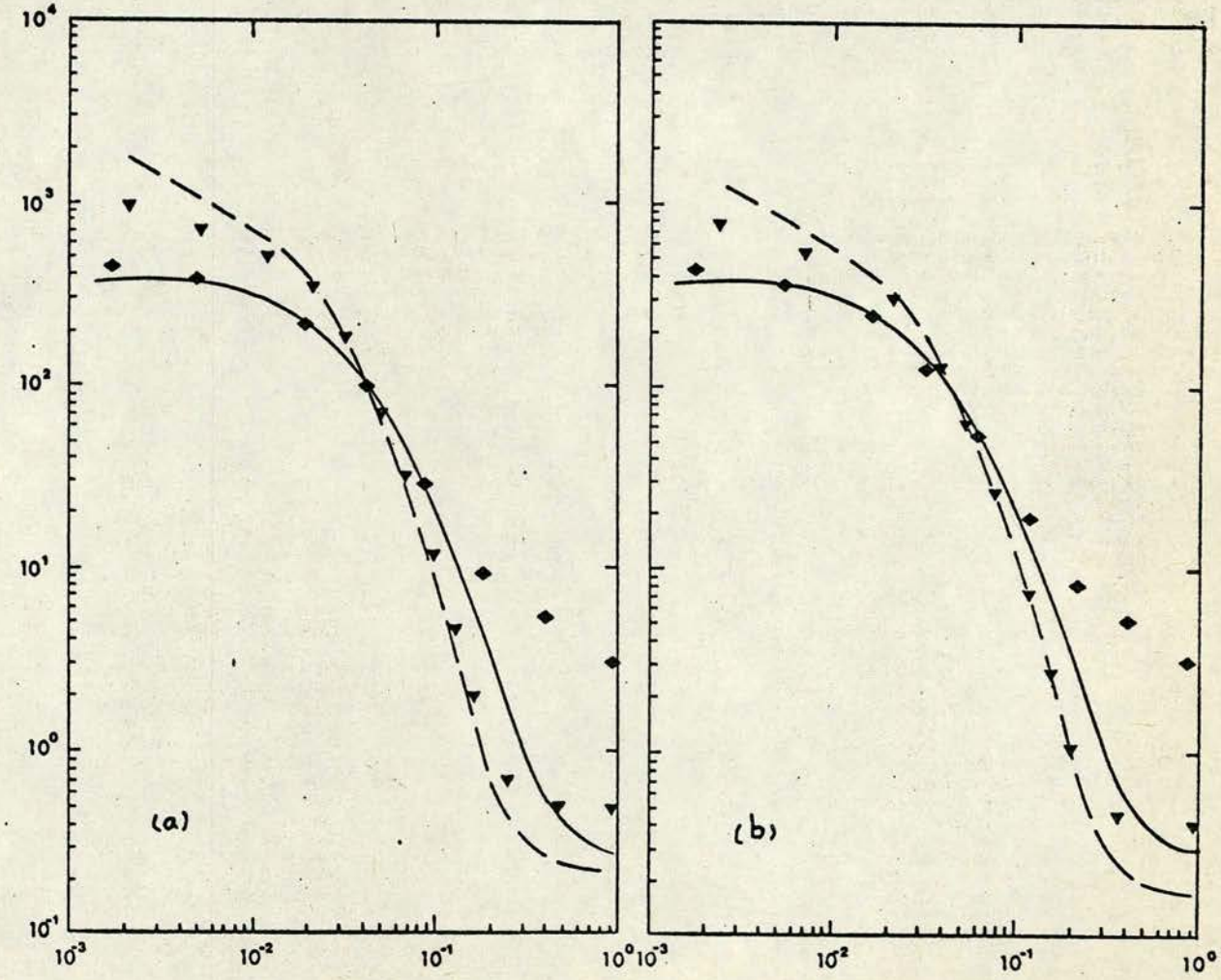

Figure 6.28

Energy Spectra for Water and Separan Solutions at ξ = 1 made dimensionless with (a) solvent kinematic viscosity and (b) solution kinematic viscosity

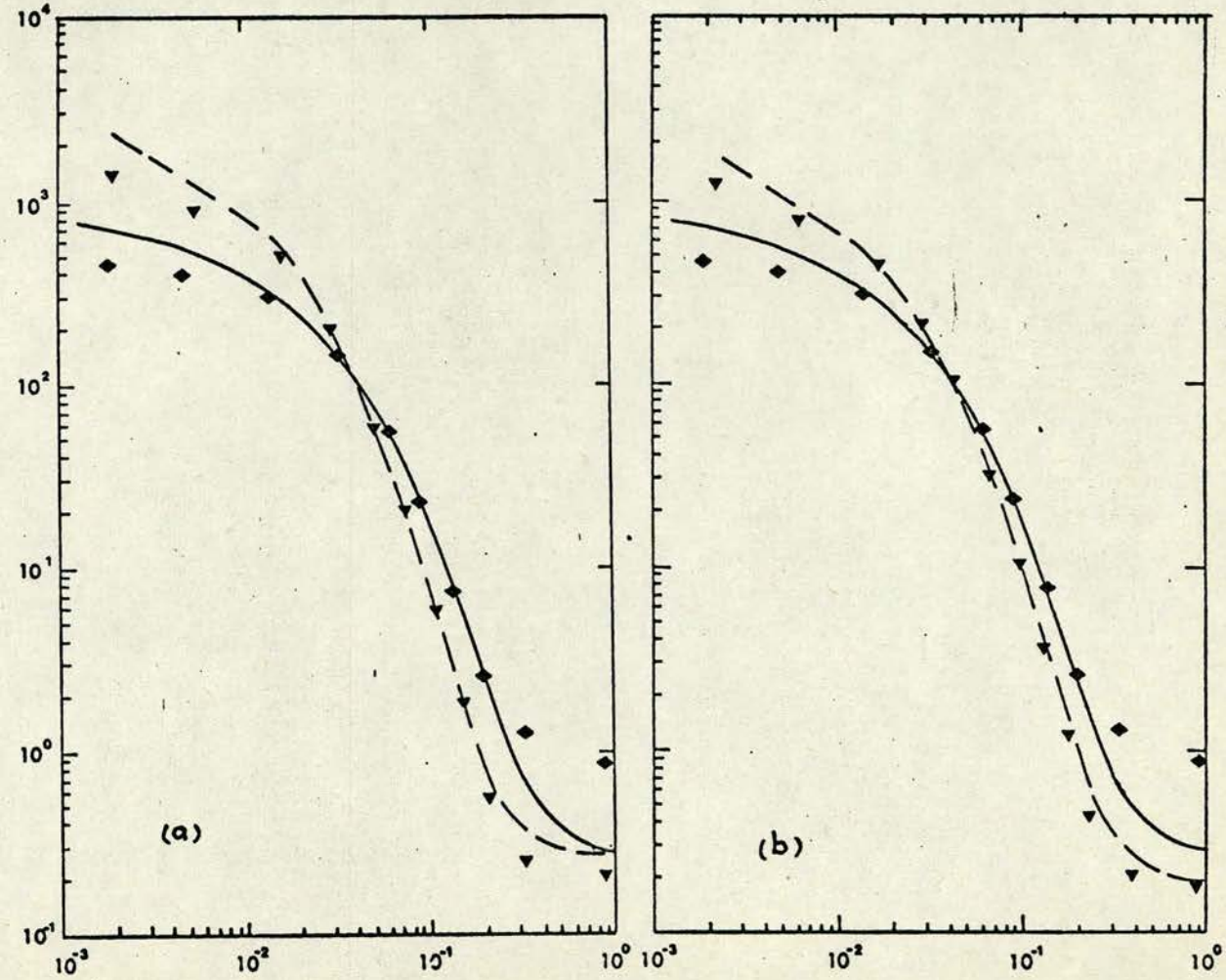

Figure 6.29

Energy Spectra for Water and Separan Solutions at ξ = 0.86 made dimensionless with (a) solvent kinematic viscosity and (b) solution kinematic viscosity

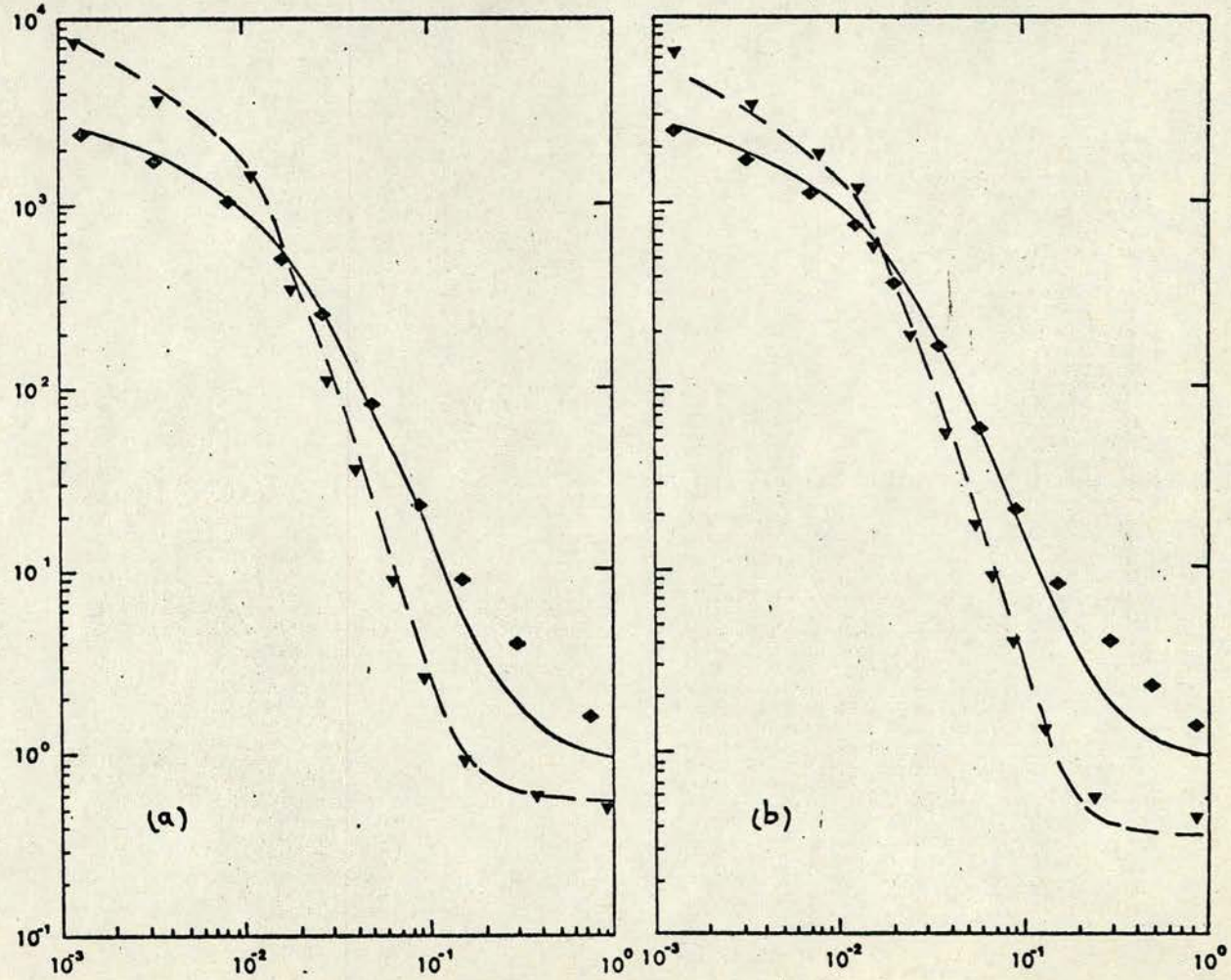

Figure 6.30

Energy Spectra for Water and Separan Solutions at $\xi = 0.43$ made dimensionless with (a) solvent kinematic viscosity and (b) solution kinematic viscosity

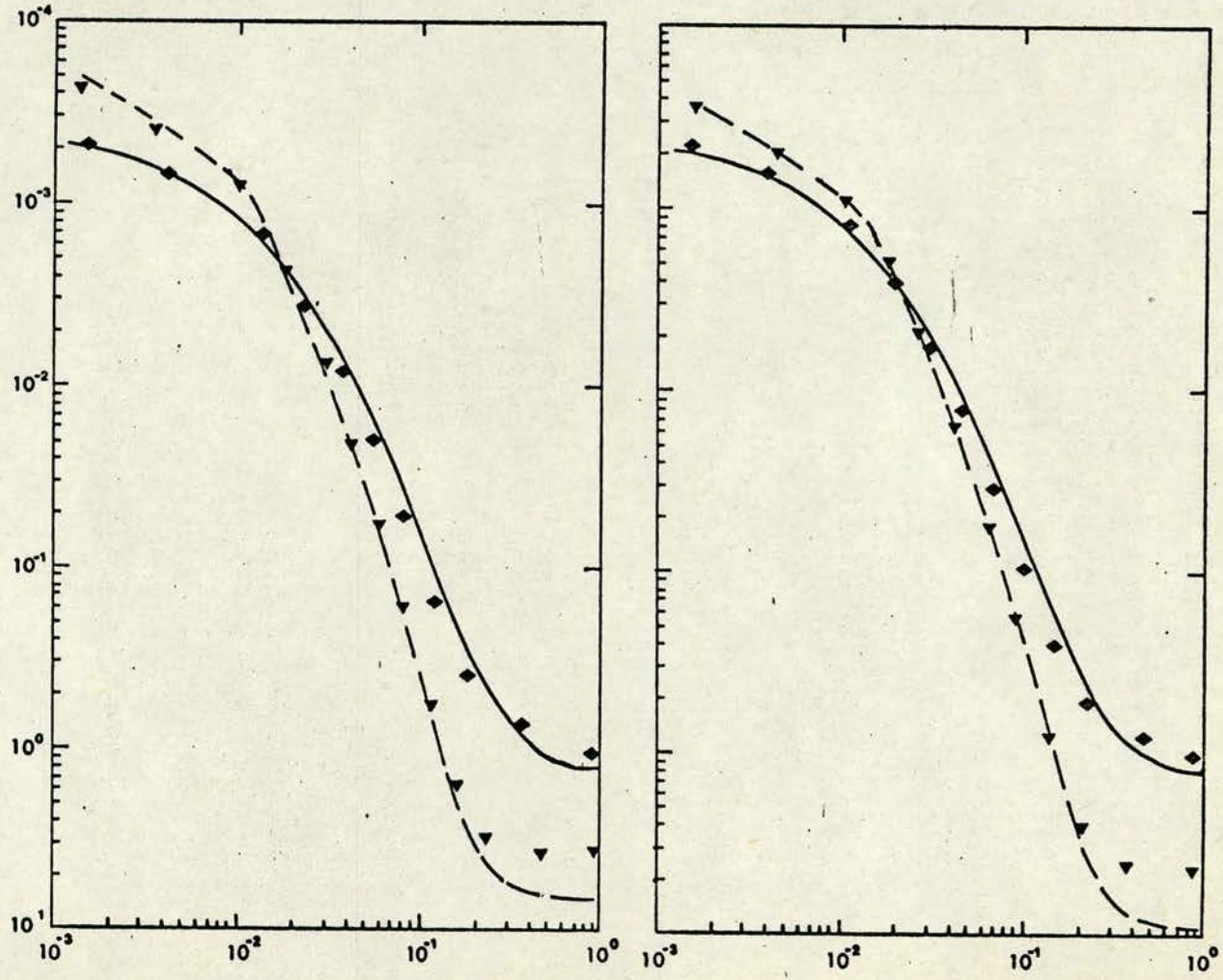

Figure 6.31

Energy spectra for Water and Separan Solutions at ξ = 0.21 made dimensionless with (a) solvent kinematic viscosity and (b) solution kinematic viscosity

6.3 DISCUSSION OF PIPE FLOW RESULTS

Like Reischman and Tiederman (1975) it was found that at conditions of less than maximum drag reduction Virk's "ultimate velocity profile" was not followed in the intermediate region. The velocity profile model of Van Driest (1970) was found to give a better fit to the data, the slope of the profile in the intermediate region gradually increasing as drag reduction increased.

Turbulent intensity profiles when made dimensionless using wall friction velocity, u_τ, were qualitatively in agreement with those of Wells et al (1968), Arunachalam et al (1972), Rudd (1972) and Logan (1972) with similar values to those for Newtonian flow near the pipe centreline but with much higher values towards the wall.

Profiles of dimensionless dissipation rate were calculated using a method developed by Lawn (1971) for Newtonian flow. The profiles show that ε^* is greater in polymers than for water away from the centreline, the difference increasing as ξ is reduced. Although our method of measuring ε^* breaks down very near to the pipe wall, since the spectrum in this region does not contain an inertial subrange, it is possible that ε^* becomes very large compared with water at positions nearer to the wall than could be measured. Increased dissipation near the pipe wall is consistent with theories like those of Walsh (1967b). Walsh suggested that the reduced generation of large scale turbulent eddies is the main mechanism and is caused by a slight alteration to the energy balance near the wall preventing the growth of the small scale eddies. The small scale eddies are destroyed by viscous dissipation and dissipation would be increased compared to the Newtonian case in this region of the flow.

The energy spectra showed a threshold concentration below which

the polymer spectra were indistinguishable from Newtonian spectra. The threshold lies between 50 ppm and 100 ppm for Polyox and between 25 and 50 ppm for Separan although the threshold may vary with concentration or drag reduction. The change in the spectrum compared to water was greatest near the wall and reduced with increasing distance from the wall although the spectra were significantly different at all flow positions including the pipe centreline. This observation together with the results from Grid flow indicate that, while the major alterations to the flow occur near the wall in pipe flow, the polymer molecules affect the process of turbulent energy decay by small scale eddy suppression.

REFERENCES

Allan, J J 1976 "Digital Analysis of Velocity Measurements in Turbulence". Research Report, Dept. of Mech. Eng., University of Edinburgh.

Arunachalam, V R
Fulford, G D 1971 Chem. Eng. Sci., 26, 1065.

Arunachalam, V R
Hummel, R L
Smith, J W 1972 Can. J. Chem. Eng., 50, 337.

Astarita, G
Nicodemo, L 1966 AIChE J., 12, 3, 478.

Astarita, G
Nicodemo, L 1969 I & E C Fund, 8, 3, 582.

Barker, S J 1973 J. Fluid Mech., 60, 721.

Barnard, B J S
Sellin, R H J 1969 Nature, 222, 1160.

Batchelor, G K
Townsend, A A 1947 Proc. Roy. Soc. A, 190, 534.

Batchelor, G K
Townsend, A A 1948 Proc. Roy. Soc. A, 193, 539.

Bendat, J S
Piersol, A G 1971 "Random Data - Analysis and Measurement Procedures". Wiley.

Berman, N S
Dunning, J W 1973 J. Fluid Mech., 61, 2, 289.

Berman, N S
George, W K 1974 Phys. Fluids, 17, 250.

Black, T J 1968 NASA Report No. CR 888.

Black, T J 1969 "Viscous Drag Reduction". 383. Plenum Press, New York.

Blackman, R B
Tukey, J W 1958 "Measurements of Power Spectra". Dover Publications, New York.

Bogue, D C
Metzner, A B 1963 I & E C Fund. 2, 143

Boston, N E J
Burling, R W 1972 J. Fluid Mech., 55, 473.

Bradshaw, P 1967 NPL Aero Report No. 1220.

Bryson, A W
Arunachalam, V R
Fulford, G D 1971 J. Fluid Mech., 47, 2, 209.

Chung, J S
Graebel, W P 1972 Phys. Fluids, 15, 4, 546.

Comte-Bellot, G
Corrsin, S 1966 J. Fluid Mech., 25, 657.

Cooley, J W
Tukey, J W 1965 Math. Comp., 19, 90, 297.

Corrsin, S 1963 Handbuch der Physik, V111/2. Springer, Berlin.

Dimant, Y
Poreh, M 1976 "Advances in Heat Transfer". 12, 77.

Dodge, D W
Metzner, A B 1959 AIChE J., 5, 2, 189.

Durrani, T S
Greated, C A
1973 Trans. IEEE, IM22, 23.

Durrani, T S
Greated, C A
1977 "Laser Systems in Flow Measurement". Plenum Press, New York and London.

Durrani, T S
Nightingale, J M
1973 Proc. IEEE, 120, 2, 299.

Durst, F
Whitelaw, J H
1971 Proc. Roy. Soc. A, 324, 157.

Eckelmann, H
1970 Max-Planck Inst. Fluid Mech., Rep. No. 48, Gottingen.

Eckelmann, H
Reichardt, H
1971 Proc. Turbulence in Liquids Symp., Univ. Missouri-Rolla, 144.

Edmonds, F N Jr
1966 Astrophysics J., 144, 733.

Edwards, R V
Angus, J C
French, M J
1971 J. Appl. Phys., 42, 2, 837.

Elata, C
Lehrer, J
Kahanovitz, A
1966 Israel Journal of Technology, 4, 1, 87.

El'perin, I T
Smol'skii, B M
Leventhal, L I
1967 Int. Chem. Eng., 7, 276.

Ernst, W D
1966 AIChE J., 12, 3, 581

Ernst, W D
1967 AIAA J., 5, 5, 906.

Fabula, A G
1966 PhD Thesis, Penn. State University, USA.

Fabula, A G
Lumley, J L
Taylor, W D
1966 "Mechanics of Continua", 100. Eskanazi, S (Ed.), Academic Press.

Forame, P C
Hansen, R J
Little, R C
1972 AIChE J., 18, 1, 213.

Frenkiel, F N
Klebanoff, P S
1967 Phys. Fluids, 10, 8, 1737.

Friehe, C A
Schwarz, W H
1969 "Viscous Drag Reduction". Plenum Press, New York. 281.

Friehe, C A
Schwarz, W H
1970 J. Fluid Mech., 44, 1, 173.

Gad-El-Hak, M
Corrsin, S
1974 J. Fluid Mech., 62, 1, 115.

Gadd, G E
1965 Nature, 206, 463.

George, W K
Lumley, J L
1973 J. Fluid Mech., 60, 321.

Gibson, C H
Schwarz, W H
1963 J. Fluid Mech., 16, 365.

Goldstein, R J
Adrian, R J
Kreid, D K
1969 I & E C Fund. 8, 3, 498.

Gordon, R J
1970 J. Appl. Polymer Sci., 14, 2097.

Goren, Y
Norbury, J F
1967 Trans. ASME Basic Eng., 89, 814.

Grant, H L 1962 J. Fluid Mech., 12, 241.
Stewart, R W
Moilliet, A

Greated, C A 1969 Nature, 224, 1196.

Hand, J H 1973 Chem. Eng. Sci., 28, 63.
Williams, M C

Hansen, R J 1972 J. Fluid Mech., 95, 23.

Hinze, J O 1959 "Turbulence". McGraw-Hill, New York.

Hinze, J O 1975 "Turbulence". McGraw-Hill, New York.

Hoyt, J W 1972 Trans. ASME, J. Basic Eng., 94, 258.

Huang, T T 1971 Naval Ship Research and Development Centre,
Santelli, N Washington D.C. Report No. 3677.

Huang, T T 1974 Phys. Fluids, 17, 298.

Hunston, D L 1976 Physics of Fluids, 18, 12, 1626.
Reischman, MM

Hussain, A K M F 1970 Stanford University, Rep. FM 6.
Reynolds, W C

Kistler, A L 1966 J. Fluid Mech., 26, 1, 37.
Vrebalovich, T

Kogelnik, H 1950 Bell Syst. and Tech. J., 43, 385.

Kolmogoroff, A N 1941a Compt. Rend. Acad. Sci., URSS, 30, 301.

Kolmogoroff, A N 1941b Compt. Rend. Acad. Sci., URSS, 32, 16.

Kozicki, W 1968 Chem. Eng. Sci., 23, 231.
Tiu, C

Landahl, M T 1972 Proc. 13th Int. Cong. Theoretical and Appl. Mechanics, Moscow.

Laufer, J 1954 NACA Tech Rep. No. 1174.

Lawn, C J 1971 J. Fluid Mech., 48, 3, 477.

Lee, W K
Vaseleski, R C
Metzner, A B 1974 AIChE J., 20, 1, 128.

Leslie, D C 1973 "Developments in the Theory of Turbulence." Clarendon Press, Oxford.

Little, R C 1969 Ind. Eng. Chem. Fundam., 8, 557.

Little, R C
Wiegard, M 1970 J. Appl. Polymer Sci., 14, 409.

Little, R C
Hansen, R J
Hunston, D L
Kim, O
Patterson, R L
Ting, R Y 1975 Ind. Eng. Chem. Fundam., 14, 4, 283.

Logan, S E 1972 AIAA, J., 10, 962.

Lumley, J L 1964 Phys. Fluids, 7, 335.

Lumley, J L 1967 Applied Mechanics Reviews, 20, 12.

Lumley, J L 1969 Annual Reviews of Fluid Mechanics, 1.

Lumley, J L 1973 Macromolecular Review, 7, 263.

McComb, W D 1974a Nature, 251, 5476, 598.

McComb, W D 1974b Proc. Roy. Soc. (Edin.) A, 72, 19, 225.

Massey, B S — 1975 "Mechanics of Fluids". Van Nostrand Reinhold Co., G.B.

Merrill, E W
Smith, K A
Shin, H
Mickley, H S — 1966 Trans. Soc. Rheol., 10, 1, 335.

Metzner, A B
Park, M G — 1964 J. Fluid Mech., 20, 291.

Middleton, D — 1960 "Introduction to Statistical Communication Theory". McGraw-Hill, New York.

Millikan, C B — 1939 Proc. 5th Int. Cong. Appl. Mech., Wiley, New York.

Morgan, D T G
Pike, E W — 1972 Rheol. Acta., 11, 179.

Nikuradse, J — 1933 NACA TM 1292 (Translation 1937).

Otnes, R K
Enochson, L D — 1972 Digital Time Series Analysis, New York.

Pao, R H F — 1967 "Fluid Dynamics". Chas. E Merrill Books Inc., USA.

Pao, Y H — 1965 Phys. Fluids, 8, 1063

Parker, C A
Hedley, A H — 1972 Nature, Phys. Sci., 236, 61.

Patel, V C — 1965 J. Fluid Mech., 22, 185.

Paterson, R W
Abernathy, F H — 1970 J. Fluid Mech., 43, 689.

Pond, S
Smith, S D
Hamblin, P F
Burling, R W
1966 J. Atmos. Sci., 23, 376.

Reichardt, H
1951 Z angew Math und Mech., 31, 7, 208.

Reischman, MM
Tiedermann, W G
1975 J. Fluid Mech., 70, 369.

Rice, S O
1944 Bell Syst. Tech. J., 27, 109.

Rollin, A
Seyer, F A
1972 Can. J. Chem. Eng. Sci., 50, 714.

Rudd, M J
1972 J. Fluid Mech., 51, 673.

Sentmen, D D
1974 Report No. 74-5, Department of Physics & Astronomy, Iowa University.

Seyer, F A
Metzner, A B
1967 Can. J. Chem. Eng. Sci., 45, 121.

Seyer, F A
Metzner, A B
1969 AIChE J., 15, 3, 426.

Shaver, R G
Merrill, E W
1959 AIChE J., 5, 2, 181.

Simmons, L F G
Salter, C
1934 Proc. Roy. Soc. A 145, 212.

Smith, K A
Merrill, E W
Mickley, H S
Virk, P S
1967 Chem. Eng. Sci., 22, 619.

Squire, W
Castro, W
Costrell, J
1967 Nature, 213, 1008.

Stewart, R W
Townsend, A A
1951 Proc. Roy. Soc. A 243, 48.

Taylor, A R
Middleman, S
1974 AIChE J., 20, 2, 454.

Taylor, G I
1935 Proc. Roy. Soc. A 151, 421.

Taylor, G I
1938 Proc. Roy. Soc. A 164, 476.

Ting, R Y
1972 J. Appl. Polymer Sci., 16, 3169.

Ting, R Y
Little, R C
1973 J. Appl. Polymer Sci., 17, 3345.

Tomita, Y
1970 Bull. JSME, 13, 61, 926.

Toms, B A
1949 Proc. 1st int. Cong. Rheology. Part 2
Amsterdam : North : Holland Publishing Company.

Van Driest, E R
1956 J. Aero Sci., 23, 1007.

Van Driest, E R
1970 J. Hydronautics, 4, 3, 120.

Virk, P S
Merrill, E W
Mickley, H S
Smith, K A
1966 Mechanics of Continua, 37. Eskanazi, S (Ed.),
Academic Press.

Virk, P S
Merrill, E W
Mickley, H S
Smith, K A
Mollo-Christensen, E L
1967 J. Fluid Mech., 30, 305.

Virk, P S
Mickley, H S
Smith, K A
1970 Trans. ASME, Journal Appl. Mech., 37, 488.

Virk, P S
1971 J. Fluid Mech., 45, 225.

Virk, P S
1975 AIChE J., 21, 4, 625.

Vleggaar, J
Dammers, W R
Tels, M
1968 Chem. Eng. Sci., 23, 1159.

Vleggaar, J
Tels, M
1973 Chem. Eng. Sci., 28, 965.

Walsh, M
1967a PhD Thesis, Cal. Tech.

Walsh, M
1967b Int. Shipbuilding Progress, 14, 134.

Wells, C S Jr
1965 AIAA J., 3, 10, 1800.

Wells, C S Jr
Harkness, J
Meyer, W A
1968 AIAA J., 6, 2, 250.

White, W D
1966 Proc. 5th US National Cong. Appl. Mech., ASME.

White, D Jr
Gordon, R J
1975 AIChE J., 21, 5, 1027.

Yeh, Y
Cummins, H
1964 Appl. Phys. Lett., 4, 176.

Effect of polymer additives on the small-scale structure of grid-generated turbulence

W. D. McComb

School of Engineering Science, University of Edinburgh, Edinburgh, Scotland

J. Allan and C. A. Greated

Department of Physics, University of Edinburgh, Edinburgh, Scotland
(Received 12 January 1976; final manuscript received 31 January 1977)

The effect of polyethyleneoxide (Polyox grade WSR 301) on grid-generated turbulence was investigated using laser anemometry and flow-visualization techniques. It was found that the polymer additive reduced both the turbulent intensity and the rate of decay behind the grid. At typical drag-reducing concentrations, turbulent energy spectra were qualitatively the same as those in water, in agreement with the results of other investigations. However, at higher additive concentrations, the dissipation-range spectra showed noticeable attenuation. This seemed to be a threshold effect with onset at a polymer concentration between 100 and 250 ppm. This result was supported by photographs of dye-injection tracer but in this case the onset concentration for small-eddy suppression was between 50 and 100 ppm.

INTRODUCTION

Although there is still no generally agreed theory of drag reduction by polymer additives, the phenomenological aspects of the subject are now well documented. However, the basic problem of determining just how the underlying structure of turbulence is affected by these additives has received much less attention and in some ways the situation is rather confused.

Among the first work in this area was a flow-visualization study of a turbulent jet by Gadd,[1] who showed that in a 30 ppm solution of Polyox WSR 301 the smaller-scale eddies were suppressed, relative to pure water. Similar behavior was reported by Barnard and Sellin[2] who studied grid-generated turbulence and found that suppression of small eddies was most complete at a concentration of only 20 ppm of Polyox WSR 301. These authors also inferred (from the reduced spreading angles of their dye traces) that turbulent intensity was reduced in the polymer solutions.

Direct measurements of turbulent energy spectra have, in the past, mainly been made using hot-film probes. Unfortunately, there are difficulties in using such probes in non-Newtonian fluids and the results must be treated with some caution. Among the most reliable measurements would seem to be those of Friehe and Schwarz[3] who examined the effect of an ionic polyacrylamide (Dowell J-100) on grid turbulence. The results obtained for additive concentrations up to 300 ppm indicated that intensity levels were increased whereas decay rates were reduced. Energy spectra were found to be unchanged from the results for pure water.

Laser anemometry should provide a more satisfactory technique for measuring spectra in polymer solutions and Greated[4] has reported that polyacrylamide (Separan AP30 in water at a concentration of 80 ppm) reduced the intensity of grid-generated turbulence. Also, the spectrum near the grid showed some attenuation of high-frequency components, although farther downstream there was no change from the spectrum in water. However, these results are open to some doubt as reference levels in water were not representative of grid-generated turbulence (see Ref. 3 for a discussion of this point). Finally, we note that Chung and Graebel[5] have used a laser anemometer to obtain spectra in turbulent pipe flow. No difference was found between spectra in water and in a 50 ppm solution of Polyox WSR 301.

To summarize, although the available evidence does not always allow us to compare like situations, on balance it seems clear that at typical drag-reducing concentrations, polymer additives do not affect the shape of the turbulent spectrum. Also, it seems that decay rates are reduced in grid turbulence. On the other hand, there are two points where the evidence is in conflict: (1) dye injection shows a striking suppression of small-scale components whereas at similar additive concentrations spectra are unchanged; (2) some experiments indicate reduced intensity levels in polymer solutions, but others indicate that intensities are increased.

In this paper we have attempted to resolve this situation (at least partially) by comparing flow visualization and laser anemometry in grid-generated turbulence. We have also had a second purpose in mind. Theoretical approaches to turbulence in polymer solutions have been in terms of the usual continuum models of non-Newtonian behavior. As examples one might mention the following communications: Lumley[6] (Reiner–Rivlin fluid), Chow and Saibel[7] (Oldroyd fluid), and McComb[8,9] (Maxwell fluid, anisotropic fluid). At the low additive concentrations used in most investigations, non-Newtonian effects can be difficult to detect. Thus, there is a need for measurements of (for example) energy spectra at higher concentration to provide data to allow this type of theory to be tested. In this investigation we have used polyethyleneoxide (PEO: Polyox grade WSR 301) in aqueous solution with concentrations ranging up to 1000 ppm.

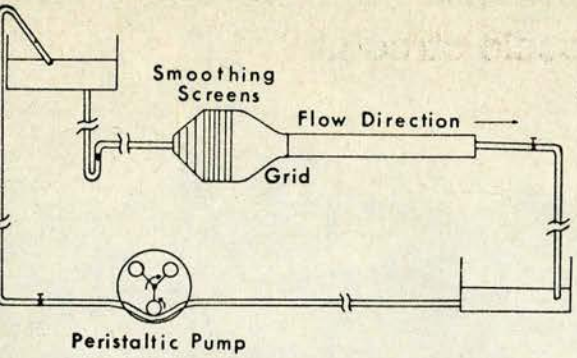

FIG. 1. The experimental setup.

EXPERIMENTAL DETAILS

The experimental setup is shown schematically in Fig. 1. The fluid flows under the action of gravity from the top tank through the water tunnel to the bottom tank, the total head being 6.3 m. The working section of the tunnel was a 7.5 cm square cross section throughout its length of 1.2 m and the grid was made up of 2.4 mm diam brass rods spaced 12 mm apart. An expansion chamber, smoothing screens, and contraction were placed upstream from the working section to ensure a uniform flow with a low level of background turbulence. A Watson–Marlow peristaltic pump was used to refill the top tank.

The flow control value was set to give a nominal flow rate of 1.2×10^4 liter/h, as measured by a rotameter. The average grid Reynolds number, calculated from the volume flow rate and the kinematic viscosity was 7.6×10^3.

For the dye-injection experiments, one of the central solid rods was replaced by a tube of the same diameter which was closed at one end. The dye was injected through a 0.73 mm diam hole drilled in the downstream side of the tube. The dye flow was adjustable by varying the height of the dye reservoir.

The polymer additive used was PEO (Polyox grade WSR 301) which is a very effective drag reducer in turbulent shear flow. Tap water was used to dissolve the polymer to give nominal concentrations of 50, 100, 250, 500, and 1000 ppm (by weight). Solutions were prepared by sprinkling the dry powder on the water surface, while taking care to avoid causing agglomeration. Low-speed agitation was used to promote mixing and when the powder appeared to be completely dissolved, solutions were left to age for three days.

All measurements were made using a laser-Doppler velocimeter. This was operated in the "real-fringe" mode and the optical arrangement is shown in Fig. 2. No tracer particles were added as it was found that there were sufficient scatterers naturally present in the system. It was assumed that the natural particles would track the motion in both water and non-Newtonian solutions. A 5 mW He–Ne laser and a Disa type 55L optical unit were employed to form the fringe pattern, using a beam separation of 5 cm and a lens of 13 cm focal length. The direct beams were blocked off from the detection optics which consisted of a convex lens, pinhole, and solid-state photodiode detector.

The output from the photodiode was high-pass filtered (cutoff 50 kHz) and fed into a frequency tracker (the Disa 55L Doppler signal processor). The signal from the tracker was dc offset, amplified and recorded on a magnetic tape using a Thermionic FM tape recorder (frequency response dc – 2.5 kHz ± 0.5 dB).

The tape recordings were low-pass filtered on replay (cutoff kHz, roll-off 18 dB/octave) and digitized with a sample rate of 2 kHz to 12 bit precision using a PDP 15 computer.

SPECTRAL RESOLUTION OF THE TURBULENCE MEASUREMENTS

When measuring turbulent spectra with a laser-Doppler anemometer it is important to know precisely the spectral resolution of the instrument, i.e., the highest wavenumber which can be measured with accuracy. The ambiguity noise levels and the spatial resolution of the measuring volume are together the limiting factors which determine this. Recently, detailed theoretical investigations[10–13] have resulted in expressions which enable one to predict the spectrum of the combined signal caused by the turbulent motions and the ambiguity noise fluctuations. We will summarize the main points here and apply the expressions with the experimental parameters used in our investigations.

The power spectrum of the instantaneous Doppler signal is given by[10]

$$\phi(f) = D^2\phi_v(f) + \phi_a(f) ,$$

where $\phi_v(f)$ is the power spectrum of the velocity fluctuation component in the streamwise direction, D is the velocity to frequency conversion constant ($D = 0.596 \times 10^6$ Hz/msec^{-1} for our system), and $\phi_a(f)$ is the spectrum of the ambiguity noise. At the low turbulent intensities encountered in our experiments, $\phi_a(f)$ can be closely approximated by the spectrum corresponding to the mean flow velocity $\overline{U}$. From the above expression it may be seen that a straightforward subtraction of the ambiguity noise spectrum will yield the true turbulence spectrum.

By applying the techniques developed by Rice[14] for the analysis of shot noise it has been shown[10,11] that for Gaussian-beam optical systems, $\phi_a(f)$ is flat at low frequencies and rolls off at a rate of f^{-1} at high frequencies. The 3 dB bandwidth is approximately Δf Hz, where Δf is the rms signal bandwidth. In our case Δf

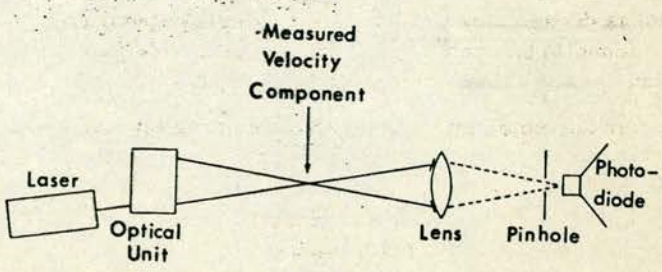

FIG. 2. The optical configuration.

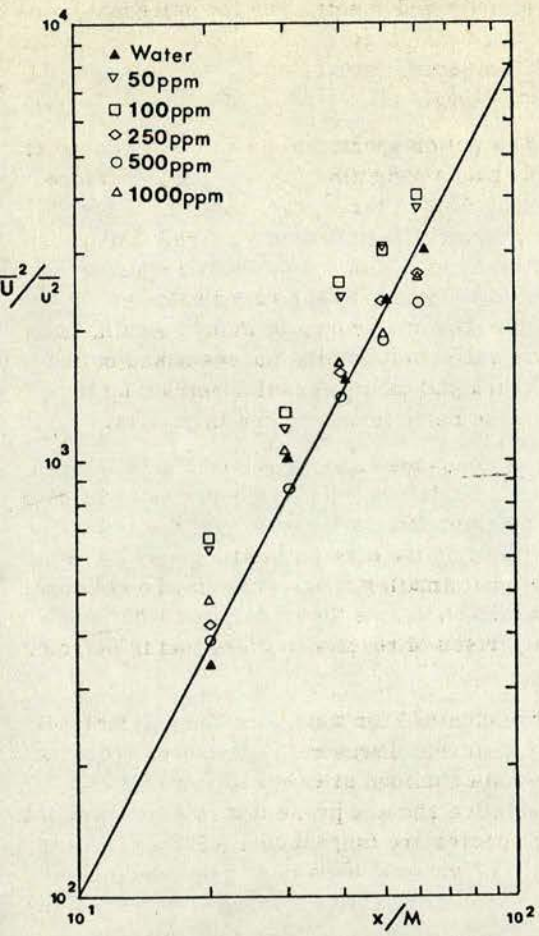

FIG. 3. Variation of turbulent intensity with downstream distance for water and solutions of Polyox WSR 301.

was found to be considerably greater than the highest turbulent frequencies of interest. Hence, $\phi_a(f)$ could be taken as flat over the complete range up to the cutoff frequency of the low-pass output filter of the frequency tracker. Thus, for a given cutoff frequency the spectrum is completely defined by the zero-frequency ordinate. For the one-sided power spectrum this is related to the Doppler bandwidth by the equation

$$\phi_a(0) = 0.737\,\Delta f$$

and Δf can be obtained from

$$\Delta f = \overline{U} r \cos\theta/\sqrt{2}\lambda F\ ,$$

where θ is the half-angle between the focused beams, λ is the wavelength of light, F is the focal length of the lens, and $2r$ is the beam diameter between the e^{-2} points on the intensity distribution. Application of this relationship with the optical parameters used in our experiments gave $\Delta f = 2.34$ kHz at the average flow velocity of 60 cm sec^{-1}. This value was checked by using a rotating disk to simulate a constant velocity situation in the following manner. A circular slot was machined close to the periphery of a perspex disk and filled with water. With the laser beams focused into the water, the disk was rotated on a record-player turntable and Δf obtained from the spectral width of the resulting Doppler signal.

The mean flow velocity varied slightly for each experimental run in the region of 60 cm/sec. At this speed it was found that $\phi_a(0) \simeq 4.9\times10^{-5}$ cm^2/sec^2 Hz^{-1}. This was just slightly below the measured level, the difference being accounted for by the effect of electronic noise in the detection and processing system. Small corrections to account for background noise were made, using the approach described in Ref. 12, and these led to close agreement with the measured levels at all flow velocities.

The measuring region in a Gaussian-beam laser-Doppler configuration is known to be ellipsoidal in shape with axes of length $2r/\cos\theta$ and $2r$ perpendicular to the optical axis and $2r/\sin\theta$ along the optical axis, measured between the e^{-1} points on the distribution. These lengths, 0.064 mm, 0.063 mm, and 0.334 mm in our case, define the spatial resolution of the anemometer, and were of the same order as the Kolmogoroff microscale. This varied for each set of measurements, but was in the region of 0.2 mm.

It will be seen that the normalized turbulence spectra have been plotted up to wavenumbers just below the Kolmogoroff microscale, the last few points at the high wavenumber end indicating how the curves flatten off to the calculated ambiguity noise level. The range of the turbulent spectra could have been extended slightly by subtracting the ambiguity noise level. This procedure was not adopted because the accuracy with which the additional points could be computed was not felt to be sufficiently great.

RESULTS

Continuous velocity records were obtained at dimensionless distances $x/M = 20$, 30, 40, 50, and 60 from the grid (where x is the downstream distance, M is the grid mesh size) for water and each of the polymer solutions. The concentrations of Polyox WSR 301 used were 50, 100, 250, 500, and 1000 ppm by weight. The mean and rms velocities were computed from the first 15 sec of each digitized velocity record and a digital power-spectral analysis performed using 8192 points of each record.

Photographs of the dye traces were taken for water and polymer solutions up to 500 ppm, using electronic flash illumination of 10 μsec duration.

Turbulence intensities for water and polymer solutions are presented in Fig. 3, where $\overline{U}^2/\overline{u^2}$ is plotted against x/M on logarithmic scales. In all cases the data may be fitted by the well-known power law

$$\overline{U}^2/\overline{u^2} = A(x/M - x_1/M)^n\ ,$$

where u is the streamwise fluctuating velocity and x_1 is the virtual origin. The scatter in the results obtained did not permit a reliable estimate x_1/M, which is a small quantity. From Fig. 3 it may be seen that turbulent intensities tended to be smaller in the polymer solutions than in water. Fitting the power law to the data resulted in the values of the constants given in Table I.

TABLE I. Values of the constants in the turbulent intensity decay law for water and polymer solutions.

Concentration of Polyox WSR 301 ppm (by weight)	A	n
0	1.2	1.9
50	3.9	1.7
100	4.7	1.7
250	2.8	1.7
500	3.1	1.6
1000	5.7	1.5

The value $n = 1.9$ for water is large (see Ref. 3 for a discussion of results obtained in Newtonian fluids), but this may be attributable to the rather low grid Reynolds number. However, the results for water were felt to be sufficiently representative to allow a comparison between Newtonian and non-Newtonian solutions. From the table it may be noted that the polymer additive tends to increase values of A and decrease values of n, thus indicating a reduced rate of decay.

The rate of decay of turbulent intensity may be calculated from the relation

$$\epsilon = -\frac{1}{2}\frac{d}{dt}(\overline{u^2} + 2\overline{v^2}) .$$

Making the transformation $dx = Udt$, we obtain

$$\epsilon = -\frac{1}{2}\frac{\overline{U}^3}{M}\frac{d}{d(x/M)}\left(\frac{\overline{u^2}}{\overline{U}^2} + 2\frac{\overline{v^2}}{\overline{U}^2}\right) ,$$

where v is a transverse component of fluctuating velocity. Neither of the transverse components was measured in our experiments, but the relationship

$$\overline{v^2} = 0.83\overline{u^2}$$

was assumed, following the interpretation by Friehe and Schwarz[3] of the results of Comte-Bellot and Corrsin.[15]

The one-dimensional spectrum, $\phi(k)$, where k is the wavenumber, and

$$\overline{u^2} = \int_0^\infty \phi(k)\,dk$$

was put in dimensionless form using Kolmogoroff variables; that is,

$$\tilde{\phi}(\tilde{k}) = \phi(k)/\nu^2 k_d ,$$

where $\tilde{k} = k/k_d$, $k_d = (\epsilon/\nu^3)^{1/4}$, the Kolmogoroff dissipation wavenumber, ν is the kinematic viscosity, and ϵ is the decay rate. In each case ϵ was calculated from the decay data for that particular run but, for simplicity, ν was taken to be the kinematic viscosity of water in all cases.

In the previous section, the effect of the ambiguity noise level on the measured spectrum was analyzed. The practical effect of this was checked by comparing the spectral measurements in water with the universal spectrum due to Pao.[16] Comparison of normalized spectra on a log-log plot against $\tilde{k}$ showed good agreement between measured spectra and the universal spectrum up to about $\tilde{k} = 0.5$. At wavenumbers greater than this value, the measured spectra flattened off to the calculated noise level.

Since the dissipation spectrum involves the square of the wavenumber as a weighting factor, it is therefore particularly sensitive at large wavenumbers to the wide-band spectrum of the ambiguity noise. To assess this, the second moments of the measured spectra were plotted against $\tilde{k}$ on linear-linear coordinates and also compared to the universal curve of Pao.[16] Again, good agreement was found between the curves based on the measured spectra and the universal spectrum up to $\tilde{k} = 0.5$, where the noise level became important.

Evidently, measurements at values of $\tilde{k}$ greater than about 0.5 should be disregarded in the present work. This leaves the approximate wavenumber band $0.1 < \tilde{k} < 0.5$ as representing the dissipation range. Although this is a somewhat smaller range than may be obtained by hot-film methods, it was thought to be adequate to permit a comparison of results in water and in polymer solutions.

Spectra were obtained for water and the polymer solutions at five different downstream distances from the grid. The results obtained at $x/M = 30$ and $x/M = 60$ were representative and are presented in Figs. 4(a) and 4(b). All the spectra are tangent to a $-5/3$ slope over a limited range of wavenumbers and in this region (the inertial range) the curves for all polymer solutions are close to the line for water. At the higher wavenumber (dissipation range) two quite different forms of behavior may be discerned, depending on polymer concentration. The results for the lower concentrations (50 and 100 ppm) fall quite close to the water curve, indicating little or no change in spectral shape, due to the additives. At the higher concentrations (250, 500, and 1000 ppm), the data points again cluster together, but in this case the dissipation range curve falls off more steeply than the spectrum in water. Thus, there is noticeable attenuation of high-frequency components at the larger concentrations.

So far as the lower polymer concentrations are concerned, our method of presenting normalized spectra based on the kinematic viscosity of water is probably not unreasonable. The effect of polyethyleneoxide on solution viscosity at concentrations up to (say) 100 ppm is (unlike certain other drag-reducing polymers) quite small.

On the other hand, although there is little specific rheological data available, at the higher concentrations these solutions are known to have larger viscosities and may exhibit marked shear-thinning behavior. The problem is further complicated by the possible relevance of other effects such as solution elasticity or anomalous extensional viscosity. Thus, in the present state of knowledge there is unlikely to be any definite answer to the problem of normalizing spectra in these solutions.

Certainly, it might seem simplest to follow Friehe and Schwarz and use an effective viscosity based on the

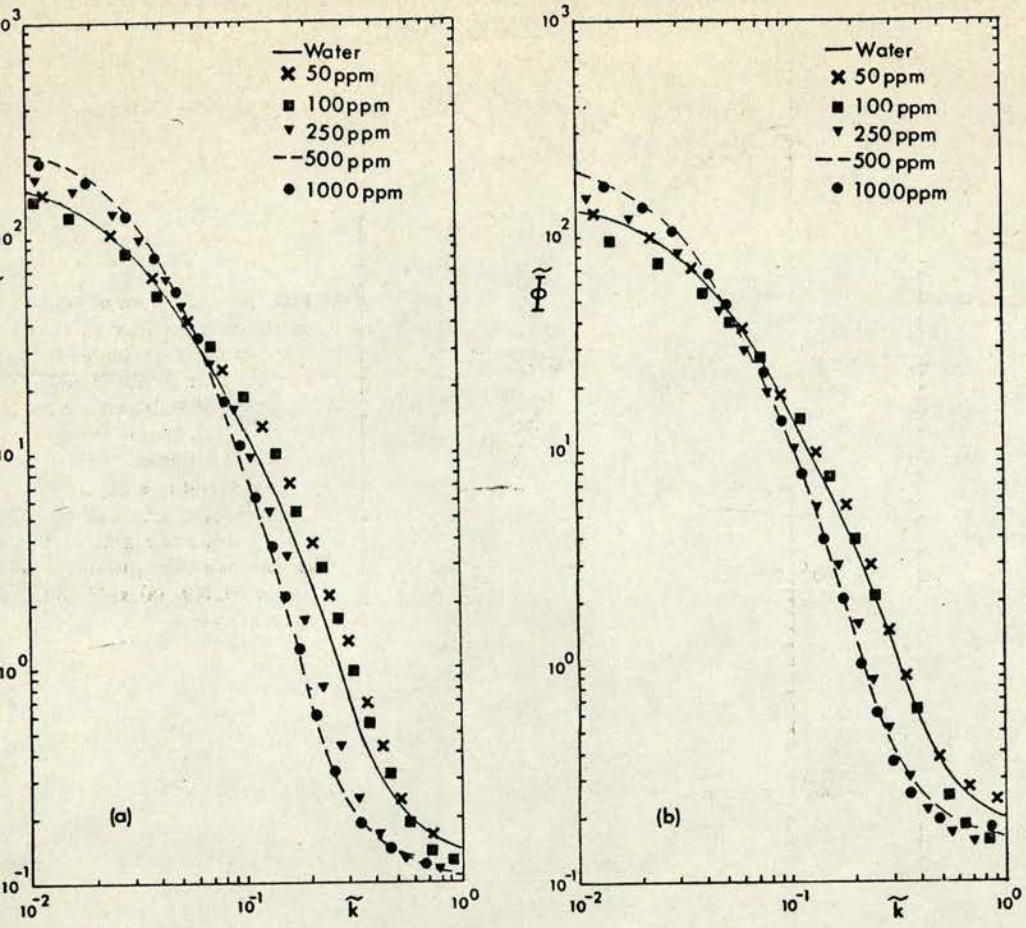

FIG. 4. Variation of one-dimensional energy spectrum with dimensionless wavenumber in water and solutions of Polyox WSR 301. (All spectra scaled using the value of the kinematic viscosity for water. The effect of noise is significant at wavenumbers greater than $\tilde{k} = 0.5$.) (a) $x/M = 30$, (b) $x/M = 60$.

rms rate of strain. To do this, one must obtain the dissipation rate and in practice, this necessitates an assumption that the inertial range spectrum (including the constant of proportionality) is unchanged in the polymer solutions. It also means evaluating the integral of the second moment of the spectrum. In our case, we would have to subtract the effect of the noise spectrum from the second moment in order to continue the integration to wave numbers greater than $0.5k_d$. We did not feel that the accuracy of this process (especially as there must be some uncertainty in the assumption about the inertial range) would be sufficient to justify the calculation of an effective viscosity.

However, the present use of the viscosity of water to scale the results for all solutions may be regarded as a lower bound on the spectral normalization. In an attempt to set an upper bound the solution viscosities were measured in an Ubbelode viscometer (a capillary flow device). As expected, the 50 and 100 ppm solutions had viscosities not very different from water alone (less than 10% increase). At the larger concentrations, relative viscosities of 1.3, 1.7, and 2.8 were recorded for the 250, 500 and 1000 ppm solutions, respectively.

Using these measured values of solution viscosity the results for 50 and 500 ppm (as presented in Fig. 4) were re-plotted in normalized form and are compared to the curves for water in Fig. 5. It is clear from these graphs that the spectra in the 50 ppm solution were very little changed by this procedure. Also, the spectra in the 500 ppm solution still show some attenuation relative to the result for water in the dissipation range, although the magnitude of the effect is undoubtedly reduced by this scaling.

Presumably for shear-thinning solutions, the correct procedure may be thought to lie somewhere between these two extremes. Indeed, Friehe and Schwarz found the effective viscosities for their 300 ppm polyacrylamide solution to be somewhat lower than their rheological values at the same rate of strain. In the absence of precise data, on the relationship between viscosity and rate of strain in PEO solutions, one can only speculate about this point. However, some aspects of our results are suggestive. Referring to Fig. 4, we note the following points:

(1) The data points for all concentrations coincide on the graph in the limited region where all spectra are tangent to the $-5/3$ slope (this is especially clear at the higher value of x/M).

(2) At higher wavenumbers, the data points fall into two distinct groups.

(3) The data points for the higher concentrations collapse onto one curve in spite of having relative viscosities ranging from 1.3 to 2.8. This alone would seem to indicate a certain insensitivity to the measured solution viscosities.

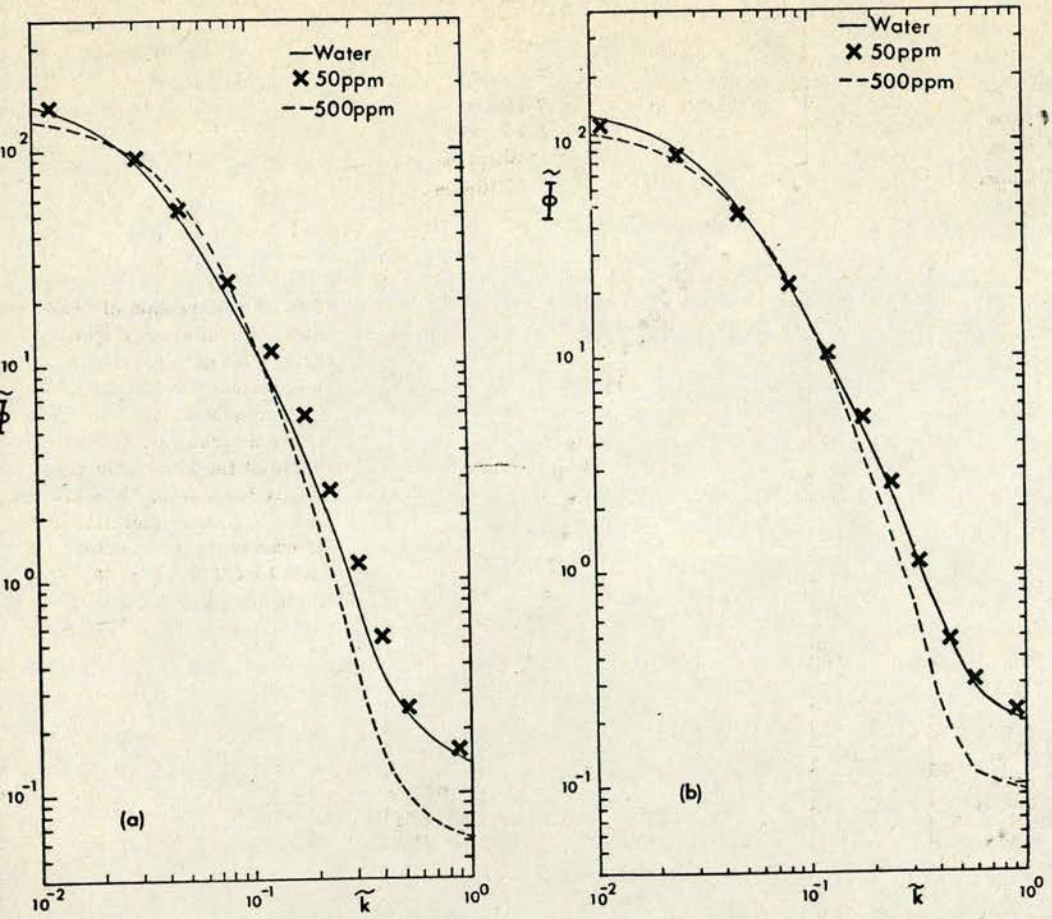

FIG. 5. Variation of one-dimensional energy spectrum with dimensionless wavenumber in water and solutions of Polyox WSR 301. (All spectra scaled using values of solution viscosity as measured in a capillary-flow viscometer. The effect of noise is significant at wavenumbers greater than $\tilde{k} = 0.5$.) (a) $x/M = 30$, (b) $x/M = 60$.

Thus, we feel that the available evidence, slight though it is, appears to favor the use of viscosities close to the value for water for normalizing spectra in PEO solutions.

The results of the flow-visualization experiments are presented in Figs. 5(a)–5(e) and show the effect of increasing polymer concentration on the dye jet. To some extent these photographs support the idea of a step change with increasing concentration, as suggested by the measurements of spectra. The photographs show that there is much fine-scale structure in water and the 50 ppm solution but at 100 ppm this seems to have been suppressed. Thus, the change in behavior would appear to be between 50 and 100 ppm as opposed to a threshold between 100 and 250 ppm for the spectra.

CONCLUSION

In summary, we have found that the presence of polymeric additives in grid-generated turbulence leads to reduced intensity levels and a change in the decay law. Like Friehe and Schwarz,[3] we found that the exponent in the decay law was reduced in value by the additives, but that there appeared to be no definite trend with increasing concentration. At typical drag-reducing concentrations, turbulent energy spectra showed no qualitative change from those in water, but at higher concentrations some attenuation of small-scale (dissipation range) components was observed. This "threshold" dependence on concentration was confined by the flow-visualization experiments although, in this case, at a lower concentration.

Two points of disagreement between our results and those of earlier experiments stand out. First, we found that Polyox WSR 301 decreased turbulent intensities whereas Friehe and Schwarz[3] found the opposite effect with Dowell J-100. The explanation may lie in the different polymers used; and we note, in partial support of our own results, that Barnard and Sellin[2] also used Polyox WSR 301 and deduced a reduction in intensity of a transverse component of velocity. Clearly, a more comprehensive investigation, involving different types of polymers and the measurement of streamwise and transverse components of fluctuating velocity, would have much to recommend it.

Second, our photographs of the dye traces indicate that complete suppression of the turbulent fine structure must take place at a polymer concentration of between 50 and 100 ppm. This is in contrast to the results of Barnard and Sellin[2] who found that a concentration of 20 ppm was sufficient for this purpose. Their experiments seem to be quite comparable to our own, the only major difference being that Barnard and Sellin injected a 1000 ppm solution, three meters upstream from the grid. Possibly this could have resulted in local concentrations higher than 20 ppm in the region of the dye injection. Certainly, Vleggaar and Tels[17] report that the injection of concentrated polymer solutions (5000 ppm Separan) at the centerline of turbulent pipe flow resulted in a polymer "thread" which remained intact for at least 200 tube diam downstream

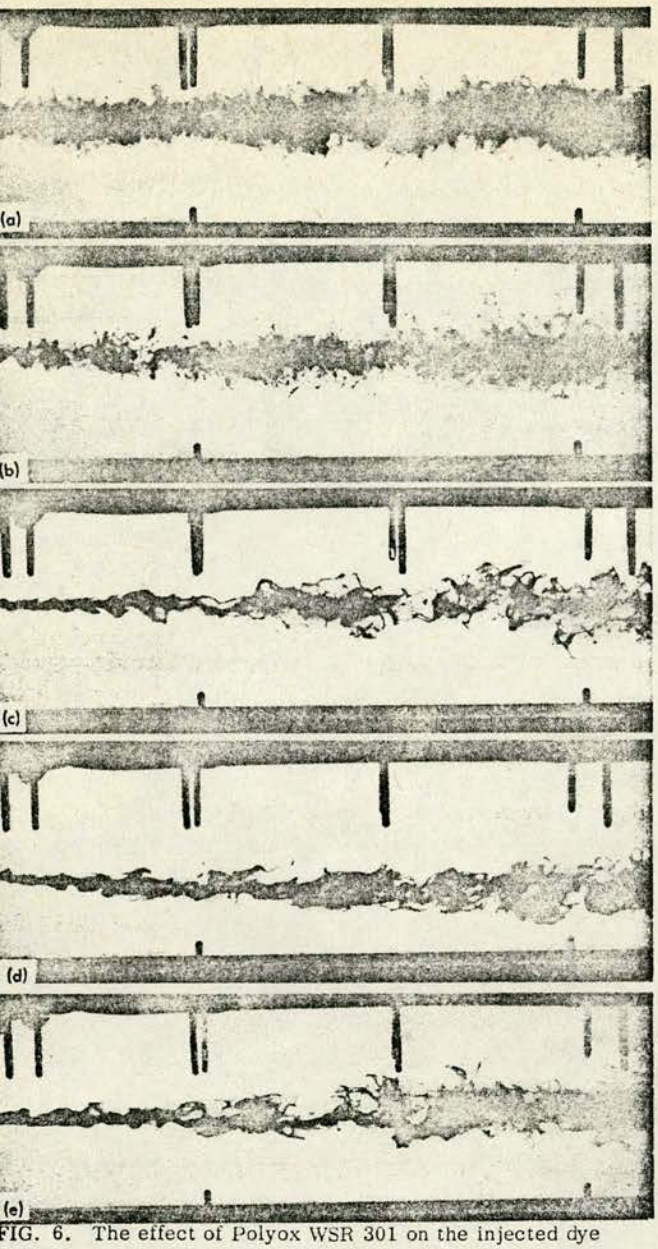

FIG. 6. The effect of Polyox WSR 301 on the injected dye trace (flow direction from left to right). (a) water, (b) 50 ppm Polyox WSR 301, (c) 100 ppm, (d) 250 ppm, (e) 500 ppm.

2 m in their experiments).

Finally, our results would seem to indicate that the discrepancy between flow-visualization and spectral measurements is somewhat less than previously thought. Both types of measurement seem to suggest that there is a threshold additive concentration for suppression of high frequency components of the turbulence. The different values for this threshold may simply reflect the sensitivity of the relative diffusion process to small changes in the fine structure of the turbulence. The existence of a threshold concentration is presumably to be related to some change in the structure of the fluid. Merrill *et al.*[18] discuss a critical concentration for polymer solutions, at which the random-coiling polymers just touch each other. For Polyox WSR 301 they estimate the critical concentration to be 406 ppm. This is apparently not a very precise criterion for non-Newtonian behavior, but these authors comment that for concentrations less than one third of the critical concentration, viscoelastic properties and gradient dependence of viscosity are difficult to detect, even with the most sensitive instruments. On this basis our present results, which seem to indicate a concentration of between 100 and 250 ppm for the onset of non-Newtonian behavior in turbulent spectra, would seem to be quite reasonable.

On the other hand, there is the possibility that this threshold effect, observed in our present measurements on grid turbulence, may be related to the onset phenomenon in shear flows.[19,20] Currently, we are extending our work to turbulent pipe flow and we intend to pursue this point.

[1]G. E. Gadd, Nature (London) 206, 463 (1965).
[2]B. J. S. Barnard and R. H. J. Sellin, Nature (London) 222, 1160 (1969).
[3]C. A. Friehe and W. H. Schwarz, J. Fluid Mech. 44, 173 (1970).
[4]C. A. Greated, Nature (London) 224, 1196 (1969).
[5]J. S. Chung and W. P. Graebel, Phys. Fluids 15, 546 (1972).
[6]J. L. Lumley, Phys. Fluids 7, 335 (1964).
[7]P. L. Chow and E. Saibel, Int. J. Eng. Sci. 5, 723 (1967).
[8]W. D. McComb, Proc. R. Soc. Edinburgh Sec. A 72, 226 (1975).
[9]W. D. McComb, Nature Phys. Sci. (London) 241, 117 (1973).
[10]T. S. Durrani and C. A. Greated, *Laser Systems in Flow Measurement* (Plenum, New York, 1976), Chap. 3.
[11]T. S. Durrani and C. A. Greated, IEEE Trans. Instrum. Meas. 22, 23 (1973).
[12]T. S. Durrani and C. A. Greated, IEEE Trans. Aerosp. Electron. Syst. 10, 418 (1974).
[13]W. K. George and J. L. Lumley, J. Fluid Mech. 60, 321 (1973).
[14]S. O. Rice, in *Selected Papers on Noise and Stochastic Processes*, edited by N. Wax (Dover, New York, 1954), p. 133.
[15]G. Comte-Bellot and S. Corrsin, J. Fluid Mech. 25, 657 (1966).
[16]Y. H. Pao, Phys. Fluids 8, 1063 (1965).
[17]J. Vleggar and M. Tels, Chem. Eng. Sci. 28, 965 (1973).
[18]E. M. Merrill, K. A. Smith, H. Shin, and H. S. Mickley, Trans. Soc. Rheol. 10, 1, 335 (1966).
[19]N. S. Berman and W. K. George, Jr., Phys. Fluids 17, 250 (1974).
[20]D. L. Hunston and M. M. Reischman, Phys. Fluids 18, 1626 (1975).

APPENDIX 2

ESTIMATION OF THE ACCURACY OF THE SPECTRAL TRANSFORMATION

It is assumed here that Taylor's hypothesis is satisfied and that the frequency spectrum is related to the wavenumber spectrum by equation (2.11) (repeated here as equation (A2.1)) viz

$$\phi(k) = \frac{\bar{U}}{2\pi}\,\phi(f) \qquad \text{with} \qquad k = \frac{2\pi}{\bar{U}}\,f \tag{A2.1}$$

To transform the spectrum $\phi(k)$ to the Kolmogoroff spectrum $\tilde{\phi}(\tilde{k})$ the following relations are used viz

$$\tilde{\phi}(\tilde{k}) = \frac{\phi(k)}{\nu^3 k_K} \qquad \text{and} \qquad \tilde{k} = \frac{k}{k_K} \tag{A2.2}$$

where

$$k_K = \left(\frac{\varepsilon}{\nu^3}\right)^{\frac{1}{4}}$$

From equations (A2.1) and (A2.2) it can be seen that

$$\tilde{\phi}(\tilde{k}) = \frac{\bar{U}}{2\pi}\left(\frac{1}{\varepsilon\nu}\right)^{\frac{1}{4}}\phi(f) \qquad \text{and} \qquad \tilde{k} = \frac{2\pi}{\bar{U}}\left(\frac{\nu^3}{\varepsilon}\right)^{\frac{1}{4}} \tag{A2.3}$$

Since $\bar{U}$ is measured directly and ν can be measured independently, the accuracy of the spectral normalisation is determined mainly by the accuracy of the method used to estimate the local dissipation rate ε.

For Grid flow ε was measured directly from the rate of decay of turbulent intensity using the method described in Chapter 5. For pipe flow it is more difficult to measure ε directly. For Newtonian pipe flow the energy spectrum is given by Lawn (1971) as

$$-\overline{uv}\frac{d\bar{U}}{dr} - \frac{1}{r}\frac{d}{dr}\left[r\left(\frac{\nu(\overline{u'^2} + \overline{v'^2} + \overline{w'^2})}{2} + \frac{vp}{\rho}\right)\right] = \nu\,\overline{\sum_{ij}\left(\frac{\partial u_i}{\partial x_j}\right)^2} \equiv \varepsilon \tag{A2.4}$$

Thus to measure local dissipation rate directly involves either the direct measurement of all nine components of the right-hand side of equation (A2.4) (or measuring some of the terms and calculating others by assuming local isotropy) or the direct measurement of Reynolds stress $\overline{u'v'}$, plus three triple velocity correlations and a pressure velocity correlation. Such very comprehensive measurements (at each flow position) were beyond the scope of the present work. Lawn, however, has measured many of the quantities needed to calculate the dissipation rate using both of these expressions. The values calculated were compared with values found by identifying an inertial subrange in the one dimensional energy spectrum where (equation (2.17))

$$\phi(k) = \alpha \varepsilon^{2/3} k^{5/3}$$

Lawn found that setting $\alpha = 0.53$ gave the best agreement between the methods although Bradshaw (1967) estimated the best value to be 0.51.

By comparing results at a number of Reynolds numbers, Lawn concluded that at a high enough Reynolds number the most accurate method of measuring local dissipation was to assume local isotropy, even for shear flows, and calculate ε by identifying the inertial subrange. This method was best provided that

$$Re_\lambda \geqslant 140 \qquad \text{(A2.5)}$$

with $Re_\lambda = \frac{U\lambda}{\nu}$ and $\lambda^2 = 15 \frac{\nu \overline{u'^2}}{\varepsilon}$

implying, for his measurements, that a Reynolds number (based on pipe diameter) greater than 10^5 would be necessary for a subrange to exist throughout the turbulent core. With a Reynolds number of 90,000 Lawn found that for $\xi \leq 0.1$, ε could be estimated with a standard deviation of 8% of the mean value.

Although the Reynolds numbers attained in our experiments were

much less than 90,000, the condition expressed in equation (A2.5) was satisfied for all values of ε estimated and spectra presented in this thesis.

To define a dimensionless dissipation rate, Lawn argued that in the core region of the flow the velocity defect and $\overline{(u'^2)}^{\frac{1}{2}}$, when made dimensionless using wall friction velocity u_τ, are invariant with change in Reynolds number. Reynolds number similarity extends also to the triple velocity products so that the production and diffusion terms in the energy equation (respectively the first and second term in the left hand side of equation (A2.1) are proportional to u_τ^3/R. The dissipation rate must have the same proportionality and hence

$$\varepsilon^* = \frac{\varepsilon R}{u_\tau^3} \qquad R = \text{pipe radius}$$

should be Reynolds number invariant.

It was demonstrated in Chapter 6, Figure 6.5, that the agreement between our measurements of ε^* and those of Lawn is very good, despite a large difference in Reynolds number, giving confidence both in the invariance of ε^* and in the method used to calculate ε. This method was therefore used, with $\alpha = 0.53$.

To find the inertial subrange the function $k^{5/3}\,\phi(k)$ was calculated from the spectral estimates and listed as a function of k. Since the uncertainty in the spectral estimates is ± 10% at 90% confidence level, the inertial subrange was identified as the region where

$$k^{5/3}\,\phi(k) = \text{constant} \quad (\pm\ 10\%)$$

ε is then given by

$$\varepsilon = \left[\frac{1}{\alpha}\, k^{5/3}\, \phi(k)\right]^{3/2}$$

so that the accuracy of ε is 50% greater than the accuracy in

determining the constant. It is also clear from equation (A2.3) that the accuracy of the spectral normalising factor is 25% of the accuracy of the estimate of ε. The accuracy in determining the constant was estimated by calculating the mean value and standard deviation of the estimates of $k^{5/3}\phi(k)$ within the identified subrange. The error was taken to be $\pm$ two standard deviations (95% confidence). The relative errors are listed in Table A2.1 (for Grid Flow) and Table A2.2 for Pipe flow at the lower Reynolds number (Run 2). The percentage error in the estimates of ε are also shown together with the percentage errors in the spectral normalising factors. It can be seen from these tables that an error of around 10% in the estimation of ε was typical although it was as high as 18% at $x/M = 40$ for grid flow. In all but two cases, the uncertainty in the normalising factors is less than half of the uncertainty in the spectral estimates themselves. The evidence therefore indicates that the procedure used was satisfactory for Newtonian spectra.

Since ε could not be calculated easily in any other way, it was assumed that the same procedure could be applied to the polymer spectra. In general, an inertial subrange could be found for most but not all of the polymer spectra. (In particular, such a range appeared to be absent in all spectra from the 200 ppm Separan solution and in some spectra obtained at positions nearer to the wall than those presented.) In locating the subrange it was sometimes found that one or two of the estimates of $k^{5/3}\phi(k)$ were outside the $\pm$ 10% range demanded in the Newtonian case. This condition was therefore relaxed for one or two isolated points but the values at the end points of the identified range were always within $\pm$ 10% of the mean value of the range.

Estimates of the accuracy of the procedure are shown in Tables A2.3 - A2.6 for all of the concentrations of Polyox studied. In

general, the accuracy of estimating ε is less than for the Newtonian cases and the error can be as high as 48%, giving an uncertainty of 12% in the spectral normalisation. This extreme case was not typical however and it can be seen from the tables that in 13 of the 16 cases studied the error in normalising factors is within the 10% uncertainty in the spectral estimates themselves. The evidence therefore suggests that the procedure adopted was not unreasonable.

Measuring Position (x/M)	Re_λ	Extent of Subrange (k_{max} / k_{min})	% error in $\langle k^{5/3}\ \phi(k)\rangle$	% error in ε	% error in transformation
20	48.1	2.7	6.4	9.6	2.4
30	29.6	2.7	6.4	9.6	2.4
40	29.6	2.5	11.8	18	4.4
50	27.3	1.7	6.8	10	2.5
60	27.9	3.3	7.2	11	2.7

Table A2.1

Estimates of the Accuracy of the Spectral Transformations

Grid Flow - Water

Measuring Position (ξ)	Re_λ	Extent of Subrange (k_{max} / k_{min})	% error in $\langle k^{5/3} \phi(k) \rangle$	% error in ε	% error in transformation
0	879	2.0	7.8	11.7	2.9
0.21	1173	2.1	5.8	8.7	2.2
0.43	1400	2.2	10	15	3.8
0.86	1502	2.4	8	12	3.0

Table A2.2

Estimates of the Accuracy of the Spectral Transformations

Pipe Flow - Water, Re = 24,600

Measuring Position (ξ)	Re_λ	Extent of Subrange (k_{max} / k_{min})	% error in $\langle k^{5/3}\ \phi(k)\rangle$	% error in ε	% error in transformation
0	1443	2.3	14	21	5.3
0.21	1539	3.0	6	9	2.3
0.43	1102	1.9	8	12	3.0
0.86	891	2.0	8	12	3.0

Table A2.3

Estimates of the Accuracy of the Spectral Transformations

Pipe Flow, 50 ppm WSR 301

Measuring Position (ξ)	Re_λ	Extent of Subrange (k_{max} / k_{min})	% error in $\langle k^{5/3} \phi(k) \rangle$	% error in ε	% error in transformation
0	1232	2.1	32	48	12
0.21	1594	2.3	20	30	7.5
0.43	1935	2.8	12	18	4.5
0.86	1894	2.2	10	15	3.8

Table A2.4

Estimates of the Accuracy of the Spectral Transformations

Pipe Flow - 100 ppm WSR 301

Measuring Position (ξ)	Re_λ	Extent of Subrange (k_{max} / k_{min})	% error in $\langle k^{5/3} \phi(k) \rangle$	% error in ε	% error in transformation
0	935	2.4	28	42	10
0.21	1279	3.2	12	18	4.5
0.43	1606	2.7	8	12	3
0.86	1626	2.2	8	12	3

Table A2.5

Estimates of the Accuracy of the Spectral Transformations

Pipe Flow - 250 ppm WSR 301

Measuring Position (ξ)	Re_λ	Extent of Subrange (k_{max} / k_{min})	% error in $\langle k^{5/3} \phi(k) \rangle$	% error in ε	% error in transformation
0	851	2.7	30	45	11
0.21	1092	2.4	32	48	12
0.43	1543	2.1	5.4	8.1	2
0.86	1590	2.6	7.0	11	2.6

Table A2.6

Estimates of the Accuracy of the Spectral Transformations

Pipe Flow - 500 ppm WSR 301